UNIWERSYTET ŚLĄSKI
WYDZIAŁ NAUK ŚCISŁYCH I TECHNICZNYCH
INSTYTUT CHEMII

ROZPRAWA DOKTORSKA

Biokompatybilne materiały polimerowe o ściśle kontrolowanej makrostrukturze i ich wpływ na stabilność substancji aktywnych w mieszaninach binarnych

Luiza Orszulak
9119

Promotor:
prof. dr hab. Kamil Kamiński

Katowice 2026

Składam serdeczne podziękowania mojemu Promotorowi,
***Panu prof. dr hab. Kamilowi Kamińskiemu** za nieocenioną opiekę merytoryczną,*
cierpliwość, inspirujące rozmowy, okazaną życzliwość
oraz stworzenie pełnej wsparcia przestrzeni dla mojego rozwoju naukowego

*Serdecznie dziękuję **Pani prof. dr hab. Ewie Oziminie-Kamińskiej***
za wszelką okazaną pomoc oraz cenne uwagi
udzielone mi podczas pracy nad tekstami publikacji

*Pragnę również podziękować **Pani dr inż. Roksanie Wygodzie***
za wprowadzenie mnie w tematykę polimerów, pomoc w syntezach,
ogromne wsparcie, cenne wskazówki oraz miłą atmosferę

*Dziękuję **Kolegom i Koleżankom z Zespołu** za stworzenie*
przyjaznej atmosfery, cenne rozmowy, codzienną życzliwość
oraz wiele dobrze spędzonych wspólnie chwil

Badania przeprowadzone na potrzeby niniejszej pracy doktorskiej były finansowane przez Ministerstwo Nauki i Szkolnictwa Wyższego w ramach projektu Perły Nauki pt. *„Biozgodne polimery o kontrolowanej taktyczności i ich wpływ na stabilność API w układach binarnych”* o numerze PN/01/0078/2022.

Dodatkowo, badania prowadzone na potrzeby niniejszej pracy doktorskiej były również w części finansowane przez Narodowe Centrum Nauki w ramach projektu OPUS 21 pt. *„Korelacje między strukturą supramolekularną, dynamiką molekularną, stabilnością fizyko-chemiczną i rozpuszczalnością w czystych farmaceutycznych substancjach aktywnych (APIs) oraz systemach binarnych API-substancja pomocnicza”* o numerze 2021/41/B/NZ7/01654, a także przez Narodowe Centrum Badań i Rozwoju w ramach projektu LIDER pt. *„Opracowanie innowacyjnych metod poprawy parametrów farmakokinetycznych i farmakodynamicznych wybranych substancji farmaceutycznie aktywnych (APIs)”* o numerze LIDER/28/0152/L-12/20/NCBR/2021.

Spis treści

Wykaz oznaczeń i skrótów

API	substancja aktywna (ang. *Active Pharmaceutical Ingredient*)
ASD	amorficzne stałe dyspersje (ang. *Amorphous Solid Dispersion*)
ATRP	polimeryzacja rodnikowa z przeniesieniem atomu (ang. *Atom Transfer Radical Polymerization*)
BDS	szerokopasmowa spektroskopia dielektryczna (ang. *Broadband Dielectric Spectroscopy*)
CRP	kontrolowana polimeryzacja rodnikowa (ang. *Controlled Radical Polymerization*)
CTA	czynnik przenoszący łańcuch (ang. *Chain Transfer Agent*)
Đ	dyspersyjność (ang. *dispersity*)
DDS	systemy dostarczania leków (ang. *Drug Delivery System*)
DSC	różnicowa kalorymetria skaningowa (ang. *Differential Scanning Calorimetry*)
ε_n"	znormalizowane straty dielektryczne
FaSSIF	symulowany płyn jelitowy w stanie na czczo o pH=6.5 (ang. *Fasted State Simulated Intestinal Fluid*)
FDA	Agencja Żywności i Leków (ang. *Food and Drug Administration*)
FRP	polimeryzacja wolnorodnikowa (ang. *Free Radical Polymerization*)
FT-IR	spektroskopia w podczerwieni z transformatą Fouriera (ang. *Fourier-Transform Infrared Spectroscopy*)
I	faza izotropowa
ITZ	itrakonazol
LAMs	monomery mniej aktywowane (ang. *Less Active Monomers*)
LC	ciekły kryształ (ang. *Liquid Crystal*)
***lin*PVP**	homopolimer PVP o topologii liniowej
MADIX	projektowanie makrocząsteczek poprzez wymianę ksantogenianów (ang. *Macromolecular Design by Interchange of Xanthate*)
MAMs	monomery bardziej aktywowane (ang. *More Active Monomers*)
M_n	liczbowo średnia masa cząsteczkowa (ang. *numer average molecular weight*)
MTZ	metronidazol
N	faza nematyczna
NAP	naproksen

NMR	spektroskopia magnetycznego rezonansu jądrowego (ang. *Nuclear Magnetic Resonance*)
PBD	pirybedyl
PVP	poliwinylopirolidon
PVP K30	homopolimer PVP komercyjnie dostępny
Q	wektor rozpraszania
RAFT	polimeryzacja z odwracalnym addycyjno-fragmentacyjnym przeniesieniem łańcucha (ang. *Reversible Addition-Fragmentation Chain-Transfer*)
SEC	chromatografia wykluczania (ang. *Size Exclusion Chromatography*)
Sm	faza smektyczna
***star*PVP**	homopolimer PVP o topologii trójramiennej gwiazdy
T	temperatura (ang. *temperature*)
T_c	temperatura krystalizacji (ang. *crystallization temperature*)
T_g	temperatura zeszklenia (ang. *glass transition temperature*)
T_m	temperatura topnienia (ang. *melting temperature*)
$T_{N\text{-}I}$	temperatura przejścia z fazy nematycznej do izotropowej
$T_{Sm\text{-}N}$	temperatura przejścia z fazy smektycznej do nematycznej
w/w	stosunek wagowy (ang. *weight/weight*)
XRD	dyfrakcja rentgenowska (ang. *X-Ray Diffraction*)
α	stopień krystalizacji
η	lepkość
ϕ	tempo grzania/chłodzenia

Wykaz rycin

1. Wprowadzenie

1.1. Polimery w naukach chemicznych i farmaceutycznych – właściwości, wymagania i znaczenie aplikacyjne

W ostatnich dekadach polimery stały się jedną z kluczowych grup materiałów wykorzystywanych zarówno w nauce, przemyśle, jak i w życiu codziennym. Ich szczególna wartość wynika z możliwości precyzyjnego projektowania struktury chemicznej, a tym samym dostosowywania właściwości fizykochemicznych do konkretnych zastosowań. Dzięki tej wszechstronności polimery znalazły zastosowanie nie tylko w klasycznych obszarach technologicznych, lecz także w nowoczesnych i wysoko wyspecjalizowanych rozwiązaniach medycznych.[1] Szczególnie dynamiczny rozwój materiałów polimerowych obserwuje się w naukach biomedycznych, gdzie stanowią one podstawę wielu funkcjonalnych systemów wykorzystywanych w diagnostyce, terapii oraz regeneracji tkanek. Polimery stosuje się m.in. do wytwarzania implantów i elementów wyrobów medycznych, takich jak stenty naczyniowe, cewniki, protezy czy komponenty wzierników medycznych. Ważną grupę ich zastosowań stanowią również specjalistyczne opatrunki, rusztowania wspomagające odbudowę tkanek oraz nośniki substancji aktywnych (API, ang. *Active Pharmaceutical Ingredient*).[2] Należy jednak podkreślić, że polimery przeznaczone do zastosowań biomedycznych muszą spełniać znacznie bardziej rygorystyczne wymagania niż materiały wykorzystywane w typowych aplikacjach technicznych. Przede wszystkim powinny cechować się biokompatybilnością, rozumianą jako brak działania toksycznego, immunogennego i kancerogennego. W zależności od przeznaczenia materiału istotna może być także jego bioinertność lub przeciwnie - kontrolowana bioaktywność, umożliwiająca pożądaną interakcję z otaczającymi tkankami. W wielu zastosowaniach kluczowe znaczenie ma również biodegradowalność, pozwalająca na stopniowy rozkład materiału w organizmie bez powstawania szkodliwych produktów ubocznych i bez konieczności jego późniejszego usuwania po spełnieniu odpowiedniej funkcji w organizmie (np. jak ma to miejsce w przypadku nici chirurgicznych). Ponadto polimery biomedyczne powinny charakteryzować się odpowiednimi właściwościami mechanicznymi, stabilnością chemiczną w warunkach fizjologicznych oraz możliwością sterylizacji bez utraty swojej funkcjonalności.[3,4]

Do grupy polimerów dopuszczonych do kontaktu z tkankami ludzkimi należą zarówno materiały naturalne, jak i syntetyczne. Wśród makrocząsteczek naturalnych szczególne znaczenie mają polisacharydy i białka, takie jak celuloza, chitozan czy kolagen. Z kolei do szeroko stosowanych

polimerów syntetycznych zalicza się m.in. poli(kwas mlekowy), poli(kwas glikolowy), ich kopolimery, a także poliuretany oraz polietylen o wysokiej gęstości.[5] Dobór odpowiedniego materiału jest każdorazowo uzależniony od konkretnego zastosowania oraz wymaganych właściwości biologicznych, mechanicznych i fizykochemicznych. Szczególnie interesującą, a zarazem wymagającą grupę stanowią polimery wykorzystywane w doustnych systemach dostarczania leków (DDS, ang. *Drug Delivery Systems*). W tym przypadku materiał polimerowy musi nie tylko pozostawać bezpieczny dla organizmu, lecz także spełniać dodatkowe wymagania związane z kontrolą uwalniania substancji czynnej. Polimery stosowane w tego typu formulacjach powinny być odporne na zmienne warunki panujące w przewodzie pokarmowym, w tym różnice pH oraz obecność enzymów trawiennych. Jednocześnie powinny umożliwiać precyzyjne sterowanie kinetyką uwalniania API, zapewniając odpowiednią biodostępność i stabilność leku. Istotna jest również ich zdolność do tworzenia pożądanych form farmaceutycznych, takich jak tabletki, kapsułki, mikrosfery czy hydrożele. Kluczowe znaczenie dla funkcjonalności polimerów w zastosowaniach farmaceutycznych ma ich struktura. Zarówno skład chemiczny, jak i architektura makrocząsteczek wpływają na szereg parametrów fizykochemicznych, takich jak stopień krystaliczności, mieszalność, przejścia fazowe, promień hydrodynamiczny czy elastyczność łańcuchów polimerowych. Właściwości te determinują z kolei cechy reologiczne i mechaniczne materiału, jego rozpuszczalność, zdolność do pęcznienia oraz tempo biodegradacji. W kontekście systemów DDS szczególnie istotne są również parametry makrostrukturalne, topologia, porowatość, powierzchnia właściwa, zdolność do tworzenia sieci przestrzennych oraz właściwości transportowe. Ich odpowiednia kontrola umożliwia projektowanie materiałów o pożądanej kinetyce uwalniania API. Przykładowo, zwiększenie porowatości może przyspieszać dyfuzję leku, podczas gdy wyższy stopień usieciowania zwykle prowadzi do jej spowolnienia.

Pomimo znaczącego postępu w obszarze projektowania polimerowych systemów dostarczania leków, nadal istnieje wiele wyzwań wymagających rozwiązania. Liczba materiałów polimerowych dopuszczonych do zastosowań farmaceutycznych i zaakceptowanych przez amerykańską Agencję Żywności i Leków (FDA, ang. *Food and Drug Administration*) pozostaje relatywnie ograniczona. Jednocześnie rosnące wymagania regulacyjne oraz konieczność zapewnienia wysokiego poziomu bezpieczeństwa sprawiają, że proces wprowadzania nowych polimerów do zastosowań medycznych i farmaceutycznych jest długotrwały, kosztowny i obarczony licznymi ograniczeniami. Z tego względu szczególnie istotne staje się pełniejsze zrozumienie, w jaki sposób właściwości fizykochemiczne oraz parametry powszechnie stosowanych materiałów polimerowych wpływają na biodostępność API. Należą do nich m.in. masa cząsteczkowa (M_n), dyspersyjność ($Đ$),

architektura i topologia makrocząsteczki, zdolność do samoorganizacji, taktyczność łańcucha polimerowego oraz charakter oddziaływań międzycząsteczkowych. Takie podejście pozwala nie tylko lepiej wykorzystać potencjał istniejących już polimerów, lecz także ograniczyć konieczność poszukiwania całkowicie nowych materiałów funkcjonalnych, których wdrożenie wymagałoby czasochłonnych i kosztownych badań bezpieczeństwa oraz skuteczności. W tym kontekście szczególnego znaczenia nabiera ponowna analiza znanych makrocząsteczek pod kątem aspektów ich struktury i funkcjonalności, które dotychczas nie zostały w pełni rozpoznane. Dotyczy to zwłaszcza wpływu architektury polimeru na oddziaływania z API, stabilność fizyczną formulacji, kontrolę krystalizacji, kinetykę uwalniania oraz poprawę rozpuszczalności i biodostępności substancji czynnych.

1.2. Poli(*N*-winylopirolidon) jako nośnik w systemach dostarczania leków – właściwości, ograniczenia i wyzwania syntetyczne

Wśród polimerów o ugruntowanym znaczeniu biomedycznym szczególnie istotne miejsce zajmuje poli(*N*-winylopirolidon) (PVP). Wynika to z szeregu jego korzystnych właściwości fizykochemicznych i biologicznych. Polimer ten charakteryzuje się wysoką rozpuszczalnością w wodzie oraz wielu rozpuszczalnikach organicznych, zdolnością do tworzenia kompleksów z substancjami czynnymi, a także właściwościami stabilizującymi i powłokotwórczymi. Dodatkowo wykazuje pełną biokompatybilność, nietoksyczność oraz zdolność do poprawy biodostępności leków poprzez zwiększenie ich rozpuszczalności i stabilności w środowisku biologicznym. Z tego względu PVP został dopuszczony do zastosowań medycznych oraz farmaceutycznych przez organizację FDA i od wielu lat znajduje szerokie zastosowanie jako nośnik w amorficznych stałych dyspersjach (ASD, ang. *Amorphous Solid Disspersion*), stabilizator w nanosystemach oraz składnik matryc umożliwiających kontrolowane uwalnianie API.[6–9]

W praktyce farmaceutycznej stosowane są przede wszystkim komercyjnie dostępne związki PVP o liniowej topologii łańcucha polimerowego. W konsekwencji w literaturze naukowej brakuje systematycznych badań dotyczących wpływu bardziej złożonej architektury makrocząsteczek (takich jak struktury rozgałęzione, gwiaździste czy sieciowane) na właściwości farmakokinetyczne i biofarmaceutyczne konkretnych substancji czynnych. Jest to istotne, ponieważ polimery liniowe mogą znacząco różnić się właściwościami od polimerów o takim samym składzie chemicznym, lecz odmiennej, nieliniowej topologii. Szczególne zainteresowanie badaczy budzą polimery gwiaździste i hiperrozgałęzione (dendrymeryczne), które w porównaniu ze swoimi liniowymi analogami

o zbliżonej masie cząsteczkowej posiadają unikalne właściwości, takie jak: (*i*) lepsza rozpuszczalność wynikająca ze zredukowanego stopnia splątań łańcuchów; (*ii*) mniejszy promień hydrodynamiczny; (*iii*) niższa lepkość roztworów; (*iv*) niższe temperatury przejść fazowych, tj. topnienia (T_m), zeszklenia (T_g) i krystalizacji (T_c) oraz (*v*) większa liczba funkcyjnych grup końcowych łańcucha, otwierająca liczne ścieżki do dalszych modyfikacji makrocząsteczek.[10–13] Mając na uwadze, że topologia polimeru istotnie wpływa na jego właściwości fizykochemiczne, można przypuszczać, że będzie ona również determinować sposób oddziaływania polimeru z substancją czynną w formulacji. Architektura makrocząsteczki może wpływać m.in. na zdolność do enkapsulacji leku, szybkość jego uwalniania, biodostępność oraz stabilność fizyczną układu. Pomimo tej pozornie oczywistej zależności, zagadnienie wpływu architektury makrocząsteczek na ich interakcje z lekami, a w konsekwencji także na możliwość zwiększania biodostępności API, pozostaje w literaturze naukowej wciąż niedostatecznie rozpoznane.

Jedną z głównych przyczyn tego stanu rzeczy są trudności syntetyczne związane z otrzymywaniem PVP o dobrze zdefiniowanej strukturze. Monomer, *N*-winylopirolidon (VP) jest związkiem zawierającym tzw. nieskoniugowaną grupę winylową, co oznacza, że grupa winylowa nie jest sprzężona z grupą karbonylową (**Rysunek 1**). Z tego względu VP zaliczany jest do monomerów *„mniej aktywowanych”* (LAMs, ang. *Less Activated Monomers*), których polimeryzacja w warunkach kontrolowanych jest szczególnie utrudniona. Obecność wiązania podwójnego w sąsiedztwie atomu azotu, będącego silnym donorem elektronów, sprzyja wysokiej reaktywności utworzonego centrum rodnikowego, które nie jest efektywnie stabilizowane rezonansowo. Cecha ta istotnie odróżnia monomery *N*-winylowe od monomerów zawierających sprzężone grupy winylowe (np. akrylany czy akrylamidy) oraz w bezpośredni sposób determinuje przebieg ich polimeryzacji. W rezultacie wzrasta podatność układu na reakcje uboczne, przede wszystkim przeniesienie łańcucha do monomeru lub rozpuszczalnika, co ogranicza kontrolę nad wzrostem makrocząsteczki i sprzyja powstawaniu produktów o szerokim rozkładzie mas molowych. W konsekwencji kontrolowana synteza PVP, mimo dynamicznego rozwoju chemii polimerów w ostatnich latach, nadal stanowi istotne wyzwanie. Dotyczy to zwłaszcza otrzymania materiałów o ściśle określonej M_n, niskiej $Đ$ oraz złożonej architekturze makrocząsteczkowej, co jest szczególnie ważne w kontekście zastosowań w sektorze farmaceutycznym.

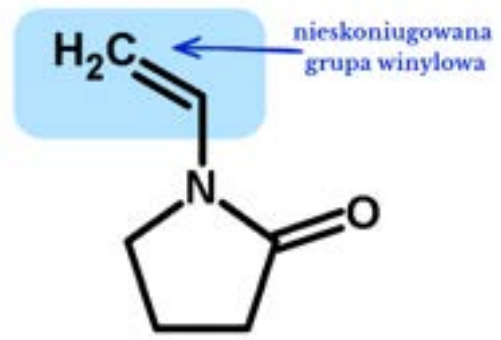

Rysunek 1. Struktura chemiczna *N*-winylopirolidonu wraz z zaznaczoną nieskoniugowaną grupą winylową.

Z technologicznego punktu widzenia podstawową i nadal najczęściej stosowaną metodą otrzymywania PVP pozostaje klasyczna polimeryzacja wolnorodnikowa (FRP, ang. *Free Radical Polymerization*) prowadzona w roztworze. W skali przemysłowej wysokocząsteczkowe związki PVP otrzymuje się głównie w środowisku wodnym, często z zastosowaniem nadtlenku wodoru jako inicjatora.[14,15] Metoda ta jest relatywnie prosta, wydajna i dobrze dostosowana zarówno do reaktywności VP, jak i do wymagań procesu przemysłowego. Jej zasadniczym ograniczeniem pozostaje jednak niewielka kontrola nad parametrami otrzymywanego polimeru. Choć poprzez regulację stężenia nadtlenku wodoru w układzie można w pewnym stopniu modulować masę molową finalnego produktu, FRP nie pozwala na precyzyjne kontrolowanie wzrostu łańcuchów makrocząsteczkowych. W efekcie, charakterystyczną cechą komercyjnie dostępnego PVP jest szeroki rozkład M_n, wynikający m.in. z reakcji przeniesienia łańcucha oraz ograniczonej kontroli nad przebiegiem procesu. Zjawisko to może być niekorzystne z punktu widzenia wybranych zastosowań biomedycznych, szczególnie w projektowaniu nowych systemów DDS o kontrolowanym profilu uwalniania substancji czynnej. Ponadto PVP otrzymywany klasyczną drogą wolnorodnikową nie zawiera aktywnych grup końcowych, co istotnie ogranicza możliwość jego dalszej funkcjonalizacji, na przykład poprzez syntezę kopolimerów blokowych. W rezultacie możliwości modyfikowania właściwości PVP poprzez świadome projektowanie jego struktury makrocząsteczkowej pozostają w dużej mierze niewykorzystane.

W celu zwiększenia kontroli nad przebiegiem procesu polimeryzacji można stosować różne techniki kontrolowanej polimeryzacji rodnikowej (CRP, ang. *Controlled Radical Polymerization*). Metody te polegają na szybkim ustaleniu równowagi między aktywnym, propagującym łańcuchem polimerowym a jego uśpioną formą. Niestety, alternatywne techniki CRP, takie jak polimeryzacja z przeniesieniem atomu (ATRP, ang. *Atom Transfer Radical Polymerization*), które z powodzeniem stosuje się w przypadku monomerów bardziej aktywowanych (MAMs, ang. *More Activated Monomers*), nie mogą być w prosty sposób przeniesione na układ *N*-winylopirolidonowy.[16,17] Wynika to przede wszystkim z niekorzystnej równowagi pomiędzy formami aktywnymi i nieaktywnymi łańcuchów, ograniczonej stabilności odpowiednich kompleksów katalitycznych oraz trudności w kontrolowaniu reakcji propagacji i terminacji. Dodatkowo obecność ugrupowania laktamowego w strukturze monomeru może wpływać na przebieg reakcji poprzez oddziaływania z inicjatorem i/lub katalizatorem, co prowadzi do jego dezaktywacji (zatrucia) i znacząco komplikuje proces polimeryzacji.[17,18] W efekcie uzyskanie PVP o wąskim rozkładzie M_n i dobrze zdefiniowanych końcach łańcuchów przy użyciu ATRP jest bardzo mało efektywne. Dotychczas w literaturze odnotowano tylko jedną udaną próbę otrzymania PVP przy zastosowaniu tej strategii syntetycznej,

uzyskując makromolekuły o M_n=18 600 i $Đ$=1.26.[19] Z kolei, próby zwiększenia masy molowej otrzymywanych polimerów prowadzą do znacznego pogorszenia kontroli nad przebiegiem polimeryzacji, a tym samym nad parametrami makrocząsteczkowymi produktu. W praktyce oznacza to, że synteza PVP metodą ATRP jest możliwa, wymaga jednak niezwykle starannego doboru katalizatora, ligandu i warunków reakcji oraz pozwala na otrzymywanie polimerów tylko w wąskim zakresie M_n. Z tego względu nie stanowi ona najprostszej ani najbardziej naturalnej techniki kontrolowanej syntezy PVP. Dodatkowym ograniczeniem tej metody jest konieczność stosowania związków kompleksowych metali przejściowych, co w przypadku materiałów przeznaczonych do zastosowań biomedycznych wiąże się z koniecznością bardzo dokładnego oczyszczania produktu końcowego z pozostałości katalizatora. Może to istotnie komplikować proces technologiczny oraz ograniczać atrakcyjność tej metody w kontekście potencjalnych zastosowań farmaceutycznych.

Znacznie większe znaczenie w kontrolowanej syntezie PVP, zwłaszcza w przypadku materiałów o dobrze zdefiniowanej budowie, takich jak kopolimery blokowe czy układy o bardziej złożonej, rozgałęzionej architekturze, zyskała polimeryzacja z odwracalnym addycyjno-fragmentacyjnym przeniesieniem łańcucha (RAFT, ang. *Reversible Addition-Fragmentation Chain-Transfer Polymerization*). W przypadku monomerów *N*-winylowych szczególnie istotne okazały się strategie wykorzystujące odpowiednio dobrane ksantogeniany lub ditiokarbaminiany, określane również jako MADIX (ang. *Macromolecular Design by Interchange of Xanthate*).[16,20] Techniki te umożliwiają otrzymywanie polimerów o precyzyjnie kontrolowanych parametrach strukturalnych. Do istotnych zalet polimeryzacji RAFT należy także możliwość prowadzenia reakcji w szerokim zakresie warunków oraz w różnych środowiskach reakcyjnych. Kluczową rolę w tym rodzaju polimeryzacji odgrywają czynniki przeniesienia łańcucha (CTA, ang. *Chain Transfer Agents*), odpowiedzialne za ustanowienie odwracalnej równowagi addycji i fragmentacji (**Rysunek 2**). W pierwszym etapie reakcji generowany jest rodnik inicjujący, który zapoczątkowuje wzrost łańcucha polimerowego. Propagujący łańcuch reaguje następnie z czynnikiem RAFT, co prowadzi do funkcjonalizacji jego końca odpowiednim ugrupowaniem stabilizującym (grupa *Z*) oraz przejścia makrocząsteczki w formę uśpioną. Jednocześnie fragment opuszczający (grupa *R*) cząsteczkę pierwotnego czynnika RAFT inicjuje wzrost kolejnego łańcucha polimerowego. W dalszym przebiegu reakcji dochodzi do dynamicznej wymiany pomiędzy formami aktywnymi i uśpionymi, dzięki czemu poszczególne łańcuchy polimerowe rosną w zbliżonym tempie (**Rysunek 2**). W efekcie możliwe jest otrzymywanie makrocząsteczek o porównywalnej długości, a tym samym o węższym rozkładzie mas molowych.[21,22] Należy jednak podkreślić, że skuteczność tego typu polimeryzacji w dużym stopniu zależy od właściwego dopasowania CTA do rodzaju zastosowanego monomeru.

W przypadku monomerów *N*-winylowych dostępne są dobrze dopasowane, komercyjne czynniki RAFT umożliwiające otrzymywanie liniowych homopolimerów PVP. Nadal jednak ograniczona pozostaje dostępność wielofunkcyjnych CTA, które pozwalałyby na bezpośrednią syntezę bardziej złożonych architektur makrocząsteczkowych.

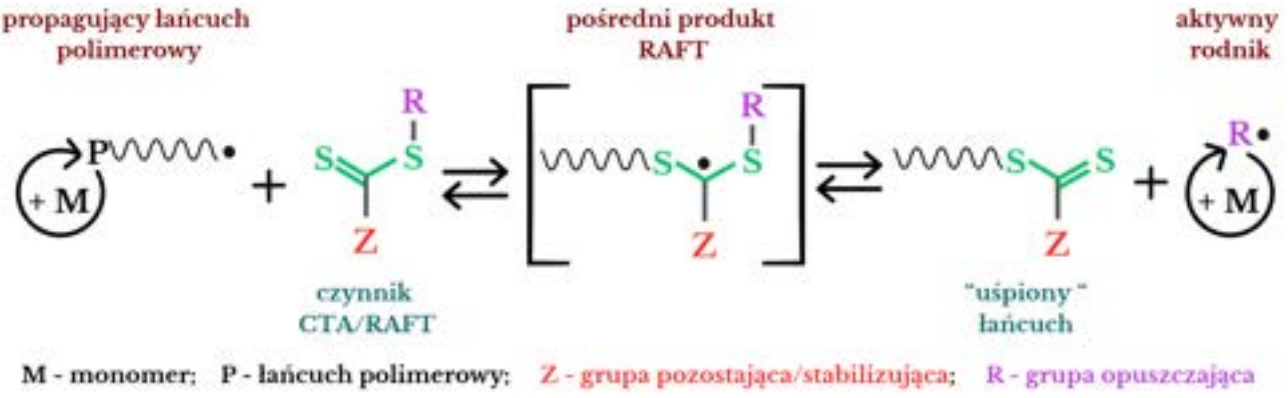

Rysunek 2. Uproszczony schemat mechanizmu polimeryzacji typu RAFT.

Podsumowując, dobór metody syntezy PVP powinien być ściśle uzależniony od oczekiwanych właściwości końcowego materiału. W przypadku konwencjonalnego PVP, przeznaczonego do standardowych zastosowań użytkowych, najbardziej odpowiednią metodą pozostaje klasyczna polimeryzacja wolnorodnikowa. Jeżeli jednak celem jest otrzymanie polimeru do zastosowań specjalnych, charakteryzującego się kontrolowaną M_n, niską $Đ$ oraz precyzyjnie zaprojektowaną architekturą, niezbędne staje się zastosowanie wyspecjalizowanych strategii kontrolowanej polimeryzacji rodnikowej, przede wszystkim RAFT/MADIX. Ma to szczególne znaczenie w kontekście zastosowań biomedycznych i farmaceutycznych, w których wymagane są nie tylko wysoka czystość i biokompatybilność materiału, lecz także ścisła kontrola jego struktury. Dotyczy to zwłaszcza polimerów o złożonej architekturze, takich jak układy gwiaździste, rozgałęzione czy szczotkowe, których otrzymywanie jest znacznie bardziej wymagające niż synteza klasycznych makrocząsteczek liniowych. Z tego względu rozwój kontrolowanych strategii syntezy PVP oraz innych polimerów przeznaczonych do zastosowań biomedycznych, a także nowych wielofunkcyjnych układów katalityczno-inicjujących, należy uznać za jeden z kluczowych kierunków współczesnej chemii polimerów, warunkujący dalszy postęp w projektowaniu nowoczesnych materiałów medycznych i farmaceutycznych.

1.3. Amorficzne formy substancji leczniczych – stabilność fizyczna i rola układów API-polimer

Zapotrzebowanie na precyzyjnie zaprojektowane biokompatybilne makrocząsteczki wynika bezpośrednio z wyzwań stojących przed współczesnym sektorem farmaceutycznym. Jednym z najistotniejszych jest poprawa rozpuszczalności API. Najnowsze dane wskazują, że aż 50% substancji aktywnych (w formie krystalicznej) wprowadzanych na rynek oraz nawet 70–90% API będących w fazie rozwoju charakteryzuje się niską rozpuszczalnością – są one zaliczane do II lub IV klasy według systemu BCS (ang. *Biopharmaceutics Classification System*, **Rysunek 3**).[23,24] Ograniczona rozpuszczalność tych substancji prowadzi do słabego wchłaniania w organizmie, a w konsekwencji do niskiej biodostępności po podaniu doustnym. Aby pokonać ten problem, opracowano szereg różnych strategii. Jako jedną z nich można wymienić tworzenie soli, jednak metoda ta wymaga modyfikacji struktury chemicznej cząsteczki API, co wiąże się z koniecznością przeprowadzenia na późniejszym etapie dodatkowych, kosztownych badań bezpieczeństwa i skuteczności.[25,26] Z kolei jednym z bardziej uniwersalnych i powszechnie stosowanych rozwiązań, niewymagających ingerencji w strukturę chemiczną API jest amorfizacja.[26,27] Proces ten polega na przekształceniu formy krystalicznej w formę amorficzną, charakteryzującą się brakiem uporządkowania dalekiego zasięgu (**Rysunek 4**). Dzięki temu substancje czynne w formie amorficznej wykazują znacznie większą rozpuszczalność i biodostępność, jednak ich praktyczne zastosowanie ogranicza niska stabilność termodynamiczna, prowadząca do niepożądanego procesu rekrystalizacji podczas przechowywania.[28,29] Wspomniane ograniczenia sprawiają, że wiele obiecujących substancji nie trafia do pacjentów, gdyż ich formulacja nie gwarantuje wystarczającej trwałości. Z tego powodu kluczowym zagadnieniem badawczym staje się skuteczna stabilizacja stanu amorficznego API.

Rysunek 3. Podział substancji aktywnych według systemu klasyfikacji BCS.

Jedną z najczęściej stosowanych strategii w tym zakresie jest tworzenie amorficznych stałych dyspersji (ASD)/mieszanin binarnych API–polimer, w których obecność makrocząsteczek ogranicza mobilność API oraz hamuje proces nukleacji i wzrostu kryształów.[30–33] W tym kontekście kluczową, choć często niedocenianą rolę odgrywają parametry fizykochemiczne substancji pomocniczych. To one w dużej mierze determinują prawidłowe działanie leku, wpływają na jego biodostępność, kontrolowane uwalnianie, stabilność i trwałość produktu, a tym samym na realną skuteczność terapeutyczną. Wśród substancji pomocniczych stosowanych w formulacjach farmaceutycznych szczególne znaczenie zyskały w ostatnich latach polimery. Mimo ich dużego potencjału liczba komercyjnie dostępnych makrocząsteczek przeznaczonych do zastosowań farmaceutycznych pozostaje ograniczona. Wynika to przede wszystkim z szeregu restrykcyjnych wymagań (prawnych i jakościowych), które muszą zostać spełnione przed wprowadzeniem danego polimeru do formulacji z API. Jednocześnie polimery obecnie stosowane w formulacjach farmaceutycznych zazwyczaj nie charakteryzują się ściśle kontrolowaną strukturą i nie są projektowane z myślą o konkretnych substancjach aktywnych. Może to prowadzić do wyciągania zbyt daleko idących wniosków dotyczących korelacji między parametrami makrostrukturalnymi polimeru a stabilnością API. W przypadku makromolekuł o niejednorodnej budowie, wynikającej m.in. z szerokiego rozrzutu długości łańcuchów polimerowych, a tym samym wysokiej dyspersyjności, jednoznaczne powiązanie zachowania API z właściwościami matrycy polimerowej jest szczególnie trudne. Tymczasem pełne zrozumienie zależności między architekturą polimeru a zachowaniem substancji aktywnej ma kluczowe znaczenie dla racjonalnego projektowania zaawansowanych układów binarnych o ulepszonych właściwościach fizykochemicznych i farmakokinetycznych. W tym kontekście zaskakujące pozostaje, że sektor farmaceutyczny wciąż w dużej mierze opiera się na komercyjnie dostępnych polimerach o słabo zdefiniowanych parametrach makromolekularnych. Jest to tym bardziej istotne, że współczesna inżynieria polimerowa oferuje szerokie możliwości precyzyjnego sterowania topologią, taktycznością, masą molową, dyspersyjnością oraz funkcjonalnością łańcucha polimerowego. Parametry te mogą z kolei znacząco wpływać na właściwości finalnego produktu farmaceutycznego. W tym aspekcie, szczególnie interesującym rozwiązaniem wydaje się zastosowanie poli(*N*-winylopirolidonu) (PVP), omówionego szczegółowo w poprzednim podrozdziale.

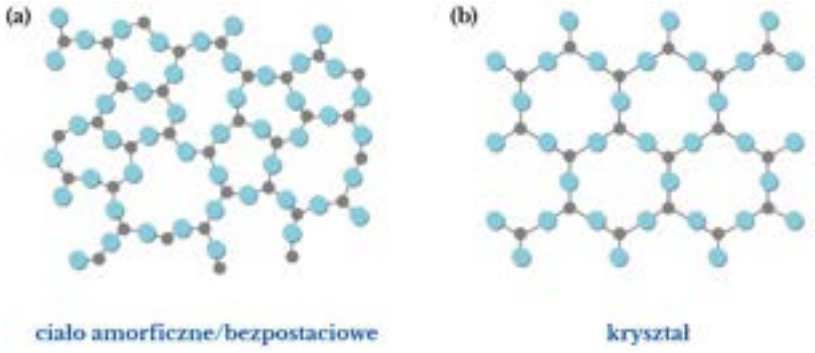

Rysunek 4. Schemat prezentujący (a) ciało amorficzne oraz (b) ciało krystaliczne.

Makrocząsteczka ta łączy szereg korzystnych cech (takich jak wysoka temperatura zeszklenia (T_g), biokompatybilność oraz dobra rozpuszczalność), które czynią ją atrakcyjną matrycą do stabilizacji amorficznych form substancji aktywnych.[7,34] Jednocześnie, ze względu na trudności syntetyczne związane z otrzymywaniem PVP o kontrolowanej architekturze, wpływ topologii tego polimeru na stabilność fizyczną układów amorficznych pozostaje zagadnieniem praktycznie nierozpoznanym.

1.4. Charakterystyka modeli substancji aktywnych wykorzystanych w rozprawie

W kontekście przedstawionych powyżej zagadnień zasadne jest systematyczne zbadanie wpływu architektury PVP na zachowanie substancji leczniczych o zróżnicowanej strukturze chemicznej oraz odmiennych właściwościach fizykochemicznych. W niniejszej rozprawie jako związki modelowe wybrano cztery substancje aktywne: metronidazol (MTZ), naproksen (NAP), itrakonazol (ITZ) oraz pirybedyl (PBD). Struktury chemiczne niniejszych API zaprezentowano na **Rysunku 5**. Dobór ten pozwala na wszechstronne porównanie, ponieważ każdy z wymienionych związków reprezentuje odmienny problem formulacyjny, co umożliwia analizę różnych aspektów naukowych.

Pierwszą grupę badanych substancji aktywnych stanowiły związki wykazujące wysoką tendencję do rekrystalizacji, tj. MTZ oraz NAP. Zostały one wykorzystane jako modelowe API do oceny wpływu PVP o różnej budowie na proces krystalizacji w układach binarnych typu API–polimer. Jak szczegółowo opisano w poprzednim podrozdziale, przekształcenie substancji aktywnej do postaci amorficznej należy do najskuteczniejszych strategii poprawy jej rozpuszczalności, a w konsekwencji również biodostępności. Należy jednak podkreślić, że ze względu na brak uporządkowania dalekiego zasięgu układy amorficzne charakteryzują się podwyższoną energią swobodną Gibbsa, co czyni je termodynamicznie niestabilnymi.[28] W przypadku substancji o wysokiej

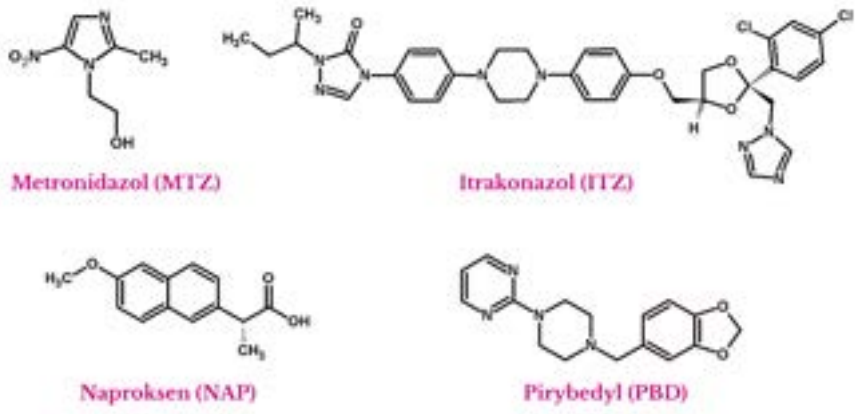

Rysunek 5. Struktury chemiczne substancji aktywnych badanych w rozprawie doktorskiej.

skłonności do krystalizacji spontaniczne przejście z fazy amorficznej do stabilniejszej fazy krystalicznej może zachodzić bardzo szybko zarówno na etapie wytwarzania i przechowywania formulacji, jak i *in vivo*, podczas rozpuszczania leku w płynach ustrojowych.

Konsekwencją tego zjawiska może być szybka precypitacja API w przewodzie pokarmowym, prowadząca do istotnego obniżenia jego stężenia w miejscu wchłaniania. W rezultacie korzyści wynikające z amorfizacji mogą zostać znacząco ograniczone lub całkowicie utracone, co przekłada się na nieprzewidywalny profil farmakokinetyczny oraz zwiększone ryzyko niepowodzenia terapii. Z tego względu jednym z kluczowych wyzwań technologicznych pozostaje stabilizacja układów amorficznych poprzez hamowanie nukleacji oraz wzrostu kryształów, najczęściej z wykorzystaniem odpowiednio dobranych lub zaprojektowanych matryc polimerowych. Do rzetelnej oceny skuteczności nowych strategii stabilizacji niezbędny jest dobór takich API, które ze względu na swoje właściwości fizykochemiczne stanowią szczególnie wymagający model badawczy. W tym kontekście MTZ i NAP (**Rysunek 5**) stanowią wartościowe związki modelowe, ponieważ wykazują silną tendencję do szybkiej krystalizacji ze stanu przechłodzonej cieczy.[35–37] Otrzymanie tych substancji w postaci amorficznej bez udziału efektywnych inhibitorów krystalizacji jest praktycznie niemożliwe, ponieważ wymagałoby zastosowania bardzo dużych szybkości chłodzenia, rzędu setek tysięcy K/s, co pozostaje poza zakresem typowych warunków laboratoryjnych. Zastosowanie MTZ i NAP w badaniach formulacyjnych pozwala poddać badane polimery PVP rygorystycznej ocenie pod kątem ich zdolności do hamowania niepożądanego procesu rekrystalizacji. Umożliwia to nie tylko porównanie skuteczności poszczególnych topologii PVP w stabilizacji układów amorficznych, lecz także lepsze zrozumienie mechanizmów oddziaływań API–polimer, które determinują stabilność nowoczesnych postaci leku.

Kolejną niezwykle interesującą grupę substancji aktywnych stanowią związki wykazujące właściwości ciekłokrystaliczne. Ciekłe kryształy (LC, ang. *Liquid Crystal*) definiuje się jako fazy pośrednie pomiędzy stanem ciekłym a stałym. Łączą one cechy obu tych stanów: z jednej strony charakteryzują się częściowym uporządkowaniem molekularnym, typowym dla ciał stałych, z drugiej zaś zachowują pewien stopień ruchliwości cząsteczek, właściwy cieczom (**Rysunek 6**).[38] Należy przy tym zaznaczyć, że zdolność do tworzenia faz ciekłokrystalicznych nie jest cechą wszystkich związków chemicznych. Występuje ona przede wszystkim w przypadku cząsteczek o anizotropowym kształcie, najczęściej wydłużonych struktur prętopodobnych lub układów dyskopodobnych.[39,40] Wykorzystanie właściwości ciekłokrystalicznych niektórych substancji aktywnych może stanowić jedną ze strategii modulowania szybkości ich uwalniania, a tym samym poprawy biodostępności. Dotychczas zidentyfikowano i opisano kilka API zdolnych do tworzenia faz ciekłokrystalicznych,

uwzględniając zarówno rodzaje generowanych przez nie mezofaz, jak i metody ich otrzymywania. W zależności od mechanizmu powstawania fazy ciekłokrystalicznej LC dzieli się na dwie główne grupy: (*i*) ciekłe kryształy termotropowe, w których mezofaza pojawia się wskutek zmiany temperatury (podczas ogrzewania lub chłodzenia) oraz (*ii*) ciekłe kryształy liotropowe, w których powstanie mezofazy zależy od osiągnięcia określonego stężenia molekuł, czyli mezogenów, w rozpuszczalniku, przy danej temperaturze.[41] Badania ukierunkowane na szczegółową charakterystykę farmaceutyków tworzących fazy ciekłokrystaliczne są w pełni uzasadnione. Odmienna organizacja przestrzenna cząsteczek oraz wyższa energia swobodna Gibbsa substancji aktywnej w mezofazie mogą bowiem prowadzić do zwiększenia szybkości rozpuszczania, a w konsekwencji do poprawy biodostępności w porównaniu z jej krystalicznym odpowiednikiem.[42]

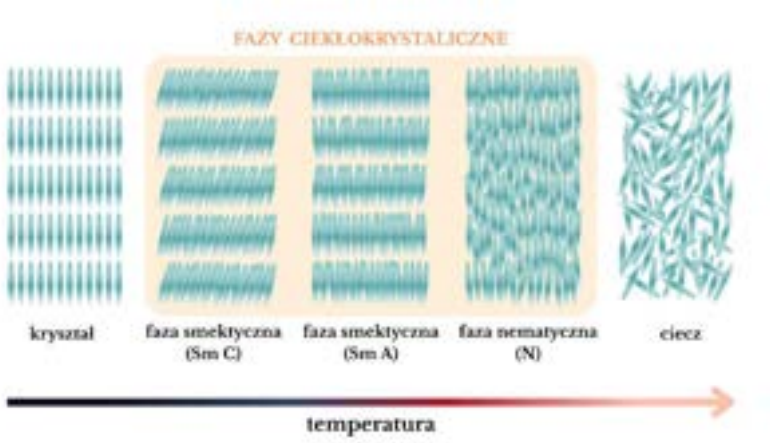

Rysunek 6. Schematyczne porównanie uporządkowania molekularnego w fazie krystalicznej, wybranych fazach ciekłokrystalicznych oraz fazie ciekłej wraz ze wzrostem temperatury.

W ciągu ostatnich dwóch dekad szczególnym zainteresowaniem w kontekście badań nad fazami ciekłokrystalicznymi oraz stanem amorficznym/szklistym cieszy się itrakonazol (ITZ). Jest to substancja aktywna z grupy azolowych leków przeciwgrzybiczych, należąca do II klasy według systemu BCS (**Rysunek 5**), charakteryzująca się wyjątkowo niską rozpuszczalnością w wodzie, wynoszącą zaledwie 1 ng/mL.[43] Liczne badania dotyczące ITZ wykazały, że jego uporządkowanie ciekłokrystaliczne można modulować za pomocą różnych metod fizycznych i chemicznych, co stwarza możliwość kontrolowania wybranych właściwości tej substancji aktywnej. Przykładowo, osadzanie par ITZ, ograniczenie przestrzenne, a także kontrola szybkości chłodzenia tego związku z fazy ciekłej umożliwiają otrzymywanie materiałów o odmiennym stopniu uporządkowania ciekłokrystalicznego.[44–48] Jednocześnie wciąż brakuje badań koncentrujących się na wpływie struktury wysokocząsteczkowych substancji pomocniczych na organizację molekularną modelowej cząsteczki ITZ, a w konsekwencji również na jej rozpuszczalność i potencjalną biodostępność. Zagadnienie to wydaje się szczególnie istotne w kontekście projektowania formulacji, w których odpowiednio dobrana matryca polimerowa mogłaby nie tylko stabilizować wybraną formę fizyczną tej API, lecz także wpływać na jej uporządkowanie molekularne i właściwości użytkowe.

Ponadto, interesującymi substancjami aktywnymi do badań nad wpływem topologii makrocząsteczek w ASD są związki, których zastosowanie terapeutyczne wiąże się z istotnymi ograniczeniami biodostępności. W tym kontekście szczególną uwagę zwraca pirybedyl (PBD) - API stosowana w terapii choroby Parkinsona. Jego skuteczność kliniczna po podaniu doustnym jest istotnie ograniczona ze względu na bardzo niską biodostępność, wynoszącą poniżej 10%. Wynika ona przede wszystkim z intensywnego metabolizmu pierwszego przejścia przez wątrobę oraz krótkiego biologicznego okresu półtrwania. W konsekwencji PBD wymaga częstego dawkowania, zwykle w zakresie 3–5 tabletek na dobę.[49,50] Należy jednak podkreślić, że choć metabolizm pierwszego przejścia stanowi główną przyczynę niskiej biodostępności tej API, istotne znaczenie może mieć również ograniczona ilość leku dostępna do wchłonięcia w przewodzie pokarmowym. Około 50% podanej dawki jest eliminowane z organizmu w ciągu 24 godzin, co dodatkowo wskazuje na nieefektywność obecnej doustnej drogi podania. W związku z tym poprawa rozpuszczalności PBD przy zastosowaniu odpowiednio dobranych substancji pomocniczych mogłaby potencjalnie zwiększyć ilość API wchłanianej w jelitach, a następnie przedostającego się do krążenia ogólnego. Większa ilość zaabsorbowanej substancji mogłaby z kolei przełożyć się na poprawę skuteczności terapeutycznej, mimo utrzymującego się wpływu metabolizmu wątrobowego. Co istotne, badania prowadzone w ciągu ostatnich dwóch dekad wykazały, że oprócz łagodzenia objawów motorycznych choroby Parkinsona, PBD może również korzystnie wpływać na objawy niemotoryczne, takie jak apatia czy zaburzenia funkcji poznawczych. Obserwacje te przyczyniły się do ponownego wzrostu zainteresowania tą API i mogą w przyszłości zwiększyć zakres jego zastosowania klinicznego.[50–52] Z uwagi na niską efektywność obecnie stosowanej doustnej drogi podawania PBD, poszukiwanie nowych matryc polimerowych oraz ich wykorzystanie w nowoczesnych systemach DDS stanowią ważne i perspektywiczne kierunki badań.[53] W tym kontekście PBD może być traktowany jako wartościowy model do oceny, czy odpowiednio zaprojektowana architektura polimeru jest w stanie poprawić właściwości formulacyjne substancji aktywnych o szczególnie niekorzystnym profilu farmakokinetycznym.

Podsumowując, pomimo dynamicznego rozwoju badań nad amorficznymi wieloskładnikowymi układami farmaceutycznymi, nadal istnieje istotna luka poznawcza dotycząca relacji między architekturą polimeru a jego rzeczywistą funkcją stabilizującą i modulującą w odniesieniu do różnych API. W literaturze szeroko opisano pozytywny wpływ polimerów na hamowanie krystalizacji, jednak znacznie rzadziej podejmowano systematyczną analizę tego, jak topologia makrocząsteczek wpływają na przebieg przemian fazowych, mobilność molekularną, porządek mezomorficzny (ciekłokrystaliczny) czy końcowe właściwości biofarmaceutyczne układu.

Wypełnienie tej luki jest istotne zarówno z punktu widzenia badań podstawowych, jak i projektowania formulacji farmaceutycznych opartych na racjonalnym doborze nośników polimerowych. Należy podkreślić, że choć wpływ długości łańcucha polimerowego na zachowanie API był już przedmiotem badań literaturowych, dotychczas analizowane polimery cechowały się wysoką $Đ$, co ogranicza możliwość jednoznacznej interpretacji uzyskanych wyników. Natomiast w niniejszej pracy podjęto próbę systematycznego zbadania wpływu długości łańcucha (M_n) polimerów o niskiej/umiarkowanej $Đ$ przy jednoczesnym uwzględnieniu roli topologii makrocząsteczek na stabilność fizyczną, przejścia fazowe czy biodostępność API w mieszaninach binarnych. Tym samym praca ta może stanowić podstawę do bardziej racjonalnego projektowania układów polimer–substancja czynna oraz wyznaczać kierunek dalszych badań nad zależnościami między strukturą makrocząsteczki a właściwościami API.

2. Cele i założenia pracy

W świetle zagadnień przedstawionych w Rozdziale 1 głównym celem niniejszej rozprawy doktorskiej było otrzymanie dobrze zdefiniowanych makrocząsteczek poli(*N*-winylopirolidonu) (PVP) o zróżnicowanej topologii oraz określenie, w jaki sposób ich architektura i parametry makrostrukturalne wpływają na właściwości fizyczne i biofarmaceutyczne wybranych substancji aktywnych. Polimery o ściśle kontrolowanych parametrach, takich jak dobrze zdefiniowana M_n oraz niska $Đ$, stwarzają wyjątkową możliwość opracowania bardziej uniwersalnego obrazu zachowania API w matrycy polimerowej. Pozwala to lepiej zrozumieć wpływ właściwości polimeru na stabilność fizyczną, rozpuszczalność oraz ogólne zachowanie API w formulacjach farmaceutycznych. W związku z powyższym główne założenia badawcze niniejszej pracy obejmowały:

- opracowanie nowych dróg syntezy dobrze zdefiniowanych homopolimerów PVP o zróżnicowanej topologii oraz ściśle kontrolowanych parametrach makrostrukturalnych;
- określenie zależności między topologią, długością łańcucha polimerowego oraz dyspersyjnością PVP a zdolnością tych makrocząsteczek do hamowania rekrystalizacji wybranych substancji aktywnych w postaci amorficznej;
- ocenę wpływu topologii polimeru na charakter oddziaływań międzycząsteczkowych determinujących stabilność fizyczną formulacji typu API–polimer;
- zbadanie możliwości modulowania uporządkowania molekularnego oraz temperatur przejść fazowych API poprzez zastosowanie polimerów PVP o odpowiednio dobranej architekturze, ze szczególnym uwzględnieniem układów ciekłokrystalicznych;
- ocenę wpływu architektury oraz charakteru chemicznego polimerów, w tym ich hydrofilowości lub amfifilowości, na rozpuszczalność, stabilność fizyczną oraz parametry farmakokinetyczne wybranych API;
- określenie, czy topologia polimerów może wpływać na selektywne faworyzowanie oraz stabilizację określonych form polimorficznych substancji aktywnych.

Zatem, niniejsza rozprawa ma charakter interdyscyplinarny i łączy elementy chemii polimerów, chemii fizycznej, nauki o materiałach, technologii farmaceutycznej oraz biofarmacji. Jej istota polega nie tylko na opisaniu wpływu wybranych polimerów na konkretne substancje czynne, lecz przede wszystkim na wykazaniu, że właściwości makrocząsteczek mogą być traktowane jako narzędzie świadomego projektowania układów farmaceutycznych o kontrolowanej stabilności i ulepszonych właściwościach użytkowych. Przedstawione wyniki wpisują się tym samym w aktualny nurt badań nad racjonalnym projektowaniem formulacji dla substancji słabo

rozpuszczalnych i niestabilnych fizycznie, a zarazem wskazują kierunki dalszych prac nad wykorzystaniem architektury polimerów w technologii postaci leku.

Rezultaty wszystkich przeprowadzonych eksperymentów zostały opublikowane w międzynarodowych czasopismach naukowych z listy filadelfijskiej o łącznej punktacji Impact Factor (IF)=18.1 oraz łącznej punktacji MNiSW=480 pkt.:

P1. L. Orszulak, T. Lamrani, M. Tarnacka, B. Hachuła, K. Jurkiewicz, P. Zioła, A. Mrozek-Wilczkiewicz, E. Kamińska, K. Kamiński, **The impact of various poly(vinylpyrrolidone) polymers on the crystallization process of metronidazole**, *Pharmaceutics*, 2024, 16 (1), 136. ***(IF=4.8; MNiSW=100 pkt.)***

P2. L. Orszulak, P. Włodarczyk, B. Hachuła, T. Lamrani, K. Jurkiewicz, M. Tarnacka, M. Hreczka, K. Kamiński, E. Kamińska, **Inhibition of naproxen crystallization by polymers: The role of topology and chain length of polyvinylpyrrolidone macromolecules**, *European Journal of Pharmaceutics and Biopharmaceutics*, 2025, 207, 114581. ***(IF=4.3; MNiSW=100 pkt.)***

P3. L. Orszulak, T. Lamrani, R. Bernat, M. Tarnacka, D. Żakowiecki, K. Jurkiewicz, P. Zioła, A. Mrozek-Wilczkiewicz, A. Zięba, K. Kamiński, E. Kamińska, **The influence of PVP polymer topology on the liquid crystalline order of itraconazole in binary systems**, *Molecular Pharmaceutics*, 2024, 21 (6), 3027−3039. ***(IF=4.5; MNiSW=140 pkt.)***

P4. L. Orszulak, A. Minecka, R. Bernat, T. Lamrani, K. Jurkiewicz, B. Hachuła, M. Tarnacka, M. Geppert-Rybczyńska, M. Zubko, M. Staniszewska, M. Smoleński, J. Dobosz, G. Garbacz, K. Kamiński, E. Kamińska, **Hydrophilic and amphiphilic macromolecules as modulators of the physical stability and bioavailability of piribedil: A study on binary mixtures and micellar systems**, *Molecular Pharmaceutics*, 2025, 22 (8), 4708−4730. ***(IF=4.5; MNiSW=140 pkt.)***

Pełne teksty powyższych artykułów wraz z materiałami uzupełniającymi załączono w Rozdziale 4 *„Treści publikacji stanowiących podstawę rozprawy doktorskiej”*.

3. Omówienie i dyskusja otrzymanych wyników

3.1. Synteza PVP o różnej architekturze i ściśle kontrolowanych parametrach makrostrukturalnych

Jak wskazano w podrozdziale 1.2 *„Poli(N-winylopirolidon) jako nośnik w systemach dostarczania leków – właściwości, ograniczenia i wyzwania syntetyczne”*, makrocząsteczki PVP należą do grupy związków stosunkowo trudnych do otrzymania w sposób ściśle kontrolowany, to znaczy o precyzyjnie zaprojektowanej budowie i korzystnych parametrach makrostrukturalnych. Na skalę przemysłową poli(*N*-winylopirolidon) jest powszechnie wytwarzany metodą FRP. Warto w tym miejscu przypomnieć, że komercyjnie dostępne polimery PVP, oferowane m.in. pod nazwami handlowymi Kollidon® i/lub Povidon®, mają wyłącznie liniową architekturę i różnią się przede wszystkim masą cząsteczkową, czego przykład stanowią Kollidon® 12 (PVP K12, M_n ~ 3 000), Kollidon® 30 (PVP K30, M_n ~ 40 000) oraz Kollidon® 90 (PVP K90, M_n ~ 360 000). Należy jednak podkreślić, że ze względu na zastosowanie polimeryzacji typu FRP otrzymywane produkty charakteryzują się wysoką dyspersyjnością ($Đ \geq 2$). W praktyce oznacza to, że handlowo dostępne PVP charakteryzują się szerokim rozkładem mas molowych i stanowią mieszaninę makrocząsteczek o zróżnicowanej długości łańcucha. Tym samym nie wykazują one ściśle zdefiniowanych parametrów makrocząsteczkowych. Mimo to, większość dotychczas opublikowanych prac koncentrowała się głównie na ocenie, który z preparatów handlowych PVP wykazuje najwyższą skuteczność w poprawie parametrów farmakokinetycznych słabo rozpuszczalnych substancji czynnych. W licznych doniesieniach naukowych podkreślano przede wszystkim wpływ M_n komercyjnych polimerów PVP na poprawę biodostępności produktów farmaceutycznych,[54–56] pomijając przy tym istotny problem szerokiego rozkładu mas molowych tych makrocząsteczek.

Uwzględniając wskazaną lukę badawczą, w pierwszym etapie realizacji niniejszej pracy doktorskiej opracowano skuteczne metody otrzymywania innowacyjnych materiałów polimerowych PVP o budowie liniowej (*lin*PVP) oraz trójramiennej gwiazdy (*star*PVP), z wykorzystaniem polimeryzacji typu RAFT. Zastosowanie tej techniki polimeryzacji umożliwiło uzyskanie dobrze zdefiniowanych polimerów już w jednym etapie syntezy, tj. materiałów o niskiej $Đ$, dobrze określonej M_n oraz aktywnych grupach końcowych łańcucha, które mogą stanowić punkt wyjścia do dalszych modyfikacji chemicznych (**Rysunek 7**).

Szczególnie istotnym elementem tej części badań było także opracowanie ścieżki syntezy trójfunkcyjnego CTA, dostosowanego do polimeryzacji monomerów *N*-winylowych metodą RAFT.

Pozwoliło to na uzyskanie nowego typu materiału polimerowego, czyli gwiaździstego PVP o trójramiennej architekturze. Należy podkreślić, że zdecydowana większość komercyjnie dostępnych CTA stosowanych w procesach RAFT ma charakter jednofunkcyjny, a tym samym umożliwia syntezę przede wszystkim makrocząsteczek liniowych.

Zgodnie z danymi literaturowymi, do polimeryzacji monomerów *N*-winylowych szczególnie odpowiednie są czynniki CTA należące do grupy ksantogenianów oraz ditiokarbaminianów. Wśród tych klas związków nie są jednak dostępne komercyjnie wielofunkcyjne CTA przeznaczone do kontrolowanej polimeryzacji monomerów *N*-winylowych. Dotychczas jedynie w jednej pracy opisano udaną syntezę czteroramiennego gwiaździstego PVP metodą RAFT.[57] Warto jednak zauważyć, że autorzy wykorzystali w tym celu komercyjnie dostępny czterofunkcyjny CTA z grupy tritiowęglanów, który nie jest uznawany za czynnik optymalny do kontroli polimeryzacji monomerów *N*-winylowych.[58,59] W konsekwencji prowadzenie polimeryzacji RAFT w ciśnieniu atmosferycznym z użyciem tego CTA prowadziło do otrzymania polimerów gwiaździstych o wysokiej dyspersyjności (do $Đ$ = 2.45). Z kolei zastosowanie podwyższonego ciśnienia (250 MPa) w roli czynnika kontrolującego przebieg procesu, umożliwiło uzyskanie czteroramiennego gwiaździstego PVP o umiarkowanie niższej dyspersyjności ($Đ$ = 1.80).[57]

W oparciu o powyższe przesłanki opracowano i otrzymano trójfunkcyjny CTA z grupy ditiokarbaminianów (**Rysunek 7b**). Następnie zastosowano go do syntezy dobrze zdefiniowanego trójramiennego gwiaździstego PVP zgodnie ze strategią do rdzenia (ang. *core-first*) (**Rysunek 7c**). Z kolei komercyjnie dostępny jednofunkcyjny CTA, również należący do grupy ditiokarbaminianów, wykorzystano do otrzymania liniowego PVP, uzyskując homopolimer o korzystnych parametrach makrostrukturalnych (**Rysunek 7a**). Szczegółowy opis syntezy trójfunkcyjnego CTA oraz homopolimerów PVP, tj. *lin*PVP i *star*PVP, przedstawiono w materiałach uzupełniających (SI) do publikacji **P1** i **P3**.

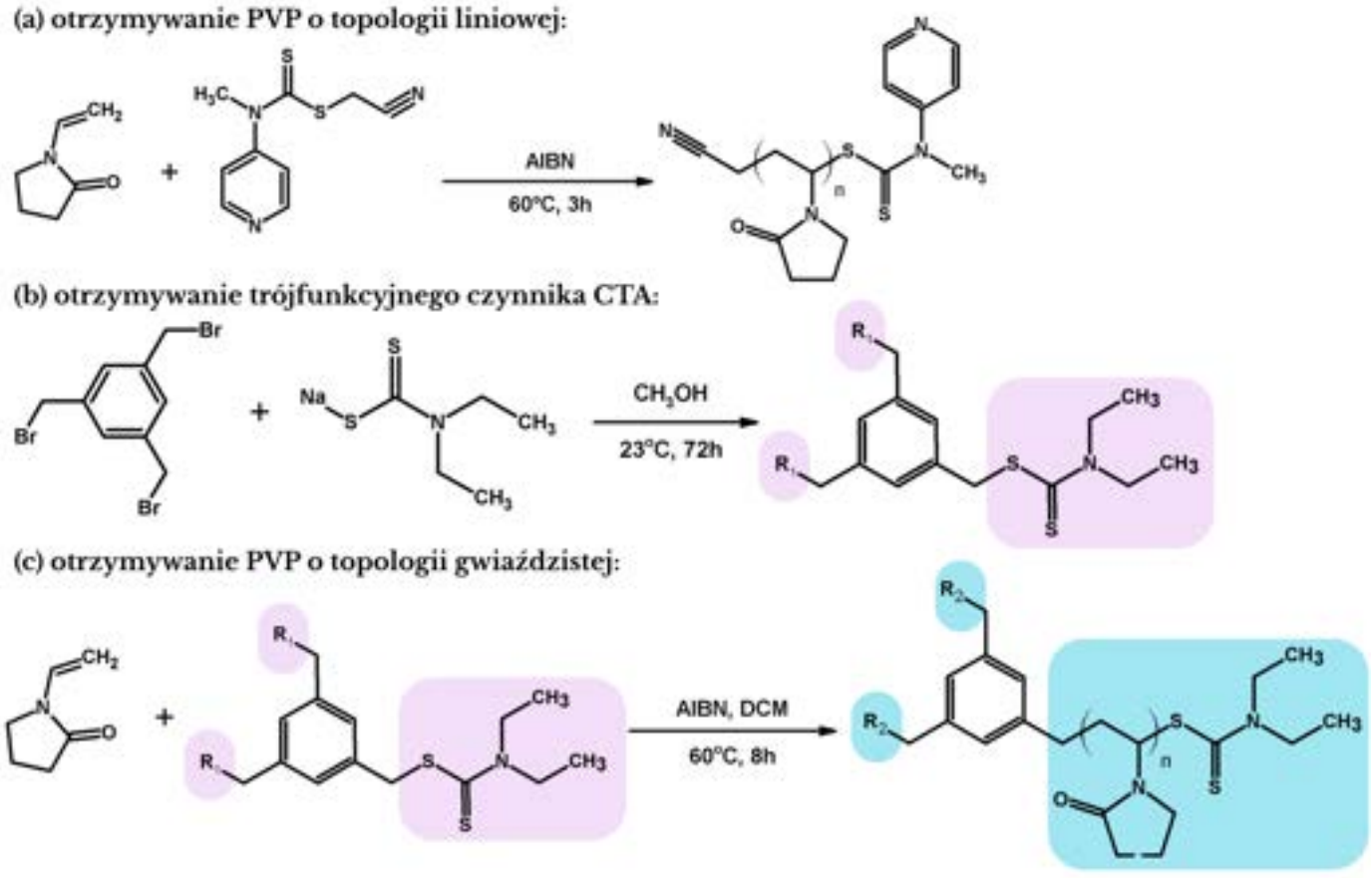

Rysunek 7. Reakcje chemiczne przedstawiające sposób otrzymywania: (a) liniowego PVP; (b) trójfunkcyjnego CTA; (c) gwiaździstego PVP.

Uzyskane homopolimery PVP o zróżnicowanej topologii poddano następnie charakterystyce spektroskopowej z wykorzystaniem techniki jądrowego rezonansu magnetycznego (NMR, ang. *Nuclear Magnetic Resonance*) oraz analizie metodą chromatografii wykluczania (SEC, ang. *Size Exclusion Chromatography*). Celem tych badań było potwierdzenie budowy chemicznej otrzymanych makrocząsteczek oraz wyznaczenie ich parametrów makrostrukturalnych (M_n, $Đ$). Widma ^{1}H NMR, potwierdzające strukturę samodzielnie zsyntezowanego czynnika CTA oraz homopolimerów PVP o zróżnicowanej topologii, a także chromatogramy otrzymanych makrocząsteczek, przedstawiono na **Rysunku 4**. Z kolei analiza wyników SEC wskazała, że uzyskane makrocząsteczki PVP charakteryzują się dobrze zdefiniowaną strukturą, o czym świadczy symetryczny i monomodalny charakter zarejestrowanych sygnałów. Dodatkowo widma ^{13}C NMR otrzymanych polimerów zamieszczono w materiałach uzupełniających do publikacji **P1** (Fig. S3 i S6) oraz **P3** (Fig. S4 i S6). Ponadto, ze względu na fakt, że otrzymane homopolimery PVP zostały zsyntezowane z wykorzystaniem czynników CTA zawierających atomy siarki, przeprowadzono

również badania cytotoksyczności. Ich celem była ocena możliwości zastosowania uzyskanych makrocząsteczek w obszarze biomedycznym i farmaceutycznym. Jako próbkę referencyjną w badaniach biologicznych zastosowano handlowy PVP K30, dopuszczony przez FDA do zastosowań formulacyjnych. Badania cytotoksyczności przeprowadzone na liniach komórkowych ludzkiej skóry potwierdziły neutralny charakter biologiczny otrzymanych makrocząsteczek, wskazując na ich potencjalną przydatność w aplikacjach biomedycznych i farmaceutycznych.

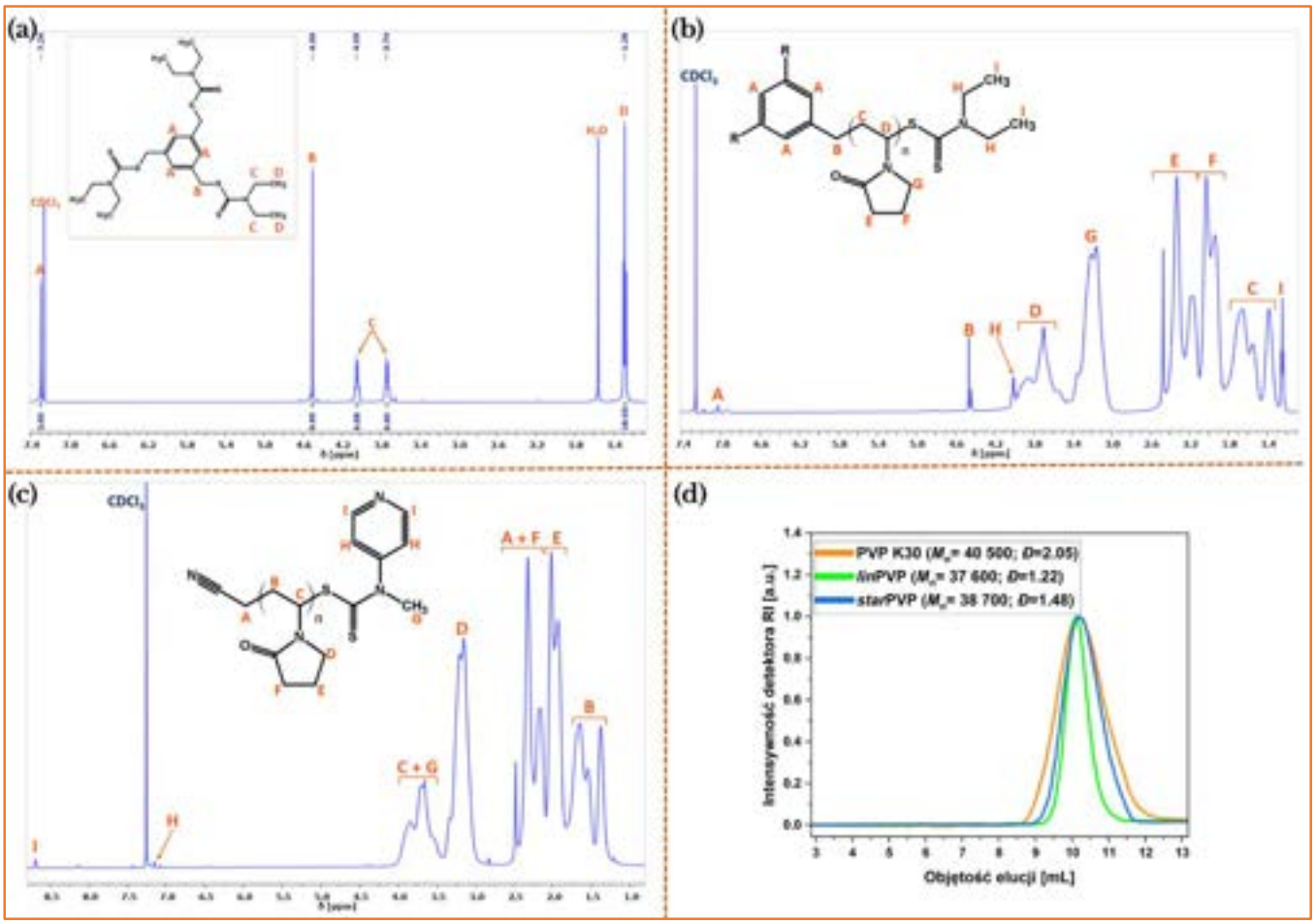

Rysunek 8. Widma ^{1}H NMR wykonane w $CDCl_3$ dla: (a) trójfunkcyjnego CTA; (b) gwiaździstego PVP; (c) liniowego PVP, a także (d) chromatogramy uzyskanych makrocząsteczek oraz komercyjnego polimeru PVP K30.

3.2. Wpływ topologii i długości łańcucha polimerowego na stabilność fizyczną silnie rekrystalizujących API (artykuł P1 i P2)

Artykuł P1

The Impact of Various Poly(vinylpyrrolidone) Polymers on the Crystallization Process of Metronidazole

Pharmaceutics, **2024**, 16 (1), 136
DOI: 10.3390/pharmaceutics16010136

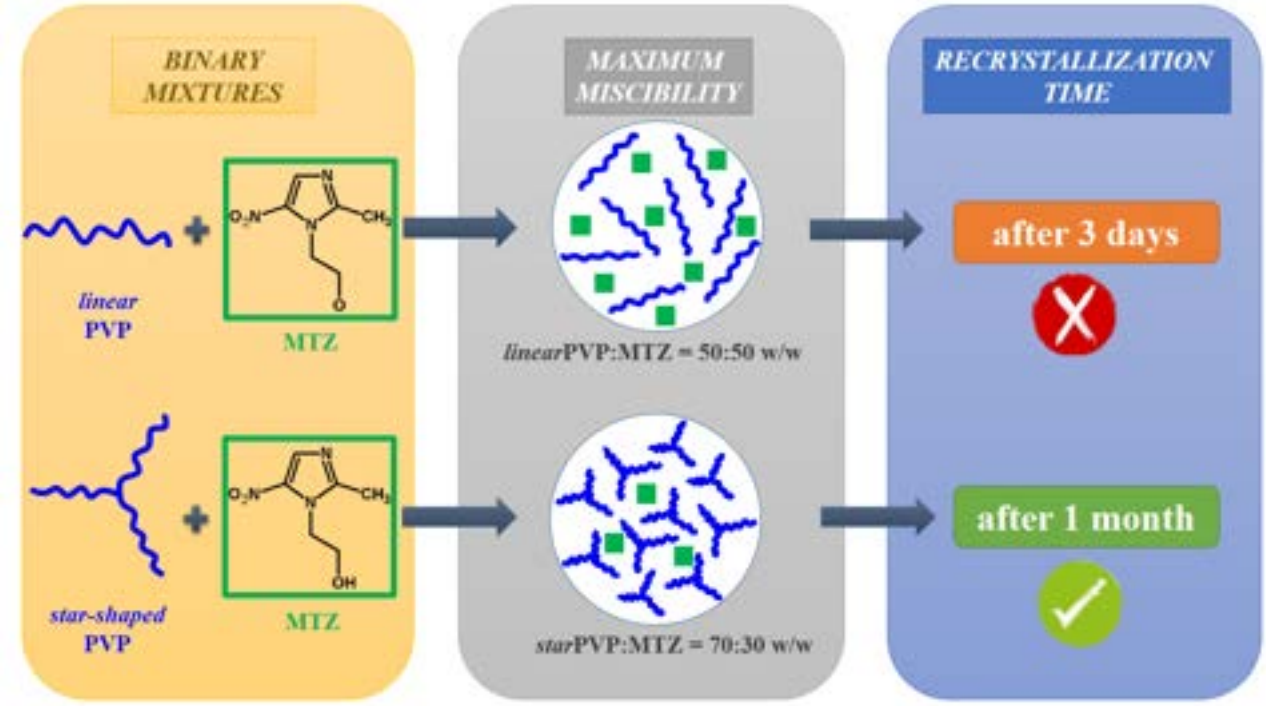

Abstrakt graficzny

Link prowadzący do artykułu:

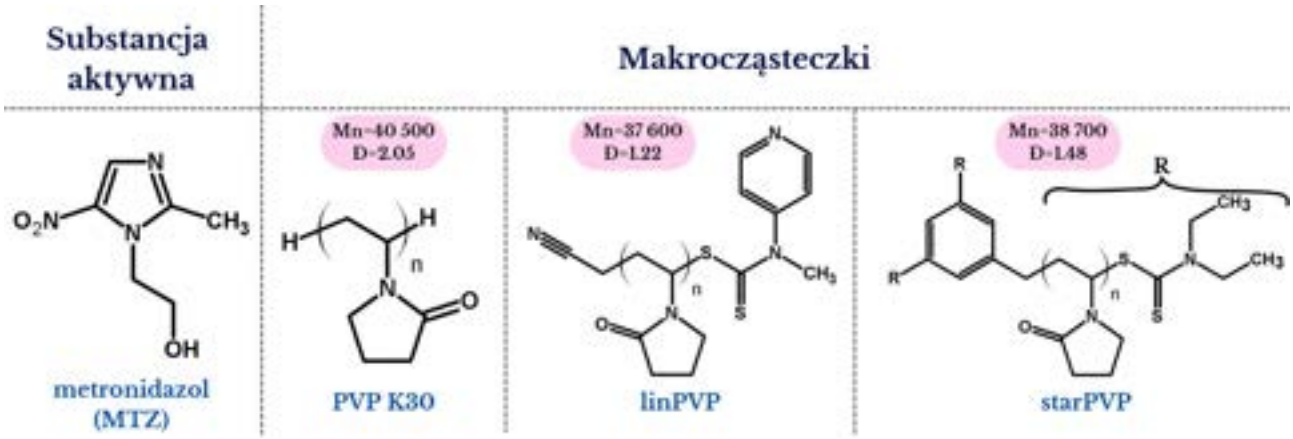

Rysunek 9. Struktury chemiczne substancji aktywnej oraz makrocząsteczek wykorzystanych w publikacji **P1**.

W ramach pierwszej pracy (**P1**) wchodzącej w cykl rozprawy doktorskiej szczególną uwagę poświęcono badaniom wpływu topologii makrocząsteczek PVP na zdolność do hamowania krystalizacji metronidazolu (MTZ). Głównym celem badań było określenie, czy architektura polimeru i/lub parametry makrostrukturalne (*Đ*), a także zawartość PVP w mieszaninach binarnych, wpływają na charakter oddziaływań międzycząsteczkowych, stabilność fizyczną i szybkość rekrystalizacji MTZ. W tym miejscu należy przypomnieć, że MTZ stanowi modelowe API w badaniach procesu rekrystalizacji. Wynika to z faktu, że związek ten wykazuje bardzo dużą skłonność do krystalizacji, a uzyskanie jego formy amorficznej przy zastosowaniu klasycznej metody witryfikacji (tj. bardzo szybkim schłodzeniu cieczy) nie jest możliwe. Struktury chemiczne API oraz zastosowanych substancji pomocniczych przedstawiono na **Rysunku 9**. W tym miejscu należy również podkreślić, że jedna z użytych matryc, tj. PVP K30, jest komercyjnie dostępnym polimerem o M_n = 40 500. Z tego względu, aby na dalszym etapie badań możliwe było porównanie wyłącznie wpływu architektury polimeru, zsyntezowano makrocząsteczki *lin*PVP oraz *star*PVP o zbliżonych wartościach M_n (**Rysunek 9**).

Co ciekawe, interesujące różnice ujawniły się już na etapie przygotowywania systemów binarnych, kiedy zaobserwowano, że mieszalność układu MTZ–PVP zależy od rodzaju zastosowanej matrycy polimerowej. Mianowice stwierdzono, że PVP o topologii liniowej (tj. PVP K30 oraz *lin*PVP) wykazują maksymalną mieszalność z MTZ przy stosunku wagowym 50:50, podczas gdy polimer o architekturze trójramiennej gwiazdy (*star*PVP) miesza się homogenicznie z API nawet przy stosunku 30:70 *w/w*. Aby wyjaśnić te obserwacje, przeprowadzono kompleksowe badania formulacji MTZ-PVP o różnej zawartości obu składników, wykorzystując spektroskopię w podczerwieni z transformacją Fouriera (FTIR), różnicową kalorymetrię skaningową (DSC) oraz dyfrakcję rentgenowską (XRD).

W celu uzyskania wglądu w możliwe specyficzne oddziaływania międzycząsteczkowe pomiędzy badanymi makrocząsteczkami PVP a API w pierwszej kolejności przeprowadzono badania spektroskopowe FTIR. Początkowo zarejestrowano widma dla wszystkich substancji, tj. MTZ, PVP K30, *lin*PVP oraz *star*PVP, które przedstawiono w SI do publikacji **P1** (Fig. S7). Następnie przystąpiono do badań ASD w całym zakresie spektralnym, tj. 4000-400 cm^{-1}. Najistotniejsze zmiany w widmach układów MTZ-PVP zaobserwowano w obrębie pasma pochodzącego od drgań rozciągających grupy karbonylowej $\nu_{C=O}$. Jak pokazano na **Rysunku 10a**, sygnał $\nu_{C=O}$ matrycy PVP K30, zlokalizowany przy 1645 cm^{-1}, wykazywał przesunięcie w kierunku wyższych liczb falowych (tzw. *„blue-shift”*) wraz ze wzrostem zawartości MTZ w mieszaninach binarnych. Obserwacja ta sugerowała, że oddziaływania pomiędzy MTZ a PVP K30 mają głównie charakter dipol–dipol, a ich znaczenie wzrasta wraz ze zwiększaniem stężenia API. Analogiczne zachowanie zaobserwowano dla układów binarnych MTZ z zsyntezowanym *lin*PVP, co również wskazywało na dominujący udział oddziaływań dipolowo-dipolowych pomiędzy API a *lin*PVP (**Rysunek 10b**). Odmienny charakter zmian spektralnych stwierdzono natomiast w przypadku ASD zawierających *star*PVP. Wprowadzenie MTZ do matrycy o topologii trójramiennej gwiazdy prowadziło do wyraźnego przesunięcia pasma $\nu_{C=O}$ w kierunku niższych liczb falowych, tzw. „*red-shift”* (z 1661 cm^{-1} dla *star*PVP do 1651 cm^{-1} dla mieszaniny 30:70 *w/w*). Tego typu przesunięcie można powiązać z tworzeniem wiązań wodorowych pomiędzy grupą hydroksylową MTZ a grupą karbonylową PVP (**Rysunek 10c**).

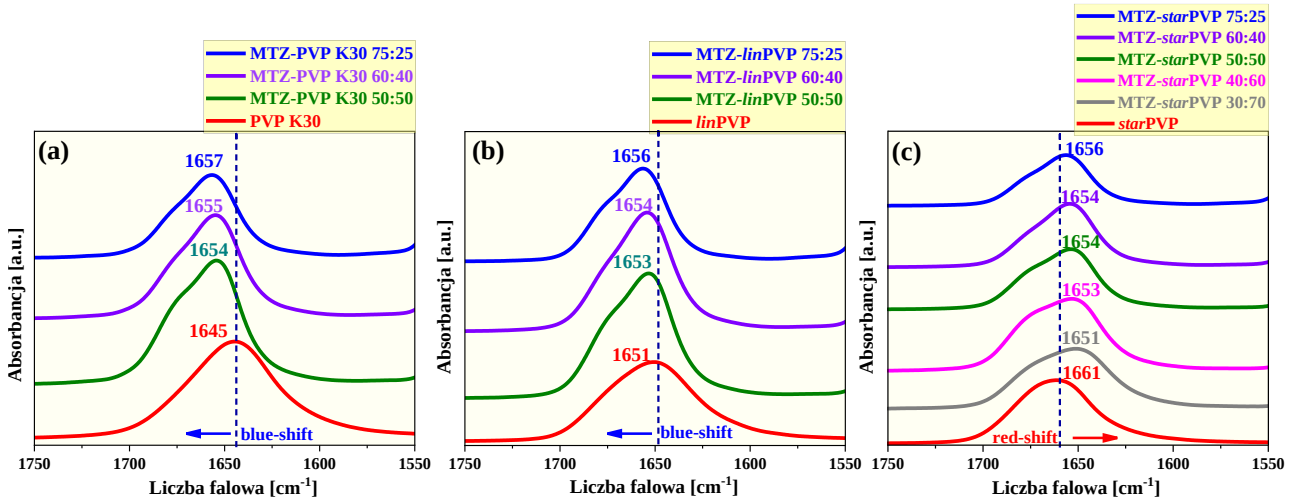

Rysunek 10. Widma FTIR dla obszaru grupy karbonylowej dla mieszanin binarnych: (a) MTZ-PVP K30; (b) MTZ-*lin*PVP oraz (c) MTZ-*star*PVP.

Na podstawie uzyskanych wyników FTIR stwierdzono, że topologia PVP istotnie wpływa na mechanizm oddziaływań API–polimer, a w konsekwencji również na mieszalność składników w układach binarnych. W przypadku liniowych matryc PVP, tj. PVP K30 oraz *lin*PVP, dominują oddziaływania dipol–dipol, czego przejawem jest przesunięcie pasma $\nu_{C=O}$ ku wyższym liczbom falowym. Taki charakter interakcji może tłumaczyć ograniczoną mieszalność MTZ z liniowymi makrocząsteczkami PVP. Z kolei w układach zawierających *star*PVP głównym mechanizmem oddziaływań jest tworzenie wiązań wodorowych, co znajduje odzwierciedlenie w przesunięciu pasma $\nu_{C=O}$ ku niższym liczbom falowym. Silniejsze oddziaływania pomiędzy MTZ a *star*PVP mogą odpowiadać za większą mieszalność tych składników w szerszym zakresie stężeń. Biorąc pod uwagę zbliżone wartości M_n badanych matryc PVP, można założyć, że różnice w mieszalności MTZ z poszczególnymi polimerami są determinowane głównie odmienną topologią makrocząsteczek.

W kolejnym etapie, w celu określenia wpływu PVP na właściwości termiczne, przejścia fazowe oraz szybkość krystalizacji MTZ, przeprowadzono pomiary DSC przygotowanych formulacji binarnych. Głównym celem tych badań było ustalenie, w jaki sposób dodatek PVP o różnej topologii oraz zróżnicowanym udziale wagowym w ASD wpływa na zdolność MTZ do tworzenia formy amorficznej, jego stabilność fizyczną i szybkość rekrystalizacji. Badania kalorymetryczne rozpoczęto od pomiarów dla MTZ (Fig. 4a w **P1**). Podczas ogrzewania krystalicznego API (przy ϕ = 10 K/min) na termogramie zaobserwowano proces endotermiczny przy T = 437 K. Następnie, po schłodzeniu stopionej próbki (przy tej samej ϕ) zarejestrowano intensywny, pojedynczy pik egzotermiczny z maksimum przy T = 326 K związany z krystalizacją próbki. W tym miejscu warto wspomnieć, że szybkość chłodzenia próbki znacząco wpływa na przemiany fazowe i umożliwia transformację krystalicznego API do formy amorficznej.[60–62] W związku z tym podjęto próby przechłodzenia/zeszklenia MTZ przy zastosowaniu różnych szybkości chłodzenia. Wszystkie przeprowadzone testy zakończyły się jednak niepowodzeniem. Wyniki te potwierdziły wyjątkowo niską zdolność MTZ do tworzenia szkła oraz wskazały, że uzyskanie tego związku w formie amorficznej za pomocą standardowej metody witryfikacji nie jest możliwe.

Następnie, przystąpiono do badań amorficznych mieszanin binarnych API-PVP z różnym udziałem wagowym obu składników. Ze względu na różnice w mieszalności analizowano układy MTZ-PVP K30 oraz MTZ-*lin*PVP w stosunkach 75:25, 60:40 oraz 50:50 *w/w*. W przypadku systemów MTZ-*star*PVP badania rozszerzono dodatkowo o formulacje o większej zawartości polimeru, tj. 40:60 oraz 30:70 *w/w*. Zgodnie w przypuszczeniami, wraz ze wzrostem zawartości polimeru w ASD obserwowano wzrost wartości T_g, podczas gdy sygnały odpowiadające procesom krystalizacji i topnienia stopniowo malały/zanikały (Fig. 4b w **P1**). Szczególnie interesujące wyniki

uzyskano dla układów MTZ–*star*PVP, w których przy stosunkach 40:60 i 30:70 *w/w* zaobserwowano całkowite stłumienie procesów topnienia i krystalizacji. Na termogramach tych formulacji widoczny był jedynie skok ciepła właściwego związanego z przejściem szklistym. Dodatkowo analiza danych kalorymetrycznych wykazała, że w zależności od zawartości PVP w ASD wartości temperatur topnienia zmieniają się znacząco, nawet o około 20 K. Może to wskazywać na obecność istotnych oddziaływań między MTZ a zastosowanymi matrycami polimerowymi. Co ważne, wniosek ten pozostaje w bardzo dobrej zgodności z wynikami analizy FTIR opisanymi powyżej.

Ostatni etap badań kalorymetrycznych obejmował pomiary krystalizacji izotermicznej w temperaturze pokojowej (295 K) dla mieszanin binarnych MTZ–PVP o stosunku wagowym 75:25. Wybór tych układów wynikał z faktu, że krystalizacja API w wybranej temperaturze zachodziła w czasie umożliwiającym wiarygodną ocenę kinetyki procesu. Dla pozostałych formulacji binarnych krystalizacja przebiegała znacznie wolniej, dlatego nie zostały one uwzględnione w tym etapie badań. Zmiany strumienia ciepła zarejestrowane dla mieszanin MTZ-PVP podczas izotermicznych pomiarów DSC przedstawiono na **Rysunku 11a** (Fig. 7a w **P1**). Jak można zaobserwować, proces krystalizacji zachodził najszybciej w układzie zawierającym polimer *star*PVP, natomiast najwolniej dla ASD z matrycą PVP K30. Stanowiło to pierwszą przesłankę wskazującą, że komercyjny polimer PVP najskuteczniej hamuje krystalizację API. W kolejnym etapie dane izotermiczne poddano bardziej szczegółowej analizie, wyznaczając zmianę stopnia krystalizacji (α) w funkcji czasu (**Rysunek 11b**, Fig. 7b w **P1**). Otrzymane krzywe dopasowano następnie za pomocą równania Avramiego, co pozwoliło na wyznaczenie stałych szybkości krystalizacji (k) w zależności od rodzaju zastosowanej matrycy polimerowej (**Rysunek 11c**, Fig. 7c w **P1**). Pełna analiza danych izotermicznych jednoznacznie wykazała, że komercyjny PVP K30 najefektywniej ograniczał krystalizację API.

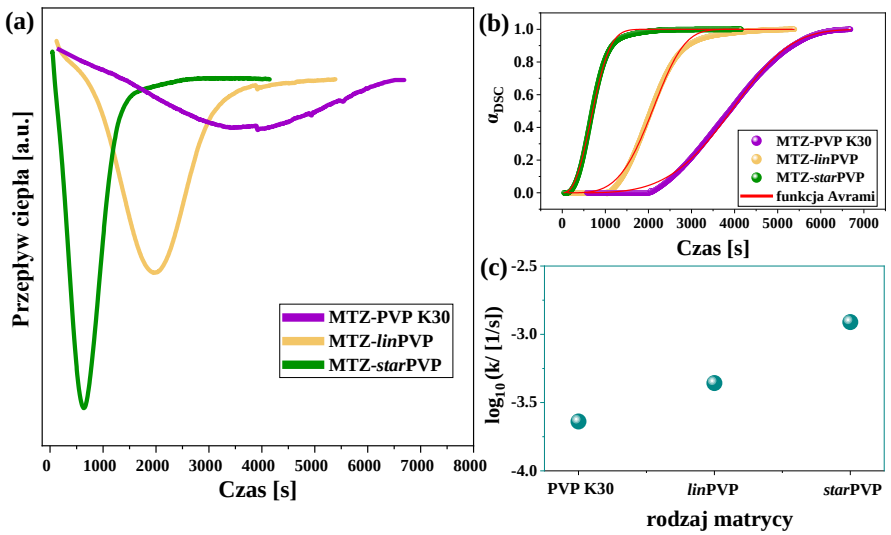

Rysunek 11. (a) Termogramy DSC pomiarów izotermicznych (T = 295 K) dla mieszanin MTZ-PVP 75:25 *w/w*; (b) Przebieg procesu krystalizacji przeprowadzonego dla badanych układów MTZ-PVP. Linie ciągłe przedstawiają dopasowania modelem Avramiego; (c) Stałe szybkości krystalizacji (k) MTZ w zależności od zastosowanego PVP w układach binarnych.

Najszybszy przebieg tego procesu odnotowano natomiast dla układu zawierającego gwiaździsty PVP, co potwierdza istotny wpływ topologii matrycy polimerowej na stabilność fizyczną badanych formulacji (**Rysunek 11**).

Ponadto przeprowadzono czasowe badania XRD dyspersji stałych MTZ-PVP w stosunku 50:50 *w/w*, rozpoczynając pomiary dla świeżo przygotowanych układów amorficznych. Rejestracja dyfraktogramów amorficznych dla mieszanin 75:25 *w/w* była niemożliwa ze względu na szybką rekrystalizację MTZ. Wyniki przedstawione na **Rysunku 12** (Fig. 9 w **P1**) wskazały, że na stabilność fizyczną MTZ w tych mieszaninach wpływa topologia PVP. W przypadku układu zawierającego *star*PVP całkowitą rekrystalizację MTZ zaobserwowano już po 15 godzinach, na co wskazywało pojawienie się ostrych refleksów Braggowskich (**Rysunek 12c**). W matrycy binarnej z dodatkiem *lin*PVP proces rekrystalizacji rozpoczął się później, tj. po 35 godzinach. Natomiast w formulacji zawierającej komercyjny PVP K30 MTZ pozostawał stabilny w formie amorficznej nawet po 35 godzinach (**Rysunek 12a**). Uzyskane wyniki jednoznacznie wykazały, że topologia polimeru odgrywa istotną rolę w hamowaniu rekrystalizacji MTZ, co jest całkowicie spójne z uzyskanymi wynikami kalorymetrycznymi. Ponadto, zarówno wyniki badań FTIR jak i XRD pokazały, że topologia zastosowanego PVP nie determinuje powstającej formy polimorficznej, tj. we wszystkich analizowanych układach binarnych MTZ rekrystalizował do tej samej odmiany krystalicznej.

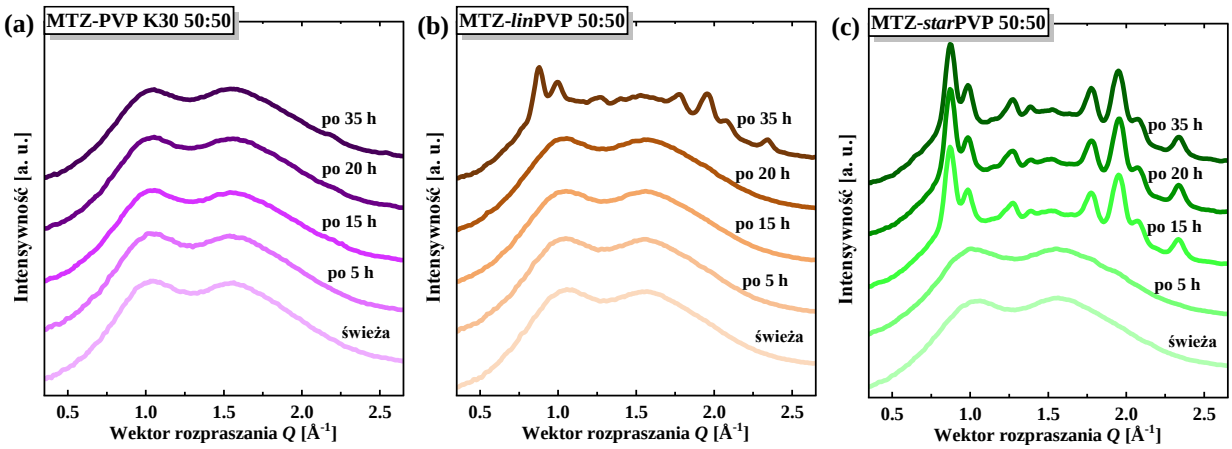

Rysunek 12. Czasowe pomiary dyfrakcyjne dla świeżo przygotowanych próbek MTZ-PVP 50:50 *w/w*: (a) MTZ-PVP K30; (b) PVP-*lin*PVP; (c) PVP-*star*PVP.

.

Szczególnie istotnym i zarazem zaskakującym wynikiem było wykazanie, że *star*PVP skutecznie hamuje rekrystalizację MTZ w mieszaninie zawierającej aż 70% wag. polimeru. Tak wysoka zawartość PVP nie była możliwa do osiągnięcia w przypadku ASD zawierających liniowe materiały polimerowe. W układzie MTZ–*star*PVP 30:70 *w/w* amorficzny MTZ zachowywał stabilność fizyczną przez ponad miesiąc, na co wskazywały identyczne dyfraktogramy zarejestrowane dla próbki świeżo przygotowanej oraz próbki przechowywanej przez ponad miesiąc (**Rysunek 13**, Fig. 10 w **P1**). Obserwacja ta wskazuje na duży potencjał tej makrocząsteczki jako skutecznej matrycy stabilizującej ASD o wysokiej zawartości polimeru.

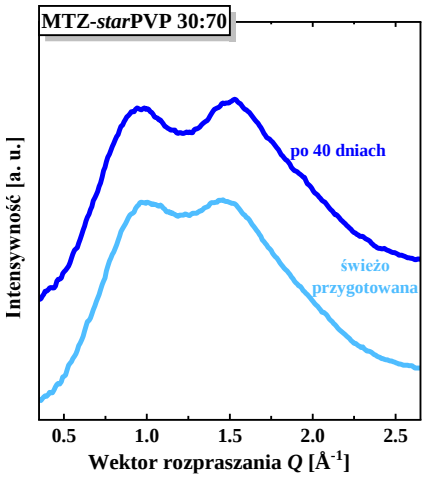

Rysunek 13. Dyfraktogram świeżo przygotowanej mieszaniny MTZ-*star*PVP 30:70 *w/w* i przechowywanej 40 dni

Artykuł P2

Inhibition of naproxen crystallization by polymers: The role of topology and chain length of polyvinylpyrrolidone macromolecules

European Journal of Pharmaceutics and Biopharmaceutics, **2025**, 207, 114581
DOI: 10.1016/j.ejpb.2024.114581

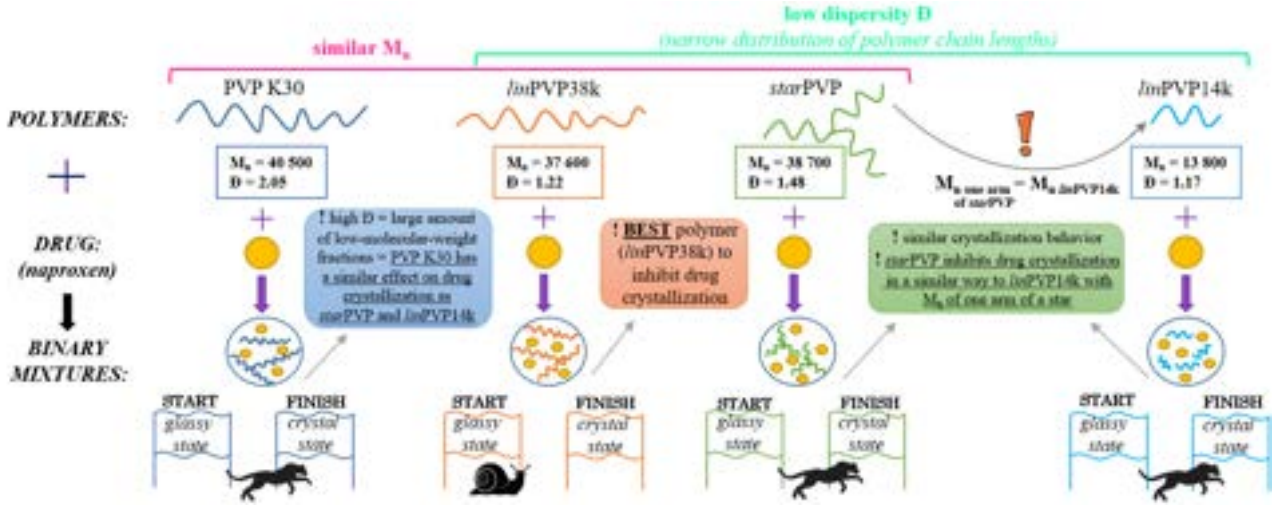

Abstrakt graficzny

Link prowadzący do artykułu:

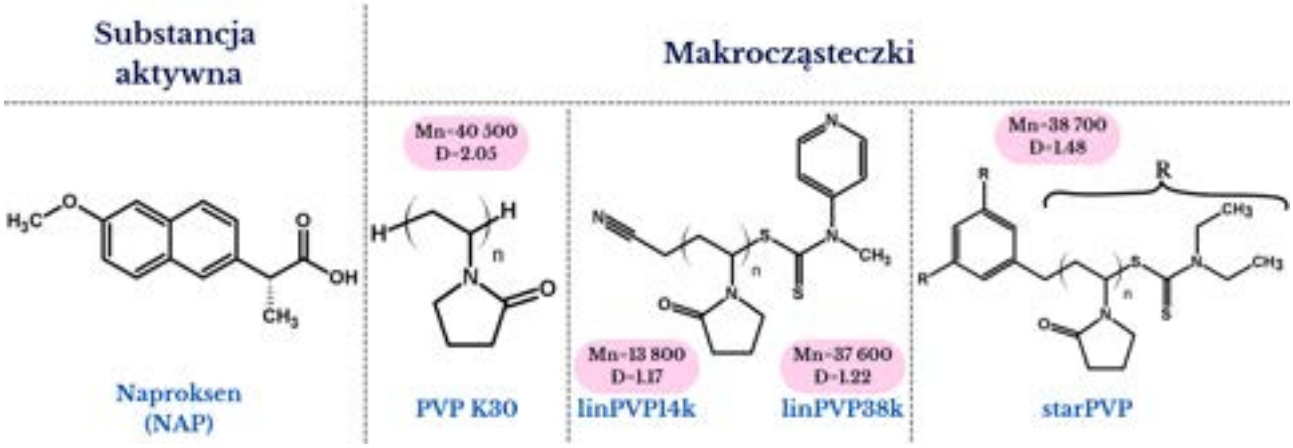

Rysunek 14. Struktury chemiczne substancji aktywnej oraz makrocząsteczek wykorzystanych w publikacji **P2**.

Publikacja **P2** stanowi kontynuację i rozwinięcie badań zaprezentowanych w artykule **P1**. W odróżnieniu od publikacji **P1**, której celem była wyłącznie weryfikacja wpływu topologii makrocząsteczek PVP na rodzaj oddziaływań międzycząsteczkowych, stabilność fizyczną i tendencję do rekrystalizacji MTZ, w niniejszych badaniach skupiono się na zbadaniu wpływu nie tylko samej architektury makrocząsteczek, ale także długości łańcucha polimerowego na stabilność amorficznej formy API. W tym celu oprócz trzech matryc użytych w badaniach **P1**, które charakteryzowały się odmienną topologią, ale podobnym/zbliżonym ciężarem cząsteczkowym, na potrzeby tej pracy zsyntezowano również liniowy PVP (*lin*PVP14k) o M_n odpowiadającej długości jednego ramienia polimeru gwiaździstego (**Rysunek 14**). Aby ułatwić rozróżnienie obu polimerów liniowych w dalszej części pracy, wprowadzono dla nich odrębne oznaczenia. Polimer liniowy o parametrach M_n=13 800 oraz $Đ$=1.22 oznaczono jako *lin*PVP14k, natomiast polimer o parametrach M_n=37 600 oraz $Đ$=1.17 jako *lin*PVP38k. Tak wyselekcjonowane matryce polimerowe zastosowano jako innowacyjne dodatki do wytworzenia ASD z NAP, czyli silnie rekrystalizującym API.

W ramach pracy **P2** przeprowadzono badania różnicowej kalorymetrii skaningowej (DSC), dyfrakcji rentgenowskiej (XRD) i spektroskopii w podczerwieni (FTIR), a także symulacje dynamiki molekularnej, aby uzyskać kompleksowy wgląd w właściwości termiczne i strukturalne, a także oddziaływania międzycząsteczkowe w układach NAP-PVP. Głównym celem wszystkich przeprowadzonych eksperymentów była dogłębna ocena wpływu struktury makrocząsteczki (topologia, M_n, a także $Đ$) na kinetykę krystalizacji NAP.

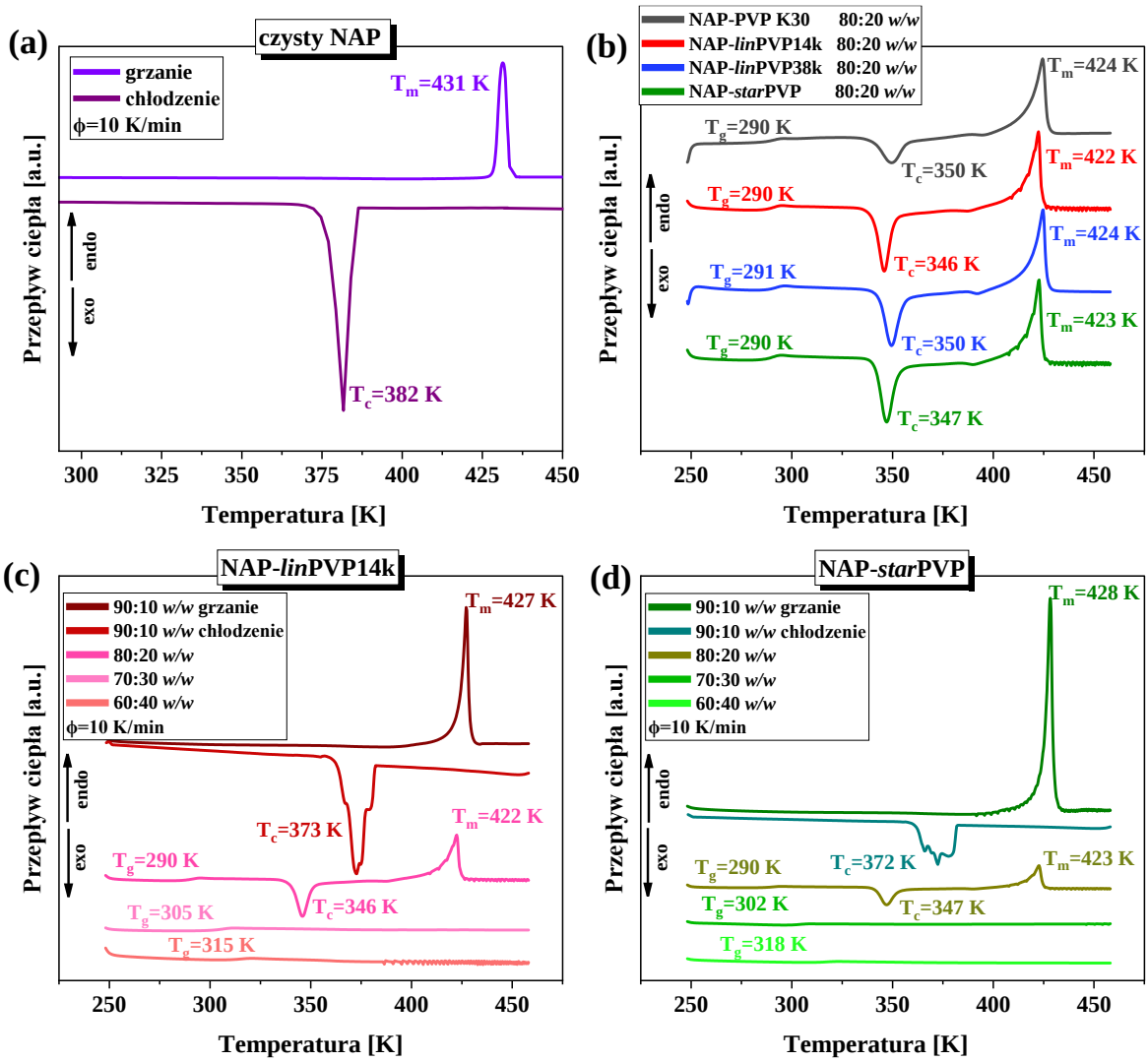

Rysunek 15. Termogramy DSC (ϕ = 10 K/min) (a) czystego NAP oraz (b) ASD NAP-PVP w takim samym stosunku wagowym (80:20 *w/w*) obu składników, a także termogramy DSC (c) NAP-*lin*PVP14k i (d) mieszanin NAP-*star*PVP w różnych stosunkach wagowych (90:10, 80:20, 70:30, 60:40 *w/w*).

W pierwszym etapie prowadzonych badań ustalono, że NAP miesza się z każdą matrycą polimerową w maksymalnym stosunku wagowym 60:40. Na tej podstawie do dalszych badań wybrano układy NAP-PVP o następujących proporcjach: 95:5, 90:10, 85:15, 80:20, 70:30 i 60:40 *w/w*. Następnie przeprowadzono szczegółowe pomiary kalorymetryczne, których celem było scharakteryzowanie właściwości termicznych i przemian fazowych dla NAP oraz układów binarnych NAP-PVP. Podobnie jak w przypadku MTZ analizowanego w pracy **P1**, ustalono, że amorficznego NAP nie można uzyskać wyłącznie za pomocą klasycznej techniki witryfikacji (**Rysunek 15a**, Fig. 2a w **P2**). Co więcej, badania przeprowadzone dla każdego układu binarnego wykazały, że dodatek polimeru do około 15% wag. nie hamuje skutecznie procesu rekrystalizacji. Trzy pierwsze

analizowane systemy, tj. 95:5, 90:10 oraz 85:15 *w/w*, charakteryzowały się bardzo podobnymi właściwościami termicznymi i nie mogły zostać otrzymane w postaci szklistej z zastosowaniem standardowej metody witryfikacji. Dopiero w przypadku układów NAP-PVP w stosunku 80:20 *w/w* możliwe było uzyskanie formulacji amorficznych, choć nadal wykazywały one stosunkowo silną tendencję do krystalizacji (**Rysunek 15b**, Fig. 2b w **P2**). Z kolei systemy NAP-PVP w stosunkach wagowych 70:30 i 60:40 wykazywały całkowitą amorficzność i bardzo silne zahamowanie krystalizacji API. Dla tych formulacji na termogramach obserwowano wyłącznie przejście szkliste, bez oznak rekrystalizacji. Wartości temperatury zeszklenia wynosiły odpowiednio T_g~302–306 K dla układów 70:30 *w/w* oraz T_g~315–322 K dla systemów 60:40 *w/w* (**Rysunek 15cd**, Fig. 2cd w **P2**). Wyniki te ujawniły, że skuteczna stabilizacja amorficznego NAP w matrycach PVP wymaga co najmniej 20% wag. polimeru, natomiast pełne zahamowanie krystalizacji obserwowane jest dopiero przy większej zawartości PVP, tj. 30–40% wag.

Następnie, aby zaobserwować wpływ rodzaju matrycy polimerowej na skalę czasu krystalizacji, przeprowadzono izotermiczne pomiary DSC dla układów NAP-PVP 80:20 *w/w*, w temperaturze 314 K, tj. w temperaturze zbliżonej do T_g. W tym miejscu należy zaznaczyć, że lepkość (η) badanych mieszanin binarnych ma istotny wpływ na przebieg procesu krystalizacji. Aby możliwe było wyodrębnienie wpływu zastosowanych matryc polimerowych, do izotermicznych badań DSC wybrano temperaturę, w której analizowane układy wykazywały zbliżoną η. Jak przedstawiono na **Rysunku 16** (Fig. 5e w **P2**), na podstawie uzyskanych danych kalorymetrycznych wyznaczono zmianę stopnia krystalizacji (α) w funkcji czasu. Analiza otrzymanych krzywych, dopasowanych z wykorzystaniem równania Avramiego, wykazała, że matryca *lin*PVP38k najskuteczniej hamowała krystalizację API. Z kolei NAP w mieszaninach z trzema pozostałymi matrycami (PVP K30, *lin*PVP14k, *star*PVP) wykazywał zbliżoną skalę czasową rekrystalizacji. Na podstawie tych wyników można wnioskować, że polimer PVP o budowie

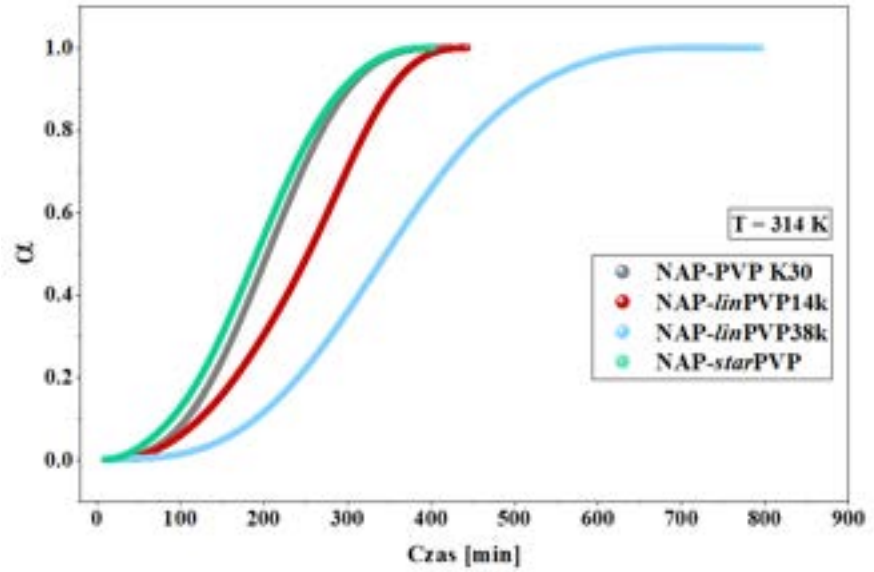

Rysunek 16. Porównanie przebiegu procesu krystalizacji dla wszystkich badanych mieszanin NAP-PVP (80:20 *w/w*) w temperaturze 314 K.

gwiazdy wpływa na zachowanie krystalizacji NAP bardzo podobnie jak polimer liniowy o M_n odpowiadającej pojedynczemu ramieniu makrocząsteczki gwiaździstej. Szczególnie interesujące jest jednak to, że dostępny komercyjnie PVP K30 (pomimo średniej M_n wynoszącej ~ 40 000) nie wykazywał podobieństwa do swojego zsyntetyzowanego odpowiednika (*lin*PVP38k). Zamiast tego hamował krystalizację API w skali czasowej zbliżonej do *lin*PVP14k oraz *star*PVP. Najbardziej prawdopodobną przyczyną tej obserwacji jest wysoka dyspersyjność PVP K30 w porównaniu z samodzielnie zsyntetyzowanymi makrocząsteczkami. Komercyjny PVP charakteryzuje się szerokim rozkładem mas molowych łańcuchów polimerowych, co oznacza, że zawiera zarówno frakcje o niższym, jak i wyższym M_n. Można zatem przypuszczać, że obecność frakcji o niższych wartościach M_n w matrycy polimerowej w istotnym stopniu determinuje szybkość krystalizacji NAP w formulacjach API–polimer.

Badania XRD wykazały natomiast, że niezależnie od topologii oraz wartości M_n zastosowanej makrocząsteczki, NAP krystalizuje do tej samej formy polimorficznej (Fig. S5 w **P2**). Ze względu na szybką krystalizację układów NAP–PVP 80:20 *w/w* nie było jednak możliwe jednoznaczne określenie za pomocą tej techniki, która z analizowanych makrocząsteczek najskuteczniej hamuje proces krystalizacji API.

Z kolei, badania w podczerwieni ujawniły bardzo subtelne różnice między widmami w zależności od M_n i topologii użytego PVP co sugeruje brak istotnych różnic w oddziaływaniach międzycząsteczkowych między API a poszczególnymi makrocząsteczkami. Natomiast zaobserwowano wyraźne różnice widmowe dla każdej mieszaniny NAP-PVP, charakteryzującej się różną zawartością polimeru. W tym miejscu należy zaznaczyć, że NAP posiada ugrupowanie karboksylowe (**Rysunek 14**), stąd też silną tendencję do asocjacji i występowania w postaci dimerów. Najbardziej intrygujące zmiany spektralne zaobserwowano w zakresie 1800–1520 cm^{-1}, w którym występują pasma przypisane drganiom rozciągającym C=O substancji aktywnej (1741 cm^{-1}, 1706

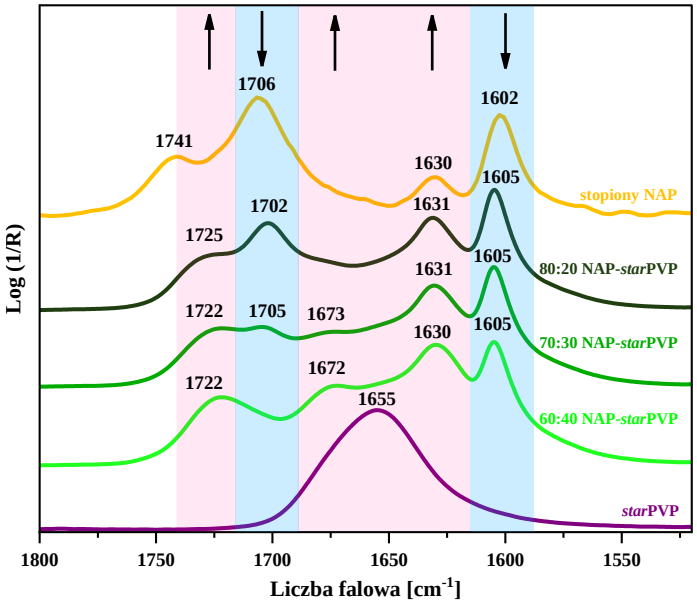

Rysunek 17. Widma FTIR amorficznych mieszanin binarnych NAP-*star*PVP w różnych stosunkach wagowych, oraz stopionego NAP i czystego *star*PVP zmierzone w zakresie 1800–1520 cm^{-1}. Wzrost intensywności piku zaznaczono odpowiednio na czerwono, a spadek na niebiesko.

cm^{-1}) i makrocząsteczki (1655 cm^{-1}) oraz drganiom rozciągającym C=C NAP (1630 i 1602 cm^{-1}) (**Rysunek 17**, Fig. 9 w **P2**). Można zauważyć, że pasmo $\nu_{C=O}$ stopionego NAP składa się z dwóch pików: (*i*) piku o wysokiej liczbie falowej (1741 cm^{-1}), wynikającego z drgań rozciągających swobodnych grup C=O, oraz (*ii*) piku o niskiej liczbie falowej (1706 cm^{-1}), przypisanego do drgań rozciągających grupy C=O wiązanej z wodorem (dimery).[63] Jak można zaobserwować na **Rysunku 17**, dla próbki NAP-*star*PVP wraz ze wzrostem udziału polimeru w mieszaninie binarnej wzrasta intensywność pików zlokalizowanych przy 1722 i 1630 cm^{-1} oraz zmniejsza się intensywność sygnałów przy 1702 i 1605 cm^{-1}. Wyniki te wyraźnie wskazują, że przy niskim stężeniu PVP (20% wag.), NAP występuje jako kombinacja dimerów (intensywne pasmo przy ~ 1702 cm^{-1}). Natomiast wraz ze zwiększaniem udziału makrocząsteczki intensywność tego pasma drastycznie maleje, co sugeruje rozpad wiązań wodorowych NAP-NAP, a faworyzowanie tworzenia wiązań pomiędzy grupą hydroksylową API, a grupą karbonylową PVP. Należy zauważyć, że NAP z innymi matrycami (PVP K30, *lin*PVP14k i *lin*PVP38k), wykazują takie same efekty spektralne po dodaniu polimeru do API, jak w przypadku NAP-*star*PVP (Fig. S15 w **P2**).

Dodatkowo, na podstawie wyników z długoterminowych badań FTIR ustalono, że największa (nawet czteromiesięczna) stabilność fizyczna mieszanin NAP-PVP w stosunku 60:40 *w/w* wynika głównie z tworzenia wiązań wodorowych między cząsteczkami API i PVP, ponieważ wysoka zawartość polimeru zapobiega samoasocjacji cząsteczek NAP, co znacząco wpływa na kinetykę rekrystalizacji i skutecznie hamuje ten proces.

W ostatnim etapie badań, wykonano symulacje dynamiki molekularnej dla czystego układu NAP oraz mieszanin API z różnymi PVP w stosunku wagowym 80:20 i 60:40, które potwierdziły wyniki badań w podczerwieni – tj. im więcej PVP użyto, tym więcej występujących wiązań wodorowych pomiędzy NAP a PVP i mniej dimerów NAP-NAP; w konsekwencji, wyższa stabilność ASD przy większej ilości polimeru. Ponadto wykazano niewielkie różnice w oddziaływaniach wiązań wodorowych w zależności od rodzaju polimeru PVP w układzie (**Rysunek 18**), a także największą jednorodność układu NAP-*lin*PVP38k (Fig. 10 w **P2**), co wyjaśnia najskuteczniejsze hamowanie krystalizacji API przez polimer o ściśle zdefiniowanej M_n i niskiej $Đ$, co również wywnioskowano z analizy izotermicznych danych DSC. Należy zatem zauważyć, że wyniki obliczeń teoretycznych są zgodne z wynikami badań eksperymentalnych. Uzyskane dane można zatem uznać za niezwykle istotne z perspektywy projektowania nowych formulacji farmaceutycznych zawierających polimery o dobrze zdefiniowanych parametrach makrocząsteczkowych i architekturze.

Podsumowując, przeprowadzone badania wyraźnie wykazały, że najskuteczniejszą matrycą w hamowaniu krystalizacji NAP jest liniowy, zsyntetyzowany PVP o wyższej M_n podobnej do komercyjnego PVP, ale o niskiej, ściśle kontrolowanej dyspersyjności. Ponadto, zaobserwowano, że NAP w mieszaninie z gwiaździstym PVP wykazuje podobne zachowanie krystalizacyjne jak w połączeniu z polimerem liniowym, w którym M_n odpowiada M_n jednego ramienia gwiaździstej makrocząsteczki. Uzyskane dane podkreślają kluczową rolę struktury polimeru w projektowaniu nowych formulacji farmaceutycznych.

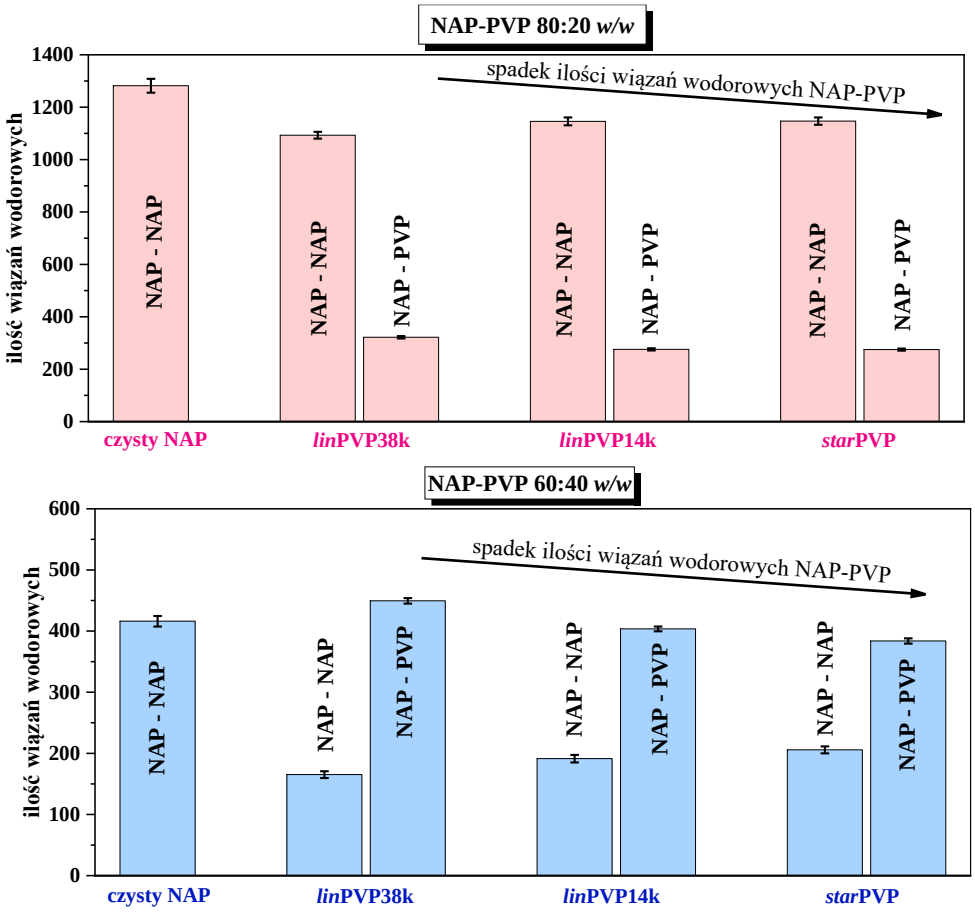

Rysunek 18. Diagramy przedstawiające liczbę wiązań wodorowych dla badanych układów NAP-PVP w dwóch stosunkach 80:20 oraz 60:40 *w/w*.

3.3. Wpływ architektury polimerów PVP na uporządkowanie ciekłokrystaliczne API w układach binarnych (artykuł P3)

Artykuł P3

The Influence of PVP Polymer Topology on the Liquid Crystalline Order of Itraconazole in Binary Systems

Molecular Pharmaceutics, **2024**, 21 (6), 3027−3039
DOI: 10.1021/acs.molpharmaceut.4c00215

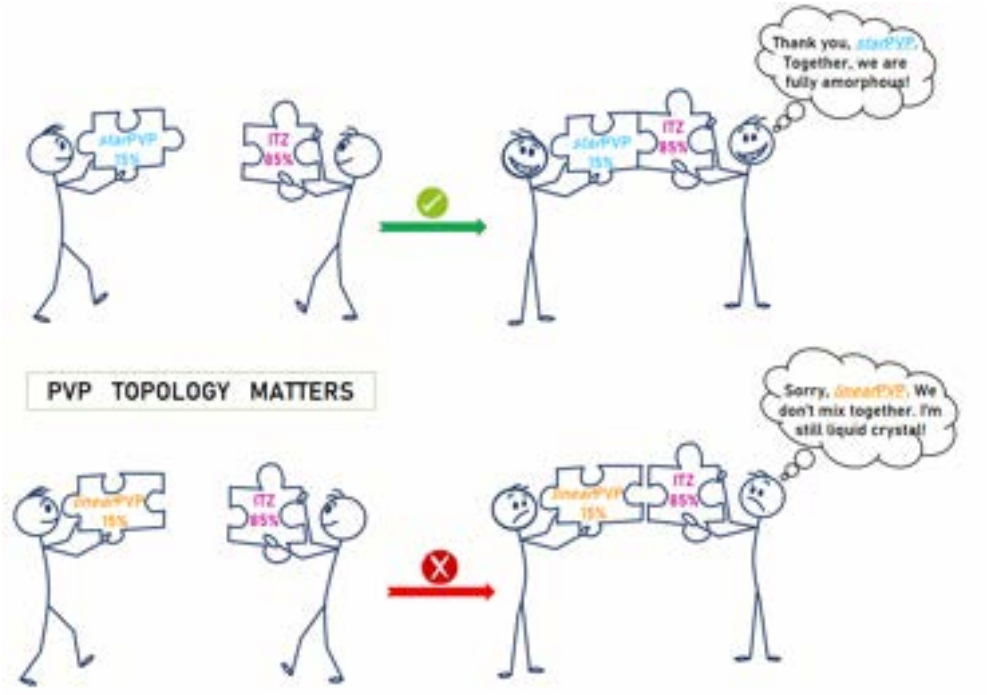

Abstrakt graficzny

Link prowadzący do artykułu:

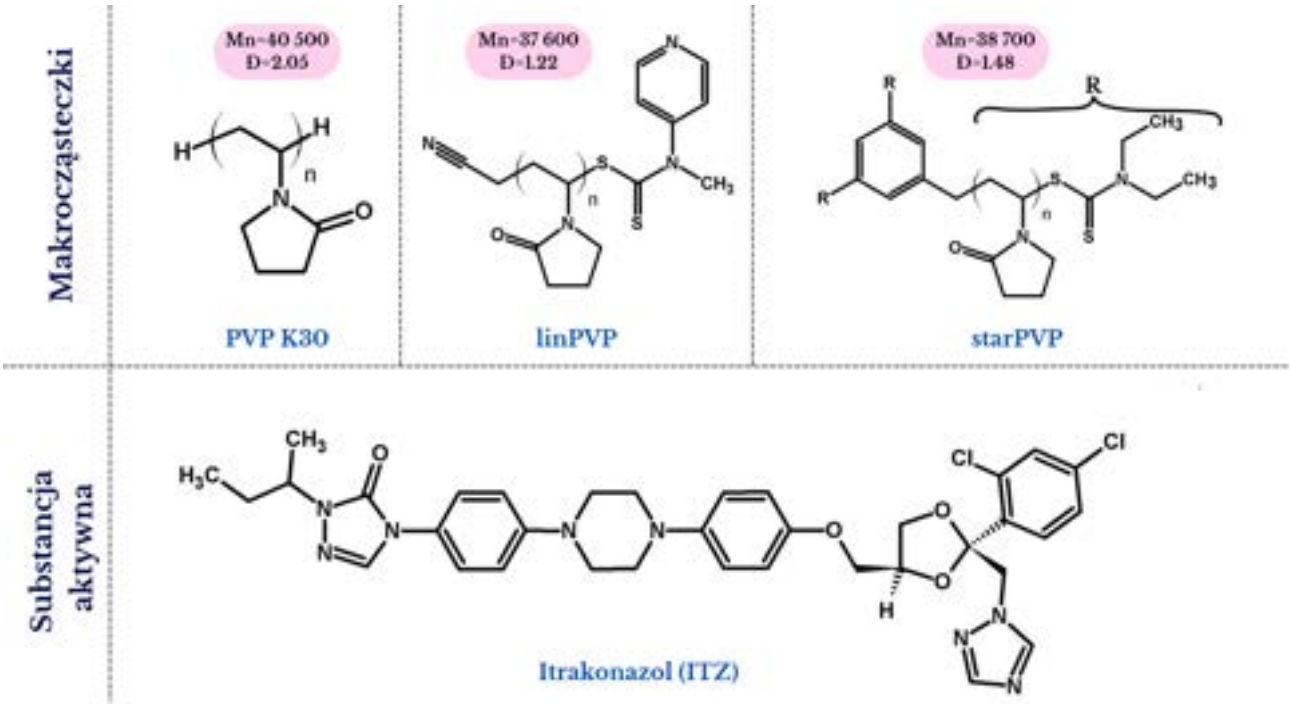

Rysunek 19. Struktury chemiczne substancji aktywnej oraz makrocząsteczek wykorzystanych w publikacji **P3**.

W kolejnej pracy (**P3**), zsyntezowane matryce polimerowe o zróżnicowanej architekturze - liniowej (*lin*PVP) i gwiaździstej (*star*PVP) oraz próbkę handlową jako referencyjną (PVP K30) o podobnych masach cząsteczkowych, ale wyraźnie różnej topologii przetestowano jako substancje pomocnicze w formulacjach binarnych z ciekawą API - itrakonazolem (ITZ) (**Rysunek 19**). Jest to substancja lecznicza bardzo trudno rozpuszczalna w wodzie (zaledwie 1 ng/mL),[43] ale wykazująca ciekawe ciekłokrystaliczne uporządkowanie molekularne, którego modulacja może potencjalnie przyczynić się do poprawy biodostępności leku. Zatem na tym etapie szczególną uwagę badawczą poświęcono zbadaniu wpływu topologii polimerów PVP na zmianę w uporządkowaniu ciekłokrystalicznym leku i poprawę jego właściwości farmakokinetycznych.

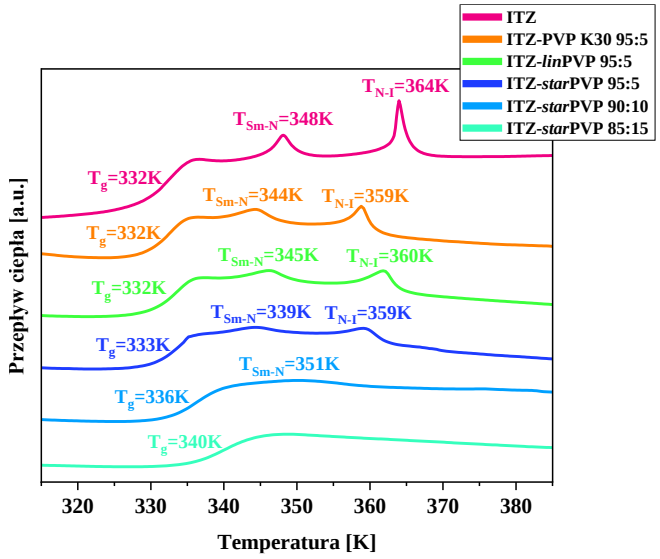

Rysunek 20. Termogramy ITZ i mieszanin binarnych ITZ-PVP.

W początkowej fazie badań odkryto bardzo intrygującą zależność, podobną do tej zaobserwowanej w pracy **P1**, a mianowicie różną mieszalność API-polimer w zależności od topologii użytej matrycy

polimerowej. Dokładniej, makrocząsteczki liniowe (PVP K30, *lin*PVP) wykazały mieszalność z API jedynie na poziomie 5% wag., natomiast PVP gwiaździsty posiadał mieszalność z ITZ aż na poziomie 15% wag. Pomiary kalorymetryczne wykazały, że każda matryca polimerowa silnie wpływa na temperatury przejść ciekłokrystalicznych w ITZ (**Rysunek 20**, Fig. 2 w **P3**). Jak widać, podczas ogrzewania API widoczne są trzy endotermiczne przejścia fazowe. Pierwsze występujące w najniższej temperaturze związane jest z przejściem szklistym (T_g=332 K). Natomiast dwa pozostałe sygnały endotermiczne przy wyższych wartościach *T* są powiązane z uporządkowaniem ciekłokrystalicznym ITZ. Dokładniej, przejście w *T*=348 K odpowiada przejściu API z fazy smektycznej (*Sm*) do nematycznej (*N*) (T_{Sm-N}), natomiast to występujące w *T*=364 K jest związane z przejściem z fazy *N* do fazy izotropowej (*I*) (T_{N-I}). Warto zauważyć, że uzyskany termogram ITZ oraz wyznaczone przejścia fazowe były całkowicie zgodne z danymi przedstawianymi w innych pracach. Następnie zarejestrowano termogramy ASD ITZ–PVP 95:5 *w/w*. Zauważono (**Rysunek 20**), że niezależnie od rodzaju polimeru zastosowanego w układzie binarnym, wartość temperatury T_g pozostaje niezmieniona w odniesieniu do czystej API, podczas gdy temperatury obu przemian ciekłokrystalicznych przesuwają się w kierunku niższych wartości *T*: do 339 K (T_{Sm-N}) i 359 K (T_{N-I}). Należy również zauważyć, że w porównaniu z czystą API, intensywności pików reprezentujących przemiany ciekłokrystaliczne uległy zmniejszeniu, przy czym najbardziej znaczącą redukcję intensywności spośród badanych układów zaobserwowano dla mieszaniny ITZ–*star*PVP. Jak wspomniano powyżej, ze względu na możliwość uzyskania jednorodnych układów ITZ–*star*PVP o wyższej zawartości polimeru, przeprowadzono również badania kalorymetryczne ASD, w których stosunki wagowe API do PVP wynosiły odpowiednio 90:10 i 85:15. Analiza uzyskanych termogramów wykazała, że w przypadku mieszaniny ITZ–*star*PVP 90:10 *w/w* występuje wyraźne przejście szkliste, ale jest ono nieco przesunięte w kierunku wyższych wartości T_g (336 K) ze względu na wyższe stężenie polimeru w próbce. Co szczególnie interesujące, przemiana *Sm–N* była całkowicie stłumiona, podczas gdy przemiana *N–I* miała bardzo niską intensywność i była silnie przesunięta w kierunku T_g ($T_{N–I}$ =351 K). Z kolei, dla układu ITZ–*star*PVP 85:15 *w/w* widoczny był tylko jeden endotermiczny skok ciepła właściwego odpowiadający przejściu szklistemu przy 340 K. Natomiast oba przejścia ciekłokrystaliczne (*Sm-N* oraz *N-I*) w tej próbce były całkowicie stłumione. Oznaczało to, że otrzymana mieszanina ITZ–*star*PVP 85:15 *w/w* była w pełni amorficzna, co nie było możliwe do osiągnięcia w przypadku układów binarnych zawierających polimery liniowe (PVP K30 i *lin*PVP).

Wyniki dalszych badań strukturalnych pozostawały spójne z obserwacjami uzyskanymi na podstawie danych kalorymetrycznych. Jak pokazano na **Rysunku 21**, zarówno dyfraktogramy ITZ, jak i jego mieszanin binarnych z różnymi próbkami PVP (95:5 *w/w*) wykazywały charakterystyczne piki w zakresie niskich wartości wektora rozpraszania (*Q*) związane z porządkiem LC. Ogólnie rzecz biorąc, w przypadku cząsteczek API występujących w fazie *Sm* (tj. ułożonych warstwowo, **Rysunek 6**), zwykle podaje się sekwencję pików dyfrakcyjnych przy $Q \sim 0{,}2$, 0,4 i 0,6 $Å^{-1}$,[44,64] natomiast dla fazy *N* piki te są silnie stłumione. Jak widać na wstawce na **Rysunku 21a**, znacznie wyższe amplitudy pików przy niskich wartościach *Q* były widoczne dla próbki ITZ w porównaniu z ASD, co świadczyło o tłumieniu uporządkowania LC w układach binarnych. Z kolei wstawka na **Rysunku 21d** pokazała, że również główny pik dyfrakcyjny ITZ zmniejsza się wraz z obecnością matrycy PVP, co oznaczało, że organizacja cząsteczek w najbliższym sąsiedztwie jest bardziej nieuporządkowana. Nie zaobserwowano jednak dużych różnic na dyfraktogramach dla różnych układów ITZ–PVP 95:5 *w/w*. Niemniej jednak dane dla systemu API-*star*PVP o różnej zawartości matrycy polimerowej pokazały, że wraz ze wzrostem zawartości polimeru następuje wyraźne tłumienie i lekkie przesunięcie głównego piku dyfrakcyjnego w kierunku niższych wartości *Q*, co wskazuje na silniejsze zaburzenie struktury międzycząsteczkowej ITZ. Co więcej, piki przy niskim *Q* były mniejsze w ASD 90:10 *w/w*, co sugerowało, że w tym układzie zachowane jest jedynie uporządkowanie *N*, podczas gdy w mieszaninie 85:15 *w/w* piki o niskim *Q* praktycznie całkowicie zanikają, więc struktura ITZ przypomina strukturę cieczy izotropowej. Co więcej, długoterminowe eksperymenty XRD wykazały największą stabilność układów ITZ-*star*PVP (Fig. 4 w **P3**).

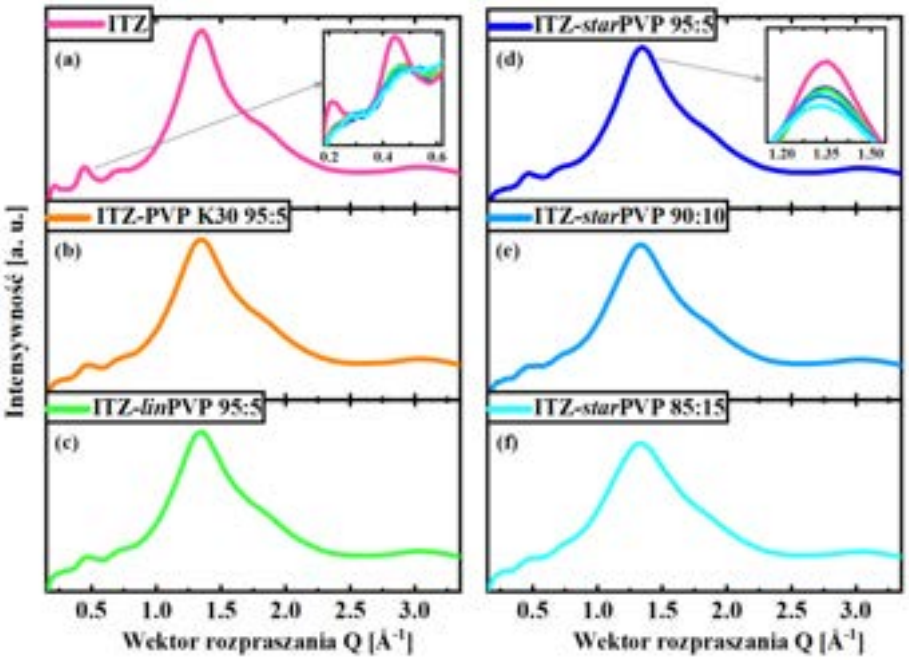

Rysunek 21. Dyfraktogramy (a) szkła ITZ i oznaczonych ASD, (b) ITZ–PVP K30 95:5 *w/w*; (c) ITZ–*lin*PVP 95:5 *w/w*; (d) ITZ–*star*PVP 95:5 *w/w*; (e) ITZ–*star*PVP 90:10 *w/w*; oraz (f) ITZ–*star*PVP 85:15 *w/w*. Pierwsza wstawka (na panelu a) przedstawia powiększony widok porównywanych dyfraktogramów w zakresie małych wartości *Q*, natomiast druga wstawka (na panelu d) przedstawia porównanie amplitudy głównego piku dyfrakcyjnego.

W ostatnim etapie pracy przeprowadzono badania rozpuszczalności ITZ, a także API zdyspergowanego w trzech różnych matrycach polimerowych (PVP K30, *lin*PVP i *star*PVP). Testy rozpuszczania API wykonano z użyciem roztworu kwasu solnego o pH=1, stanowiącego medium symulujące środowisko żołądka człowieka na czczo. Ponieważ przyjmuje się, że czas opróżniania żołądka na czczo wynosi zazwyczaj około 0,5–2 h, czas pomiaru w badaniach rozpuszczalności ustalono na 120 min. Wyniki przeprowadzonych eksperymentów przedstawiono na **Rysunku 22** (Fig. 8 w **P3**). Zauważono, że krystaliczny ITZ charakteryzuje się bardzo niską rozpuszczalność w środowisku kwaśnym, wynoszącą około 5 μg/mL, co jest w pełni zgodne z danymi opublikowanymi w literaturze.[43] Amorfizacja ITZ prowadzi natomiast do wyraźnego zwiększenia rozpuszczalności API (~100 μg/mL po około 30 minutach). W tym czasie substancja lecznicza ulega szybkiemu rozpuszczeniu, prowadząc do powstania stanu przesycenia. Po około 60 minutach obserwuje się jednak niewielki spadek ilości rozpuszczonego amorficznego ITZ, co może wskazywać na początek procesu precypitacji substancji z roztworu.

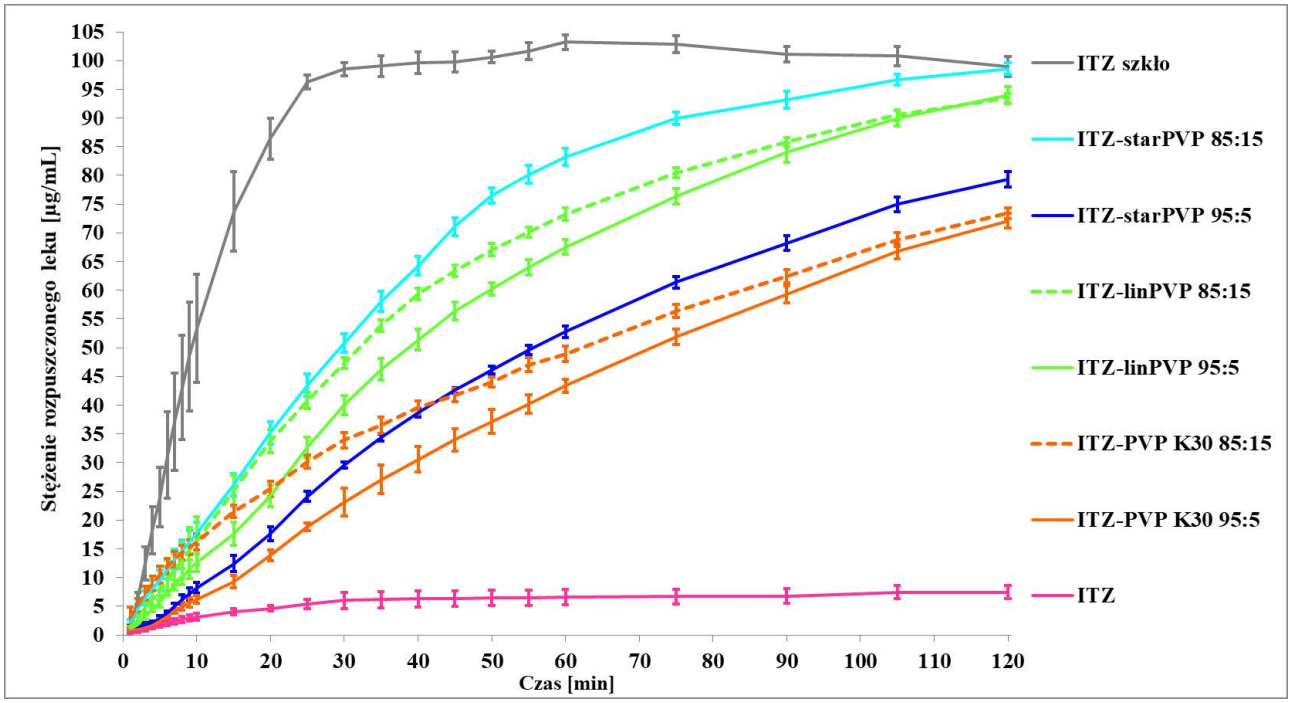

Rysunek 22. Kinetyka rozpuszczania ITZ i ITZ w mieszaninach z różnymi PVP (95:5 i 85:15 *w/w*) w 0.1 M HCl.

Z kolei, w każdym z testowanych układów ITZ–PVP zaobserwowano znaczny wzrost rozpuszczalności substancji leczniczej w porównaniu z czystą formą krystaliczną ITZ (**Rysunek 22**). Ponadto, w przeciwieństwie do amorficznego ITZ, szybkość rozpuszczania była mniejsza we wszystkich systemach binarnych. W ciągu 120 minut widoczny był stały wzrost stężenia rozpuszczonego API bez oznak precypitacji. Co ciekawe, w przypadku układów ITZ–PVP 95:5 *w/w*

największą poprawę rozpuszczalności odnotowano dla API zdyspergowanego w *lin*PVP. Po około 120 minutach eksperymentu uwolnione API z matryc PVP K30, *lin*PVP i *star*PVP osiągnęły stężenia odpowiednio 70, 90 i 75 μg/mL. Co więcej, mimo że tylko *star*PVP wykazuje zdolność tworzenia jednorodnej mieszaniny o zawartości polimeru 15% wag., zdecydowano przygotować do pomiarów rozpuszczalności formulacje binarne 85:15 *w/w* zawierające każdy badany polimer. Co istotne, jak pokazano na **Rysunku 22**, dla układów ITZ–PVP K30 i PVP–*lin*PVP, niezależnie od stosunku API-polimer, krzywe rozpuszczalności miały bardzo podobny przebieg. Jednak sytuacja była zupełnie odmienna w przypadku układu ITZ–*star*PVP. Dokładniej, rozpuszczalność ITZ–*star*PVP 85:5 *w/w* uległa znacznej poprawie (100 μg/mL) w porównaniu z układem zawierającym 5% wag. polimeru (75 μg/mL). Obserwacje te wynikają z faktu, że API nie tworzy faz LC w ASD z 15% wag. *star*PVP, co zostało potwierdzone wcześniej na podstawie wyników badań DSC i XRD. Zatem badania rozpuszczalności wyraźnie wykazały, że wybór rodzaju polimeru ma kluczowe znaczenie dla poprawy rozpuszczalności substancji leczniczej. Spośród wszystkich testowanych ASD, najniższy wzrost rozpuszczalności odnotowano dla układów ITZ–PVP K30 (95:5 i 85:15 *w/w*), natomiast najlepszy dla mieszaniny API–*star*PVP 85:15 *w/w*. Prawdopodobną przyczyną najwyższej szybkości rozpuszczania API wymieszanego z gwiaździstą matrycą PVP w porównaniu z liniowymi matrycami polimerowymi jest całkowita amorfizacja układu ITZ–*star*PVP 85:15 *w/w* (brak uporządkowania LC).

3.4. Wpływ charakteru hydrofilowo-hydrofobowego polimerów na stabilność fizyczną i biodostępność pirybedylu (artykuł P4)

Artykuł P4

Hydrophilic and Amphiphilic Macromolecules as Modulators of the Physical Stability and Bioavailability of Piribedil: A Study on Binary Mixtures and Micellar Systems

Molecular Pharmaceutics, **2025**, 22 (8), 4708−4730
DOI: 10.1021/acs.molpharmaceut.5c00276

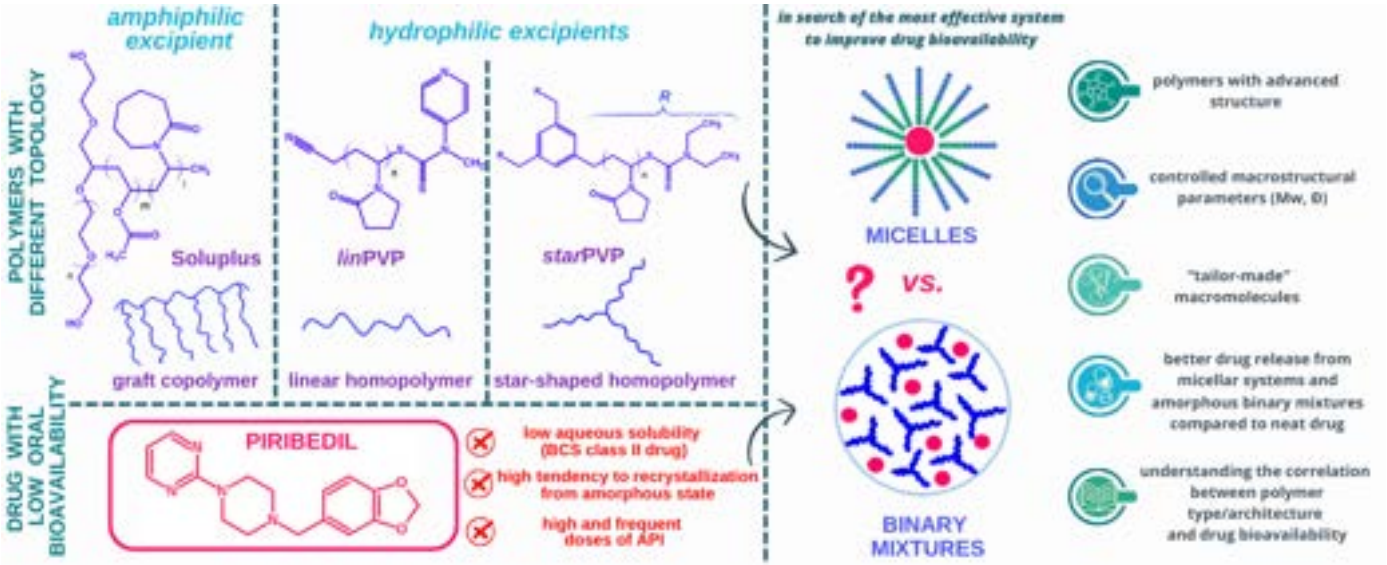

Abstrakt graficzny

Link prowadzący do artykułu:

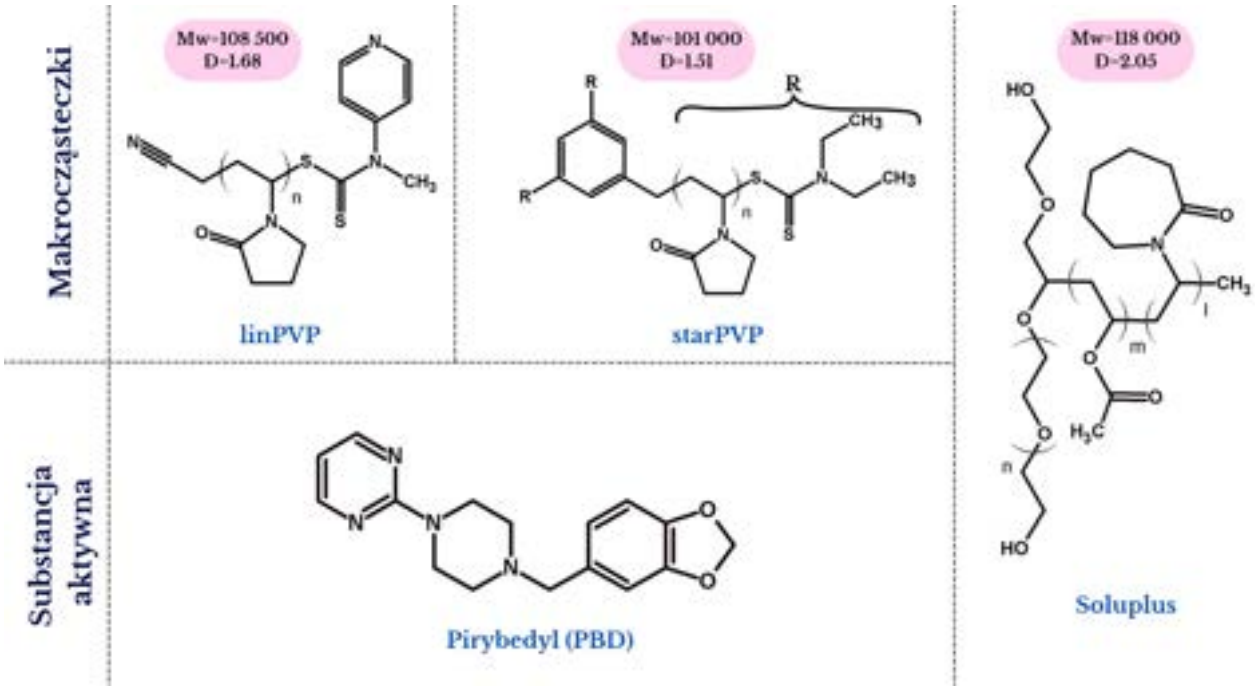

Rysunek 23. Struktury chemiczne substancji aktywnej oraz makrocząsteczek wykorzystanych w publikacji **P4**.

Celem kolejnej pracy (**P4**) było kompleksowe zbadanie ASD, a także układów micelarnych złożonych z trudno rozpuszczalnej w wodzie i charakteryzującej się ograniczoną biodostępnością substancji aktywnej – pirybedylu (PBD) – oraz trzech matryc polimerowych różniących się budową i właściwościami: (*i*) komercyjnie dostępnego amfifilowego kopolimeru o nazwie handlowej Soluplus®, (*ii*) zsyntetyzowanego *lin*PVP oraz (*iii*) trójramiennego polimeru PVP o architekturze gwiaździstej (*star*PVP). Struktury chemiczne związków wykorzystanych na potrzeby pracy **P4** zaprezentowano na **Rysunku 23**. W tym miejscu należy zwrócić uwagę, że zastosowany komercyjny kopolimer posiadał M_n = 108 500. Dlatego, analogicznie jak w przypadku prac **P1**–**P3**, na potrzeby pracy **P4** zsyntezowano homopolimery PVP o różnych topologiach, ale o zbliżonych wartościach M_n. Takie podejście umożliwiło szczegółową analizę wpływu architektury i charakteru makrocząsteczek (tj. amfifilowości lub hydrofilowości) na zdolność hamowania rekrystalizacji PBD z ASD, zmiany temperatur przejść fazowych, a także możliwość poprawy właściwości farmakokinetycznych API.

Podczas prób formulacyjnych prowadzonych z wykorzystaniem metody witryfikacji wykazano, że PBD może tworzyć jednorodne mieszaniny z substancjami pomocniczymi do maksymalnego stosunku wagowego 60:40. W celu eksperymentalnego potwierdzenia mieszalności API z makrocząsteczkami przeprowadzono analizę Flory'ego-Hugginsa. W ramach tego podejścia przeanalizowano zmianę temperatur topnienia (T_m) w funkcji udziału matrycy polimerowej, a następnie wyznaczono parametry oddziaływań (χ). Otrzymane ujemne wartości χ wskazały na

korzystne oddziaływania między składnikami oraz potwierdziły możliwość jednorodnego mieszania PBD z zastosowanymi polimerami, tj. Soluplus i PVP, w stosunku do 60:40 *w/w* (Fig. S7 i S8 w **P4**). W związku z tym do dalszych badań wybrano amorficzne układy PBD–Soluplus oraz PBD–PVP o proporcjach 90:10, 80:20, 70:30 i 60:40 *w/w*.

W pierwszym etapie wykonano pomiary kalorymetryczne API (Fig. 2a w **P4**). Podczas ogrzewania krystalicznego PBD (ϕ = 10 K/min) na termogramie zaobserwowano intensywny pik endotermiczny przy T = 370 K, odpowiadający topnieniu substancji. Po schłodzeniu stopionej próbki i jej ponownym ogrzaniu zidentyfikowano cztery przejścia fazowe. Pierwsze z nich, występujące w niższej temperaturze, przypisano przejściu szklistemu przy T_g = 260 K. W wyższym zakresie temperatur obserwowano natomiast procesy egzo- i endotermiczne, odpowiadające odpowiednio krystalizacji przy T_c = 327 K oraz topnieniu przy $T_{m(I)}$ = 371 K i $T_{m(II)}$ = 364 K. Te dwa zarejestrowane endotermiczne sygnały związane z procesem topnienia stanowiły interesującą i nieoczekiwaną obserwację, wskazującą na obecność dodatkowej formy polimorficznej PBD, która dotychczas nie była opisywana w literaturze.

Następnie przeprowadzono dodatkowe badania DSC dla układów PBD–polimer, również przy standardowej szybkości grzania (ϕ = 10 K/min), w celu określenia wpływu dodatku różnych makrocząsteczek na proces krystalizacji API oraz powstawanie jego form polimorficznych. Analiza zebranych danych wykazała, że PBD w każdej mieszaninie, nawet przy niewielkim udziale substancji pomocniczej wynoszącym 10% wag., ulegał zeszkleniu niezależnie od rodzaju zastosowanej matrycy polimerowej. We wszystkich przypadkach próby otrzymania ASD zakończyły się powodzeniem, a krzywe DSC uzyskanych formulacji wykazywały wyłącznie jeden skok ciepła właściwego, odpowiadający T_g, bez żadnych oznak rekrystalizacji (Fig. 2bcd w **P4**). Wyniki te potwierdziły amorficzny charakter badanych układów oraz skuteczne zahamowanie krystalizacji PBD przez zastosowane matryce polimerowe.

Nieizotermiczne pomiary DSC wykazały, że PBD charakteryzuje się silną tendencją do rekrystalizacji. Jednocześnie stwierdzono, że poprzez zmianę szybkości ogrzewania ϕ tej API możliwe jest modulowanie proporcji dwóch form polimorficznych, tj. formy I i II, obecnych w próbce (**Rysunek 24a**, Fig. 4a w **P4**). Co ciekawe, w przeciwieństwie do czystej substancji aktywnej, w mieszaninach binarnych 90:10 *w/w* preferowana/faworyzowana była rekrystalizacja do formy polimorficznej II, charakteryzującej się niższą temperaturą topnienia. Ponadto udział formy I, o wyższej temperaturze topnienia $T_{m(I)}$, stopniowo malał wraz ze wzrostem ϕ (**Rysunek 24b**, Fig. 4b w **P4**). Kolejną istotną obserwacją było to, że większa zawartość kopolimeru Soluplus w mieszaninie,

wynosząca 20% wag., prowadziła do rekrystalizacji PBD wyłącznie do formy polimorficznej II, o $T_{m(II)}$ = 362 K, co przedstawiono na **Rysunku 24c** (Fig. 4c w **P4**). Z kolei *lin*PVP okazał się bardziej skuteczną matrycą w tłumieniu rekrystalizacji PBD. W szczególności termogram układu PBD–*lin*PVP 90:10 *w/w* wykazywał szeroki, częściowo rozdzielony pik egzotermiczny, przypisany krystalizacji, jedynie przy najniższych szybkościach ogrzewania, tj. ϕ = 2 i 4 K/min. Przy nieco wyższej szybkości ogrzewania, wynoszącej ϕ = 6 K/min, obserwowano już wyłącznie przejście szkliste, co wskazywało na całkowicie amorficzny charakter materiału (**Rysunek 24d**, Fig. 4d w **P4**). W przypadku układu PBD–*star*PVP już dodatek zaledwie 10% wag. polimeru znacząco hamował krystalizację leku nawet przy najniższej szybkości ogrzewania, tj. ϕ = 2 K/min. Potwierdza to obecność jedynie skoku ciepła właściwego przy T_g = 259 K na krzywej DSC, widocznego we wstawce na **Rysunku 24d**.

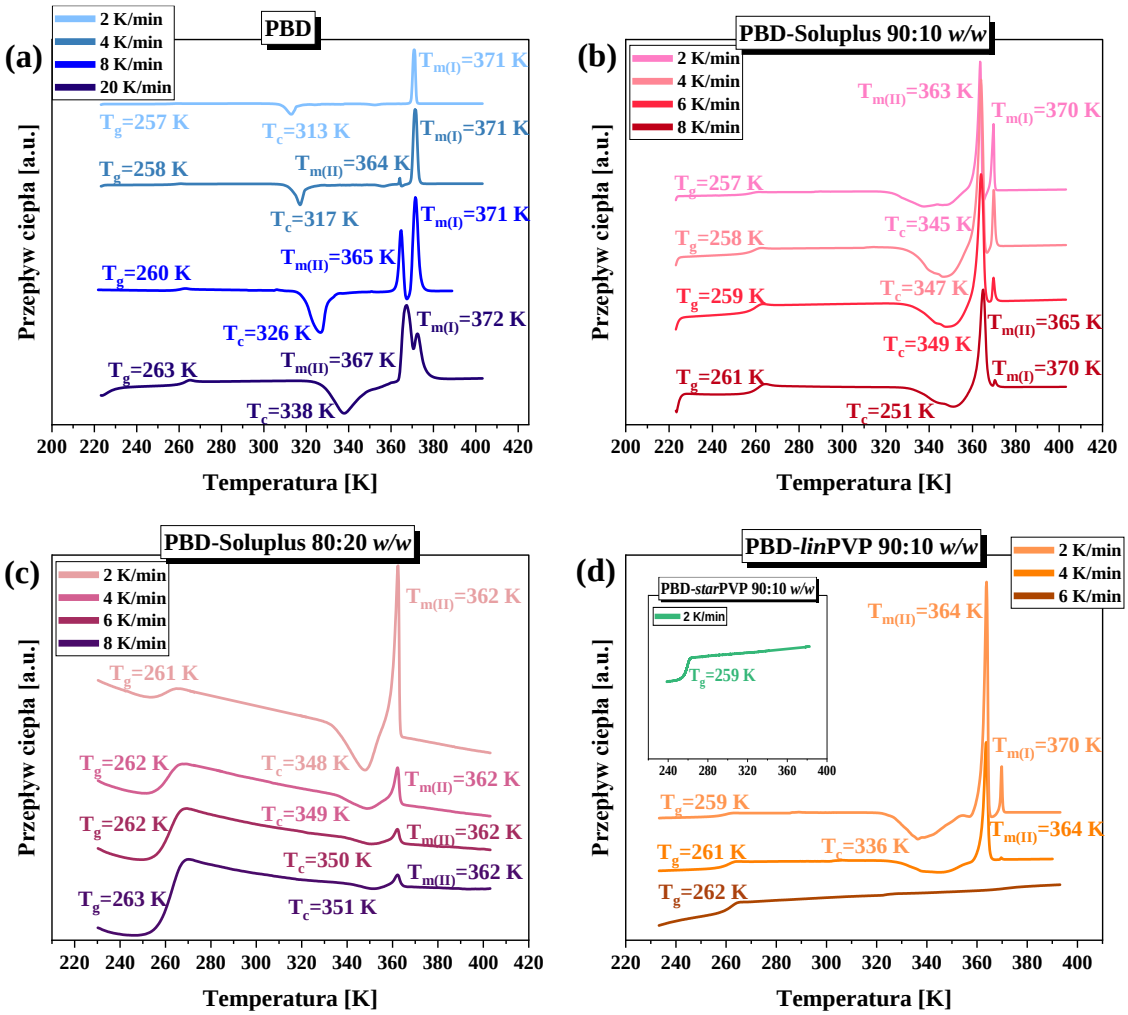

Rysunek 24. Termogramy DSC uzyskane z pomiarów nieizotermicznych (a) PBD oraz różnych mieszanin binarnych: (b) PBD-Soluplus 90:10 *w/w*, (c) PBD-Soluplus 80:20 *w/w*, (d) PBD-*lin*PVP 90:10 *w/w* (we wstawce przedstawiono termogram układu PBD-*star*PVP 90:10 *w/w* zarejestrowany przy ϕ = 2 K/min).

Istnienie II formy polimorficznej PBD zostało potwierdzone badaniami XRD, które wykazały obecność odmiennych sygnałów dyfrakcyjnych po rekrystalizacji PBD z mieszanin binarnych w porównaniu z jego formą wyjściową (**Rysunek 25**, Fig. 6 w **P4**). Odkrycie to stało się podstawą do stworzenia dwóch zgłoszeń patentowych dotyczących otrzymywania i stabilizacji nowej formy polimorficznej API. Ponadto analiza danych z długoterminowych pomiarów XRD ujawniła, że hydrofilowe polimery PVP skuteczniej stabilizują amorficzną postać PBD niż komercyjny kopolimer Soluplus. Na podstawie samych danych strukturalnych nie było jednak możliwe jednoznaczne określenie, która z matryc PVP (*lin*PVP czy *star*PVP) efektywniej stabilizuje amorficzną API (**Rysunek 25**). W związku z tym w kolejnym etapie przeprowadzono badania dielektryczne (BDS), które pozwoliły ustalić temperatury, w których η badanych mieszanin binarnych 90:10 oraz 80:20 *w/w* była zbliżona (Fig. 10 i S13 w **P4**). Zabieg ten pozwolił w następnym kroku przeprowadzić izotermiczne pomiary BDS w wyznaczonych *T*, aby ustalić w jaki sposób charakter i topologia stosowanych matryc polimerowych wpływa na zachowanie procesu rekrystalizacji. Uzyskane dielektryczne dane izotermiczne przeanalizowano pod kątem zmiany strat dielektrycznych ($\varepsilon_n^{"}$) w funkcji czasu. Następnie znormalizowane $\varepsilon_n^{"}(t)$ zostały opisane równaniem Avramiego, co pozwoliło wyznaczyć stałe szybkości krystalizacji (**Rysunek 26**, Fig. 12 w **P4**). Analiza ta jasno wskazała, że amorficzny PBD wykazuje najwyższą stabilność fizyczną w układach ASD zawierających hydrofilowe, samodzielnie otrzymane makrocząsteczki PVP. Spośród badanych matryc PVP nieco większą skuteczność w hamowaniu rekrystalizacji pirybedylu z fazy amorficznej

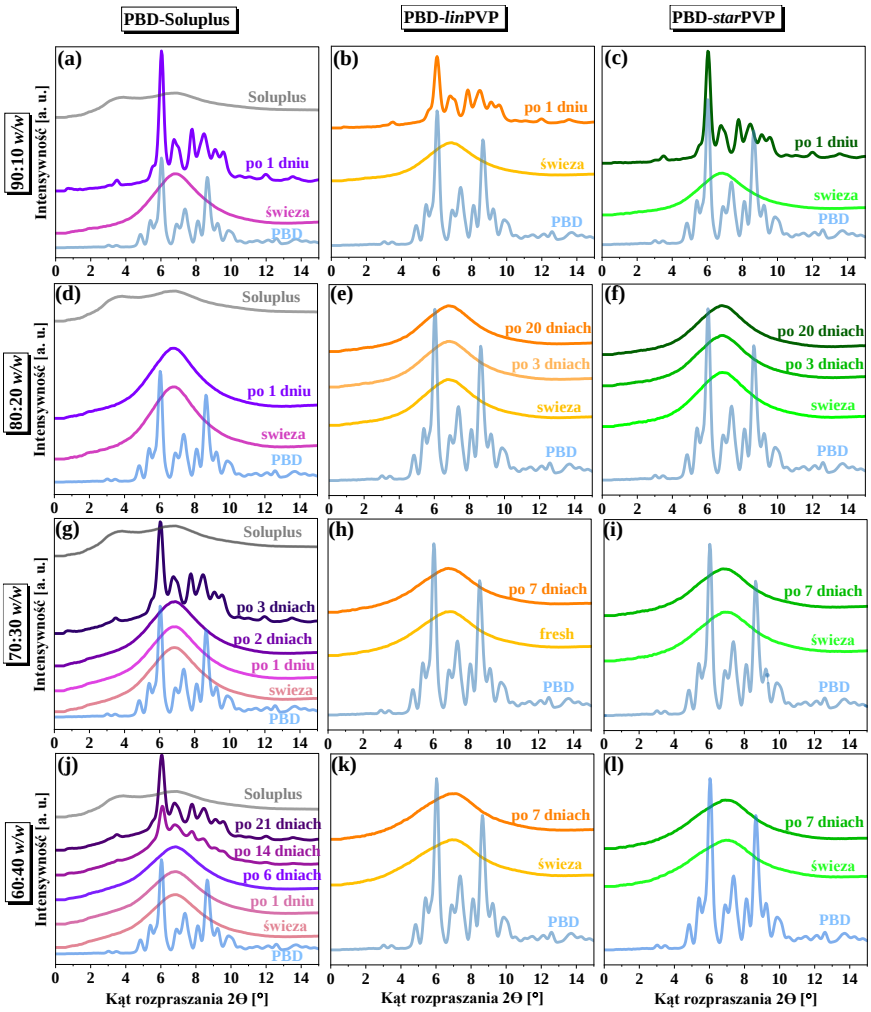

Rysunek 25. Dyfraktogramy długoterminowych pomiarów strukturalnych dla (a, d, g, j) PBD-Soluplus, (b, e, h, k) PBD-*lin*PVP oraz (c, f, i, l) PBD-*star*PVP w różnych stosunkach wagowych 90:10, 80:20, 70:30 i 60:40 *w/w*.

wykazywał jednak polimer o topologii gwiaździstej w porównaniu z jego liniowym odpowiednikiem. Jednocześnie badania FTIR oraz BDS potwierdziły brak specyficznych oddziaływań API–polimer, jak również brak istotnych zmian lepkości układu, które mogłyby tłumaczyć obserwowane różnice w zachowaniu krystalizacyjnym amorficznych mieszanin PBD–PVP i PBD–Soluplus. Na tej podstawie stwierdzono, że czynnikiem w istotny sposób determinującym stabilność fizyczną analizowanych układów binarnych jest architektura, a dokładniej topologia matryc polimerowych. Wykazano również, że komercyjnie dostępny amfifilowy kopolimer Soluplus jest natomiast bardziej odpowiedni do tworzenia układów micelarnych niż badane homopolimery PVP. Jedynie dla miceli PBD–Soluplus zaobserwowano niski i jednorodny rozkład wielkości cząstek (Fig. 13, 14, S18 w **P4**).

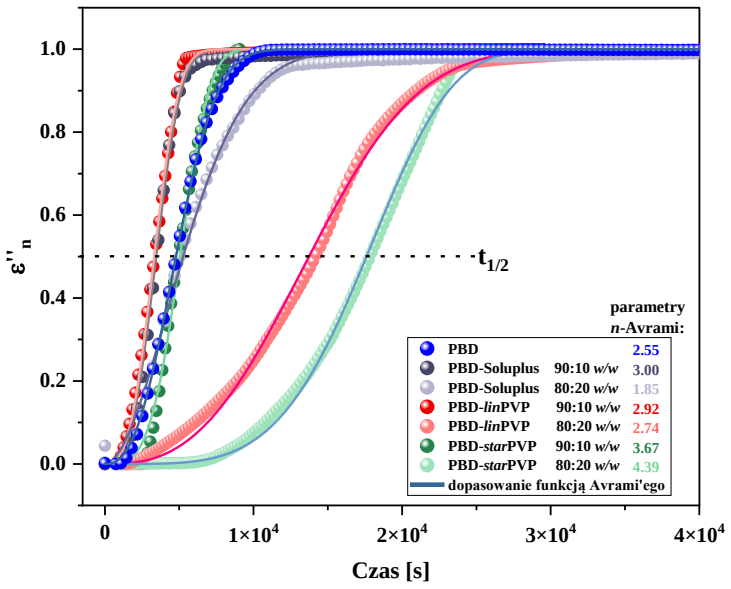

Rysunek 26. Zależność czasowa znormalizowanych strat dielektrycznych (ε_n'') dla PBD i mieszanin binarnych API-polimer w różnych proporcjach (90:10 i 80:20 *w/w*).

Końcowym etapem pracy **P4** była ocena profilu uwalniania substancji aktywnej. Pomiary wykazały, że ilość PBD uwalnianego ze wszystkich badanych formulacji (ASD i systemów micelarnych) w środowisku słabo kwaśnym (medium FaSSIF, pH = 6.5) była wyraźnie większa niż w przypadku czystej, krystalicznej postaci API (~30%). Najbardziej znaczącą poprawę rozpuszczalności odnotowano dla ASD PBD–Soluplus 60:40 *w/w* (~50%) oraz dla układu micelarnego PBD–*star*PVP (~99%). Co istotne, w przypadku tej drugiej formulacji uzyskano również najbardziej pożądany profil uwalniania, polegający na stopniowym uwalnianiu API przez około 20 godzin, zamiast szybkiego uwalniania w ciągu pierwszych 1–3,5 godziny (Fig. 16 i 17 w **P4**).

Podsumowując, uzyskane wyniki wskazały, że zastosowanie różnorodnych matryc polimerowych jako nowoczesnych nośników substancji czynnych w odmiennych typach formulacji stanowi obiecujący kierunek badań. Uzyskane wyniki wskazują, że w pełni hydrofilowe

makrocząsteczki polimerowe są bardziej odpowiednimi kandydatami na inhibitory krystalizacji PBD, przy czym szczególnie skuteczne wydają się układy o topologii rozgałęzionej. Z kolei kopolimery amfifilowe można uznać za bardziej pożądane makrocząsteczki do projektowania systemów micelarnych. Opracowane układy mogą zatem istotnie przyczyniać się do poprawy rozpuszczalności pirybedylu oraz innych słabo rozpuszczalnych API, a w konsekwencji do zwiększenia ich biodostępności. Z punktu widzenia nauk farmaceutycznych przedstawione rezultaty mają duże znaczenie poznawcze i aplikacyjne. Otwierają one nowe perspektywy badawcze dotyczące zarówno poszukiwania nowych form polimorficznych substancji leczniczych, jak i oceny wpływu rodzaju polimeru, jego topologii oraz typu formulacji na poprawę biodostępności wielu leków.

4. Treści publikacji stanowiących podstawę rozprawy doktorskiej

4.1. The impact of various poly(vinylpyrrolidone) polymers on the crystallization process of metronidazole (P1)

Autorzy: L. Orszulak, T. Lamrani, M. Tarnacka, B. Hachuła, K. Jurkiewicz, P. Zioła, A. Mrozek-Wilczkiewicz, E. Kamińska, K. Kamiński

Referencja: *Pharmaceutics*, 2024, 16 (1), 136

DOI: 10.3390/pharmaceutics16010136

Impact Factor czasopisma: 5.5

Liczba punktów ministerialnych MNiSW czasopisma: 100 (2024)

Mój udział w pracy polegał na zsyntezowaniu matryc polimerowych, ich pełnej charakterystyce spektroskopowej i chromatograficznej, tworzeniu mieszanin binarnych metodą witryfikacji, analizie danych, dyskusji wyników, przygotowywaniu tekstów manuskryptów, opracowywaniu odpowiedzi dla Recenzentów i Edytora, pozyskaniu finansowania w ramach kierowania grantem *„Perły Nauki”*.

pharmaceutics

MDPI

Article

The Impact of Various Poly(vinylpyrrolidone) Polymers on the Crystallization Process of Metronidazole

Luiza Orszulak [1,*], Taoufik Lamrani [2], Magdalena Tarnacka [2], Barbara Hachuła [1], Karolina Jurkiewicz [2], Patryk Zioła [2], Anna Mrozek-Wilczkiewicz [2,3], Ewa Kamińska [4] and Kamil Kamiński [2]

[1] Institute of Chemistry, Faculty of Science and Technology, University of Silesia in Katowice, Szkolna 9, 40-007 Katowice, Poland; barbara.hachula@us.edu.pl
[2] Institute of Physics, Faculty of Science and Technology, University of Silesia in Katowice, 75 Pułku Piechoty 1A, 41-500 Chorzow, Poland; taoufik.lamrani@us.edu.pl (T.L.); magdalena.tarnacka@us.edu.pl (M.T.); karolina.jurkiewicz@us.edu.pl (K.J.); patryk.ziola@us.edu.pl (P.Z.); anna.mrozek-wilczkiewicz@us.edu.pl (A.M.-W.); kamil.kaminski@us.edu.pl (K.K.)
[3] Biotechnology Centre, Silesian University of Technology, Boleslawa Krzywoustego 8, 44-100 Gliwice, Poland
[4] Department of Pharmacognosy and Phytochemistry, Faculty of Pharmaceutical Sciences in Sosnowiec, Medical University of Silesia in Katowice, Jagiellonska 4, 41-200 Sosnowiec, Poland; ekaminska@sum.edu.pl
* Correspondence: luiza.orszulak@us.edu.pl

Abstract: In this paper, we propose one-step synthetic strategies for obtaining well-defined linear and star-shaped polyvinylpyrrolidone (*lin*PVP and *star*PVP). The produced macromolecules and a commercial PVP K30 with linear topology were investigated as potential matrices for suppressing metronidazole (MTZ) crystallization. Interestingly, during the formation of binary mixtures (BMs) containing different polymers and MTZ, we found that linear PVPs exhibit maximum miscibility with the drug at a 50:50 weight ratio (*w*/*w*), while the star-shaped polymer mixes with MTZ even at a 30:70 *w*/*w*. To explain these observations, comprehensive studies of MTZ-PVP formulations with various contents of both components were performed using Fourier-transform infrared spectroscopy, differential scanning calorimetry, and X-ray diffraction. The obtained results clearly showed that the polymer's topology plays a significant role in the type of interactions occurring between the matrix and MTZ. Additionally, we established that for MTZ-PVP 50:50 and 75:25 *w*/*w* BMs, linear polymers have the most substantial impact on inhibiting the crystallization of API. The star-shaped macromolecule turned out to be the least effective in stabilizing amorphous MTZ at these polymer concentrations. Nevertheless, long-term structural investigations of the MTZ-*star*PVP 30:70 *w*/*w* system (which is not achievable for linear PVPs) demonstrated its complete amorphousness for over one month.

Keywords: metronidazole; polyvinylpyrrolidone; topology; star-shaped polymer; amorphous solid dispersion; binary mixtures

check for updates

Citation: Orszulak, L.; Lamrani, T.; Tarnacka, M.; Hachuła, B.; Jurkiewicz, K.; Zioła, P.; Mrozek-Wilczkiewicz, A.; Kamińska, E.; Kamiński, K. The Impact of Various Poly(vinylpyrrolidone) Polymers on the Crystallization Process of Metronidazole. *Pharmaceutics* **2024**, *16*, 136. https://doi.org/10.3390/pharmaceutics16010136

Academic Editor: Kyriakos Kachrimanis

Received: 30 December 2023
Revised: 16 January 2024
Accepted: 17 January 2024
Published: 19 January 2024

1. Introduction

For several decades, the pharmaceutical sector has faced a significant challenge in improving the solubility and bioavailability of traditional, i.e., crystalline, drugs, aiming to enhance the effective delivery of medications. Unfortunately, a large percentage of drugs available on the market (approximately 40%) and those in the research and development phase (approximately 90%) still exhibit poor water solubility, which significantly hampers their absorption and consequently leads to less effectiveness in the human body [1–4]. Therefore, in recent years, the use of amorphous active pharmaceutical ingredients (APIs) is gaining increasing interest, as they often provide better solubility, dissolution rate, and bioavailability compared to their crystalline counterparts. On the other hand, due to high free energy, APIs in this form reveal a high risk of recrystallization over time, leading to a potential loss of therapeutic efficacy [5–8]. Hence, improving physical stability during

processing and storage is crucial for the development of effective pharmaceuticals. A commonly employed method for stabilizing amorphous APIs is the formation of binary mixtures (BMs) with polymeric excipients (EXCs), referred to as amorphous solid dispersions (ASDs) [9]. In the literature, several mechanisms have been proposed to interpret the impact of macromolecules on the stability of drugs in ASDs [10,11]. For example, it has been demonstrated that hydrogen bonds formed between polymeric matrices and APIs enhance the physical stability of amorphous pharmaceuticals by reducing molecular mobility [12,13]. There are also reports showing that other types of interactions, such as ionic, dipole–dipole, and van der Waals interactions, inhibit the recrystallization of APIs from the amorphous binary systems [14,15]. Moreover, one can mention the volume fraction effect [16–19], as well as the increase in the glass transition temperature (T_g) and consequently, the reduced molecular mobility of the system, due to the addition of the polymer [12,20]. The crucial role of high-molecular-weight systems prompts scientists to conduct further in-depth studies on the ASDs of active substances with various kinds of polymers.

Herein, it should be pointed out that polymeric EXCs used in ASDs are subject to high requirements. These compounds must exhibit non-toxicity, compatibility with human tissues, and have a well-defined structure [21]. The most commonly applied macromolecules in amorphous BMs belong to three classes [22]: (i) cellulose derivatives (e.g., hydroxypropyl methylcellulose, hydroxypropyl methylcellulose acetate succinate, hydroxypropyl methylcellulose phthalate) [23–26], (ii) polyvinylpyrrolidone (PVP) and its copolymers (e.g., polyvinylpyrrolidone/vinyl acetate copolymer, PVP/VA) [27–31], and (iii) methacrylic acid and methacrylate esters (e.g., Eudragit® L100, S100) [32–34]. Undoubtedly, among the listed polymers widely used in the pharmaceutical industry, PVP stands out for its particularly advantageous properties. This macromolecule is non-toxic, inert, temperature-resistant, pH-stable, and biocompatible [21]. Moreover, it shows a complex affinity for hydrophilic and hydrophobic drugs, which is especially desirable in the formulation of BMs [35–38]. As shown in the literature, the majority of studies primarily focus on the impact of commercially available PVP on the crystallization of APIs in ASDs [39–42]. For example, Balani et al. reported that the addition of 33% of PVP K30 significantly suppresses the recrystallization of amorphous salbutamol sulfate, while an 80% polymer content completely stabilizes the amorphous form of the drug (even after a storage period) [39]. Herein, it should be noted that the large-scale production of PVP occurs through uncontrolled radical polymerization, allowing only for the attainment of poorly defined macromolecules (a broad range of molecular weights M_n and hence, high dispersity Đ) [43,44]. Meanwhile, the most desirable polymers in the pharmaceutical industry are macromolecules with precisely tailored parameters, characterized by the target M_n, low-to-moderate Đ (preferably not exceeding a value of 1.5), and possessing active chain ends enabling further modifications according to specific requirements. Unfortunately, researchers in numerous papers have still only considered the influence of molecular weight and concentration of PVP (e.g., Kollidon® K10, K30, K90) on the physical stability of drug–polymer blends [28,42,45,46]. On the other hand, aside from one paper devoted to PVP mixed with flutamide [37], the impact of microstructure/tacticity, as well as the dispersity and topology of this polymer, on the physico-chemical and pharmacokinetic properties of APIs is almost completely overlooked, creating an exceptionally intriguing research gap.

Hence, it seems relevant to perform more systematic studies to verify whether the microstructure, dispersity, or importantly topology of the polymer affect the crystallization kinetics and physical stability of a given pharmaceutical. In this context, metronidazole (MTZ), the antibacterial and antiprotozoal medication [47,48], is looming as an ideal candidate for such investigations. Briefly, one can stress that the amorphization of this active substance is a difficult task. For example, it is not possible to obtain it in the glassy form using the standard vitrification method due to its immediate crystallization after melting [49]. So far, only one successful attempt to produce a stable amorphous MTZ in ASDs has been

reported. Minecka et al. have demonstrated that acetylated cyclodextrins (especially the β form) can effectively inhibit the recrystallization of MTZ from the glassy state [49]. Therefore, further exploration of novel EXCs (both low- and high-molecular-weight) effectively stabilizing amorphous MTZ appears fully justified.

In this paper, we examine BMs of MTZ with three polymers, i.e., (i) commercial linear PVP (with high Đ), (ii) self-synthesized well-defined linear PVP (with low Đ), and (iii) self-synthesized well-defined star-shaped PVP (with low/moderate Đ). Herein, one can add that the latter two macromolecules are not available on the market. The main aim of our studies, carried out using differential scanning calorimetry (DSC), X-ray diffraction (XRD), as well as infrared spectroscopy (FTIR) techniques, is to explain how the addition of PVP with different topologies and well-defined structures (M_n, Đ) influences the recrystallization tendency of MTZ. Understanding the impact of polymer structure on the crystallization rate of APIs is of paramount importance in the rational design of amorphous formulations with excellent physical stability.

2. Materials and Methods

2.1. Materials

1-vinyl-2-pyrrolidone (VP, >99%, Sigma Aldrich, Poznan, Poland) was passed through an alumina column before use to remove the inhibitor. 2,2′-azobis(2-methylpropionitrile) solution (AIBN, 0.2 M in toluene, Sigma Aldrich), cyanomethyl methyl(4-pyridyl) carbamodithioate (CTA1, 98%, Sigma Aldrich), 1,3,5-tris(bromomethyl)benzene (97%, Sigma Aldrich), sodium diethyldithiocarbamate trihydrate (Sigma Aldrich), diethyl ether (pure for analysis, Chempur, Piekary Slaskie, Poland), methanol (99.85%, PureLand, Stargard, Poland), dichloromethane (DCM, 99%,, Karpinex, Warszawa, Poland), chloroform-d (99.8% D, contains 0.03% *v*/*v* TMS, Sigma Aldrich), PVP K30 (M_n = 40,000 g/mol, Đ = 2.05, Sigma Aldrich), and crystalline MTZ (IUPAC name 2-(2-Methyl-5-nitro-1H-imidazol-1-yl)ethanol, 99%, Sigma Aldrich) were used as received.

2.2. The Procedure of Preparing Amorphous MTZ-PVP BMs

Amorphous binary mixtures composed of MTZ and PVP polymers, including a commercial PVP K30, and synthesized linear and star-shaped PVP samples were obtained using the melt-cooling method. The MTZ-PVP systems were prepared at different weight ratios of API to polymer, i.e., 75:25, 60:40, 50:50. In the case of MTZ-starPVP, it was also possible to prepare 40:60 and 30:70 *w*/*w* systems. To obtain a homogeneous mixture, appropriate amounts of crystalline MTZ and PVP were weighed, carefully transferred to a metal plate, and preliminarily mixed using a spatula. Subsequently, the plate with the API–polymer mixture was transferred to a hot plate heated to a temperature of 438 K. After a while, MTZ began to melt and the entire BM was stirred until the complete dissolution of PVP in the API. After determining a homogeneous system, the sample was vitrified by rapidly transferring it to a pre-cooled copper plate.

2.3. Nuclear Magnetic Resonance (NMR)

^{1}H and ^{13}C NMR spectra for the samples dissolved in chloroform-d (with tetramethylsilane internal standard) were collected using a Bruker Ascend 600 MHz spectrometer. For measurements, standard experimental conditions and the standard Bruker program were applied.

2.4. Size Exclusion Chromatography (SEC)

M_n and Đ of linear and star-shaped PVP homopolymers were determined by size exclusion chromatography (SEC). For data collection, we used a Viscotek GPC Max VE 2001 (Malvern, UK) and a Viscotek TDA 305 (Malvern, UK) triple detection system (refractometer, viscosimeter, and low-angle laser light scattering). The OmniSec 5.12 was applied for data processing. The separation was carried out using two T6000M general mixed columns. The

measurements were performed in DMF/LiBr (0.01 M) as an eluent at T = 303 K, with a flow rate of 0.7 mL/min.

2.5. Cell Culture

Normal human dermal fibroblasts (NHDFs) were purchased from PromoCell. The cell line was cultured in Dulbecco's Modified Eagle's Medium (DMEM) supplemented with 15% non-inactivated FBS (Sigma Aldrich) and penicillin/streptomycin antibiotics (1% *v*/*v*; Gibco, Waltham, MA, USA). The cells were kept under standard conditions at 37 °C in a humid atmosphere with 5% CO_2 and passed as required by the manufacturer. Additionally, cells were tested against Mycoplasma contamination using the PCR technique with specific primers.

2.6. Cytotoxicity Studies

The cells were seeded in 96-well transparent plates (Nunc, Waltham, MA, USA) at a density of 4000 cells per well and incubated for 24 h at 37 °C. Approximately 24 h after seeding, the medium was removed from wells and 200 µL of various concentrations (from 0.05 to 0.001 mg/mL) of tested compounds (dissolved in DMEM) were added to the plate and incubated for 72 h at 37 °C. Next, compound solutions were exchanged with 100 µL of DMEM without phenol red and 20 µL of CellTiter 96® AQueous One Solution-MTS (Promega, Madison, WI, USA) and incubated for one hour at 37 °C. After that time, the absorbance of the samples was measured at 490 nm using a multi-plate reader (Varioskan LUX, Thermo Scientific, Waltham, MA, USA). The results were normalized to a control consisting of untreated cells. Compounds were tested in triplicate in a single experiment, each repeated three times.

2.7. Fourier-Transform Infrared (FTIR) Spectroscopy

FTIR spectra were collected on a Nicolet iS50 FTIR spectrometer (Thermo Scientific) with a built-in diamond iS50 ATR sampling station in the MIR range of 4000–400 cm^{-1}. Each spectrum was recorded from 16 scans with a resolution of 4 cm^{-1}. The high-temperature FTIR spectrum of MTZ (at the melting point of 438 K) was measured using a GladiATR accessory (Pike Technologies, Madison, WI, USA) coupled with an FTIR spectrometer in the range 4000–400 cm^{-1} (16 scans; spectral resolution of 2 cm^{-1}).

2.8. Differential Scanning Calorimetry (DSC)

Calorimetric measurements of MTZ, various PVPs (i.e., PVP K30, *lin*-PVP, and *star*-PVP), and their BMs were performed using a Mettler-Toledo DSC system, which is equipped with a liquid nitrogen cooling accessory and an HSS8 ceramic sensor. Temperature and enthalpy were calibrated using indium and zinc standards. Samples were placed in aluminum crucibles (40 µL). DSC measurements were carried out in a temperature range of 250 to 480 K. The heating/cooling rate (ϕ) during experiments was equal to 10 K/min.

Additionally, for all studied MTZ-PVP BMs, non-isothermal DSC measurements were performed over a temperature range of 250 to 460 K. They were made at a ϕ from 2.5 to 15 K/min.

2.9. X-ray Diffraction (XRD)

X-ray diffraction measurements were conducted employing a D/Max Rapid II diffractometer (Rigaku Corporation, Akishima-shi, Japan) equipped with an image plate detector, a rotating silver anode, and an incident beam (002) graphite monochromator. The wavelength (λ) of the incident beam was 0.56 . Samples were measured in borosilicate glass capillaries in the Debye–Scherrer geometry. The diffraction patterns were collected as functions of the scattering angle (2θ) in a single shot using a 2D curved image plate detector and transformed to functions of the scattering vector $Q = 4\pi\, sin(\theta)/\lambda$. Samples containing recrystallized MTZ were subjected to measurements over 1 h. The measurement time for

freshly prepared ASDs was limited to 15 min due to their high recrystallization rate. The temperature during all measurements was 295 K.

3. Results and Discussion

In the first stage of our studies, we developed procedures for obtaining well-defined linear (*lin*PVP) and three-arm star-shaped PVP (*star*PVP) homopolymers, which are thermodynamically stable amorphous macromolecules. Herein, it should be noted that despite PVP being a widely used polymer in the pharmaceutical and cosmetic industries [50], only linear PVP (with various molecular weights) and its copolymers are currently available in the commercial market. In contrast, other topologies of this polymer are entirely unavailable on a large scale. Therefore, the search for synthetic methods enabling the production of well-defined non-linear PVP polymers is an extremely interesting and ambitious research topic. A promising technique for producing complex macromolecular structures appears to be Reversible Addition–Fragmentation Chain Transfer (RAFT) polymerization, where a crucial role is played by a suitably selected Chain Transfer Agent (CTA) for a specific type of monomer [51]. As indicated in the literature, suitable CTAs for *N*-vinyl monomers (including VP) are compounds from the xanthate and dithiocarbamate groups [52,53]. It should also be emphasized that a significant majority of commercially available CTAs are single-functional compounds, allowing for the formation of linear macromolecules. In fact, one paper describes the successful synthesis of a four-arm star-shaped PVP using the RAFT method [54]. However, it is worth noting that the article's authors utilized a commercially available tetrafunctional CTA from the trithiocarbonate group, which is not considered to control the polymerization of *N*-vinyl monomers [52,53]. As a consequence, attempts to conduct RAFT polymerization at ambient pressure and using the discussed CTA led to the production of star polymers with high dispersities, Đ (up to 2.45). Interestingly, RAFT polymerization at higher pressure (p = 250 MPa) yields a four-arm star-shaped PVP with a moderate Đ = 1.80.

Based on the information presented above and noting the lack of commercially available multifunctional CTAs tailored for *N*-vinyl monomers, we decided to independently obtain a trifunctional CTA from the dithiocarbamate group. Subsequently, it was used to synthesize a well-defined three-arm star-shaped PVP (M_n = 38,700 g/mol; Đ = 1.48) using a *"core-first"* strategy. In turn, a commercial CTA also from the dithiocarbamate group was applied to synthesize linear PVP, resulting in a homopolymer with favorable macrostructural parameters (M_n = 37,600 g/mol; Đ = 1.22) (see Figure 1). The description of the synthesis of the trifunctional CTA and PVP homopolymers (*lin*PVP and *star*PVP) is included in the Supplementary Materials (SMs).

3.1. Cytotoxicity Studies

Since both synthesized *lin*PVP and *star*PVP are new materials, we decided to perform cytotoxicity tests on normal human dermal fibroblasts (NHDFs) first and compare the results with the data obtained for the commercially available PVP K30, which is thoroughly used in pharmaceutical formulations. Herein, it should be briefly mentioned that we carried out measurements with a PVP concentration no higher than 0.05 mg/mL as is usually conducted for macromolecules [55–58]. Figure 2 presents a graph of the dependence of cell survival on the concentration of the examined compounds. As illustrated, the tested polymers show no cytotoxicity against the normal human dermal fibroblast line. The survival fraction in all cases did not fall below 85%, which indicates the neutral effect of the samples on the proliferation of the tested cell line. The studies revealed that end groups with a CTA moiety in the structure of the synthesized polymer as well as the presence of a star initiator do not affect their cytotoxicity with respect to PVP K30. Such a result is extremely promising in the context of the potential use of these materials as excipients in binary formulations.

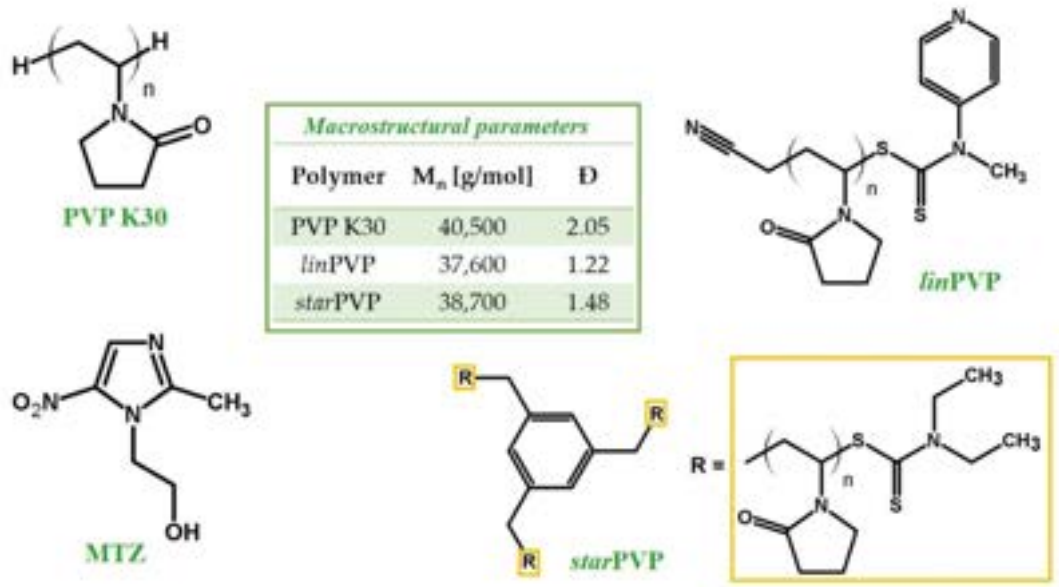

Macrostructural parameters

Polymer	M_n [g/mol]	Đ
PVP K30	40,500	2.05
*lin*PVP	37,600	1.22
*star*PVP	38,700	1.48

Figure 1. The chemical structures of metronidazole (MTZ) and the employed PVP polymers (K30, *lin*PVP, *star*PVP) along with a table presenting their macrostructural parameters.

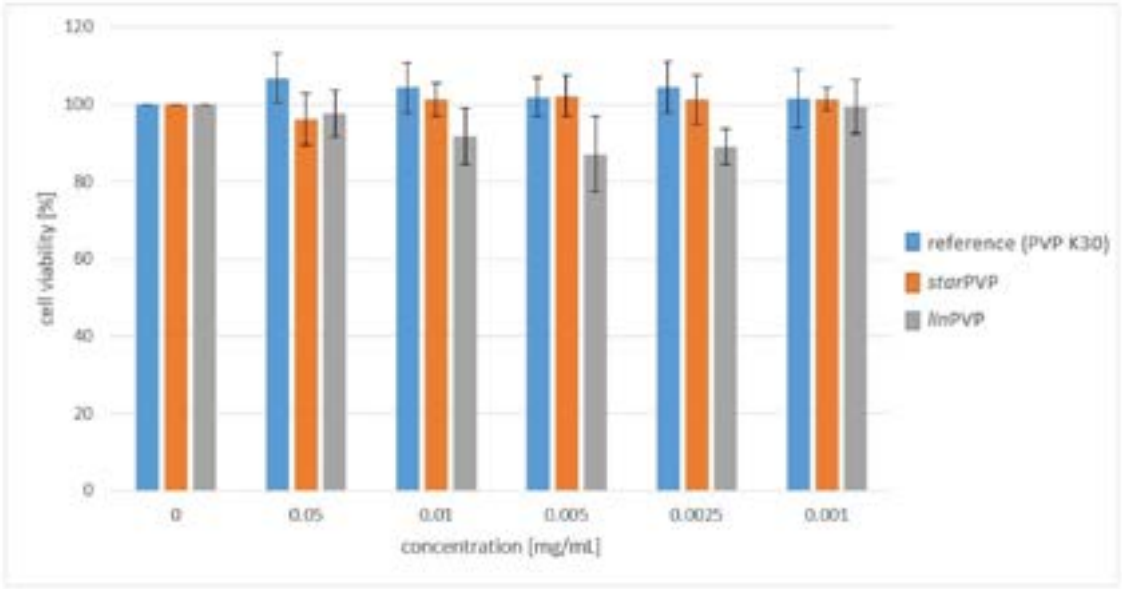

Figure 2. Cell viability seeded onto various PVP samples.

3.2. *Preparation of Amorphous Binary Mixtures of MTZ with PVP*

Having cytotoxicity data at hand, we proceeded to prepare amorphous BMs of three different PVPs with similar molecular weights ($M_n \approx 40{,}000$ g/mol) but different dispersities and topologies with MTZ—a pharmaceutical with a high tendency to crystallize. Herein, it is worth pointing out that PVP K30 exhibits relatively high dispersity (Đ = 2.05)

compared to the synthesized *lin*PVP and *star*PVP. It implies that this polymer consists of both short and long macromolecular chains, most likely due to an uncontrolled synthesis procedure on a large/industrial scale [59]. It should also be noted that each macromolecule was fully amorphous and thermodynamically stable.

Importantly, during the samples' preparation, it was found that *star*PVP mixes much better with MTZ than the other two linear macromolecules (PVP K30, *lin*PVP). Consequently, it was possible to prepare homogeneous (verified further by DSC studies) mixtures up to 30 wt% of MTZ, while in other cases, 50 wt% was a limiting drug concentration. Such a result was quite surprising for us since we expected similar miscibility properties of various PVPs and MTZ. To understand this peculiar finding, FTIR investigations on all prepared samples were carried out.

3.3. *Fourier-Transform Infrared Spectroscopy (FTIR) Data*

To gain insight into the intermolecular interactions between given macromolecules and API, Attenuated Total Reflection (ATR)-FTIR measurements for the individual components (MTZ, PVPs) and their binary systems were performed at room temperature (T = 295 K) in the spectral range from 4000 to 400 cm^{-1}. As it is impossible to obtain amorphous MTZ using the standard vitrification method due to its rapid crystallization after melting, we collected the FTIR spectrum of the molten MTZ to detect spectral differences between the crystalline and liquid samples. The spectra of the crystalline and molten MTZ, as well as three PVP samples, together with the assignment of characteristic bands to the appropriate molecular vibrations [49,60–63], are given in the SMs (see Figure S7), whereas the spectra of MTZ- PVP BMs in the supercooled liquid/or glassy and crystalline states, recorded in the regions of 3800–2400 and 1800–400 cm^{-1}, are shown in Figures S8–S10. It is worth mentioning that in the crystal, MTZ molecules are linked through O—H···N hydrogen bonds and stabilized by C—H···O weak interactions, forming chains propagating/extending along the *c*-axis direction [64]. These interactions are reflected in the higher frequency range of the IR spectrum in the form of an intense and broad band located at 3204 cm^{-1} associated with the stretching vibration of the OH group, ν_{OH} (Figure S7). In the case of molten MTZ, the ν_{OH} band is shifted towards higher wavenumbers (blue shift, 3228 cm^{-1}). The detailed assignment of other spectral bands of the MTZ sample and the peaks occurring in the spectra of three PVP samples is presented in the SMs. It is worth noting that the analyzed PVP spectra (PVP-K30, *lin*PVP, *star*PVP) essentially differ in the position of the ν_{OH} band originating from water adsorbed into the polymer (PVP-K30 ν_{OH} = 3409 cm^{-1}, *lin*PVP ν_{OH} = 3436 cm^{-1}, *star*PVP ν_{OH} = 3470 cm^{-1}), and the position of the band related to the C=O stretching vibrations (PVP-K30 $\nu_{C=O}$ = 1645 cm^{-1}, *lin*PVP $\nu_{C=O}$ = 1651 cm^{-1}, *star*PVP $\nu_{C=O}$ = 1661 cm^{-1}) (Figure S7).

We started the analysis of possible interactions between neat API and PVP samples from MTZ-PVP K30 BMs. As shown in Figure S8, MTZ in the solid dispersion shows a difference in spectral behavior compared to the molten state. It can be observed that the ν_{OH} band of MTZ in all binary systems (3700–3100 cm^{-1}) is shifted to higher frequencies as well as considerably broadened and blurred relative to that in the liquid MTZ (3228 cm^{-1}). The band originating from the C-H stretching vibrations of the H-C=C group located at 3103 cm^{-1} in the molten MTZ also shifts toward higher wavenumbers after mixing with PVP K30 (~3130 cm^{-1}), which probably suggests the lack of C-H···O interactions involving a H-C=C moiety in the mixture. Moreover, other MTZ bands occurring at lower frequency ranges of BMs are also slightly shifted compared to those in neat API. All these facts confirm complete destruction of the crystal structure of the API in these mixtures. However, the most interesting feature of the studied MTZ-PVP K30 spectra is the behavior of the $\nu_{C=O}$ band of the polymer when mixed with API. As shown in Figure 3a, the $\nu_{C=O}$ peak of neat PVP-K30 located at 1645 cm^{-1} exhibits a blue shift (shift to higher wavenumbers) with the increasing content of MTZ in BMs (50:50 *w*/*w* 1654 cm^{-1}; 60:40 *w*/*w* 1655 cm^{-1}, 75:25 *w*/*w* 1657 cm^{-1}). This fact suggests that the interaction between MTZ and PVP is a dipole–dipole intermolecular interaction, which intensifies with a higher amount of API. A

similar interaction mechanism was observed for the ketoconazole-PVP and MK-0591/PVP systems [62,65,66]. In the case of the ketoconazole–PVP mixture, molecular calculations confirmed that ketoconazole has a dipole moment that is quite large in magnitude and may, therefore, interact strongly with other polar molecules such as PVP [62,65]. Since MTZ is a polar substance, one can expect a similar pattern of behavior.

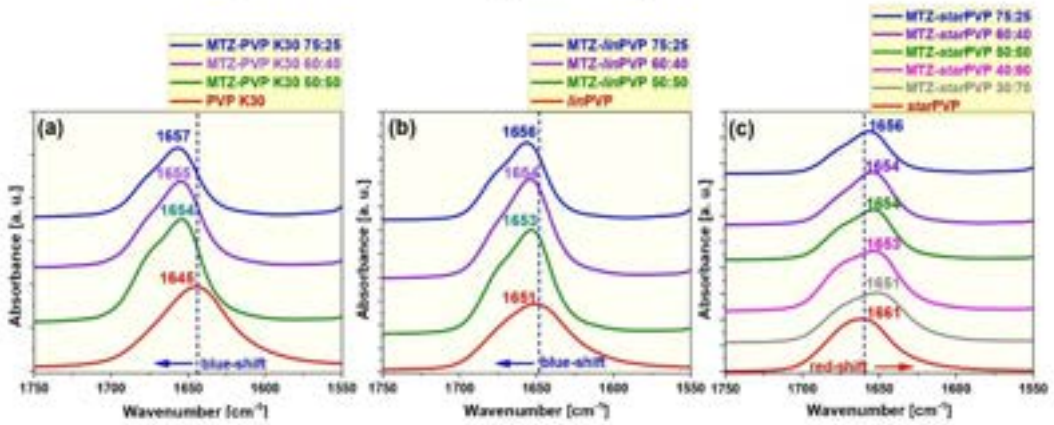

Figure 3. FTIR spectra of the carbonyl stretching region of (**a**) MTZ-PVP K30, (**b**) MTZ-*lin*PVP, and (**c**) MTZ-*star*PVP binary mixtures at different API–polymer ratios and that of the neat polymers, measured in the supercooled liquid/or glassy states.

Analyzing the spectra measured for MTZ-PVP K30 mixtures after the recrystallization process, it can be seen that the peaks related to the MTZ molecule show very similar spectral parameters (position, width, and intensity) in all studied BMs compared to these for neat crystalline APIs (Figure S9a). It indicates that MTZ occurs in the same crystalline form in the commercial sample and when mixed with PVPs. It should also be mentioned that the spectra of MTZ-*lin*PVP systems are very similar to those of MTZ-PVP K30 and reveal the same spectral effect for disordered and crystallized systems (Figures S8b and S9b). The $\nu_{C=O}$ band of *lin*PVP also shifts toward higher wavenumbers (blue shift) after mixing with polymers (50:50 *w*/*w* 1653 cm^{-1}, 60:40 *w*/*w* 1654 cm^{-1}, 75:25 *w*/*w* 1656 cm^{-1}), indicating the dipole–dipole nature of intermolecular interactions between API and *lin*PVP (Figure 3b).

During further analysis, we compared the IR spectra of MTZ-*star*PVP (75:25, 60:40, 50:50, 40:60, 30:70 *w*/*w*) systems in the supercooled liquid/glassy states with those of neat components. As shown in Figure S8c, the ν_{OH} band of MTZ in solid dispersions is blue-shifted (3700–3100 cm^{-1}) relative to that in the molten MTZ (3228 cm^{-1}). Moreover, with the increase in API content in these systems, the ν_{OH} band is located close to that of neat MTZ. Similar to linear PVP samples, the peak associated with the C-H stretching vibrations of the H-C=C group occurs at a higher frequency value than that of neat API. Surprisingly, the introduction of MTZ in the *star*PVP matrix causes a considerable red shift of the $\nu_{C=O}$ band (shift to lower wavenumbers from 1661 cm^{-1} for neat *star*PVP to 1651 cm^{-1} for 30:70 *w*/*w* mixtures) due to the formation of hydrogen bonding (HB) between the hydroxyl group of MTZ and the carbonyl group of PVP (Figure 3c). It is worth noting that HB interactions are typically detected between APIs and polymers in BMs, as reported extensively, for example, between ibuprofen and PVP [67,68], indomethacin and PVP [69], esomeprazole and hydroxypropyl methylcellulose (HPMC) [70], flurbiprofen and poly(ethylene oxide) [71], and nifedipine and Eudragit® [72], indicating that this is a key mechanism in the successful formation of amorphous or semi-crystalline solid dispersions [73]. It can also be mentioned that similar spectral effects related to the influence of PVP on API behavior were detected for MTZ-*star*PVP BMs in the recrystallized samples

(Figure S9c). Also, in these binary systems, MTZ occurred in the same crystalline form as the neat initial sample.

In the next step, the IR spectra measured for BMs of MTZ with different PVPs, K30, *lin*PVP, and *star*PVP (75:25, 60:40, and 50:50 *w*/*w*), in the supercooled liquid and crystalline states were compared (Figures S10 and S11). As can be seen, no differences were essentially observed for these spectra, i.e., the subtle variations in the υ_{OH} band region may result from various water contents (always present in PVP) in the analyzed samples. It suggests that despite the difference in API–polymer interaction mechanisms in the mixtures, i.e., dipole–dipole (linear PVP) vs. HB forces (*star*PVP), the average interaction strength between MTZ and PVP samples is nearly the same.

Overall, based on the above FTIR spectroscopy findings, it can be concluded that the topology of PVP, linear or star-shaped, can significantly impact the drug–polymer interaction mechanism and then the API-EXC miscibility. For linear PVP samples (K30, *lin*PVP), dipole–dipole interactions occur/prevail, as was suggested by the blue shift of the $\upsilon_{C=O}$ band for BMs. Therefore, there is a weaker miscibility of PVP K30 and *lin*PVP with MTZ. In the case of *star*PVP, hydrogen bonding is the prime mechanism for the interaction of API and a polymer. As a result, MTZ is miscible with *star*PVP in a wider range of concentration, which is demonstrated by the red shift of the $\upsilon_{C=O}$ band in the FTIR spectra of solid dispersions. It should be noted that due to the similar M_n (~40,000 g/mol) of the PVPs used, one can suppose that the observed differences in solubility/miscibility with MTZ are associated with the topology of macromolecules.

Noticing variations in the interactions between the API and the polymer matrix, we decided to conduct further investigations of binary systems. To study the influence of the given PVP on the thermal properties, phase or glass transitions, and the crystallization rate of MTZ, systematic DSC measurements were performed on the prepared binary formulations characterized by varying contents of API.

3.4. Differential Scanning Calorimetry (DSC) data

We started with DSC experiments of neat MTZ, and the obtained results are presented in Figure 4a. As can be seen, during the heating of crystalline API (at ϕ = 10 K/min), an endothermic peak at T = 437.3 K occurs in the thermogram (a dark blue line). Upon cooling the molten sample (with the same ϕ = 10 K/min), a single exothermic peak with a maximum at T = 326.3 K is observed (a light blue line). According to previous literature reports [44,74–76], the endothermic event at higher T corresponds to the melting of the API, while the exothermic one at lower T is attributed to the crystallization of MTZ. At this point, it is worth mentioning that inspired by studies demonstrating that the cooling rate of a sample significantly influences the phase transitions and makes it possible to transform the crystalline API into the amorphous form [77–79], we have made attempts to supercool/vitrify MTZ at various ϕ. Unfortunately, our efforts were unsuccessful. This implies that MTZ has an exceptionally low glass-forming ability, and it is not feasible to obtain it in the amorphous form using the standard vitrification method. However, in the system with two newly synthesized PVP polymers, linear and star-shaped, and a commercial sample PVP K30 (75:25, 60:40, 50:50 *w*/*w*), MTZ formed homogeneous amorphous mixtures. Therefore, we performed DSC measurements on these systems. Moreover, because *star*PVP has the ability to mix with the API in a higher range compared to PVPs with linear topology (PVP K30, *lin*PVP), which was mentioned in the previous section, we conducted DSC experiments on two additional MTZ-*star*PVP systems with the predominance of the polymer, i.e., 40:60 and 30:70 *w*/*w*. The main purpose of these investigations was to check how the addition of PVP with different topologies and weight percents will affect the glass-forming ability of MTZ, its physical stability, and the rate of recrystallization.

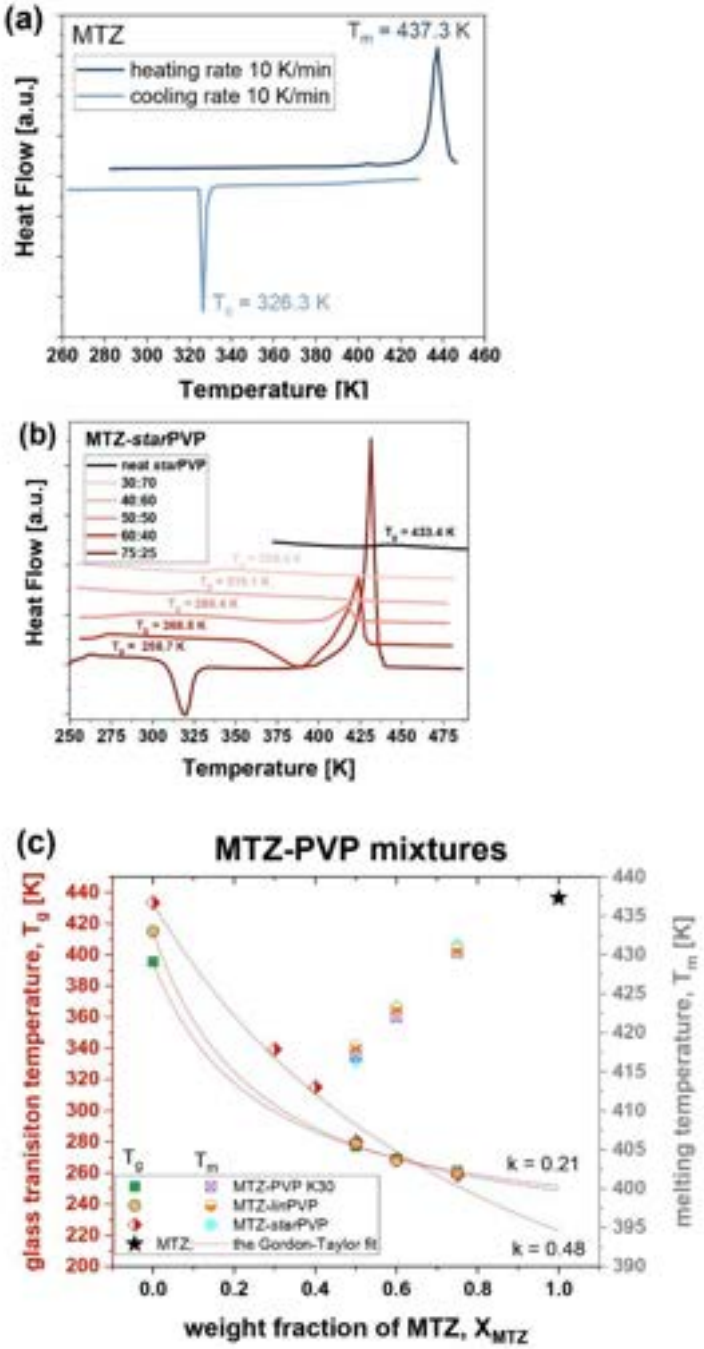

Figure 4. (**a**) DSC thermogram (ϕ = 10 K/min) of neat MTZ; (**b**) DSC thermograms (ϕ = 10 K/min) of neat *star*PVP and MTZ-*star*PVP mixtures with different weight ratios; (**c**) The dependency of calorimetric T_g and T_m versus weight fraction of MTZ for the examined binary systems. The solid red lines represent fits using the Gordon–Taylor equation (Equation (1)).

In Figure 4b, representative thermograms collected during the heating of amorphous API-*star*PVP ASDs with a rate of 10 K/min are presented. As can be seen, with increasing polymer content in solid dispersions, the T_g value increases. On the other hand, the peaks corresponding to the crystallization and melting processes gradually diminish/disappear. Interestingly, in the case of MTZ-*star*PVP in 40:60 and 30:70 *w*/*w* formulations, a complete suppression of the melting and crystallization processes is visible (only a thermal event connected to the glass transition can be detected). The values of T_g and T_m obtained for all examined systems (those determined for two other BMs, i.e., MTZ-PVP K30 and MTZ-*lin*PVP, have been given in Tables S1 and S2 in the SMs) are presented versus the weight fraction of MTZ (X_{MTZ}) in Figure 4c. Analyzing the obtained data, one can conclude that depending on the content of PVP in ASDs, the T_ms change significantly (up to 20 K). This may indicate substantial interactions between MTZ and the used polymeric matrices. Importantly, this conclusion agrees very well with the outcome of the FTIR analysis described above. Furthermore, other publications also suggest that the most likely explanation for the observed differences in T_m values of BMs appears to be the interactions occurring between the API and the polymer. For example, Kozyra et al. proposed such a scenario for BMs of itraconazole with three polymers, Eudragit L100, Carbopol 981, and hypromellose acetate succinate [80], while Chmiel et al. did so for nimesulide–Kollidon VA64 solid dispersions [81].

Furthermore, we can notice that the values of both T_g and T_m are independent of the type of PVP applied in a binary system. To characterize T_g vs. X_{MTZ} plots determined for each ASD and simultaneously estimate the T_g of MTZ, the Gordon–Taylor equation was applied [82]:

$$T_g = \frac{X_1 T_{g1} + kX_2 T_{g2}}{X_1 + kX_2} \quad (1)$$

where T_{g1} and T_{g2} are the glass transition temperatures (the subscript 1 refers to the component of the mixture with the lower T_g), X_1 is the weight fraction of component 1, while k is the constant, which represents a fitting parameter characterizing the curvature of the T_g vs. X_1 evolution. In our studies, the data presented in Figure 4c (T_g vs. X_{MTZ} plots) were analyzed using Equation (1) with the T_g of API being a fitting parameter. As illustrated, the value of k determined for the MTZ-*star*PVP system (k = 0.48) is greater compared to the one obtained for MTZ-PVP K30 and MTZ-*lin*PVP ASDs (k = 0.21). There is also a slight difference (~5 K) in the T_g of MTZ estimated from this analysis. The observed difference might be due to the fact that for the BM with the star-shaped polymer, we added two additional points at a higher polymer concentration. For other systems studied herein, it was not possible.

Noticing that MTZ-PVP 75:25, 60:40, and 50:50 *w*/*w* ASDs crystallize, we subsequently decided to perform non-isothermal DSC measurements to determine the activation energy (E_a) for the crystallization of API in formulations with different PVPs.

Figure 5 shows representative thermograms for the freshly prepared mixtures that crystallize most rapidly, i.e., MTZ-PVP 75:25 *w*/*w*. Note that the same measurements (with various ϕ ranging from 2.5 to 15 K/min) were performed for other API-PVP systems, i.e., 60:40 and 50:50 *w*/*w*. The values of crystallization temperatures (T_c) for all studied BMs, prepared at various weight ratios, are presented in tabular form in the SMs (see Tables S3–S5). As can be observed in Figure 5, three thermal events are visible during each scan. Except for two endothermic peaks occurring at the lowest and highest T (attributed to the glass transition and the melting, respectively), there is an exothermic peak corresponding to the crystallization of MTZ. It is visible that in the case of each MTZ-PVP system, the T_c values (the peak temperature of crystallization) increase with increasing ϕ. In turn, the T_gs and T_ms do not significantly vary depending on the heating rate. The analysis of non-isothermal DSC data obtained for all studied systems (Figure 6a) used the Kissinger method [83]:

$$\ln\left(\frac{\phi}{T_c}\right) = C_k - \frac{E_a}{RT_c}; \quad (2)$$

where C_k is a fitting parameter and R is a gas constant, enabling us to calculate the activation energy (E_a) of the crystallization of MTZ in various ASDs.

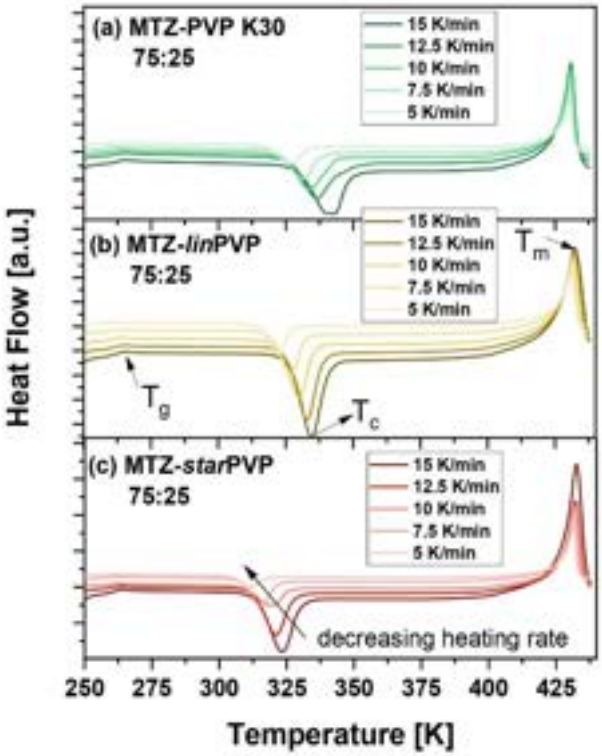

Figure 5. DSC thermograms for non-isothermal measurements of 75:25 *w*/*w* binary mixtures: (**a**) MTZ-PVP K30, (**b**) MTZ-*lin*PVP, (**c**) MTZ-*star*PVP.

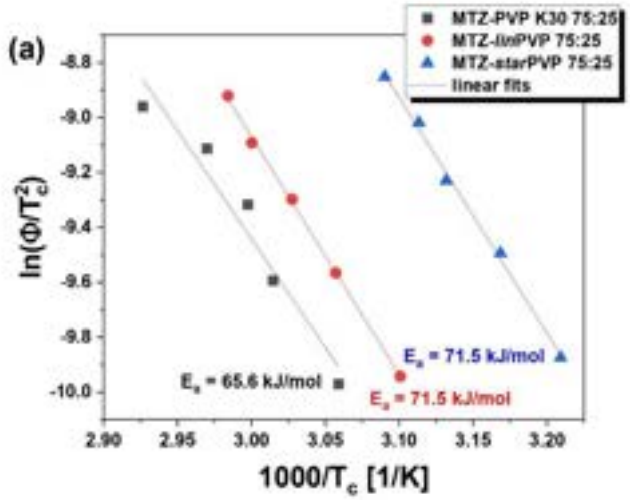

Figure 6. *Cont.*

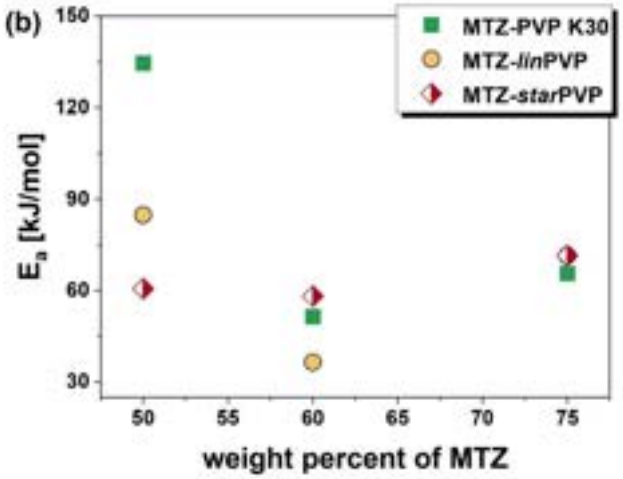

Figure 6. (**a**) Kissinger plots for the exothermic crystallization peaks in the representative MTZ-PVP 75:25 *w*/*w* ASDs. The solid red lines represent linear fits; (**b**) The dependency of E_a versus weight percent of MTZ in the examined binary systems.

It is well observed that for the MTZ-PVP 75:25 *w*/*w* BMs, the values of the E_a for the API crystallization are very similar (65.6–71.5 kJ/mol). The lowest E_a (65.6 kJ/mol) was determined for the mixture with commercial PVP (PVP K30). However, as the polymer content increases in the system, the differences in crystallization energies become greater. Interestingly, in the case of MTZ-PVP 50:50 *w*/*w* BMs, E_a changes as follows: $E_{aMTZ\text{-}PVPK30} > E_{aMTZ\text{-}linPVP} > E_{aMTZ\text{-}starPVP}$.

In the last step of calorimetric studies, we conducted isothermal crystallization measurements at T = 295 K for MTZ-PVP 75:25 *w*/*w* binary mixtures. Herein, it should be mentioned that we selected only systems with such content of both components because they crystallized quickly at this temperature. In other BMs, the crystallization was much longer. Therefore, such studies were not performed.

In Figure 7a, we plotted the heat released during the crystallization process versus time. At first sight, it can be seen that the time scale of crystallization of MTZ in various PVP matrices is different. To quantify this observation, the following formula was applied:

$$\alpha_{DSC} = \frac{\Delta H(t)}{\Delta H_{total}} \quad (3)$$

where α_{DSC} is the progress of crystallization, while $\Delta H(t)$ and ΔH_{total} mean the enthalpy variation at different times and the total heat of the crystallization, respectively. With the crystallization kinetic curves constructed (see Figure 7b), we described them using the Avrami model:

$$\alpha(t) = 1 - \exp(-kt^n) \quad (4)$$

where k is the rate constant of crystallization and n is the Avrami exponent, which is generally assigned to a dimension of growing crystals. As can be deduced from Figure 7c, there is a clear variation in the constant rate of MTZ crystallization in the studied systems. Importantly, a commercial PVP K30 turned out to be the most effective polymer in slowing down API crystallization. On the other hand, this process was the fastest in the binary system with *star*PVP. Herein, it is worth noting that although Figure 6b shows very similar (within the measuring error) values of the E_a for the MTZ crystallization in all 75:25 *w*/*w* BMs, isothermal DSC measurements (T = 295 K) for the same binary systems revealed that the crystallization rate constants (k) of API vary significantly depending on the polymer

used. According to literature reports, the crystallization rate has a clear correlation with the activation energy of this process. Generally, k increases with a decrease in E_a [84,85]. However, it should be emphasized that the crystallization rate is also significantly influenced by the viscosity of the mixtures, molecular interactions, and the degree of cooling. This may be the reason for the lack of correlation between both parameters in the case of examined BMs.

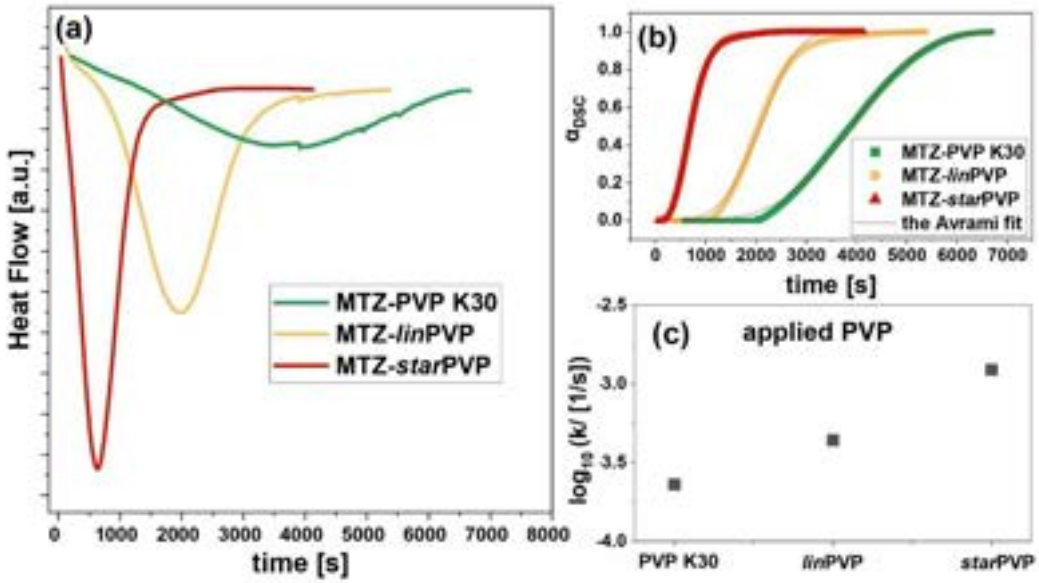

Figure 7. (**a**) DSC thermograms of isothermal measurements (T = 295 K) for MTZ-PVP 75:25 *w*/*w* mixtures; (**b**) The progress of the crystallization process carried out for the examined MTZ-PVP systems. Solid lines represent Avrami fits; (**c**) Crystallization rate constants (k) of MTZ depending on the applied PVP in BMs.

To explain the data presented and discussed above, one can suppose that the substantial difference in the activation barrier and the constant rate of crystallization of MTZ from BMs with various PVPs might be due to different intermolecular interactions occurring between both components in solid dispersions, as concluded from FTIR measurements. However, there is also another possibility that the API in binary systems crystallizes into a different polymorphic form. Although the second scenario is less probable since FTIR investigations indicated that, irrespective of the macromolecule, MTZ forms the same crystals, we decided to verify this hypothesis as well. For that purpose, XRD studies on BMs composed of API and three PVP polymers mixed in different weight ratios were performed.

3.5. X-ray Diffraction (XRD) Data

XRD patterns of MTZ-PVP BMs prepared in two weight ratios, 75:25 and 50:50, are illustrated in Figure 8a and Figure 8b, respectively. They were collected for systems in which MTZ recrystallized (after around one day after preparation). For all cases, despite the different PVP topologies, it can be seen that MTZ recrystallized to the same polymorphic form as crystalline MTZ (the diffractogram of neat crystalline API was set together for comparison). The crystal structure of this MTZ form belongs to the monoclinic $P2_1/c$ space group with lattice parameters $a \approx 7.03$, $b \approx 8.73$, $c \approx 12.82$, and cell angles $\alpha \approx 90°$, $\beta \approx 94.5°$, $\gamma \approx 90°$ (CCDC number 1212679 in Cambridge Crystallographic Data Centre). Moreover, Figure 8c demonstrates the XRD data collected for freshly prepared

API-PVP 50:50 *w*/*w* binary systems. They are very similar to each other, exhibiting two broad diffraction maxima at nearly the same positions. The recording of amorphous diffractograms for 75:25 *w*/*w* BMs was impossible due to the fast recrystallization of MTZ. Further, temporal XRD studies of the MTZ-PVP 50:50 *w*/*w* solid dispersions were performed, starting from the freshly prepared amorphous systems. The results presented in Figure 9 indicate that the physical stability of MTZ in these mixtures is affected by the topology of PVP. MTZ in the BM with *star*PVP recrystallized fully after 15 h; in the BM with *lin*PVP, MTZ started to recrystallize later—after 35 h; while in the system with PVP K30, it was still stable in the amorphous form after 55 h.

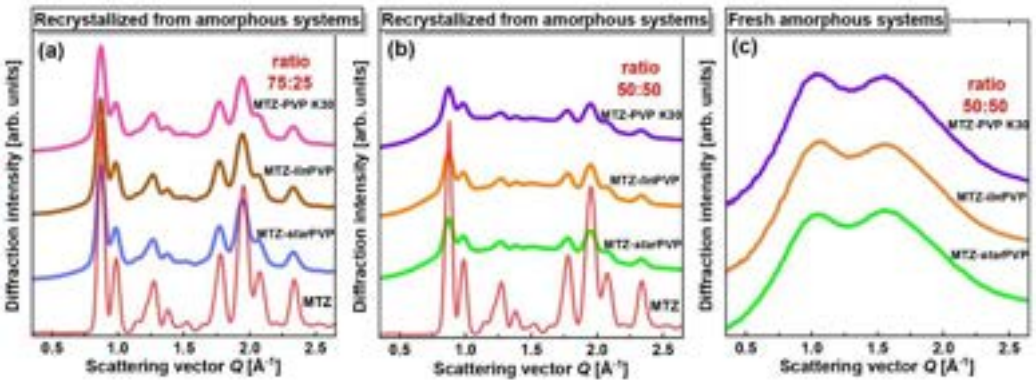

Figure 8. XRD patterns of neat MTZ and its solid dispersions with different PVP polymers: (**a**) in 75:25 (*w*/*w*) ratio after recrystallization, (**b**) in 50:50 (*w*/*w*) ratio after recrystallization, and (**c**) in 50:50 (*w*/*w*) ratio for fresh amorphous systems.

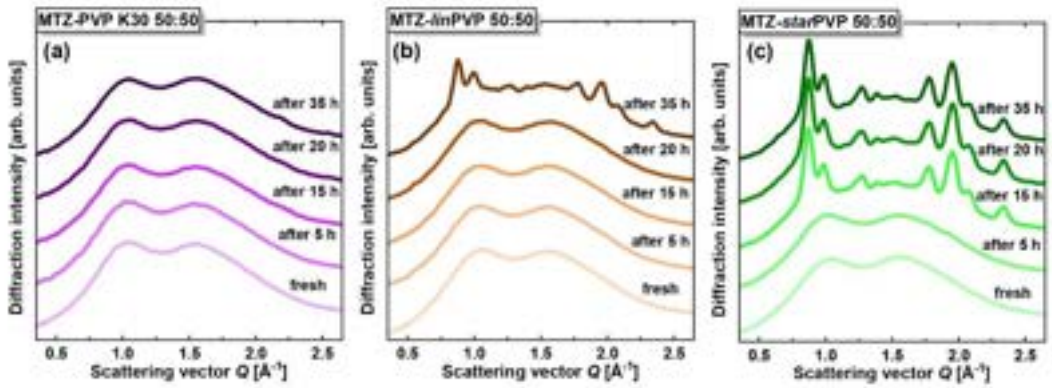

Figure 9. The temporal evolution of the XRD patterns for freshly prepared MTZ-PVP 50:50 *w*/*w* binary systems: (**a**) MTZ-PVP K30, (**b**) MTZ-*lin*PVP, and (**c**) MTZ-*star*PVP.

Herein, it is worth emphasizing that we also conducted preliminary long-term XRD studies for the MTZ-*star*PVP system containing the highest possible amount of the matrix (i.e., 70 wt%). This research showed that the recrystallization of API was strongly inhibited, and the amorphous form of MTZ was stable for over one month (see Figure 10). This is evidenced by exactly the same pattern of diffractograms for both samples, i.e., the fresh BM measured immediately after preparation and the formulation stored for over a month at room temperature.

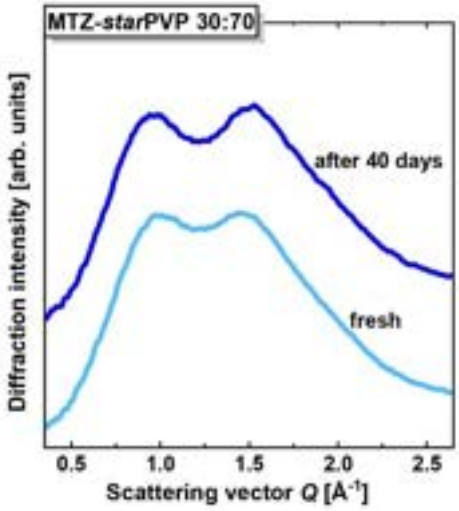

Figure 10. XRD patterns of the MTZ-*star*PVP 30:70 *w*/*w* binary mixture for a fresh sample (light blue line) and after 40 days of storage (dark blue line).

Thus, the obtained data indicated that with respect to the linear PVPs of similar M_n, the star-shaped macromolecule is the least effective in stabilizing amorphous APIs at a similar range of concentrations (50:50, 75:25 *w*/*w*). However, at a higher star-shaped polymer content in BMs, which is not attainable for the linear PVP due to weaker miscibility, the crystallization of MTZ is strongly suppressed and not detectable for more than one month.

4. Conclusions

To sum up, we successfully obtained novel PVP homopolymers with different architectures (linear and three-arm star) using thermally initiated RAFT processes. Hence, three polymers, (i) PVP K30 (M_n = 40,500 g/mol, Đ = 2.05), (ii) *lin*PVP (M_n = 37,600 g/mol, Đ = 1.22), and (iii) *star*PVP (M_n = 38,700 g/mol, Đ = 1.48) with similar molecular weights but varying dispersities and topologies were employed to create BMs with a fast-crystallizing drug—MTZ. Our main goal was to investigate whether the polymer architecture and/or macrostructural parameters (Đ), as well as the PVP content in the mixtures, influence the intermolecular interactions, physical stability, and the rate of MTZ recrystallization. The first remarkable effect observed during the samples' preparation was the enhanced miscibility of the API with star-shaped polymers compared to the linear-synthesized and commercial PVP. Interestingly, FTIR studies indicated that this may be related to a different interaction mechanism between various PVPs and examined pharmaceutical. As demonstrated, dipole–dipole interactions dominate between linear polymers (PVP K30, *lin*PVP) and MTZ, while interactions between the star-shaped macromolecule (*star*PVP) and the API primarily occur through hydrogen bonds. In turn, detailed isothermal DSC studies on 75:25 *w*/*w* systems allowed us to conclude that among the tested polymer matrices, PVP K30 most effectively retards the crystallization of MTZ, while the *star*PVP exhibits the weakest ability to inhibit this process effectively. These results were also confirmed by XRD studies performed on MTZ-PVP BMs with 50 wt% of API. Moreover, non-isothermal DSC measurements revealed differences in the activation barrier for API crystallization depending on the topology of the polymer and its content in solid dispersions. Additionally, FTIR and XRD investigations indicated that in BMs with all examined PVPs, MTZ recrystallizes into the same polymorphic form. Surprisingly, the new polymer material, *star*PVP, turned out to have the ability to strongly inhibit the recrystallization of MTZ in a mixture containing a high percentage of the polymer (i.e., 70 wt%, which is impossible to

achieve for linear PVPs). For this binary system (MTZ-*star*PVP 30:70 *w*/*w*), we observed the stability of amorphous MTZ for over one month.

Supplementary Materials: The following are available online at https://www.mdpi.com/article/10.3390/pharmaceutics16010136/s1, Figure S1: ^{1}H NMR spectrum of trifunctional CTA2 in $CDCl_3$ (500 MHz); Figure S2: ^{1}H NMR spectrum of *lin*PVP in $CDCl_3$ (600 MHz); Figure S3: ^{13}C NMR spectrum of *lin*PVP in $CDCl_3$ (600 MHz); Figure S4: SEC traces of PVP samples: commercial (PVP K30 - grey line) and self-synthesized (*lin*PVP-red line, *star*PVP-blue line); Figure S5: ^{1}H NMR spectrum of *star*PVP in $CDCl_3$ (600 MHz); Figure S6: ^{13}C NMR spectrum of *star*PVP in $CDCl_3$ (600 MHz); Figure S7: Infrared spectra of crystalline and molten MTZ as well as PVP samples. Data were presented in two spectral regions: (a) 3800–2400 cm^{-1} and (b)1800–400 cm^{-1}; Figure S8: Infrared spectra of (a) MTZ-PVP K30, (b) MTZ-*lin*PVP, and (c) MTZ-*star*PVP binary mixtures prepared in different weight ratios, measured at T=295 K (in the supercooled liquid/or glassy states) together with the spectra registered for the molten MTZ and neat PVP polymers, presented in the ranges of 3800–2400 cm^{-1} (left) and 1800–400 cm^{-1} (right); Figure S9: Infrared spectra of (a) MTZ-PVP K30, (b) MTZ-*lin*PVP, and (c) MTZ-*star*PVP binary mixtures (samples after recrystallization) prepared in different molar ratios together with the spectra registered for the crystalline MTZ and neat PVP polymers, presented in the ranges of 3800–2400 cm^{-1} (left) and 1800–400 cm^{-1} (right); Figure S10: Infrared spectra of binary mixtures of MTZ with all PVP samples (K30, *lin*PVP and *star*PVP) ((a) 75:25, (b) 60:40, (c) 50:50 *w*/*w*) measured in the supercooled liquid state, presented in the ranges of 3800–2400 cm^{-1} (left) and 1800–400 cm^{-1} (right); Figure S11: Infrared spectra of binary mixtures of MTZ with all PVP samples (K30, *lin*PVP and *star*PVP) ((a) 75:25, (b) 60:40, (c) 50:50 *w*/*w*) measured in the crystalline state, presented in the ranges of 3800–2400 cm^{-1} (left) and 1800–400 cm^{-1} (right); Table S1: The calorimetric glass transition temperature values (heating rate, ϕ = 10 K/min) for neat PVPs and examined MTZ-PVP binary mixtures in various weight ratios; Table S2: The calorimetric melting temperature values (ϕ = 10 K/min) for neat MTZ and the examined MTZ-PVP binary mixtures in various weight ratios; Table S3: The crystallization temperature values for MTZ-PVP K30 mixtures depending on the heating rate (ϕ); Table S4: The crystallization temperature values for MTZ-*lin*PVP mixtures depending on the heating rate (ϕ); Table S5: The crystallization temperature values for MTZ-*star*PVP mixtures depending on the heating rate (ϕ). Details concerning the synthesis of CTA2, *lin*PVP, and *star*PVP (including ^{1}H NMR and ^{13}C NMR spectra and SEC traces of PVP samples).

Author Contributions: L.O.: Formal analysis, investigation, methodology, visualization, writing—original draft preparation, writing—review and editing, and funding acquisition. T.L.: Investigation, formal analysis, and visualization. M.T.: Investigation, formal analysis, and visualization. B.H.: Investigation, formal analysis, and visualization. K.J.: Investigation, formal analysis, and visualization. P.Z.: Investigation, formal analysis, and visualization. A.M.-W.: Investigation, formal analysis, and visualization. E.K.: Conceptualization, writing—original draft preparation, writing—review and editing, and funding acquisition. K.K.: Conceptualization, supervision, and project administration. All authors have read and agreed to the published version of the manuscript.

Funding: L.O. is thankful for financial support from the Ministry of Education and Science (Poland) within the Pearls of Science grant (No. PN/01/0078/2022), while E.K. is thankful for financial support from the Medical University of Silesia (Poland), Contract No. BNW-1-014/K/3/F. This research was funded in part by the National Science Centre (Poland), Grant No. Opus 21 No. 2021/41/B/NZ7/01654. For the purpose of Open Access, the author has applied a CC-BY public copyright license to any Author Accepted Manuscript (AAM) version arising from this submission.

Institutional Review Board Statement: Not applicable.

Informed Consent Statement: Not applicable.

Data Availability Statement: Data are contained within the article and Supplementary Materials.

Conflicts of Interest: The authors declare no conflicts of interest.

References

1. Benet, L.Z.; Broccatelli, F.; Oprea, T.I. BDDCS Applied to over 900 Drugs. *AAPS J.* **2011**, *13*, 519–547. [CrossRef] [PubMed]
2. Babu, N.J.; Nangia, A. Solubility Advantage of Amorphous Drugs and Pharmaceutical Cocrystals. *Cryst. Growth Des.* **2011**, *11*, 2662–2679. [CrossRef]

3. Ku, M.S. Use of the Biopharmaceutical Classification System in Early Drug Development. *AAPS J.* **2008**, *10*, 208–212. [CrossRef] [PubMed]
4. Bhujbal, S.V.; Mitra, B.; Jain, U.; Gong, Y.; Agrawal, A.; Karki, S.; Taylor, L.S.; Kumar, S.; Zhou, Q. Pharmaceutical Amorphous Solid Dispersion: A Review of Manufacturing Strategies. *Acta Pharm. Sin. B* **2021**, *11*, 2505–2536. [CrossRef] [PubMed]
5. Huang, Y.; Dai, W.-G. Fundamental Aspects of Solid Dispersion Technology for Poorly Soluble Drugs. *Acta Pharm. Sin. B* **2014**, *4*, 18–25. [CrossRef] [PubMed]
6. Newman, A.; Knipp, G.; Zografi, G. Assessing the Performance of Amorphous Solid Dispersions. *J. Pharm. Sci.* **2012**, *101*, 1355–1377. [CrossRef] [PubMed]
7. Williams, H.D.; Trevaskis, N.L.; Charman, S.A.; Shanker, R.M.; Charman, W.N.; Pouton, C.W.; Porter, C.J.H. Strategies to Address Low Drug Solubility in Disc. *Pharmacol. Rev.* **2013**, *65*, 315–499. [CrossRef] [PubMed]
8. Jermain, S.V.; Brough, C.; Williams, R.O. Amorphous Solid Dispersions and Nanocrystal Technologies for Poorly Water-Soluble Drug Delivery—An Update. *Int. J. Pharm.* **2018**, *535*, 379–392. [CrossRef]
9. Baghel, S.; Cathcart, H.; O'Reilly, N.J. Polymeric Amorphous Solid Dispersions: A Review of Amorphization, Crystallization, Stabilization, Solid-State Characterization, and Aqueous Solubilization of Biopharmaceutical Classification System Class II Drugs. *J. Pharm. Sci.* **2016**, *105*, 2527–2544. [CrossRef]
10. Tambosi, G.; Coelho, P.F.; Soares, L.; Lenschow, I.C.S.; Zétola, M.; Stulzer, H.K.; Pezzini, B.R. Challenges to Improve the Biopharmaceutical Properties of Poorly Water-Soluble Drugs and the Application of the Solid Dispersion Technology. *Rev. Mater.* **2018**, *23*, e12224. [CrossRef]
11. Pandi, P.; Bulusu, R.; Kommineni, N.; Khan, W.; Singh, M. Amorphous Solid Dispersions: An Update for Preparation, Characterization, Mechanism on Bioavailability, Stability, Regulatory Considerations and Marketed Products. *Int. J. Pharm.* **2020**, *586*, 119560. [CrossRef] [PubMed]
12. Mistry, P.; Suryanarayanan, R. Strength of Drug-Polymer Interactions: Implications for Crystallization in Dispersions. *Cryst. Growth Des.* **2016**, *16*, 5141–5149. [CrossRef]
13. Kothari, K.; Ragoonanan, V.; Suryanarayanan, R. Influence of Molecular Mobility on the Physical Stability of Amorphous Pharmaceuticals in the Supercooled and Glassy States. *Mol. Pharm.* **2014**, *11*, 3048–3055. [CrossRef] [PubMed]
14. Nair, A.R.; Lakshman, Y.D.; Anand, V.S.K.; Sree, K.S.N.; Bhat, K.; Dengale, S.J. Overview of Extensively Employed Polymeric Carriers in Solid Dispersion Technology. *AAPS PharmSciTech* **2020**, *21*, 309. [CrossRef] [PubMed]
15. Chen, Y.; Liu, C.; Chen, Z.; Su, C.; Hageman, M.; Hussain, M.; Haskell, R.; Stefanski, K.; Qian, F. Drug-Polymer-Water Interaction and Its Implication for the Dissolution Performance of Amorphous Solid Dispersions. *Mol. Pharm.* **2015**, *12*, 576–589. [CrossRef] [PubMed]
16. Kumar, S.K.; Ganesan, V.; Riggleman, R.A. Perspective: Outstanding Theoretical Questions in Polymer-Nanoparticle Hybrids. *J. Chem. Phys.* **2017**, *147*, 020901. [CrossRef] [PubMed]
17. Jabbarzadeh, A. The Origins of Enhanced and Retarded Crystallization in Nanocomposite Polymers. *Nanomaterials* **2019**, *9*, 1472. [CrossRef]
18. Jabbarzadeh, A.; Halfina, B. Unravelling the Effects of Size, Volume Fraction and Shape of Nanoparticle Additives on Crystallization of Nanocomposite Polymers. *Nanoscale Adv.* **2019**, *1*, 4704–4721. [CrossRef]
19. Genix, A.C.; Oberdisse, J. Nanoparticle Self-Assembly: From Interactions in Suspension to Polymer Nanocomposites. *Soft Matter* **2018**, *14*, 5161–5179. [CrossRef]
20. Frank, D.S.; Matzger, A.J. Probing the Interplay between Amorphous Solid Dispersion Stability and Polymer Functionality. *Mol. Pharm.* **2018**, *15*, 2714–2720. [CrossRef]
21. Kurakula, M.; Rao, G.S.N.K. Pharmaceutical Assessment of Polyvinylpyrrolidone (PVP): As Excipient from Conventional to Controlled Delivery Systems with a Spotlight on COVID-19 Inhibition. *J. Drug Deliv. Sci. Technol.* **2020**, *60*, 102046. [CrossRef]
22. Iyer, R.; Jovanovska, V.P.; Berginc, K.; Jakličˇ, M.; Fabiani, F.; Harlacher, C.; Huzjak, T.; Sanchez-Felix, M.V. Amorphous Solid Dispersions (ASDs): The Influence of Material Properties, Manufacturing Processes and Analytical Technologies in Drug Product Development. *Pharmaceutics* **2021**, *13*, 1682. [CrossRef] [PubMed]
23. Bachmaier, R.D.; Monschke, M.; Faber, T.; Krome, A.K.; Pellequer, Y.; Stoyanov, E.; Lamprecht, A.; Wagner, K.G. In Vitro and in Vivo Assessment of Hydroxypropyl Cellulose as Functional Additive for Enabling Formulations Containing Itraconazole. *Int. J. Pharm. X* **2021**, *3*, 100076. [CrossRef] [PubMed]
24. Fan, N.; He, Z.; Ma, P.; Wang, X.; Li, C.; Sun, J.; Sun, Y.; Li, J. Impact of HPMC on Inhibiting Crystallization and Improving Permeability of Curcumin Amorphous Solid Dispersions. *Carbohydr. Polym.* **2018**, *181*, 543–550. [CrossRef] [PubMed]
25. Huang, S.; O'Donnell, K.P.; Keen, J.M.; Rickard, M.A.; McGinity, J.W.; Williams, R.O. A New Extrudable Form of Hypromellose: AFFINISOL™ HPMC HME. *AAPS PharmSciTech* **2016**, *17*, 106–119. [CrossRef] [PubMed]
26. Mosquera-Giraldo, L.I.; Borca, C.H.; Meng, X.; Edgar, K.J.; Slipchenko, L.V.; Taylor, L.S. Mechanistic Design of Chemically Diverse Polymers with Applications in Oral Drug Delivery. *Biomacromolecules* **2016**, *17*, 3659–3671. [CrossRef] [PubMed]
27. Yuan, X.; Xiang, T.X.; Anderson, B.D.; Munson, E.J. Hydrogen Bonding Interactions in Amorphous Indomethacin and Its Amorphous Solid Dispersions with Poly(Vinylpyrrolidone) and Poly(Vinylpyrrolidone-Co-Vinyl Acetate) Studied Using ^{13}C Solid-State NMR. *Mol. Pharm.* **2015**, *12*, 4518–4528. [CrossRef]
28. Pacult, J.; Rams-Baron, M.; Chrząszcz, B.; Jachowicz, R.; Paluch, M. Effect of Polymer Chain Length on the Physical Stability of Amorphous Drug-Polymer Blends at Ambient Pressure. *Mol. Pharm.* **2018**, *15*, 2807–2815. [CrossRef]

29. Chmiel, K.; Knapik-Kowalczuk, J.; Jurkiewicz, K.; Sawicki, W.; Jachowicz, R.; Paluch, M. A New Method to Identify Physically Stable Concentration of Amorphous Solid Dispersions (I): Case of Flutamide + Kollidon VA64. *Mol. Pharm.* **2017**, *14*, 3370–3380. [CrossRef]
30. Weuts, I.; Kempen, D.; Decorte, A.; Verreck, G.; Peeters, J.; Brewster, M.; Van Den Mooter, G. Phase Behaviour Analysis of Solid Dispersions of Loperamide and Two Structurally Related Compounds with the Polymers PVP-K30 and PVP-VA64. *Eur. J. Pharm. Sci.* **2004**, *22*, 375–385. [CrossRef]
31. Weuts, I.; Kempen, D.; Decorte, A.; Verreck, G.; Peeters, J.; Brewster, M.; Van Den Mooter, G. Physical Stability of the Amorphous State of Loperamide and Two Fragment Molecules in Solid Dispersions with the Polymers PVP-K30 and PVP-VA64. *Eur. J. Pharm. Sci.* **2005**, *25*, 313–320. [CrossRef] [PubMed]
32. Riekes, M.K.; Dereymaker, A.; Berben, P.; Augustijns, P.; Stulzer, H.K.; Van den Mooter, G. Development of Enteric-Coated Fixed Dose Combinations of Amorphous Solid Dispersions of Ezetimibe and Lovastatin: Investigation of Formulation and Process Parameters. *Int. J. Pharm.* **2017**, *520*, 49–58. [CrossRef] [PubMed]
33. Maniruzzaman, M.; Morgan, D.J.; Mendham, A.P.; Pang, J.; Snowden, M.J.; Douroumis, D. Drug-Polymer Intermolecular Interactions in Hot-Melt Extruded Solid Dispersions. *Int. J. Pharm.* **2013**, *443*, 199–208. [CrossRef] [PubMed]
34. Wendelboe, J.; Knopp, M.M.; Khan, F.; Chourak, N.; Rades, T.; Holm, R. Importance of in Vitro Dissolution Conditions for the in Vivo Predictability of an Amorphous Solid Dispersion Containing a PH-Sensitive Carrier. *Int. J. Pharm.* **2017**, *531*, 324–331. [CrossRef] [PubMed]
35. Kurakula, M.; Koteswara Rao, G.S.N. Moving Polyvinyl Pyrrolidone Electrospun Nanofibers and Bioprinted Scaffolds toward Multidisciplinary Biomedical Applications. *Eur. Polym. J.* **2020**, *136*, 109919. [CrossRef]
36. Zhang, J.; Guo, M.; Luo, M.; Cai, T. Advances in the Development of Amorphous Solid Dispersions: The Role of Polymeric Carriers. *Asian J. Pharm. Sci.* **2023**, *18*, 100834. [CrossRef] [PubMed]
37. Heczko, D.; Hachuła, B.; Maksym, P.; Kamiński, K.; Zięba, A.; Orszulak, L.; Paluch, M.; Kamińska, E. The Effect of Various Poly (N-Vinylpyrrolidone) (PVP) Polymers on the Crystallization of Flutamide. *Pharmaceuticals* **2022**, *15*, 971. [CrossRef] [PubMed]
38. Szafraniec, J.; Antosik, A.; Knapik-Kowalczuk, J.; Gawlak, K.; Kurek, M.; Szlęk, J.; Jamróz, W.; Paluch, M.; Jachowicz, R. Molecular Disorder of Bicalutamide—Amorphous Solid Dispersions Obtained by Solvent Methods. *Pharmaceutics* **2018**, *10*, 194. [CrossRef]
39. Balani, P.N.; Wong, S.Y.; Ng, W.K.; Widjaja, E.; Tan, R.B.H.; Chan, S.Y. Influence of Polymer Content on Stabilizing Milled Amorphous Salbutamol Sulphate. *Int. J. Pharm.* **2010**, *391*, 125–136. [CrossRef]
40. Shi, N.Q.; Lei, Y.S.; Song, L.M.; Yao, J.; Zhang, X.B.; Wang, X.L. Impact of Amorphous and Semicrystalline Polymers on the Dissolution and Crystallization Inhibition of Pioglitazone Solid Dispersions. *Powder Technol.* **2013**, *247*, 211–221. [CrossRef]
41. Sui, X.; Chu, Y.; Zhang, J.; Zhang, H.; Wang, H.; Liu, T.; Han, C. The Effect of PVP Molecular Weight on Dissolution Behavior and Physicochemical Characterization of Glycyrrhetinic Acid Solid Dispersions. *Adv. Polym. Technol.* **2020**, *2020*, 1–13. [CrossRef]
42. Mohapatra, S.; Samanta, S.; Kothari, K.; Mistry, P.; Suryanarayanan, R. Effect of Polymer Molecular Weight on the Crystallization Behavior of Indomethacin Amorphous Solid Dispersions. *Cryst. Growth Des.* **2017**, *17*, 3142–3150. [CrossRef]
43. Devasia, R.; Bindu, R.L.; Borsali, R.; Mougin, N.; Gnanou, Y. Controlled Radical Polymerization of N-Vinylpyrrolidone by Reversible Addition-Fragmentation Chain Transfer Process. *Macromol. Symp.* **2005**, *229*, 8–17. [CrossRef]
44. Bielas, R.; Maksym, P.; Tarnacka, M.; Minecka, A.; Jurkiewicz, K.; Talik, A.; Geppert-Rybczyńska, M.; Grelska, J.; Mielańczyk, Ł.; Bernat, R.; et al. Synthetic Strategy Matters: The Study of a Different Kind of PVP as Micellar Vehicles of Metronidazole. *J. Mol. Liq.* **2021**, *332*, 115789. [CrossRef]
45. Kestur, U.S.; Lee, H.; Santiago, D.; Rinaldi, C.; Won, Y.Y.; Taylor, L.S. Effects of the Molecular Weight and Concentration of Polymer Additives, and Temperature on the Melt Crystallization Kinetics of a Small Drug Molecule. *Cryst. Growth Des.* **2010**, *10*, 3585–3595. [CrossRef]
46. Sahoo, A.; Suryanarayanan, R.; Siegel, R.A. Stabilization of Amorphous Drugs by Polymers: The Role of Overlap Concentration (C*). *Mol. Pharm.* **2020**, *17*, 4401–4406. [CrossRef]
47. Atia, A.J.K. Synthesis and Antibacterial Activities of New Metronidazole and Imidazole Derivatives. *Molecules* **2009**, *14*, 2431–2446. [CrossRef]
48. Naveed, S.; Waheed, N.; Nazeer, S. Degradation Study of Metronidazole in Active and Different Formulation by UV Spectroscopy. *J. Bioequivalence Bioavailab.* **2014**, *6*, 124–127. [CrossRef]
49. Minecka, A.; Tarnacka, M.; Jurkiewicz, K.; Hachuła, B.; Wrzalik, R.; Brodka, A.; Kamiński, K.; Kamińska, E. The Impact of the Size of Acetylated Cyclodextrin on the Stability of Amorphous Metronidazole. *Int. J. Pharm.* **2022**, *624*, 122025. [CrossRef]
50. Teodorescu, M.; Bercea, M. Poly(Vinylpyrrolidone)—A Versatile Polymer for Biomedical and Beyond Medical Applications. *Polym. Plast. Technol. Eng.* **2015**, *54*, 923–943. [CrossRef]
51. Perrier, S. 50th Anniversary Perspective: RAFT Polymerization—A User Guide. *Macromolecules* **2017**, *50*, 7433–7447. [CrossRef]
52. Moad, G. RAFT Polymerization to Form Stimuli-Responsive Polymers. *Polym. Chem.* **2017**, *8*, 177–219. [CrossRef]
53. Roka, N.; Kokkorogianni, O.; Kontoes-Georgoudakis, P.; Choinopoulos, I.; Pitsikalis, M. Recent Advances in the Synthesis of Complex Macromolecular Architectures Based on Poly(N-Vinyl Pyrrolidone) and the RAFT Polymerization Technique. *Polymers* **2022**, *14*, 701. [CrossRef] [PubMed]
54. Maksym, P.; Tarnacka, M.; Bernat, R.; Bielas, R.; Mielańczyk, A.; Hachuła, B.; Kaminski, K.; Paluch, M. Pressure-Assisted Strategy for the Synthesis of Vinyl Pyrrolidone-Based Macro-Star Photoiniferters. A Route to Star Block Copolymers. *J. Polym. Sci.* **2020**, *58*, 1393–1399. [CrossRef]

55. Veeren, A.; Bhaw-Luximon, A.; Mukhopadhyay, D.; Jhurry, D. Mixed Poly(Vinyl Pyrrolidone)-Based Drug-Loaded Nanomicelles Shows Enhanced Efficacy against Pancreatic Cancer Cell Lines. *Eur. J. Pharm. Sci.* **2017**, *102*, 250–260. [CrossRef]
56. Ramalingam, V.; Varunkumar, K.; Ravikumar, V.; Rajaram, R. Target Delivery of Doxorubicin Tethered with PVP Stabilized Gold Nanoparticles for Effective Treatment of Lung Cancer. *Sci. Rep.* **2018**, *8*, 1–12. [CrossRef] [PubMed]
57. Matiyani, M.; Rana, A.; Pal, M.; Rana, S.; Melkani, A.B.; Sahoo, N.G. Polymer Grafted Magnetic Graphene Oxide as a Potential Nanocarrier for PH-Responsive Delivery of Sparingly Soluble Quercetin against Breast Cancer Cells. *RSC Adv.* **2022**, *12*, 2574–2588. [CrossRef]
58. Vihola, H.; Laukkanen, A.; Valtola, L.; Tenhu, H.; Hirvonen, J. Cytotoxicity of Thermosensitive Polymers Poly(N-Isopropylacrylamide), Poly(N-Vinylcaprolactam) and Amphiphilically Modified Poly(N-Vinylcaprolactam). *Biomaterials* **2005**, *26*, 3055–3064. [CrossRef]
59. Nuber, A.; Lang, S.; Sanner, A.; Schroeder, G. Preparation of Polyvinylpyrrolidone. US Patent US4786699A, 19 January 1988.
60. Bensouiki, S.; Belaib, F.; Sindt, M.; Rup-Jacques, S.; Magri, P.; Ikhlef, A.; Meniai, A.H. Synthesis of Cyclodextrins-Metronidazole Inclusion Complexes and Incorporation of Metronidazole—2-Hydroxypropyl-β-Cyclodextrin Inclusion Complex in Chitosan Nanoparticles. *J. Mol. Struct.* **2022**, *1247*, 131298. [CrossRef]
61. Socrates, G. *Infrared and Raman Characteristic Group Frequencies: Tables and Charts*; John Wiley & Sons, Inc.: Hoboken, NJ, USA, 2001.
62. Rahma, A.; Munir, M.M.; Khairurrijal; Prasetyo, A.; Suendo, V.; Rachmawati, H. Intermolecular Interactions and the Release Pattern of Electrospun Curcumin-Polyvinyl(Pyrrolidone) Fiber. *Biol. Pharm. Bull.* **2016**, *39*, 163–173. [CrossRef]
63. Abdelghany, A.M.; Meikhail, M.S.; Oraby, A.H.; Aboelwafa, M.A. Experimental and DFT Studies on the Structural and Optical Properties of Chitosan/Polyvinyl Pyrrolidone/ZnS Nanocomposites. *Polym. Bull.* **2023**, *80*, 13279–13298. [CrossRef]
64. Kalaiarasi, C.; George, C.; Gonnade, R.G.; Hathwar, V.R.; Poomani, K. Experimental and Theoretical Charge Density, Intermolecular Interactions and Electrostatic Properties of Metronidazole. *Acta Crystallogr. Sect. B Struct. Sci. Cryst. Eng. Mater.* **2019**, *75*, 942–953. [CrossRef] [PubMed]
65. Marsac, P.J.; Li, T.; Taylor, L.S. Estimation of Drug-Polymer Miscibility and Solubility in Amorphous Solid Dispersions Using Experimentally Determined Interaction Parameters. *Pharm. Res.* **2009**, *26*, 139–151. [CrossRef] [PubMed]
66. Khougaz, K.; Clas, S.D. Crystallization Inhibition in Solid Dispersions of MK-0591 and Poly(Vinylpyrrolidone) Polymers. *J. Pharm. Sci.* **2000**, *89*, 1325–1334. [CrossRef] [PubMed]
67. Niemczyk, A.J.; Williams, A.C.; Rawlinson-Malone, C.F.; Hayes, W.; Greenland, B.W.; Chappell, D.; Khutoryanskaya, O.; Timmins, P. Novel Polyvinylpyrrolidones to Improve Delivery of Poorly Water-Soluble Drugs: From Design to Synthesis and Evaluation. *Mol. Pharm.* **2012**, *9*, 2237–2247. [CrossRef]
68. Rawlinson, C.F.; Williams, A.C.; Timmins, P.; Grimsey, I. Polymer-Mediated Disruption of Drug Crystallinity. *Int. J. Pharm.* **2007**, *336*, 42–48. [CrossRef]
69. Taylor, L.S.; Zografi, G. Spectroscopic Characterization of Interactions between PVP and Indomethacin in Amorphous Molecular Dispersions. *Pharm. Res.* **1997**, *14*, 1691–1698. [CrossRef]
70. Van Nguyen, H.; Baek, N.; Lee, B.J. Enhanced Gastric Stability of Esomeprazole by Molecular Interaction and Modulation of Microenvironmental pH with Alkalizers in Solid Dispersion. *Int. J. Pharm.* **2017**, *523*, 189–202. [CrossRef]
71. Ozeki, T.; Yuasa, H.; Kanaya, Y. Application of the Solid Dispersion Method to the Controlled Release of Medicine. IX. Difference in the Release of Flurbiprofen from Solid Dispersions with Poly(Ethylene Oxide) and Hydroxypropylcellulose and the Interaction between Medicine and Polymers. *Int. J. Pharm.* **1997**, *155*, 209–217. [CrossRef]
72. Huang, J.; Wigent, R.J.; Schwartz, J.B. Drug-Polymer Interaction and Its Significance on the Physical Stability of Nifedipine Amorphous Dispersion in Microparticles of an Ammonio Methacrylate Copolymer and Ethylcellulose Binary Blend. *J. Pharm. Sci.* **2008**, *97*, 251–262. [CrossRef]
73. Shan, X.; Moghul, M.A.; Williams, A.C.; Khutoryanskiy, V.V. Mutual Effects of Hydrogen Bonding and Polymer Hydrophobicity on Ibuprofen Crystal Inhibition in Solid Dispersions with Poly(N-Vinyl Pyrrolidone) and Poly(2-Oxazolines). *Pharmaceutics* **2021**, *13*, 659. [CrossRef]
74. De Souza, N.A.B.; Medeiros, A.C.D.; Santos, A.F.O.; Macêdo, R.O. Thermal Stability of Metronidazole Drug and Tablets. *J. Therm. Anal. Calorim.* **2003**, *72*, 535–538. [CrossRef]
75. Aleanizy, F.S.; Alqahtani, F.; Al Gohary, O.; El Tahir, E.; Al Shalabi, R. Determination and Characterization of Metronidazole-Kaolin Interaction. *Saudi Pharm. J.* **2015**, *23*, 167–176. [CrossRef]
76. Dyba, A.J.; Wiącek, E.; Nowak, M.; Janczak, J.; Nartowski, K.P.; Braun, D.E. Metronidazole Cocrystal Polymorphs with Gallic and Gentisic Acid Accessed through Slurry, Atomization Techniques, and Thermal Methods. *Cryst. Growth Des.* **2023**, *23*, 8241–8260. [CrossRef]
77. Skotnicki, M.; Czerniecka-Kubicka, A.; Neilsen, G.; Woodfield, B.F.; Pyda, M. Application of Advanced Thermal Analysis for Characterization of Crystalline and Amorphous Phases of Carvedilol. *J. Pharm. Biomed. Anal.* **2022**, *217*, 114822. [CrossRef] [PubMed]
78. Lapuk, S.E.; Mukhametzyanov, T.A.; Schick, C.; Gerasimov, A.V. Crystallization Kinetics and Glass-Forming Ability of Rapidly Crystallizing Drugs Studied by Fast Scanning Calorimetry. *Int. J. Pharm.* **2021**, *599*, 120427. [CrossRef] [PubMed]

79. Hurley, D.; Davis, M.; Walker, G.M.; Lyons, J.G.; Higginbotham, C.L. The Effect of Cooling on the Degree of Crystallinity, Solid-State Properties, and Dissolution Rate of Multi-Component Hot-Melt Extruded Solid Dispersions. *Pharmaceutics* **2020**, *12*, 212. [CrossRef] [PubMed]
80. Kozyra, A.; Mugheirbi, N.A.; Paluch, K.J.; Garbacz, G.; Tajber, L. Phase Diagrams of Polymer-Dispersed Liquid Crystal Systems of Itraconazole/Component Immiscibility Induced by Molecular Anisotropy. *Mol. Pharm.* **2018**, *15*, 5192–5206. [CrossRef]
81. Chmiel, K.; Knapik-Kowalczuk, J.; Kamińska, E.; Tajber, L.; Paluch, M. High-Pressure Dielectric Studies—A Way to Experimentally Determine the Solubility of a Drug in the Polymer Matrix at Low Temperatures. *Mol. Pharm.* **2021**, *18*, 3050–3062. [CrossRef]
82. Gordon, M.; Taylor, J.S. Ideal Copolymers and the Second-Order Transitions of Synthetic Rubbers. i. Non-Crystalline Copolymers. *J. Appl. Chem.* **1952**, *2*, 493–500. [CrossRef]
83. Kissinger, H.E. Variation of Peak Temperature with Heating Rate in DTA. *J. Res. Natl. Bur. Stand.* **1956**, *57*, 217–221. [CrossRef]
84. Eslami, H.; Müller-Plathe, F. Self-Assembly Pathways of Triblock Janus Particles into 3D Open Lattices. *Small* **2023**, 2306337. [CrossRef] [PubMed]
85. Auer, S.; Frenkel, D. Numerical Prediction of Absolute Crystallization Rates in Hard-Sphere Colloids. *J. Chem. Phys.* **2004**, *120*, 3015–3029. [CrossRef] [PubMed]

Supplementary Materials

The Impact of Various Poly(vinylpyrrolidone) Polymers on the Crystallization Process of Metronidazole

Luiza Orszulak [1,*], Taoufik Lamrani [2], Magdalena Tarnacka [2], Barbara Hachuła [1], Karolina Jurkiewicz [2], Patryk Zioła [2], Anna Mrozek-Wilczkiewicz [2,3], Ewa Kamińska [4] and Kamil Kamiński [2]

[1] Institute of Chemistry, Faculty of Science and Technology, University of Silesia in Katowice, Szkolna 9, 40-007 Katowice, Poland; barbara.hachula@us.edu.pl
[2] Institute of Physics, Faculty of Science and Technology, University of Silesia in Katowice, 75 Pułku Piechoty 1A, 41-500 Chorzow, Poland; taoufik.lamrani@us.edu.pl (T.L.); magdalena.tarnacka@us.edu.pl (M.T.); karolina.jurkiewicz@us.edu.pl (K.J.); patryk.ziola@us.edu.pl (P.Z.); anna.mrozek-wilczkiewicz@us.edu.pl (A.M.-W.); kamil.kaminski@us.edu.pl (K.K.)
[3] Biotechnology Centre, Silesian University of Technology, Bolesława Krzywoustego 8, 44-100 Gliwice, Poland
[4] Department of Pharmacognosy and Phytochemistry, Faculty of Pharmaceutical Sciences in Sosnowiec, Medical University of Silesia in Katowice, Jagiellońska 4, 41-200 Sosnowiec, Poland; ekaminska@sum.edu.pl
* Correspondence: luiza.orszulak@us.edu.pl

1. Experimental

1.1. Synthesis of trifunctional chain transfer agent (CTA2)

Trifunctional chain transfer agent (1,3,5-benzyl tri(diethyldithiocarbamate), CTA2) was prepared in a single-step route by the reaction of 1,3,5-tribromomethyl benzene with sodium diethyldithiocarbamate according to the following procedure. In a 100 mL two-neck round-bottom flask equipped with a magnetic stirrer, inlet-outlet nitrogen, and dropping funnel, sodium diethyldithiocarbamate trihydrate (2 g, 8.88 mmol) was dissolved in methanol (40 mL) under a nitrogen atmosphere and cooled to 273 K. A solution of 1,3,5-tribromomethyl benzene (1 g, 2.80 mmol) in methanol (10 mL) was added dropwise over a 30 min period. The reaction was gradually warmed to room temperature and remained under magnetic stirring for a further 72 h. Then, the yellowish precipitate was filtered, washed with cold methanol, and left to dry to constant mass. The structure of the obtained 1,3,5-benzyl tri(diethyldithiocarbamate) was confirmed by ^{1}H NMR spectrum (see **Figure S1**).

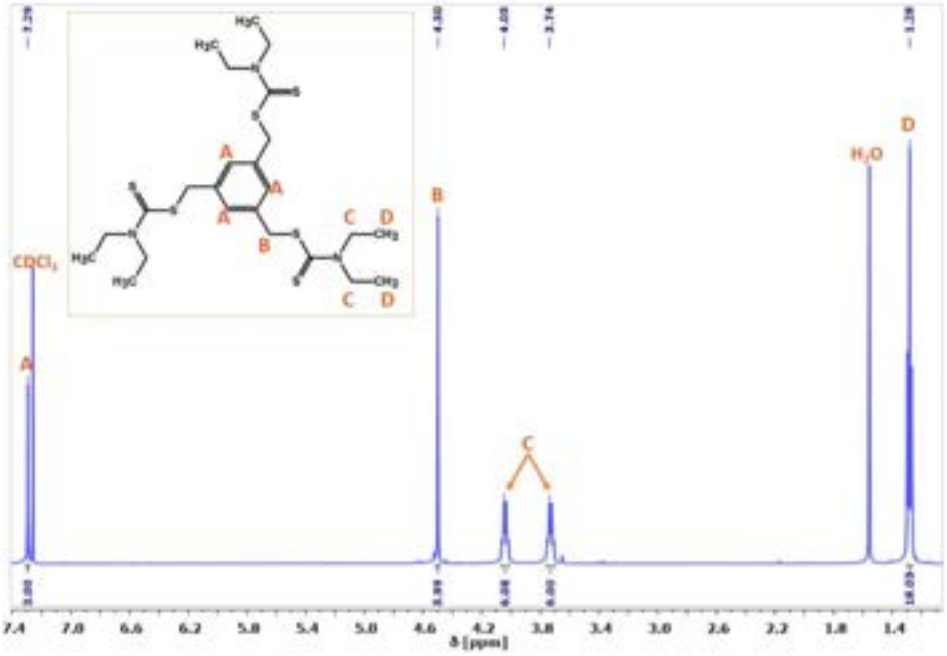

Figure S1. ^{1}H NMR spectrum of trifunctional CTA2 in $CDCl_3$ (500 MHz).

1.2. Synthesis of PVP with linear topology (linPVP)

Thermally-initiated Reversible Addition Fragmentation Chain Transfer (RAFT) polymerization of N-vinylpyrrolidone (VP) using CTA1 as a chain transfer agent and 2,2'-azobis(2-methylpropionitrile) (AIBN) as an initiator with molar ratios $[VP]_0/[CTA1]_0/[AIBN]_0$ = 500/1/0.25) was carried out as follows. Prior to polymerization, VP was passed through an alumina column to remove the inhibitor. CTA1 (33.5 mg, 0.15 mmol) and VP (8 mL, 74.86 mmol) were placed in a Schlenk flask with a magnetic stirring bar. The solution was purged under nitrogen and purified by three freeze-pump-thaw cycles. Then, the solution of AIBN (187 μL, 0.037 mmol) was added to the reaction mixture and the flask was immersed in an oil bath thermostated at 60 °C to start the reaction. The polymerization was quenched after a predetermined time (t = 3.5 h) by cooling and exposing the reaction mixture to air. The product was precipitated with cold diethyl ether and re-dissolved in chloroform and this cycle was repeated twice. The polymer was isolated, filtered, and then dried under vacuum to a constant mass. The structure of the obtained linear PVP was confirmed by ^{1}H and ^{13}C NMR spectra (see **Figures S2 and S3**). The molecular weight and dispersity of the produced *lin*PVP were determined by size exclusion chromatography (SEC) (see **Figure S4**).

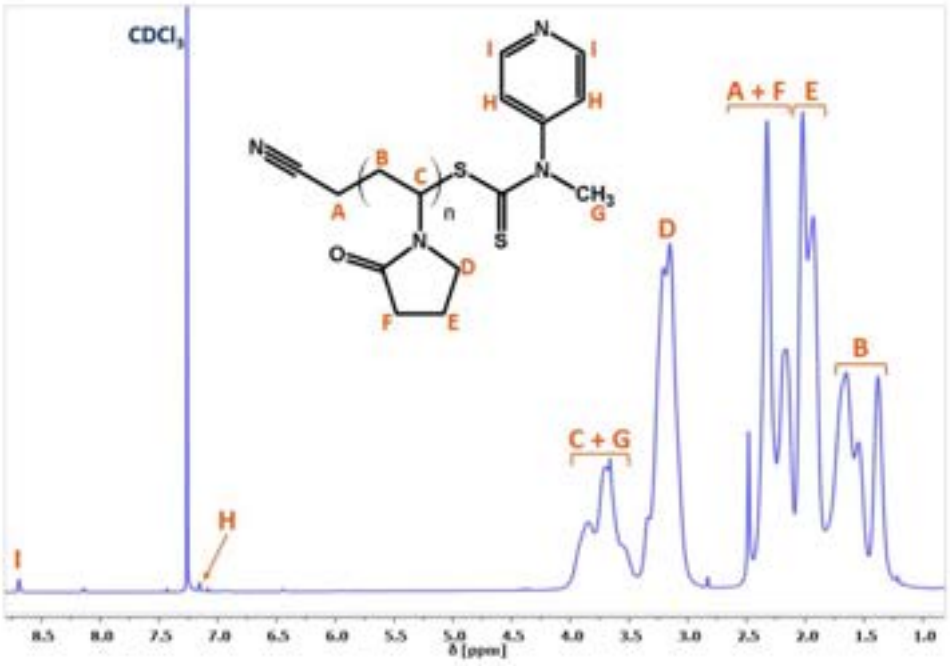

Figure S2. ^{1}H NMR spectrum of *lin*PVP in $CDCl_3$ (600 MHz).

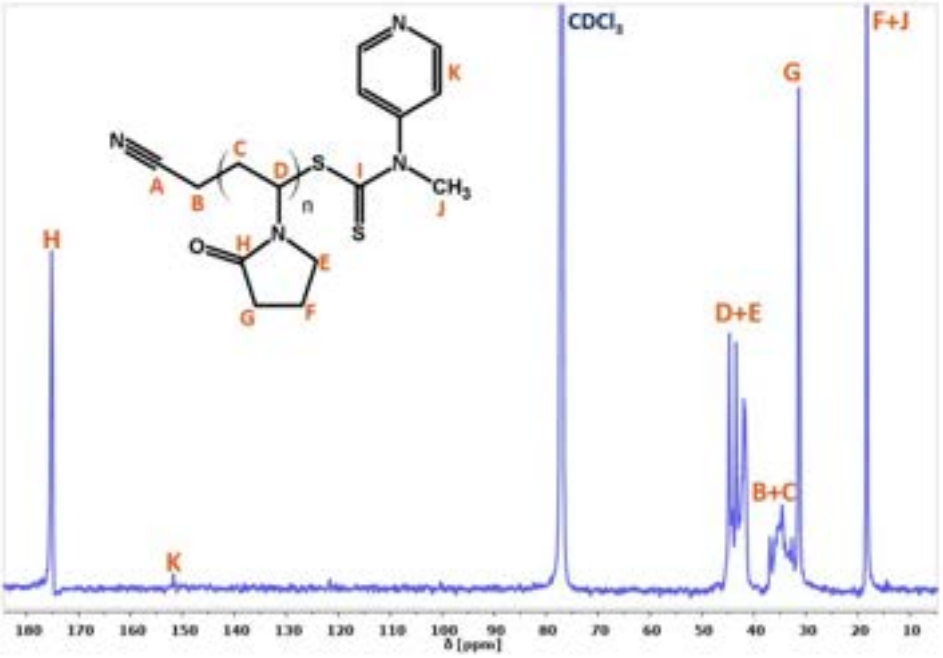

Figure S3. ^{13}C NMR spectrum of *lin*PVP in $CDCl_3$ (600 MHz).

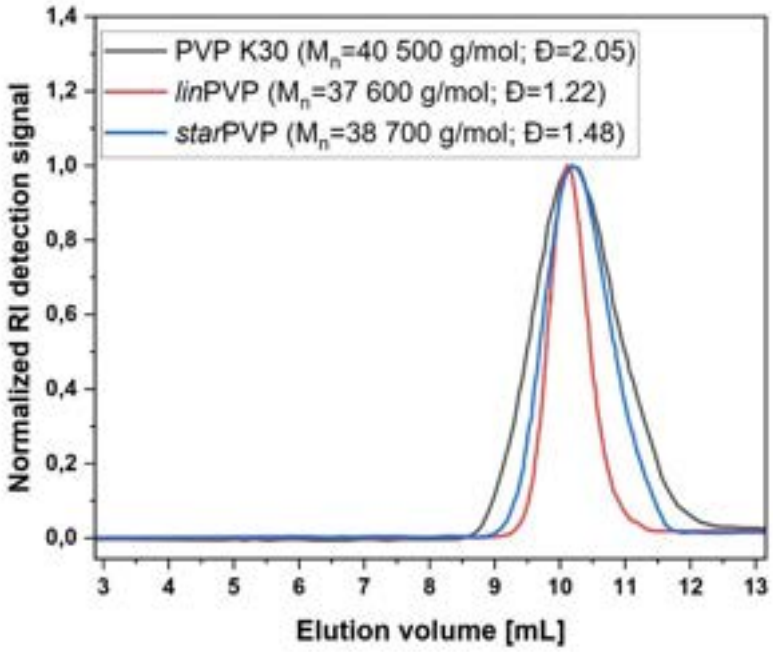

Figure S4. SEC traces of PVP samples: commercial (PVP K30 - grey line) and self-synthesized (*lin*PVP - red line, *star*PVP - blue line).

1.3. Synthesis of PVP with star topology (starPVP)

Thermally-initiated RAFT polymerization of VP using previously synthesized CTA2 as a chain transfer agent and AIBN as an initiator with molar ratios $[VP]_0/[CTA2]_0/[AIBN]_0 = 400/5/1$) was carried out as follows. Before polymerization, VP was passed through an alumina column to remove the inhibitor. CTA2 (0.13148 g, 0.23 mmol), VP (2 mL, 18.72 mmol) and DCM (4 mL, 200% v/v in relation to the monomer) were placed in a Schlenk flask with a magnetic stirring bar. The solution was purged under nitrogen and purified by three freeze-pump-thaw cycles. Then, the solution of AIBN (234 µL, 0.047 mmol) was added to the reaction mixture and the flask was immersed in an oil bath thermostated at 60 °C to start the reaction. The polymerization was quenched after a predetermined time (t = 8 h) by cooling and

exposing the reaction mixture to air. The product was precipitated with cold diethyl ether and re-dissolved in chloroform, and this cycle was repeated twice. The polymer was isolated, filtered, and then dried under vacuum to a constant mass. The structure of the obtained three-arm star-shaped PVP was confirmed by ^{1}H and ^{13}C NMR spectra (see **Figures S5 and S6**). The molecular weight and dispersity of the produced *star*PVP were determined by SEC (see **Figure S4**).

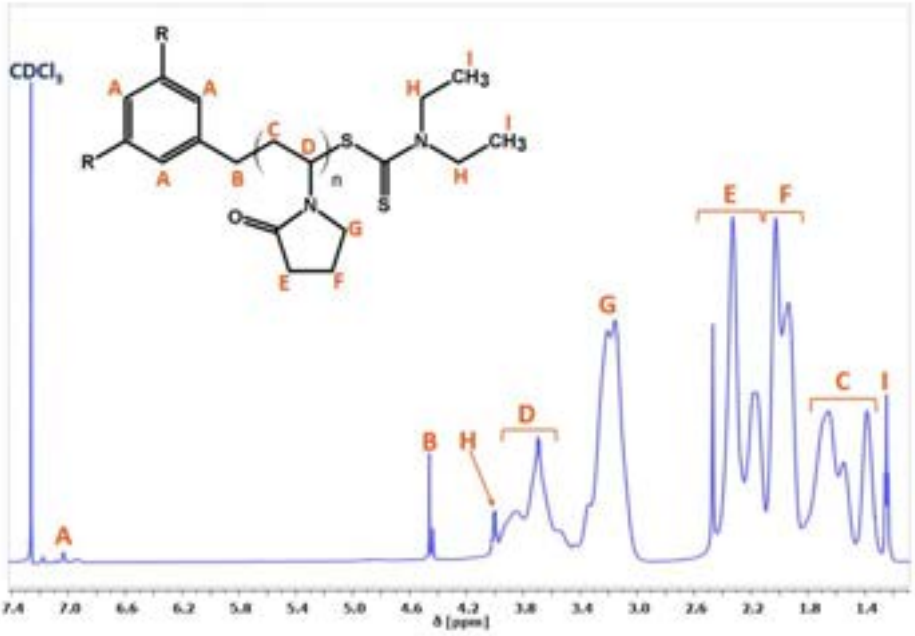

Figure S5. ^{1}H NMR spectrum of *star*PVP in $CDCl_3$ (600 MHz).

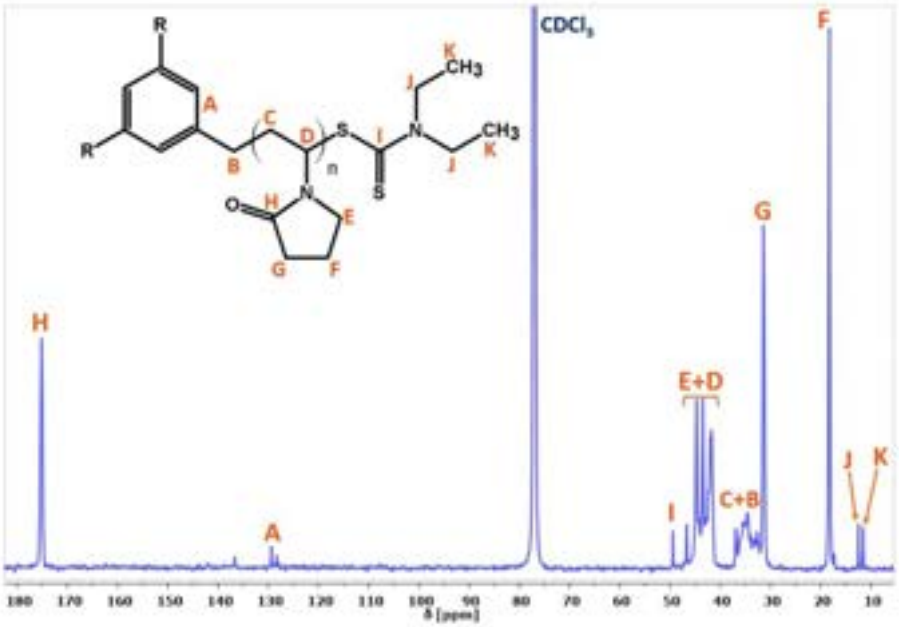

Figure S6. ^{13}C NMR spectrum of *star*PVP in $CDCl_3$ (600 MHz).

2. FTIR data

In the IR spectrum of crystalline MTZ, shown in **Figure S7**, one can see a sharp peak at 3099 cm^{-1} assigned to the CH stretching vibrations of the H-C=C group. The bands located from 3000 to 2800 cm^{-1} correspond to the aliphatic CH stretching vibrations of methyl and methylene groups. The absorption signals occurring at a lower frequency region at 1534 and 1367 cm^{-1} are related to the asymmetric and symmetric stretching vibrations of the NO_2 group, respectively. The peaks detected at 1472 and 1427 cm^{-1} originate from the mixed C=C and C=N stretching vibrations as well as the CH bending of methyl and methylene groups. At 1264 and 1185 cm^{-1}, there are the bands associated with in-plane bending of the CH group (H-C=C) and the C-N stretching (tertiary amine group) [1–3]. The peak due to the in-plane OH deformation and CH_2 twisting out-of-plane vibration occurs at 1073 cm^{-1}. The scissoring in-plane bending of NO_2 moiety gives rise to a band at 825 cm^{-1}. A peak at 743 cm^{-1} corresponds to the NO_2 wagging vibration.

IR spectra of PVP samples in the higher wavenumber range are characterized by the bands originating from the stretching vibrations of OH groups, because PVP is hygroscopic, (3700-3100 cm^{-1}) and CH groups (3100-2800 cm^{-1}). In more detail, the peak at 2952 cm^{-1} corresponds to the asymmetric stretching vibrations of the CH_2 groups of the pyrrole ring, whereas the signal at 2925 cm^{-1} is related to the symmetric stretching vibrations of the CH_2 groups of a chain [4]. The band located at about 1650 cm^{-1} (1645 cm^{-1} for PVP K30, 1651 cm^{-1} for *lin*PVP, 1661 cm^{-1} for *star*PVP) is associated with the stretching vibrations of C=O moiety (**Figure 2** in the main manuscript). The signals assigned to the bending vibrations of CH groups occur at 1461 and 1374 cm^{-1} [5]. The peak observed at 1287 cm^{-1} originates from the wagging vibrations of CH_2 moieties and the stretching vibrations of the C-N group [4]. At 1019 cm^{-1}, the band associated with the CH_2 rocking vibrations and the stretching vibrations of C-C moieties is observed. The peak at 934 cm^{-1} corresponds to the stretching vibrations of C-C groups, while that at 845 cm^{-1} is related to the bending vibrations of CH_2 moieties. The signal at 572 cm^{-1} is assigned to the bending vibrations of the N-C=O group.

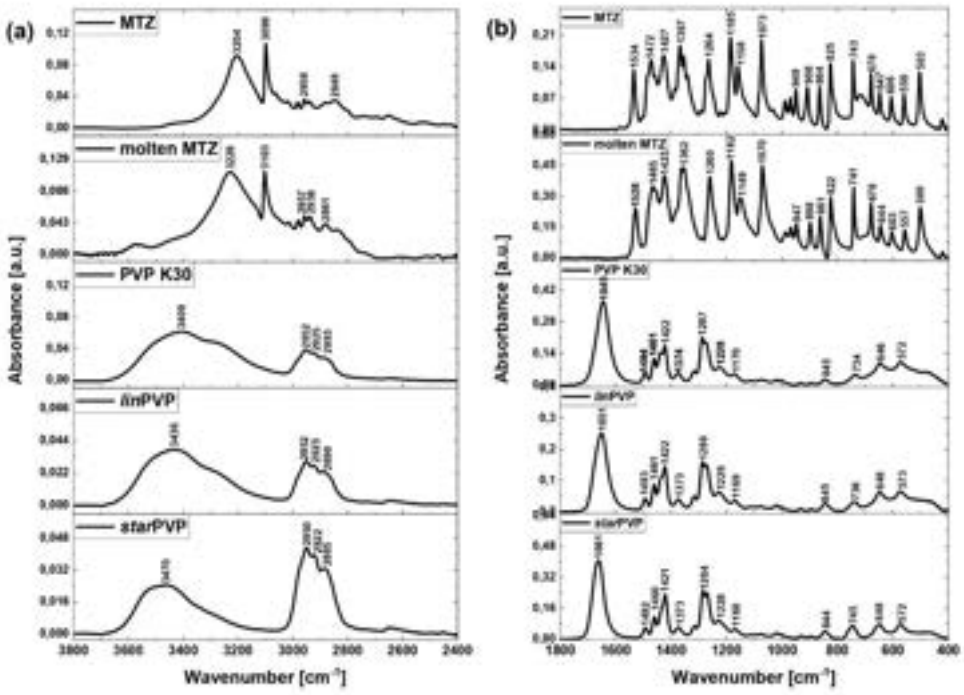

Figure S7. Infrared spectra of crystalline and molten MTZ as well as PVP samples. Data were presented in two spectral regions: (a) 3800–2400 cm^{-1} and (b)1800–400 cm^{-1}.

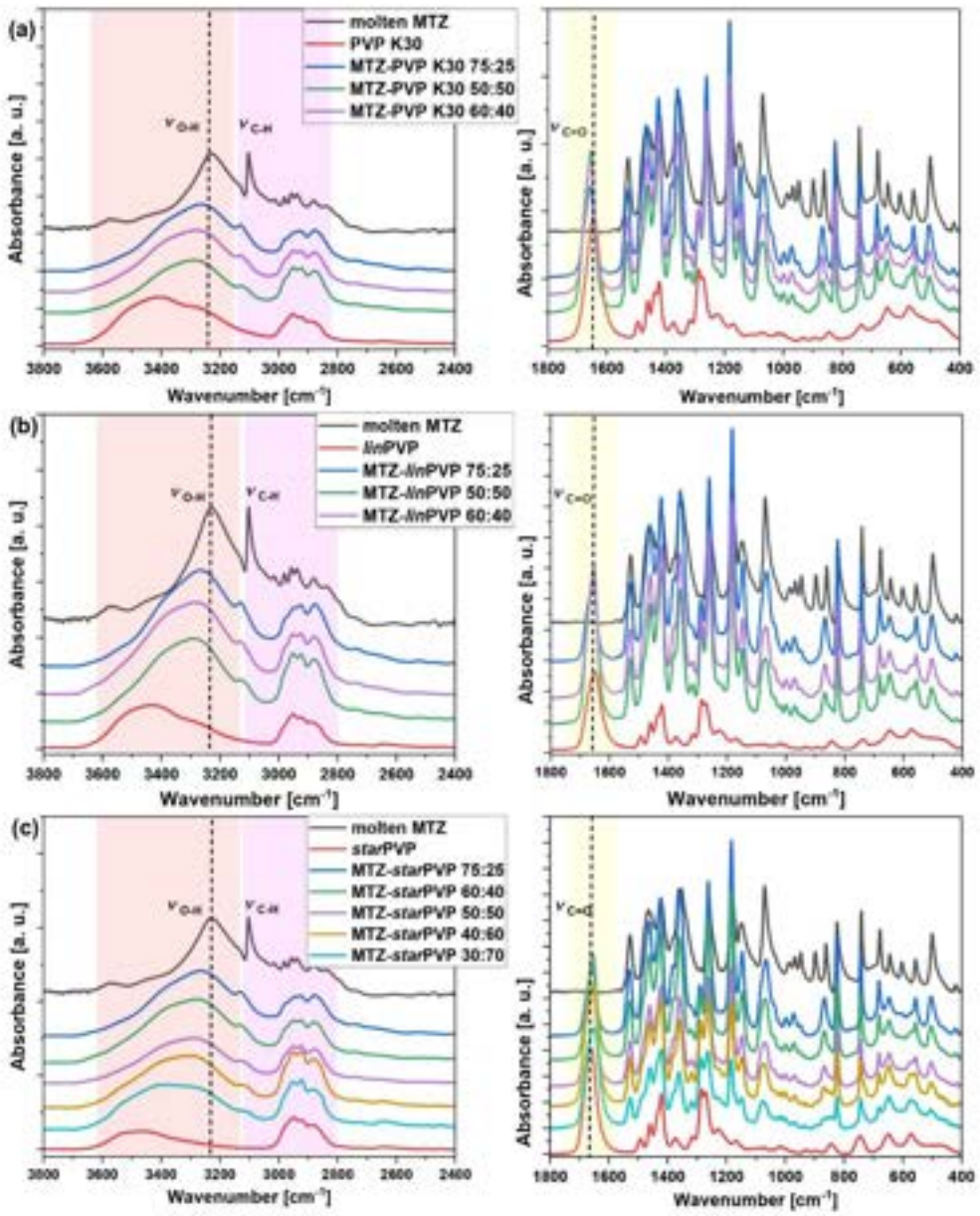

Figure S8. Infrared spectra of (a) MTZ-PVP K30, (b) MTZ-*lin*PVP, and (c) MTZ-*star*PVP binary mixtures prepared in different weight ratios, measured at T=295 K (in the supercooled liquid/or glassy states) together with the spectra registered for the molten MTZ and neat PVP polymers, presented in the ranges of 3800–2400 cm^{-1} (left) and 1800–400 cm^{-1} (right).

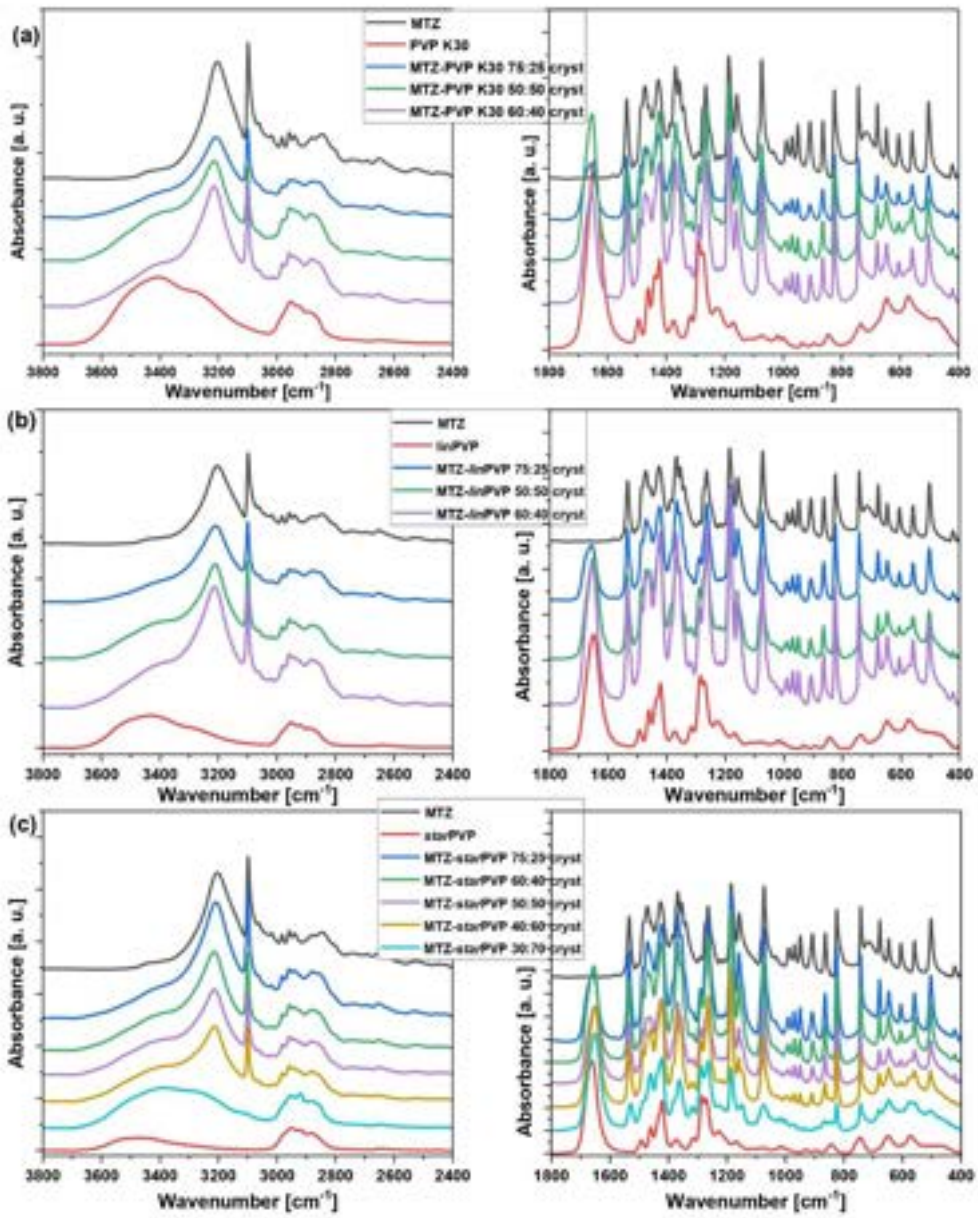

Figure S9. Infrared spectra of (a) MTZ-PVP K30, (b) MTZ-*lin*PVP, and (c) MTZ-*star*PVP binary mixtures (samples after recrystallization) prepared in different molar ratios together with the spectra registered for the crystalline MTZ and neat PVP polymers, presented in the ranges of 3800–2400 cm^{-1} (left) and 1800–400 cm^{-1} (right).

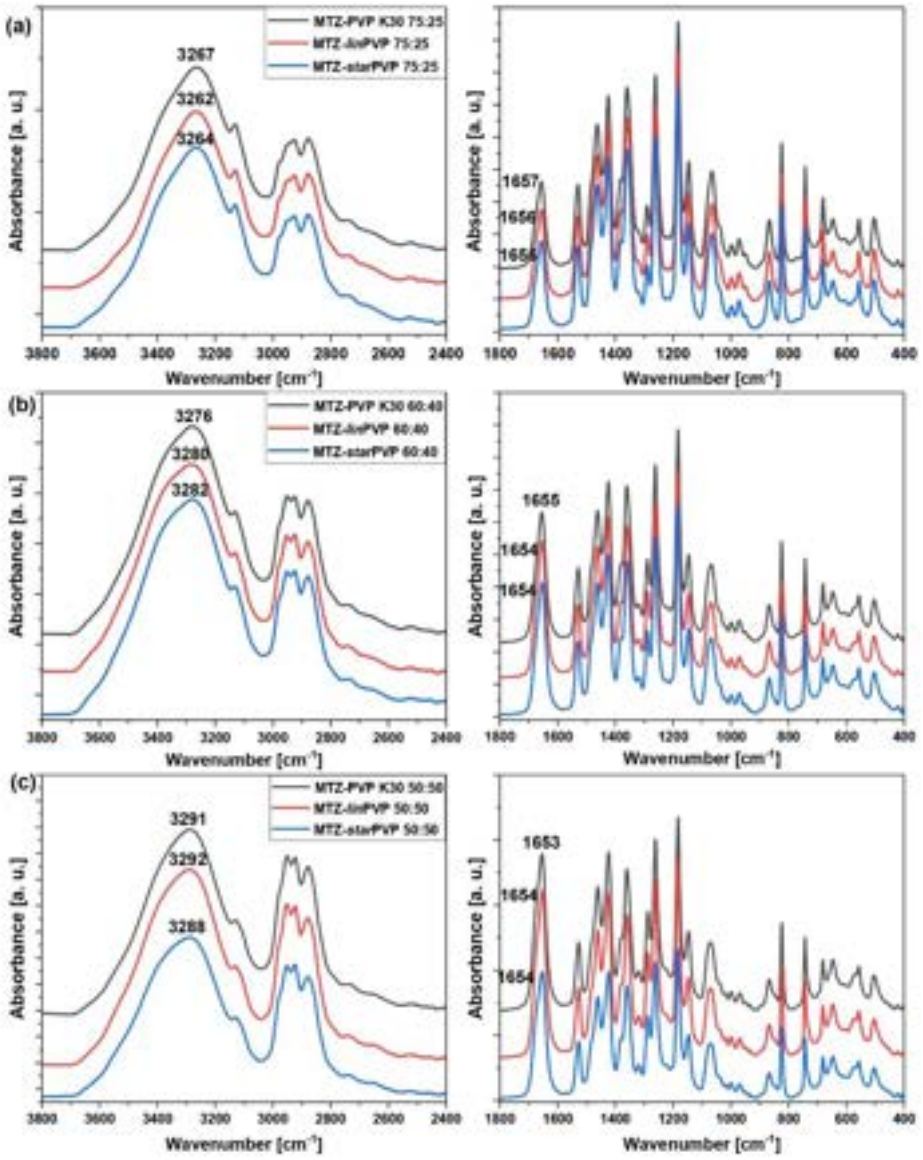

Figure S10. Infrared spectra of binary mixtures of MTZ with all PVP samples (K30, *lin*PVP and *star*PVP) ((a) 75:25, (b) 60:40, (c) 50:50 w/w) measured in the supercooled liquid state, presented in the ranges of 3800–2400 cm^{-1} (left) and 1800–400 cm^{-1} (right).

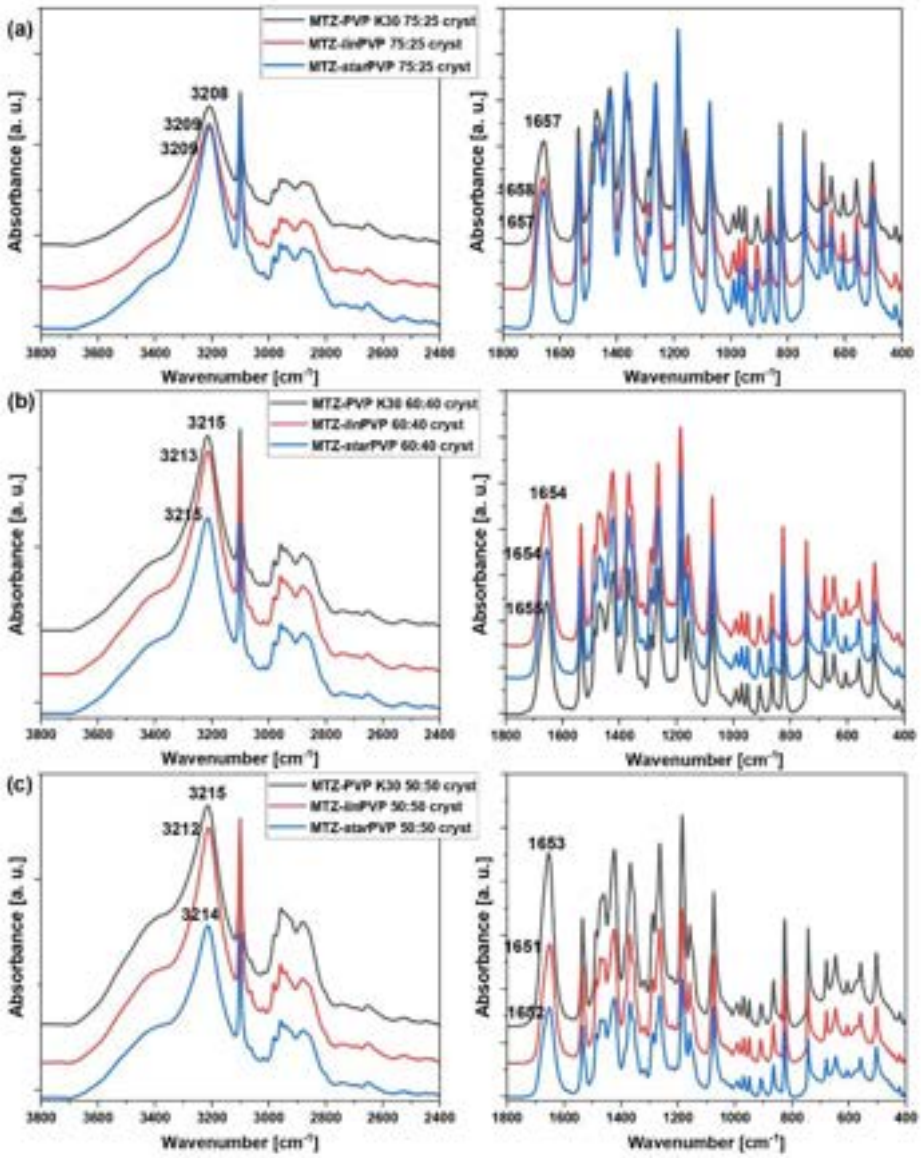

Figure S11. Infrared spectra of binary mixtures of MTZ with all PVP samples (K30, *lin*PVP and *star*PVP) ((a) 75:25, (b) 60:40, (c) 50:50 w/w) measured in the crystalline state, presented in the ranges of 3800–2400 cm^{-1} (left) and 1800–400 cm^{-1} (right).

3. DSC data

Table S1. The calorimetric glass transition temperature values (heating rate, ϕ =10 K/min) for neat PVPs and examined MTZ-PVP binary mixtures in various weight ratios.

Binary mixture, w/w	Glass transition temperature, T_g [K]		
	MTZ-PVP K30	MTZ-*lin*PVP	MTZ-*star*PVP
75:25	261.3	260.3	258.7
60:40	269.1	267.9	268.5
50:50	277.1	278.5	280.4
40:60	-	-	315.1
30:70	-	-	339.4
neat PVP	395.6	415.0	433.4

Table S2. The calorimetric melting temperature values (ϕ =10 K/min) for neat MTZ and the examined MTZ-PVP binary mixtures in various weight ratios.

Binary mixture, w/w	Melting temperature, T_m [K]		
	MTZ-PVP K30	MTZ-*lin*PVP	MTZ-*star*PVP
neat MTZ	437.3		
75:25	430.3	430.8	431.3
60:40	422.0	423.2	423.4
50:50	417.0	418.3	416.4

Table S3. The crystallization temperature values for MTZ-PVP K30 mixtures depending on the heating rate (ϕ).

MTZ-PVP K30			
ϕ [K/min]	T_c [K]		
	75:25	60:40	50:50
15	341.7		
12.5	336.7	389.7	
10	333.6	385.8	386.5
7.5	331.7	376.6	383.2
5	326.9	372.3	376.1
2.5			369.1

Table S4. The crystallization temperature values for MTZ-*lin*PVP mixtures depending on the heating rate (ϕ).

MTZ-*lin*PVP			
ϕ [K/min]	T_c [K]		
	75:25	60:40	50:50
15	335.1		
12.5	333.3	397.3	
10	330.3	388.5	387.7
7.5	327.1	382.6	385.2
5	322.5	359.1	381.8
2.5			375.8

Table S5. The crystallization temperature values for MTZ-*star*PVP mixtures depending on the heating rate (ϕ).

MTZ-*star*PVP			
ϕ [K/min]	T_c [K]		
	75:25	60:40	50:50
15	323.6		
12.5	321.2	394.5	
10	319.3	395.7	386.5
7.5	315.6	387.6	385.1
5	311.6	354.5	374.3
2.5			364.3

4. References:

1. Minecka, A.; Tarnacka, M.; Jurkiewicz, K.; Hachuła, B.; Wrzalik, R.; Bródka, A.; Kamiński, K.; Kamińska, E. The Impact of the Size of Acetylated Cyclodextrin on the Stability of Amorphous Metronidazole. *Int. J. Pharm.* **2022**, *624*, 122025, doi:10.1016/J.IJPHARM.2022.122025.
2. Bensouiki, S.; Belaib, F.; Sindt, M.; Rup-Jacques, S.; Magri, P.; Ikhlef, A.; Meniai, A.H. Synthesis of Cyclodextrins-Metronidazole Inclusion Complexes and Incorporation of Metronidazole - 2-Hydroxypropyl-β-Cyclodextrin Inclusion Complex in Chitosan Nanoparticles. *J. Mol. Struct.* **2022**, *1247*, 131298, doi:10.1016/j.molstruc.2021.131298.
3. Socrates, G. Infrared and Raman Characteristic Group Frequencies : Tables and Charts.; 2001.
4. Rahma, A.; Munir, M.M.; Khairurrijal; Prasetyo, A.; Suendo, V.; Rachmawati, H. Intermolecular Interactions and the Release Pattern of Electrospun Curcumin-Polyvinyl(Pyrrolidone) Fiber. *Biol. Pharm. Bull.* **2016**, *39*, 163–173, doi:10.1248/bpb.b15-00391.
5. Abdelghany, A.M.; Meikhail, M.S.; Oraby, A.H.; Aboelwafa, M.A. Experimental and DFT Studies on the Structural and Optical Properties of Chitosan/Polyvinyl Pyrrolidone/ZnS Nanocomposites. *Polym. Bull.* **2023**, *80*, 13279–13298, doi:10.1007/s00289-023-04700-0.

4.2. Inhibition of naproxen crystallization by polymers: The role of topology and chain length of polyvinylpyrrolidone macromolecules (P2)

Autorzy: L. Orszulak, P. Włodarczyk, B. Hachuła, T. Lamrani, K. Jurkiewicz, M. Tarnacka, M. Hreczka, K. Kamiński, E. Kamińska

Referencja: *European Journal of Pharmaceutics and Biopharmaceutics*, 2025, 207, 114581

DOI: 10.1016/j.ejpb.2024.114581

Impact Factor czasopisma: 4.3

Liczba punktów ministerialnych MNiSW czasopisma: 100 (2025)

Mój udział w pracy polegał na zsyntezowaniu matryc polimerowych, ich pełnej charakterystyce spektroskopowej i chromatograficznej, tworzeniu mieszanin binarnych metodą witryfikacji, analizie danych, dyskusji wyników, przygotowywaniu tekstów manuskryptów, opracowywaniu odpowiedzi dla Recenzentów i Edytora, pozyskaniu finansowania w ramach kierowania grantem *„Perły Nauki”*.

European Journal of Pharmaceutics and Biopharmaceutics 207 (2025) 114581

Contents lists available at ScienceDirect

European Journal of Pharmaceutics and Biopharmaceutics

journal homepage: www.elsevier.com/locate/ejpb

Research paper

Inhibition of naproxen crystallization by polymers: The role of topology and chain length of polyvinylpyrrolidone macromolecules

Luiza Orszulak [a,*], Patryk Włodarczyk [b], Barbara Hachuła [a], Taoufik Lamrani [c], Karolina Jurkiewicz [c], Magdalena Tarnacka [c], Marek Hreczka [b,d], Kamil Kamiński [c], Ewa Kamińska [a,*]

[a] Institute of Chemistry, Faculty of Science and Technology, University of Silesia in Katowice, Szkolna 9 40-007, Katowice, Poland
[b] Institute of Non Ferrous Metals, Sowińskiego 5 44 100, Gliwice, Poland
[c] Institute of Physics, Faculty of Science and Technology, University of Silesia in Katowice, 75 Pułku Piechoty 1, 41-500 Chorzow, Poland
[d] Department of Mechatronics, Silesian University of Technology, Akademicka 10A 44-100, Gliwice, Poland
[e] Department of Pharmacognosy and Phytochemistry, Faculty of Pharmaceutical Sciences in Sosnowiec, Medical University of Silesia in Katowice, Jagiellonska 4 41-200, Sosnowiec, Poland

ARTICLE INFO

Keywords:
Naproxen
Poly(vinylpyrrolidone)
Topology
Chain length
Dispersity
Crystallization process
Amorphous solid dispersions

ABSTRACT

This paper presents an innovative approach that utilizes self-synthesized homopolymers of polyvinylpyrrolidone (PVP) with different architectures as effective matrices for inhibiting the crystallization of naproxen (NAP). We have thoroughly investigated amorphous solid dispersions containing NAP and (i) self-synthesized linear PVP, (ii) self-synthesized three-armed star-shaped PVP, and (iii) self-synthesized linear PVP with a mass (M_w) corresponding to the length of one arm of the star polymer, as well as (iv) commercial linear PVP K30 as a reference. Differential scanning calorimetry, X-ray diffraction, and infrared spectroscopy studies, as well as molecular dynamics simulations were conducted to gain comprehensive insights into the thermal and structural properties, as well as intermolecular interactions in the NAP-PVP systems. The main purpose of all experiments was to assess the impact of macromolecule structure (topology, molecular weight) on the kinetics of the crystallization of NAP – a drug that is very difficult to vitrify. Our studies clearly showed that the most effective matrix in inhibiting the NAP crystallization is linear, self-synthesized PVP with higher molecular weight (M_w) similar to that of the commercial PVP K30, but lower, strictly controlled dispersity. We also found that crystallization of API proceeds at a similar pace for the binary mixture composed of a star-shaped PVP and linear polymer with M_w corresponding to M_w of one arm of the star-shaped macromolecule in the vicinity of the T_g. The obtained data highlight the key role of polymer structure in designing new pharmaceutical formulations.

1. Introduction

The pharmaceutical industry has been struggling with the problem of low bioavailability of active pharmaceutical ingredients (APIs) for many years. According to the latest data, currently around 50 % of drugs (APIs in the crystalline form) introduced to the market and 70–90 % of those in the development stage are characterized by low solubility (i.e., they are class II or IV of Biopharmaceutics Classification System, BCS), which, in turn, contributes to low drug efficacy after oral administration due to poor systemic absorption [1,2]. To resolve this problem, i.e., to increase

Abbreviations: AIBN, 2,2′-azobis(2-methylpropionitrile); APIs, Active Pharmaceutical Ingredients; ASDs, Amorphous Solid Dispersions; BCS, Biopharmaceutics Classification System; BMs, binary mixtures; CTA, Chain Transfer Agent; Đ, dispersity; DCM, dichloromethane; DSC, Differential Scanning Calorimetry; $E_{a,iso}$, isothermal crystallization energy; $E_{a,non-iso}$, non-isothermal crystallization energy; FTIR, Fourier-Transform Infrared; HBs, hydrogen bonds; HPMC, hydroxypropyl methylcellulose; HPMCAS, hydroxypropyl methylcellulose acetate succinate; MD simulations, Molecular Dynamics simulations; M_w, molecular weight; NAP, naproxen; NMR, Nuclear Magnetic Resonance; NSAID, nonsteroidal anti-inflammatory drug; PEG, polyethylene glycol; PVP, poly(vinylpyrrolidone); RAFT, Reversible Addition-Fragmentation Chain Transfer; SEC, Size-Exclusion Chromatography; SM, Supplementary Material; T, temperature; T_c, crystallization temperature; T_g, glass transition temperature; T_m, melting temperature; $t_{1/2}$, crystallization half-time; VP, vinylpyrrolidone; XRD, X-Ray Diffraction; ΔC_p, heat capacity change at T_g; ΔH_m, melting enthalpy; ϕ, heating/cooling rate; X_{NAP}, weight fraction of NAP.

* Corresponding authors.
E-mail addresses: luiza.orszulak@us.edu.pl (L. Orszulak), ekaminska@sum.edu.pl (E. Kamińska).

https://doi.org/10.1016/j.ejpb.2024.114581
Received 14 August 2024; Received in revised form 7 November 2024; Accepted 13 November 2024
Available online 27 November 2024

the bioavailability of crystalline APIs, various methods have been discovered, e.g., salt formation,[3] micronization,[4] amorphization,[5] the creation of cocrystals,[6,7] or different polymorphic forms.[8] Among them, the amorphization, i.e., the formation of solid forms, in which the API is in the amorphous form rather than in a crystalline state, deserves special attention.[5,9,10] This relatively simple method generally leads to improved pharmacokinetic parameters of drugs from II and IV groups of BCS. On the other hand, APIs in this form are characterized by a higher Gibbs free energy compared to the crystalline state, therefore, they are thermodynamically/physically unstable, i.e., they tend to recrystallize (return to a more stable crystalline form) during storage, losing their extraordinary properties.[10] The great challenge of modern pharmacy is to stabilize amorphous pharmaceuticals long enough and in such a way as to enable their commercial fabrication, distribution, and in-house storage.[10,11] The most popular ways to achieve this is the formation of amorphous solid dispersions (ASDs) composed of API and different low- and high-molecular weights excipients, e.g., modified saccharides, amino and organic acids, polymers (e.g., polyvinylpyrrolidone (PVP), polyethylene glycol (PEG), hydroxypropyl methylcellulose (HPMC), hydroxypropyl methylcellulose acetate succinate (HPMCAS)).[12–15].

According to the literature data, compounds from the latter group are very effective excipients for preventing drug crystallization from the amorphous phase.[14,15] Many macromolecules easily form amorphous/glassy phase and have relatively high glass transition temperatures ,T_g (hence, they increase the T_g of a binary system). They act as stabilizers mainly by reducing molecular mobility as well as interacting with the active substance (usually through hydrogen bonds).[14] However, it should be noted that these systems are not free of drawbacks. One of the most important is the lack of control over the homogeneity of API-polymer binary mixtures.[9].

Currently, there is a quite lively discussion regarding the selection of appropriate macromolecules that would effectively stabilize easily crystallizing drugs. Herein, it is important to note that not only the type of polymer used in the ASD with APIs is crucial, but also the architecture/structure of these excipients. It is widely known that even with the same chemical composition and molecular weight (M_w), the structural and dynamical properties of polymers can be significantly changed by varying their molecular architecture, i.e., by using either a linear or branched structure.[16,17] It should be recalled that in polymer chemistry, besides the common linear compounds, more advanced polymer structures such as star-shaped, brush, comb, hyperbranched systems, and dendrimers can also be distinguished.[18] Theoretical and experimental studies have clearly shown that branching of polymer structures results in more compact and less deformed structures compared to linear chains of the same M_w due to the high segment density. As a result, significant changes in mechanical, thermodynamic, and rheological properties may occur.[19–21] In particular, star-shaped polymers have attracted the attention of researchers because they possess several unique features compared to their linear counterparts: (*i*) improved solubility, (*ii*) reduced hydrodynamic radius, (*iii*) low solution and melt viscosity, (*iv*) lower phase transition temperatures, (*v*) reduced crystallinity, and (*vi*) increased number of functional groups at the chain ends allowing for further modifications according to application needs.[17,22–24] Therefore, the topology of polymers can significantly alter their physicochemical properties, and, consequently, it can be expected that the structure of the polymers used in ASDs will also have a significant impact on the behavior of APIs in binary systems.

In the context of such research, naproxen (NAP) appears to be an ideal candidate for testing various polymers as inhibitors of the crystallization process. It is a widely used nonsteroidal anti-inflammatory drug (NSAID) commonly prescribed to relieve pain and reduce fever and inflammation. This API exhibits a very strong crystallization tendency and cannot be prepared in the glassy state by cooling from a melt due to spontaneous crystallizastion regardless of the applied cooling rate.[25,26] Numerous reports indicate that the therapeutic efficacy and stability of NAP are closely related to its molecular structure, making the study of its amorphization and subsequent control of the crystallization process a critical aspect of its development and production.[27–29] Additionally, depending on the crystallization conditions and the type of excipients or solvents used, NAP can exist in many polymorphic forms, each exhibiting distinct physical and chemical properties.[30,31] Low-molecular-weight compounds (e.g., acetylated saccharides),[32,33] and increasingly, polymeric materials,[34] have been used to manipulate the crystallization behavior of NAP. However, it should be clearly emphasized that most research efforts aimed at examining the impact of macromolecules on the stabilization of amorphous drugs have focused mainly on linear, commercially available polymers, while the aspect of branched macromolecular compounds has not yet been well-explored by scientists. What is worth, this research direction is highly justified because the strategic application and strict selection of polymer topologies to control crystallization can lead to the production of improved binary mixtures, ensuring higher stability, better solubility, and bioavailability of the drugs, ultimately providing desirable benefits for patients. Therefore, studying ASDs of NAP with macromolecules other than those commercially available is an important task that can contribute to a better understanding of the impact of polymer architecture on the API's crystallization process, and consequently, on its therapeutic features.

In this paper, we examined amorphous binary mixtures composed of NAP and four different PVP homopolymers, (*i*) commercial PVP K30, and self-synthesized macromolecules, namely (*ii*) linear PVP, (*iii*) three-arm star-shaped PVP, and (*iv*) linear PVP with M_w similar to that of one arm of the star-shaped polymer. At this point, it should be mentioned that commercial PVP (one of the most popular macromolecules used in the pharmaceutical industry) has a long history as a multifunctional biomaterial with a wide range of applications, e.g., in tissue engineering and drug delivery systems.[35,36] Despite a significant pharmaceutical relevance, it is still produced on a commercial scale using uncontrolled radical methods.[37,38] As a result, the products obtained have high dispersity ($Đ > 2$), meaning that the molecular weights provided are merely average values, while, in reality, these PVPs have a rather broad range of polymer chain lengths (with no strictly defined macromolecular parameters). Consequently, many scientific reports continue to emphasize primarily the impact of the number-average molecular weight of such PVP polymers on improving the bioavailability of pharmaceutical products,[39–44] often overlooking important aspects related to the broad M_w distribution of these macromolecules. Recognizing this relatively unexplored area of research, we have recently developed effective methods for producing innovative PVP polymer materials with linear and three-armed star-shaped topologies using reversible addition-fragmentation chain transfer (RAFT) polymerization. These materials can serve as new polymer matrices in pharmaceutical formulations. It is worth noting that the synthesized macromolecules described above have only been used twice so far – first, to investigate their impact on the physical stability of amorphous metronidazole,[45] and second, to assess the effect of PVP polymer topology on the molecular ordering of itraconazole (a liquid-crystalline drug) and the associated improvement in API solubility.[46] In the first case, it was found that linear polymers better stabilize the amorphous form of the API, but the star-shaped polymer mixes with the drug in a higher weight ratio.[45] In the research on itraconazole-PVP mixtures, a higher miscibility of the star-shaped PVP with the API was also observed. Furthermore, it was determined that the branched polymer has the ability to completely disrupt the liquid-crystalline order of the drug, resulting in a fully amorphous material.[46] Herein, we continue exploring the influence of PVP on the kinetics of drug (NAP) crystallization, focusing not only on the polymer topology but also on macromolecular parameters (molecular weight, dispersity). A physicochemical characterization of NAP-PVP ASDs (prepared using the vitrification, i.e., melt-cooling method) as well as studying the NAP's crystallization kinetics were carried out using differential scanning calorimetry (DSC), X-ray diffraction (XRD),

and Fourier-transform Infrared (FT-IR) spectroscopy. Additionally, we performed computer simulations, which allowed us to get a better insight into intermolecular interactions occurring in the studied systems and elucidate differences between them on the molecular scale.

2. Materials and methods

2.1. Materials

1-vinyl-2-pyrrolidone (VP, >99 %, *Sigma Aldrich*) was passed through an alumina column before use to remove the inhibitor. 2,2'-azobis(2-methylpropionitrile) solution (AIBN, 0.2 M in toluene, *Sigma Aldrich*), cyanomethyl methyl(4-pyridyl) carbamodithioate (CTA, 98 %, *Sigma Aldrich*), 1,3,5-tris(bromomethyl)benzene (97 %, *Sigma Aldrich*), sodium diethyldithiocarbamate trihydrate (*Sigma Aldrich*), diethyl ether (pure for analysis, *Chempur*), methanol (99.85 %, *PureLand*), dichloromethane (DCM, 99 %, *Karpinex*), chloroform-d (99.8 % D, contains 0.03 % v/v TMS, *Sigma Aldrich*), PVP K30 (M_n = 40 500, Đ=2.05, *Sigma Aldrich*), crystalline NAP (IUPAC name (2S)-2-(6-methoxy-2-naphthyl) propanoic acid, 99 %, *TCI Europe*) were used as received.

2.2. Methods

2.2.1. Synthesis of PVP macromolecules

The self-synthesized PVP macromolecules (i.e., *lin*PVP14k, *lin*PVP38k, and *star*PVP) were obtained *via* thermally-initiated RAFT polymerization of *N*-vinylpyrrolidone (VP). Commercially available chain transfer agent, CTA (cyanomethyl methyl(4-pyridyl) carbamodithioate) was used for the synthesis of linear macromolecules, while a self-developed trifunctional CTA was employed for the synthesis of the star-shaped PVP polymer. In all reactions, 2,2'-azobis(2-methylpropionitrile) (AIBN) served as the initiator. The polymerization processes were carried out at 60 °C. Upon observing significant thickening of the reaction mixture, the reactions were terminated, and the products

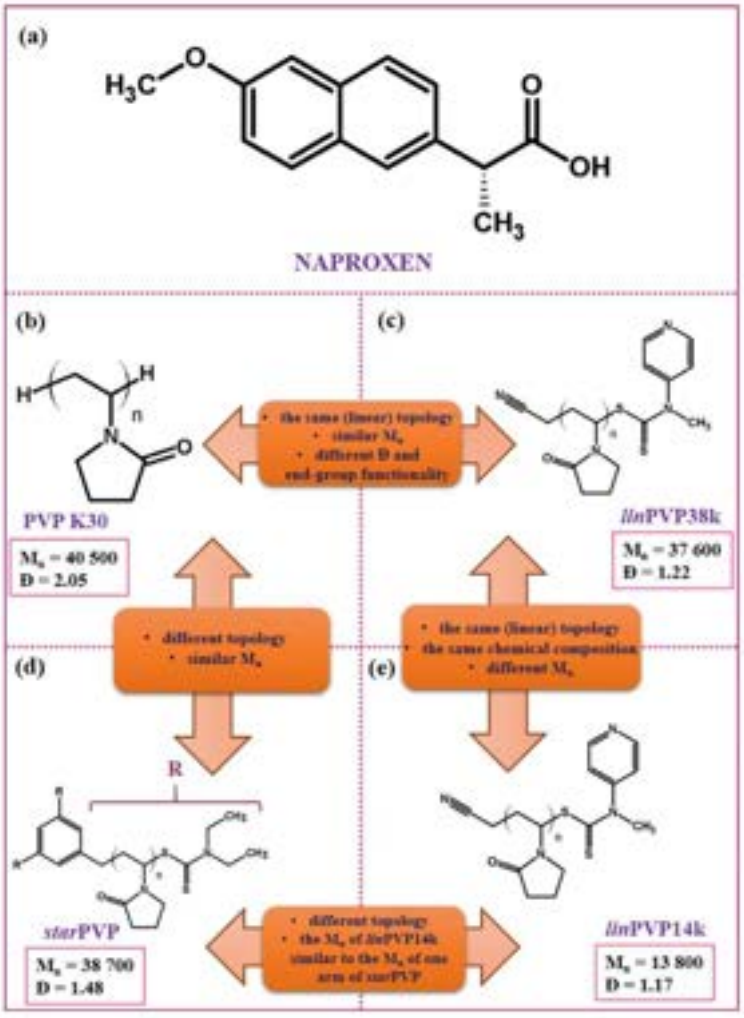

Fig. 1. Chemical structure of **(a)** NAP, **(b)** commercially available PVP K30, **(c)** self-synthesized *lin*PVP38k, **(d)** self-synthesized *star*PVP, **(e)** self-synthesized *lin*PVP14k, with important differences between individual macromolecules highlighted.

were purified by repeated precipitation in cold diethyl ether. The structures of the obtained PVPs were confirmed by ^{1}H and ^{13}C NMR techniques, while the molecular weight (M_n) and dispersity (Đ) of the macromolecules were determined by size exclusion chromatography (SEC). More detailed descriptions of the macromolecules and trifunctional CTA agent synthesis, ^{1}H and ^{13}C NMR spectra, SEC traces, and cytotoxicity studies can be found in our previous publications.[45,46].

All structures of the polymers used in this study, along with macromolecular parameters (M_n, Đ) and highlighted differences between the individual molecules are illustrated in Fig. 1.

2.2.2. The procedure of preparing amorphous NAP-PVP formulations

Amorphous binary mixtures (BMs) composed of NAP and PVP polymers, including a commercial PVP K30, and synthesized linear and star-shaped PVP samples, were obtained by melt cooling method. The NAP-PVP systems were prepared at different weight ratios of API to polymer, i.e., 90:10, 95:5, 80:20, 85:15, 70:30, and 60:40 *w/w*. Herein, it is also worth noting that due to the melting temperature of neat NAP (T_m = 431 K), all binary mixtures were prepared slightly above this temperature, i.e., T=433 K. To obtain a homogeneous mixture, appropriate amounts of crystalline NAP and PVP were weighed, carefully transferred to a metal plate, and preliminarily mixed using a spatula. Subsequently, the plate with the API-polymer mixture was transferred to a hot plate heated to a temperature of 433 K. After a while, NAP began to melt and the entire BM was stirred until complete dissolution of PVP in the API. After determining a homogeneous system, each sample was vitrified by rapidly transferring it to a pre-cooled copper plate.

2.2.3. Differential scanning calorimetry (DSC)

Preliminary calorimetric measurements of BMs containing NAP and various PVPs (i.e., PVP K30, *lin*PVP14k, *lin*PVP38k, and *star*PVP) with different weights ratios (95:5, 90:10, 85:15, 80:20, 70:30, 60:40 *w/w*), as well as neat NAP and PVP polymers were performed using a Mettler-Toledo DSC system, which is equipped with a liquid nitrogen cooling accessory and an HSS8 ceramic sensor. Temperature and enthalpy were calibrated using indium and zinc standards. Samples were placed in aluminum crucibles (40 μL). The examined NAP-PVP 80:20, 70:30, and 60:40 *w/w* binary mixtures were heated from 293 K to 460 K, then cooled to 250 K, and reheated to 460 K. An analogous procedure (heating-cooling-heating) was applied in the case of the neat polymers (PVP K30, *lin*PVP14k, *lin*PVP38k, *star*PVP), but within a different temperature range (they were heated from 293 to 480 K, then cooled to room temperature, and reheated to 480 K). In turn, neat NAP as well as 95:5, 90:10, 85:15 *w/w* NAP-PVP BMs were heated from 250 to 460 K, and subsequently cooled to 250 K. The heating/cooling rate (ϕ) during all experiments was equal to 10 K/min.

Additionally, for all studied NAP-PVP 80:20 *w/w* BMs, isothermal and non-isothermal DSC measurements with applying Netzsch DSC 214 Polyma calorimeter were performed. All samples were measured in aluminum crucibles under an argon atmosphere. For isothermal experiments, we chose five different temperatures (T = 314, 317, 319, 321, 323 K), while non-isothermal studies at a ϕ from 5 to 40 K/min were carried out over a temperature range of 250 to 460 K. It should be mentioned that all described calorimetric measurements for the NAP-PVP systems were carried out immediately after sample preparation to avoid water absorption by the hygroscopic PVP.

2.2.4. X-ray diffraction (XRD)

XRD measurements were conducted utilizing a Rigaku D/Max Rapid II diffractometer equipped with a rotating silver anode. A graphite (002) monochromator was used for the incident radiation, and the wavelength of the beam (λ) was 0.5608 Å. Fresh binary mixtures of NAP and various PVPs at different weight ratios were probed in borosilicate glass capillaries, in transmission Debye-Scherrer geometry. The diffraction patterns were collected in a single shot using a 2D curved image plate detector. The collected 2D diffraction patterns were integrated and rescaled to the scattering vector (Q) scale as follows: $Q = 4\pi\sin(\theta)/\lambda$, where 2 θ is the scattering angle. The background from an empty capillary was also measured and subtracted from the data collected for NAP sample. The NAP-PVP binary systems were placed in capillaries immediately after preparation and tightly closed just after packing the samples. The storage and measurement temperature for all samples was constant, 298 K.

2.2.5. Fourier transform infrared (FT-IR) spectroscopy

Infrared experiments were carried out with a Thermo Scientific Nicolet iS50 FT-IR spectrometer using a diamond attenuated total reflection (ATR) accessory. The data were recorded in the range of 4000–400 cm^{-1} by averaging 16 scans at a resolution of 4 cm^{-1}.

All examined binary mixtures were measured immediately after preparation, while the NAP-PVP 60:40 *w/w* systems were additionally stored in tightly closed vials at room temperature (298 K) for 4 months. Prior to FT-IR measurement, they were also placed in a vacuum desiccator for 24 h and measured immediately afterward.

2.2.6. Simulations

All the simulations carried out in this study were performed in the Gromacs 2024 program package.[47–52] Mixtures were equilibrated in the NPT ensemble at T = 380 K and p = 1 bar conditions with the use of v-rescale and c-rescale thermostat and barostat, respectively. The equilibration time needed to achieve stable density was in the range of 50 – 100 ns. After the equilibration, the 40 ns production runs in the NPT ensemble with T = 314 K and p = 1 bar were carried out. All the analyzed parameters, such as partial densities and hydrogen bonds were recorded from the last 5 ns of production run simulation. The AMBER GAFF forcefield with BCC charges was used. Topology was prepared by the antechamber package.[53,54] Initial PVP polymers were constructed by the HTPolyNet package[55], which enables polymer curing from monomers. Three different polymer systems were prepared, which can be further related to *lin*PVP14k, *lin*PVP38k, and *star*PVP systems. In order to get linear systems with two different average chain lengths, a curing parameter was set to 99 % and 95 % for the preparation of long and short chains respectively. In turn, to get the star system, the four center units of the star were reacted with PVP monomers, where the curing parameter was set to 98 % (the four generated star structures have been presented in the Supplementary Material (SM), see Fig. S1). Obtaining the *lin*PVP38k system by HTPolyNet would be difficult for the reasonable system size for simulation purposes, therefore we have decided to make smaller systems but with proportions reflecting experimental systems, which should be sufficient for qualitative analysis. In the case of the short chain system, which should be related to the *lin*PVP14k, we obtained the average size of the chain consisting of 970 atoms, which is related to approximately 51 PVP monomers with a mass of 5.7 k. For the long chain system, which should be comparable to *lin*PVP38k, we had an average chain consisting of 2930 atoms, which is related to approximately 154 PVP units with a mass of 17 k. To prepare PVP polymers with a star topology, one has to mix a few central units (i.e., c1(cc(cc(c1)C)C)C units in SMILES notation) with the PVP monomers. By choosing the number of central units and the curing parameter in HTPolyNet, it was possible to obtain the system with the desired average side chain length as well as overall star size. In our case, we obtained an average star single chain composed of 1364 atoms, which is related to approximately 71 PVP units with an average mass of 7.9 k, with an average star mass of 24 k. This was achieved by the use of four central units (i.e., four total stars in the system) and a curing parameter set to 98 %.

Additionally, a viscosity of three different NAP-PVP 80:20 *w/w* systems was calculated by evaluating the non-equilibrium cosine acceleration method as implemented in Gromacs. Non-equilibrium runs were performed at the same thermodynamic conditions as the former simulations. Time of the non-equilibrium runs was set to 5 ns. For each system, 3 different acceleration values were used and then the

calculated reciprocal viscosity values were extrapolated to the 0 acceleration in order to obtain viscosity at equilibrium state.

3. Results and discussion

3.1. DSC and XRD data

The first step of our research involved calorimetric measurements. Their purpose was to characterize the thermal properties and phase transitions in neat NAP, PVP polymers, and NAP-PVP binary systems. As shown in Fig. 2a, the DSC curve of neat API measured on heating exhibits only one endothermic process located at T = 431 K, which is associated with the melting process. Upon cooling, the compound immediately crystallized, which is visible in the thermogram as an intense exothermic peak at T = 382 K. These observations clearly show that NAP is a drug with a strong tendency to crystallize, making it a good model active substance for studying the kinetics of API crystallization in binary systems. In turn, the thermograms of the neat PVPs, shown in Fig. S2 in the SM, reveal only the presence of glass transition event at T_g = 434 K (PVP K30), 435 K (*lin*PVP 14 k), 447 K (*lin*PVP38k) and 441 K (*star*PVP).

To study the effect of the topology and chain length of PVP homopolymers on the crystallization tendency of NAP, we prepared BMs with varying amount of the excipient. After many trials, it was determined that NAP mixes with each polymer matrix at a maximum weight ratio of 60:40 using the melt-cooling method. As a result, NAP-PVP 95:5, 90:10, 85:15, 80:20, 70:30, and 60:40 *w/w* systems were selected and subjected to detailed studies (a description of the preparation of BMs can be found in the Materials and Methods section). Preliminary calorimetric measurements conducted on each BM showed that the first three systems (95:5, 90:10, and 85:15 *w/w*) exhibit very similar thermal properties, i.e., they could not be obtained in the glassy form using the standard melt-cooling method. Therefore, results of DSC studies were presented for only NAP-PVP, 90:10 *w/w* mixtures, being representative samples. As can be seen in Fig. 2(c,d) and Fig. S3(a,b) in the SM, API in each 90:10 *w/w* system cannot be vitrified regardless of the type of polymer matrix used. In every case, attempts to prepare amorphous mixtures resulted in immediate recrystallization. Therefore, for these formulations, we observed two thermal events in DSC curves. Specifically, during the heating (ϕ = 10 K/min) of BMs with 10 wt% of the polymer, a strong endothermic transition corresponding to the melting of API in the mixture (T_m) can be observed, while during the cooling, a distinct exothermic peak, attributed to the crystallization process (T_c), is visible. Only for the 80:20 *w/w* systems, it was possible to obtain fully amorphous mixtures, although they showed a relatively strong tendency to crystallization. In Fig. 2b, the compilation of DSC data for all glassy/

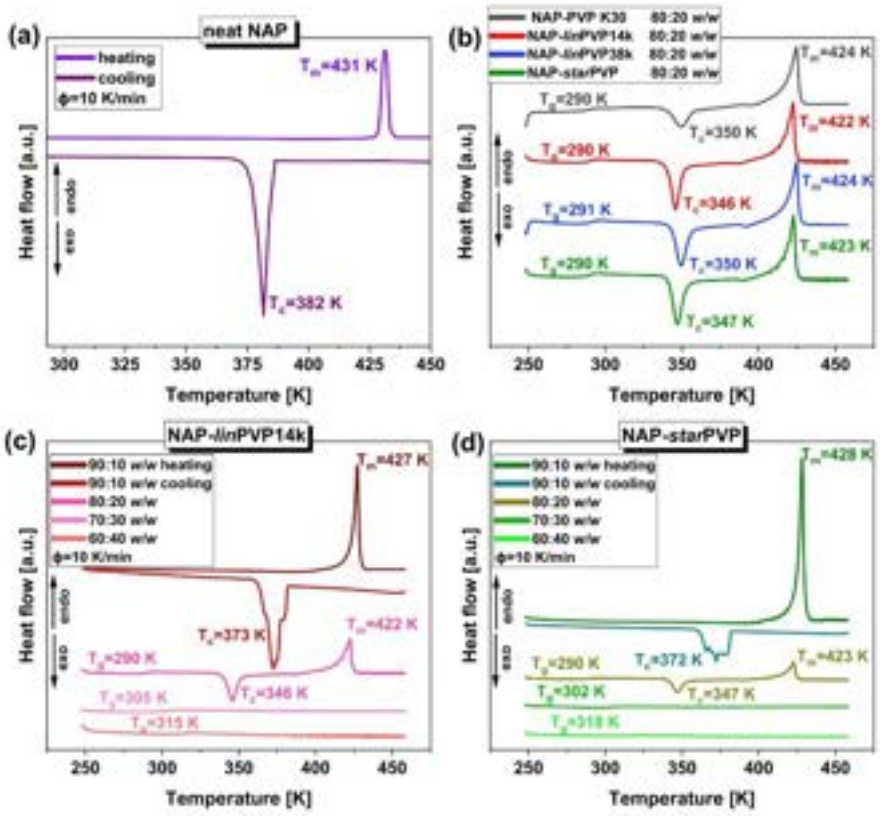

Fig. 2. DSC thermograms (ϕ = 10 K/min) of **(a)** neat NAP and **(b)** NAP-PVP ASDs with the same weight ratio (80:20 *w/w*) of both components, as well as DSC thermograms (ϕ = 10 K/min) of **(c)** NAP-*lin*PVP14k, and **(d)** NAP-*star*PVP mixtures with different weight ratios (90:10, 80:20, 70:30, 60:40 *w/w*). The thermograms for neat NAP and NAP-PVP 90:10 *w/w* systems were collected on heating and subsequent cooling, while the thermograms for other binary systems were collected on heating (after previous heating and cooling). T_g was determined as the midpoint of the heat capacity increment, while T_c and T_m – from the maximum of the exothermic and endothermic events, respectively.

amorphous NAP-PVP 80:20 w/w mixtures is presented. As seen, the thermogram of each sample shows three thermal events. The first, occurring at lower temperatures (T), is assigned to the glass transition phenomenon (T_g ~ 290 K). Additionally, at higher T, there are exothermic and endothermic processes related to the crystallization (T_c ~ 350 K) and melting (T_g ~ 423 K) of NAP, respectively. On the other hand, NAP-PVP 70:30 and 60:40 w/w systems (see Fig. 2**c,d** and Fig. S3**a,b** in the SM) exhibit complete amorphousness and very strong inhibition of the NAP crystallization. For these formulations, the thermograms show only the glass transition (at T_g ~ 302–306 K for 70:30 w/w and T_g ~ 315–322 K for 60:40 w/w BMs), with no signs of recrystallization. It should be mentioned that in Fig. 2**c,d,** and Fig. S3**a,b**, DSC curves measured on heating and subsequent cooling were presented only for the 90:10 w/w systems to clearly indicate that only these mixtures cannot be vitrified (there is an exothermic peak visible on cooling). Similar calorimetric data for the NAP-PVP BMs at other weight ratios: 80:20, 70:30, and 60:40 w/w (the representative ones for API-PVP K30 system are illustrated in Fig. S4 in the SM), show a completely different behavior, i.e., a thermal event related to the glass formation during cooling and subsequent heating. It is also worth noting that for these BMs, the endothermic peak associated with the glass transition/amorphization is observed only at lower T (290–322 K), while at T higher than 430 K, which are close to T_g of neat PVPs, there is no additional endothermic event. This means that fully homogeneous NAP-PVP binary mixtures were obtained, with no signs of phase separation.

The values of T_g and T_m obtained for all investigated BMs are presented as a function of the weight fraction of NAP (X_{NAP}) in Fig. 3. Additionally, they are presented in tabular form together with the values of heat capacity changes at T_g (ΔC_p) and melting enthalpies (ΔH_m) in the SM (see Tables S1 and S2). As expected, it is observed that the lower X_{NAP} (the higher X_{PVP}) in the mixtures, the higher T_g of the system. The obtained DSC data also reveals that depending on the PVP content in the ASD, the T_m s do not change significantly (up to 8 K). Importantly, other publications suggest that distinct differences in the T_m values for BMs are most often associated with different kind or strength of interactions between the API and the polymer.[56,57] Therefore, in the case of NAP-PVP mixtures, it can initially be assumed that regardless of the type of polymer matrix used and its amount, no significant variations in intermolecular interactions between the API and macromolecules are observed. However, to confirm our preliminary assumptions, we conducted infrared studies supported by Molecular Dynamics (MD) simulations, which are detailed in the following sections of the manuscript.

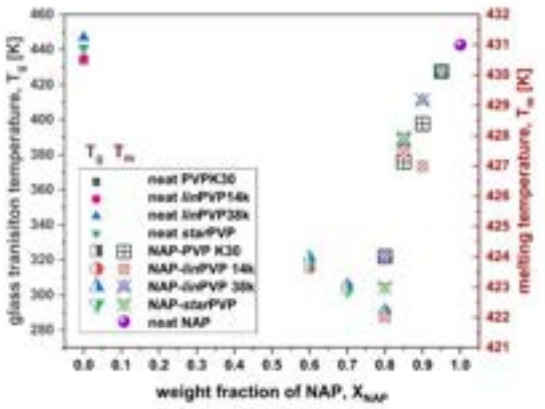

Fig. 3. The dependency of calorimetric T_g and T_m vs. weight fraction of NAP for the examined binary formulations (ϕ = 10 K/min). The left y-axis and the left column of symbols represent T_g values, while the right y-axis and the right column of symbols represent T_m values.

Additionally, keeping in mind that among the studied NAP-PVP BMs, the 80:20 w/w formulations show the possibility of vitrification but also a tendency for relatively rapid recrystallization from the supercooled liquid, we decided to carry out non-isothermal and isothermal DSC measurements to determine the activation energy for the crystallization process of the API in the mixtures with various PVP polymers.

Fig. 4 presents representative DSC curves for freshly prepared NAP-PVP 80:20 w/w BMs. Measurements for these systems were conducted with different ϕ ranging from 5 to 40 K/min. As observed in Fig. 4 **a-d**, each scan shows three thermal events. Aside from the two endothermic peaks occurring at the lowest and highest T (attributed to the glass transition and melting, respectively), there is an exothermic peak corresponding to the crystallization of NAP. The values of T_c for all studied 80:20 w/w BMs are presented in tabular form in the SM (see Table S3). It is evident in Fig. 4 that for each examined NAP-PVP system, as the heating rate increases, the exothermic peak shifts towards higher T (there is an increase in T_c). Conversely, the T_g s and T_m s do not differ significantly and do not show a clear dependence on the change in ϕ. In the analysis of non-isothermal DSC data obtained for all investigated mixtures, the Kissinger approach, which is based on the variation of the crystallization peak temperature (T_c) with ϕ, was used to calculate the activation barrier for the NAP crystallization $E_{cr,non-iso}$ in various ASDs (see Fig. 4**e**):

$$\ln\left(\frac{\phi}{T_c^2}\right) = C_k - \frac{E_{cr,non-iso}}{RT_c} \quad (1)$$

where C_k is a fitting parameter and R is a gas constant.[58]

It should be noted that $E_{cr,non-iso}$ is a kinetic parameter commonly used to describe the crystallization phenomenon. It is defined as the minimum amount of energy required to initiate this process.[59,60].

As can be observed in Fig. 4**e**, the values of $E_{cr,non-iso}$ are very similar for all examined mixtures, ranging from 67 to 77 kJ/mol. The changes in activation barrier for the NAP crystallization can be ordered as follows: $E_{cr(NAP-linPVP38k)} < E_{cr(NAP-starPVP)} < E_{cr(NAP-linPVP14k)} < E_{cr(NAP-PVPK30)}$. Hence, one can conclude that M_n and topology of PVP polymer have only a small impact on $E_{cr,non-iso}$. In the context of NAP, it should be noted that the E_{cr} values we obtained are similar or slightly lower compared to the data reported for BMs of this API with low-molecular-weight excipients, e.g., NAP-acetylated maltose ($E_{cr,non-iso}$ = 64 kJ/mol), NAP-acetylated raffinose ($E_{cr,non-iso}$ = 109 kJ/mol), NAP-acetylated stachyose ($E_{cr,non-iso}$ = 99 kJ/mol) systems.[33] In turn, regarding the systems of other drugs with polyvinylpyrrolidone, similar E_{cr} values were recorded for BMs of metronidazole with different PVPs, 75:25 w/w ($E_{cr,non-iso}$ 65–71.5 kJ/mol).[45] In turn, flutamide-PVP mixtures (90:10 w/w) exhibited significantly higher $E_{cr,non-iso}$(170–200 kJ/mol). [61] It should be emphasized that the discrepancies in $E_{cr,non-iso}$ for various binary formulations most likely result from various concentrations of the API in the examined systems as well as differences in the interactions between the API and the excipient.

In the final stage of the calorimetric studies, we conducted isothermal crystallization measurements at selected T = 314, 317, 319, 321, and 323 K for NAP-PVP 80:20 w/w BMs. It should be mentioned once again that we chose only the system with this composition because it crystallized quickly. In other mixtures, due to the crystallization process being too long, such experiments were not performed. To estimate the time scale necessary for NAP crystallization at each T, the following formula was used in the first step:

$$\alpha = \frac{\Delta H(t)}{\Delta H_{total}} \quad (2)$$

where α is the progress of crystallization, while $\Delta H(t)$ and ΔH_{total} mean the enthalpy variation at different time and the total heat of the crystallization, respectively.

Next, for each studied 80:20 w/w system, we plotted isothermal

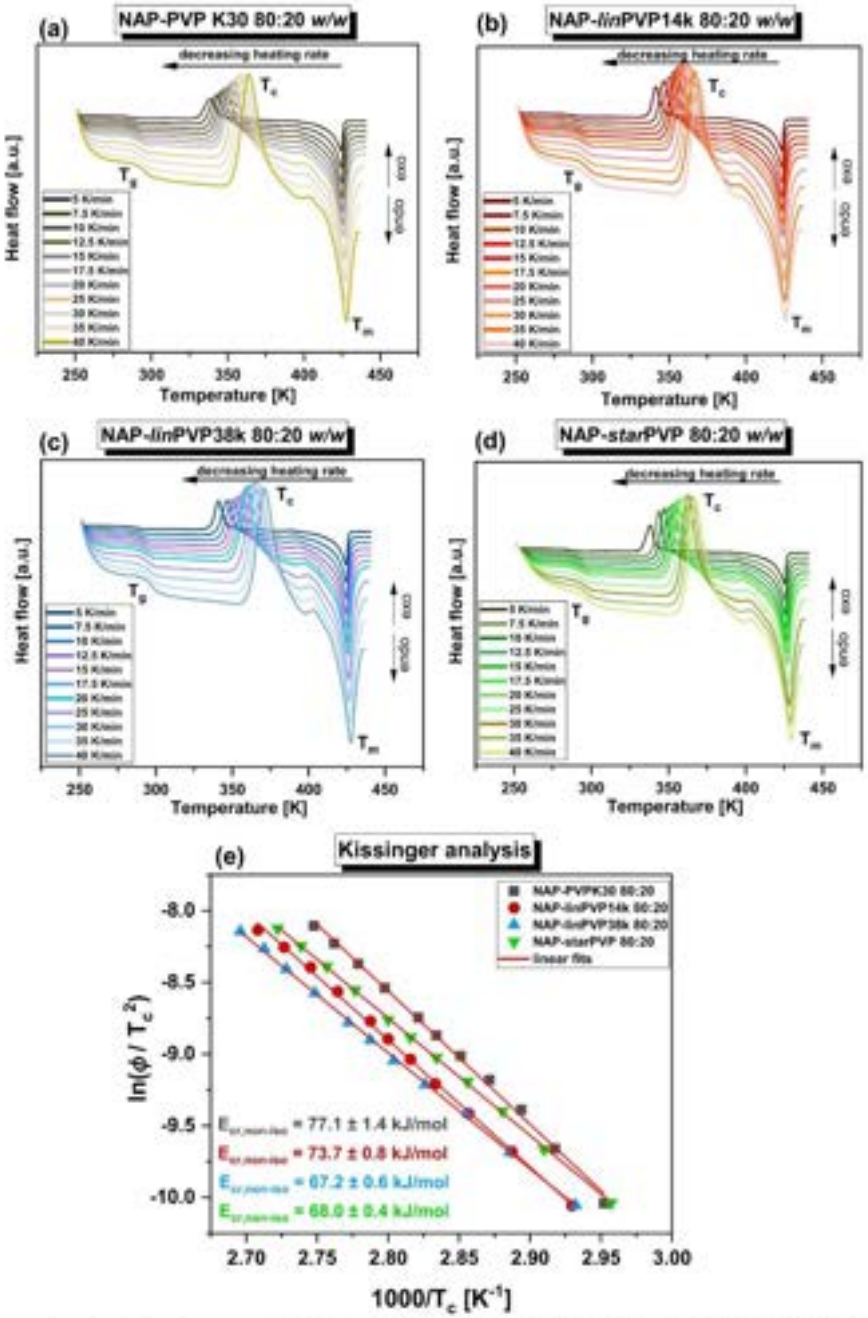

Fig. 4. DSC thermograms for non-isothermal measurements of 80:20 w/w BMs (**a**) NAP-PVP K30, (**b**) NAP-*lin*PVP14k, (**c**) NAP-linPVP38k, (**d**) NAP-*star*PVP, as well as (**e**) Kissinger plots for the exothermic crystallization peaks in the representative NAP-PVP 80:20 w/w systems (the solid red lines represent linear fits). (For interpretation of the references to color in this figure legend, the reader is referred to the web version of this article.)

crystallization kinetics curves (see Fig. 5 **a-d**), which subsequently were described using the Avrami model:

$$\alpha(t) = 1 - \exp(-kt^n) \quad (3)$$

where k is the rate constant of crystallization and n is the Avrami exponent, which is generally assigned to a dimension of growing crystals [62].

As can be seen, for all considered samples, as the temperature increases, the time of API crystallization gradually shortens. This change is most commonly attributed to the temperature gradient ($T - T_r$). [63] Specifically, for the higher tested T (i.e., closest to the value of T_r), the $T - T_r$ value is the smallest, resulting in the fastest crystallization. Conversely, the lowest tested T gives a higher gradient, and a longer time scale is visible due to slower crystallization. Next, to observe the effect of the polymer matrix on the crystallization time scale, the isotherms for each examined NAP-PVP 80:20 w/w systems obtained at 314 K (close to the T_g) were compared. It can be clearly observed in Fig. 5**e** that *lin*PVP38k most strongly inhibits drug crystallization, while NAP in the mixtures with the other three matrices (K30, *lin*PVP14k, *star*PVP) shows a fairly similar crystallization time scale. From this finding, we can deduce that the star-shaped PVP polymer affects the crystallization behavior of NAP similarly to the linear polymer with a length corresponding to one arm of the star polymer. What is really interesting, commercially available PVP (despite having an average M_n of around 40 000) does not show similarity to its self-synthetized counterpart (*lin*PVP38k) but inhibits API crystallization on a similar time scale to *lin*PVP14k and *star*PVP. The most likely cause of this observation is the high dispersity of PVP K30 compared to the self-synthesized macromolecules. This means that commercial PVP has a wide distribution of chain molecular weights – in other words, it contains both low- and high-molecular-weight fractions. Hence, the presence of low-M_n fractions in the polymer matrices determines the crystallization rate of NAP in drug-polymer formulations. That is why there is no significant difference in the rate of crystallization between commercial PVP and *lin*PVP14k.

Next, based on the results of isothermal measurements, the half-times ($t_{1/2}$) of NAP crystallization ($t_{1/2}$ is the time required to reach 50 % of the final crystallinity) in the 80:20 w/w mixtures were determined. The values of $t_{1/2}$ plotted as a function of T are illustrated in Fig. 6**a**. As expected, at the lowest T (314 K), the half-time of NAP crystallization in all systems are the longest. However, as the T increases, $t_{1/2}$ progressively decreases, and the differences between the BMs with different polymer matrices become smaller.

Additionally, the Avrami equation was used to describe the data presented in Fig. 5 and calculate the constant rates of crystallization (k). The logarithm of k was further plotted *vs.* reciprocal T in Fig. 6**b** to evaluate the activation energies for isothermal crystallization of NAP ($E_{cr,iso}$) in the examined binary systems from the Arrhenius equation:

$$\ln(k) = \ln(k_0) - \frac{E_{cr,iso}}{RT} \quad (4)$$

Subsequently, determined $E_{cr,iso}$s were compared in Fig. 6**c** with the activation barriers obtained from non-isothermal measurements ($E_{cr,non-iso}$). As seen, values of $E_{cr,iso}$ and $E_{cr,non-iso}$ differ significantly. It is important to emphasize that observing such behavior is entirely natural because the crystallization under isothermal and non-isothermal conditions have different contributions of the energy barriers related to nucleation and crystal growth. As it is commonly known, crystallization is a typical first-order phase transition consisting of two main steps: (i) nucleation (the formation of crystalline nuclei) and (ii) crystal growth (the increase in size of crystallites).[64,65] However, non-isothermal conditions can affect both steps in a different way than isothermal conditions. More precisely, under isothermal conditions, the crystallization process is observed over time at a constant T, allowing for the slow, time-dependent development of nucleation sites and subsequent crystal growth. This can lead to encountering and measuring higher energy barriers. In contrast, non-isothermal conditions, with continuous temperature changes, can probe mainly crystal growth, reducing the observed activation energy. Therefore, it is often assumed that $E_{cr,non-iso}$ delivers information primarily about crystal growth – hence the lower values of this energy barrier. In contrast, isothermal crystallization provides information both about crystal growth and nucleation – hence the higher $E_{cr,iso}$ values.[66–69] Thus, the observed more than twofold increase in activation energy for the NAP crystallization is likely related to the significant energy barrier of the nucleation stage in isothermal measurements.

It should also be added that the values of $E_{cr,iso}$ determined for studied NAP-PVP systems vary in the range of 202 kJ/mol (NAP-*lin*PVP14k) to 266 kJ/mol (NAP-*star*PVP). Nearly the same $E_{cr,iso}$ (~260 kJ/mol) was obtained for BMs of NAP with *star*PVP and *lin*PVP38k, Fig. 6**b**. On this basis, it can be concluded that as in the case of $E_{cr,non-iso}$, $E_{cr,iso}$ values are very similar and depend only slightly on the polymer topology. The impact of M_n of PVP on $E_{cr,iso}$ is somewhat greater.

To summarize this part of the studies, the DSC experiments demonstrated that the polymer structure plays a significant role in the effective stabilization of NAP in the amorphous form. It was established that the self-synthesized PVP with linear topology (*lin*PVP38k), characterized by slightly lower M_n with respect to PVP K30 but relatively uniform chain lengths (low Đ), most effectively inhibits API crystallization around the T_g. It was also shown that the star-shaped PVP has a similar effect on the NAP isothermal crystallization as its linear arm counterparts (*lin*PVP14k). Moreover, commercially available PVP exhibits similar effectiveness in suppressing API crystallization as *lin*PVP14k and *star*PVP. It can be explained by the high dispersity of PVP K30 and the corresponding presence of low-molecular-weight fractions, which determine the time scale of the API recrystallization process.

To elucidate whether some slight differences in activation energies for crystallization of NAP from BMs are actually due to the topology/M_n of PVP, not the formation of different polymorphs of this API, further X-ray diffraction studies were performed. In Fig. S5 in the SM, the XRD patterns for neat crystalline NAP and PVP polymers are presented. In turn, Fig. S6 in the SM shows the XRD patterns for various NAP-PVP BMs (strictly the results of the long-term physical stability studies of these systems). The diffraction data clearly indicate that all NAP-PVP 80:20 w/w BMs were amorphous just after the preparation but recrystallized after 16 days of storage at 298 K to the same polymorphic form of NAP, regardless of the type of PVP matrix used (Fig. S6**a**). The identified polymorphic form 1, according to the nomenclature used in Ref. [30], turned out to be the same as of the initial commercial NAP powder (Fig. S5). Hence, it can be stated that the observed differences in activation barriers (both $E_{cr,non-iso}$ and $E_{cr,iso}$, Fig. 6**c**) for all examined NAP-PVP systems are rather due to the topology/or molecular weight of the polymer used. In turn, the BMs with lower content of NAP – 70:30 and 60:40 w/w did not recrystallize 15 and even 30 days after the preparation (Fig. S6**b and c**), indicating they are more physically stable than the BMs with 80:20 w/w composition.

3.2. FTIR data

As mentioned in the subsection describing DSC data, the lack of significant differences in T_g for binary systems of NAP with various PVPs initially suggested that there is a similar type of intermolecular interactions between the API and all the polymer matrices used. To verify these suppositions, detailed studies using the FTIR technique were conducted.

In the first step of the spectroscopic studies, the neat active substance was analyzed in both crystalline and molten states. Fig. S7 in the SM presents the FTIR spectrum of crystalline NAP with band assignments and its comparison with the molten NAP. Subsequently, infrared spectra were recorded for neat polymer matrices, see Fig. S8. As is widely

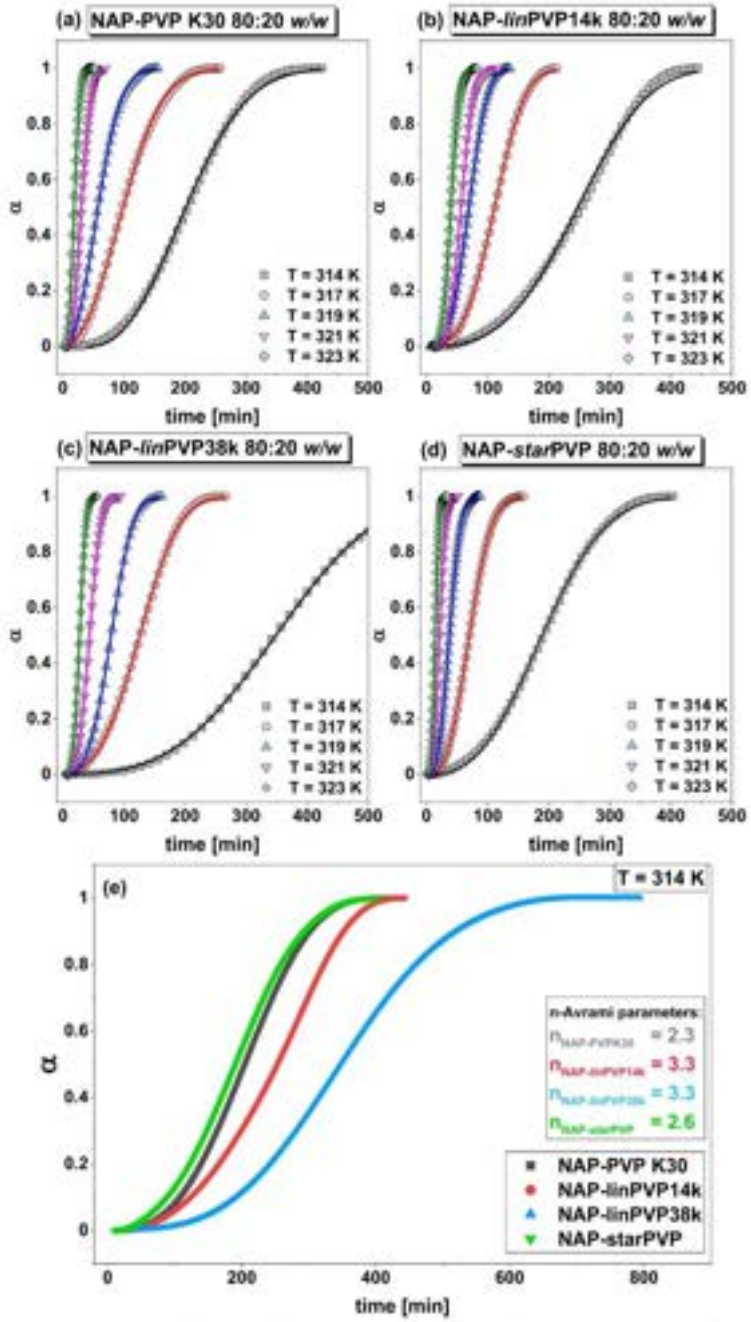

Fig. 5. The progress of the crystallization process for the examined NAP-PVP 80:20 w/w systems: **(a)** NAP-PVP K30; **(b)** NAP-linPVP14k; **(c)** NAP-linPVP38k; **(d)** NAP-starPVP. Solid lines represent Avrami fits. **(e)** A comparison of the progress of the crystallization process for all tested 80:20 w/w mixtures at a measurement temperature of 314 K. In the figure, the values of the Avrami exponent (n) are also provided.

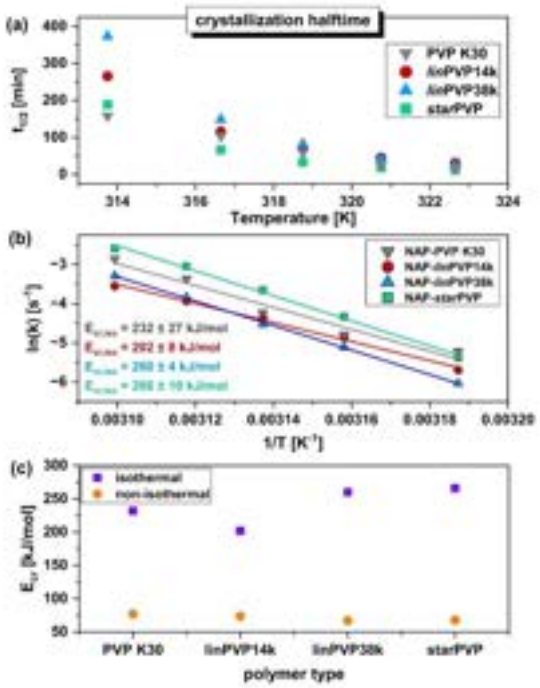

Fig. 6. (a) Isothermal crystallization half-time ($t_{0.5}$) of NAP-PVP 80:20 w/w mixtures as a function of isothermal temperatures; (b) Plot of ln(*k*) against 1/*T*, which allowed determining the activation energy of isothermal crystallization process (the solid lines represent linear fits); (c) E_a s of the NAP crystallization depending on the applied PVP in BMs, obtained from isothermal and non-isothermal measurements.

known, PVP is a highly hygroscopic compound, which means that binary mixtures containing this polymer can be challenging to interpret using FT-IR spectroscopy due to water absorption, which disturbs the spectral regions around 1650 and 3400 cm^{-1}. However, a detailed discussion of this aspect, along with a description of the water content control in the samples, is provided in the SM, please see also Fig. S9.

Next, we conducted FTIR measurements on binary formulations composed of the API and PVPs with different topologies. Fig. 7 presents the infrared spectra of NAP-PVP (PVP K30, *lin*PVP14k, *lin*PVP 38 k, and *star*PVP) BMs at 60:40 w/w, measured in the supercooled liquid/glassy states. The spectra of NAP-PVP formulations at other weight ratios, 70:30 and 80:20 w/w, are shown in Fig. S10 in the SM. For comparison, the spectrum of molten NAP (due to the inability to obtain it in the amorphous form *via* vitrification) is also presented in both figures. As illustrated, the spectra recorded in two wavenumber regions, 3700–2400 cm^{-1} and 1800–400 cm^{-1}, for the systems with the same content of API and PVP (Fig. 7 and Fig. S10), are very similar to each other, suggesting no substantial influence of polymer topology on the crystallization behavior of NAP. Additionally, it can be noted that the amorphous API-PVP 60:40 w/w BMs were stable even for four months after preparation (see Fig. S11 in the SM). In contrast, the stability of all NAP-PVP 80:20 w/w mixtures was relatively poor, since IR spectra indicated the recrystallization of API after 16 days of storage (note also that NAP-PVP 90:10 w/w systems recrystallized immediately after vitrification – see Fig. S12 in the SM, which agrees with DSC data). It is well seen in Fig. 8 that NAP in all 80:20 w/w BMs recrystallized to the same crystalline form as NAP in a commercial sample despite the different PVP topologies, which is in accordance with the outcomes of XRD studies.

To determine the factors responsible for the stability/instability of the examined BMs, the FTIR spectra of amorphous NAP-PVP systems with different amount of each polymer were compared. It was found that these spectra are not just a sum/an accumulation of the individual amorphous components, and significant differences between the mixtures can be identified in the two spectral ranges: 3700–3100 cm^{-1} and 1800–1520 cm^{-1}. The representative IR spectra of NAP-*star*PVP, 80:20, 70:30, and 60:40 w/w systems are shown in Fig. S13 in the SM file and Fig. 9. The higher wavenumber region is attributed to the stretching vibrations of the OH groups of NAP molecules as well as the OH groups originating from water adsorbed into the polymer, whereas the lower wavenumber corresponds to the stretching vibrations of the C = O and C = C groups of NAP and the C = O moieties of *star*PVP. Thus, both regions partially overlap and essentially pertain to groups that can engage in H-bonding interactions. As illustrated in Fig. S13, as the concentration of *star*PVP increases in the mixture, the intensity of the ν_{OH} band located in the range of 3400–3100 cm^{-1} decreases (highlighted in blue) and that at 3600–3400 cm^{-1} increases (highlighted in red) compared to the same band in neat molten API. It can be mentioned that NAP molecules exist as H-bonded dimers in the liquid phase, as referenced in the literature. [70] Thus, the changes of the band intensities in these spectral regions due to a higher amount of *star*PVP may suggest the reduction of H-bonded dimers (3400–3100 cm^{-1}) and the increase of non-H-bonded OH groups of NAP or their participation in the generation of weak H-bonds with carbonyl groups of API or polymer.

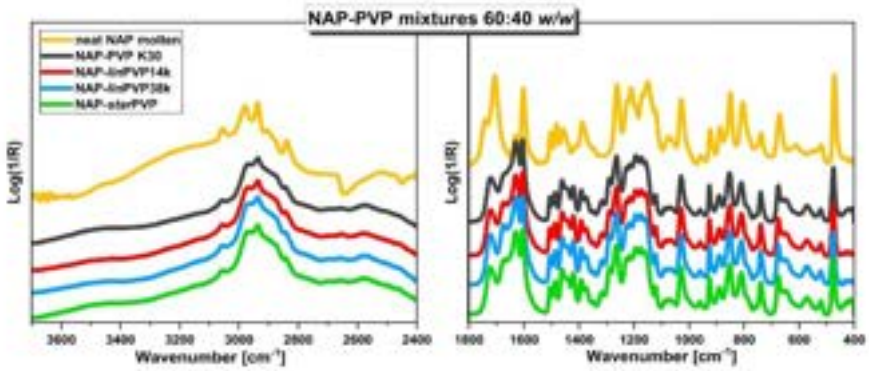

Fig. 7. FTIR spectra of binary mixtures containing NAP and PVP of different topologies at 60:40 w/w, measured in the supercooled liquid/or glassy states, and that of neat molten NAP.

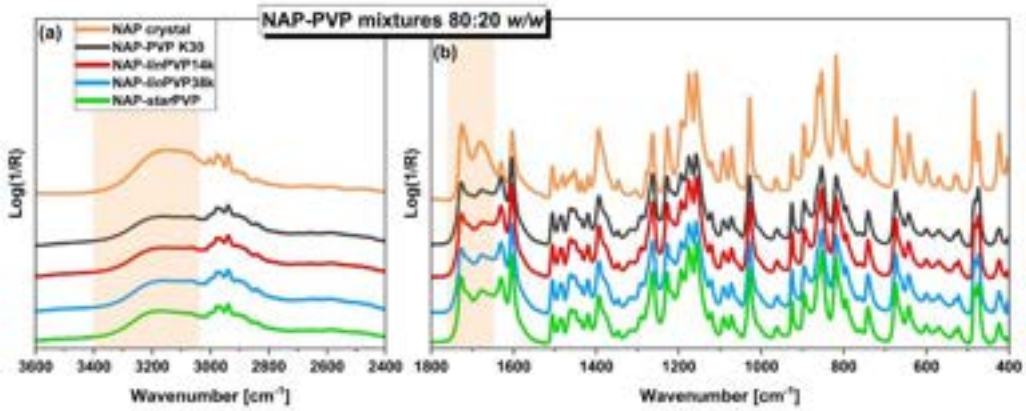

Fig. 8. FTIR spectra of NAP-PVP 80:20 w/w binary systems: NAP-PVP K30, NAP-linPVP 14 k, NAP-linPVP38k, and NAP-*star*PVP, measured after recrystallization in two wavenumber ranges of **(a)** 3600–2400 and **(b)** 1800–400 cm^{-1}. The spectrum of neat crystalline API was drawn for comparison.

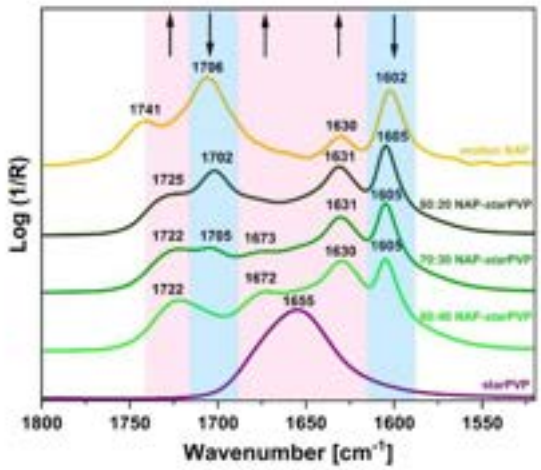

Fig. 9. FTIR spectra of amorphous NAP-*star*PVP BMs with different weight ratios, measured in the region 1800–1520 cm^{-1}. The spectra of molten NAP and neat *star*PVP were also drawn for comparison. An increase in peak intensity as the concentration of *star*PVP increases in the mixture is highlighted in red and a decrease in blue, respectively. (For interpretation of the references to color in this figure legend, the reader is referred to the web version of this article.)

Much more intriguing spectral changes are observed in the range 1800–1520 cm^{-1}, in which the bands assigned to the C = O stretching vibrations of NAP (1741 cm^{-1}, 1706 cm^{-1}) and *star*PVP (1655 cm^{-1}) as well as the C = C stretching vibrations of NAP (1630 and 1602 cm^{-1}) occur (Fig. 9). It can be noted that the $\nu_{C=O}$ band of molten NAP consists of two peaks: the high-wavenumber one due to the stretching vibration of the non-H-bonded (free) C = O groups and the low- wavenumber component assigned to the stretching vibration of the H-bonded C = O moieties.[71] At first glance, it can be seen that the intensity of peaks located at ca. 1720 and 1630 cm^{-1} grows with increasing polymer content in the mixture. Meanwhile, there is a reduction in the intensity of signals at 1700 and 1600 cm^{-1}, and the weak peak at 1670 cm^{-1} appears. However, it should be mentioned that the peak of PVP carbonyl vibrations ($\nu_{C=O}$) may coincide with that of the C = O and C = C of NAP, making it difficult to study. For this reason, we have decided to subtract this band from the spectra of BMs. As illustrated in Fig. S14, after performing this procedure, the changes in FTIR spectra of BMs with different PVP content are much more visible. Moreover, one can observe the growth in the peak intensities located at 1722 and 1630 cm^{-1} and the diminution of signal intensities at 1702 and 1605 cm^{-1}. These results clearly indicate that at low PVP concentration (80:20 w/w), NAP occurs as a combination of dimers (1702 cm^{-1}) and non-H bonded O–H units (1722 cm^{-1}). More precisely, the peak at 1722 cm^{-1} is assigned to the non-H-bonded carbonyl stretch of the acid group of a NAP molecule, which is H-bonded through the hydroxyl group to a PVP molecule. A similar peak position of the C = O group of carboxylic acid (1726 cm^{-1}) was reported for NAP-PVP K25 [71] and indomethacin-PVP systems. [72] On the other hand, the peak position of H-bonded PVP carbonyl in the referenced mixture was 1636 cm^{-1}. In the case of NAP-PVP systems, it can be assumed that some part of the $\nu_{C=O}$ PVP band may shift towards a lower wavenumber due to the formation of H-bonds with hydroxyl groups of NAP. This fact may be confirmed by the intensity growth as well as the broadening in the signal width located at 1630 cm^{-1}. Moreover, the appearance of ca. 20 cm^{-1} shift in the vibrational frequency of C = O groups of NAP (1680 cm^{-1}) reflects the association of carboxyl groups in other kinds of H-bonded aggregates rather than dimers in the mixtures. It should be noted that BMs of NAP with other PVPs, i.e., PVP K30, linPVP14k, and linPVP38k, exhibit the same spectral effects after the addition of polymer to API, as in the case of NAP-*star*PVP, see Fig. S15. Therefore, the intensities of peaks located at ca. 1720, 1675, and 1630 cm^{-1} increase with increasing PVP amount, whereas those at ca. 1705 and 1605 cm^{-1} decrease. This suggests that the mechanism of intermolecular interactions between NAP and PVP in the examined BMs with varying content of the excipient is independent of the polymer architecture (linear or branched).

The above-mentioned findings clearly indicate that the addition of PVP to molten NAP results in the degradation/destruction of NAP dimers (the higher the PVP concentration, the fewer NAP dimers, and the more H-bonding interactions between NAP and PVP). As a result, the combination of different structural units in the studied BMs occurs, i.e., the free OH groups, the free C = O groups of NAP and PVP, the H-bonded dimers of NAP, the H-bonding aggregates with another arrangement of NAP molecules, and the H-bonded aggregates of NAP and PVP. Furthermore, noticeable differences in intermolecular interactions between API and macromolecules are observed depending on the polymer content (60:40, 70:30, and 80:20 w/w), regardless of its topology (linear or star-shaped). Thus, based on the results of FTIR studies, one can conclude that the stability of NAP-PVP mixtures is mainly associated with the formation of H-bonds between API and PVP molecules as PVP

may influence the crystallization kinetics by preventing the self-association of NAP molecules. Combining various kinds of H-bonds better stabilizes the API-polymer systems; thus, it is not surprising that the amorphous systems with higher concentrations of PVP inhibiting the crystallization of NAP (70:30 and 60:40 w/w) are more stable.

3.3. Molecular dynamics (MD) simulations

After conducting XRD and FTIR studies, which showed that (i) NAP crystallizes into the same polymorphic form in each mixture, and (ii) there are no significant differences in intermolecular interactions between API and excipient in BMs composed of NAP and PVPs with various architectures/topologies, we decided to undertake complementary MD simulations.

The seven various binary formulations have been simulated, i.e.: NAP bulk system, two short-chain systems (equivalent to NAP-*lin*PVP14k mixtures), two long-chain systems (equivalent to NAP-*lin*PVP38k mixtures), and two star systems (equivalent to NAP-*star*PVP mixtures) in 60:40 and 80:20 *w/w*. Previous experimental studies indicated considerable differences in the crystallization tendency between NAP-PVP BMs, prepared in both mentioned weight ratios. All 80:20 *w/w* mixtures were fully crystalline after 16 days of storage at ambient *T*, while 60:40 *w/w* systems were amorphous even after four months of storage. To explain this phenomenon, we have compared MD simulations of two types of mixtures containing *lin*PVP38k and *lin*PVP14k. Fig. 10 shows the 2D density plots in the xy dimensions for both NAP-PVP systems with different content of API and polymer (80:20 and 60:40 *w/w*). In panels b and d of this figure, which presents the data for 80:20 *w/w* mixtures, the phase separation is well visible. There is a central area, approximately 6x6 nm in size, where the polymers are concentrated and NAP is separated to the box borders. In the 60:40 *w/w* systems, NAP-NAP large cluster formation is effectively suppressed by the polymer network, while in the 80:20 *w/ w* mixtures, it is no longer possible. To look closely at the NAP-NAP clusters, H-bonds (HBs) were analyzed in both binary formulations, see Fig. 11. One can observe that in the NAP-PVP 60:40 *w/w* BMs, the number of H-bonds between API molecules is reduced by more than 50 %, while in the 80:20 *w/w* mixtures, it is reduced by approximately 10 %. On the other hand, in the 60:40 *w/w* system, extensive HBs are formed between NAP and PVP. The amount of HBs between NAP and *lin*PVP38k exceeds even the number of HBs in neat NAP. This effect is not visible for the 80:20 *w/w* mixtures, where NAP-PVP HBs constitute only about 20 % of all HBs in the systems. The NAP-NAP H-bonds can be viewed as a crucial parameter indicating the crystallization ability of API as it is related to the formation of larger NAP clusters. This analysis explains the results of experimental considerations, i.e., the tendency of the examined API to this phase transition in the 80:20 *w/w* binary system.

Moreover, as illustrated in Fig. 11, in the case of both NAP-PVP 80:20

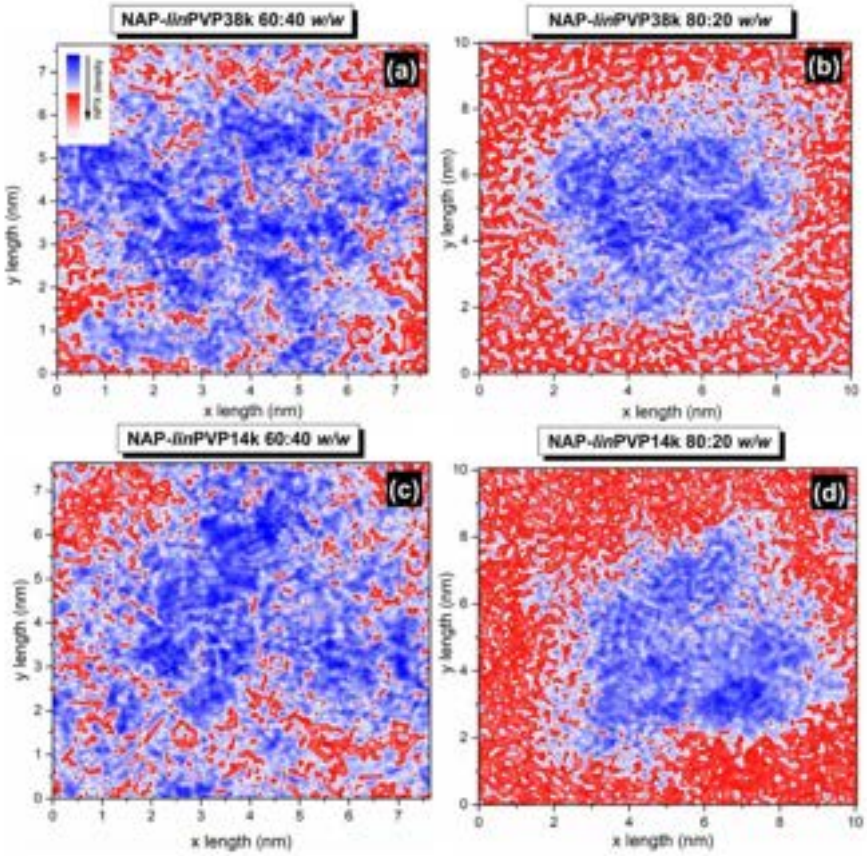

Fig. 10. The 2D density plots of examined NAP-PVP mixtures. The density of NAP is covered by the red color. In panels **(b)** and **(d)** for 80:20 *w/w* BMs, the NAP segregation is evident. (For interpretation of the references to color in this figure legend, the reader is referred to the web version of this article.)

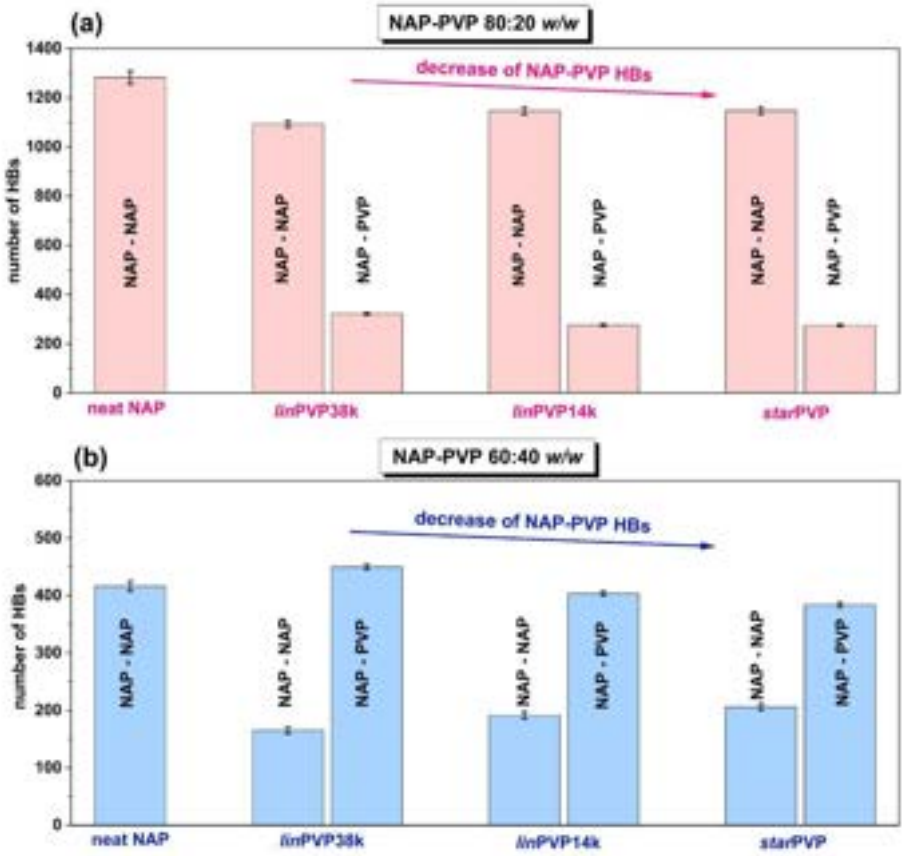

Fig. 11. The diagrams representing the number of H-bonds (HBs) for all studied NAP-PVP systems, prepared in two weight ratios: **(a)** 80:20 and **(b)** 60:40 w/w.

and 60:40 w/w BMs systems, some differences in the intermolecular interactions depending on the type of PVP polymer in the mixture, can be observed. Note that previous DSC studies revealed differences between isothermal crystallization rates in the 80:20 w/w mixture containing PVPs with various topologies and lengths. The crystallization process at $T = 314$ K was the slowest for the long-chain system (*lin*PVP38k) and the fastest for the branched system (*star*PVP). As HBs have a major impact on the crystallization phenomenon, we analyzed the H-bond numbers in the mixtures of NAP with different PVPs (Fig. 11). It was found that the amount of HBs between NAP molecules in 80:20 w/w (and also 60:40 w/w) mixtures rises in the line from *lin*PVP38k to *star*PVP (*lin*PVP38k < *lin*PVP14k < *star*PVP). On the other hand, the amount of NAP-PVP HBs increases in the reverse order, i.e., from *star*PVP to *lin*PVP38k. Although the observed variations in HBs are not large, they can explain the different crystallization behavior in BMs of NAP with PVPs of different topologies and M_w.

In Fig. 12, NAP partial density fluctuations (a difference between actual and average density) are presented in the one dimension of the simulation box for the 60:40 w/w mixtures. As can be seen, for the long chain (*lin*PVP38k) system, the differences are small, up to 0.15 g/cm^3, while for two other systems, they can be twice as high, up to 0.30 g/cm^3. It means that for the 60:40 w/w BMs, the mixture with *lin*PVP38k has higher homogeneity compared to those with *lin*PVP14k and *star*PVP. This fact together with the analysis of H-bond number show that the long chains with the highest average mass (*lin*PVP38k) are the best for the stabilization of NAP in the amorphous phase. Therefore, NAP should exhibit the smallest crystallization tendency from the BM composed of *lin*PVP38k with respect to the other studied polymers. On the other hand, both *star*PVP and *lin*PVP14k should be less effective in suppressing the crystallization of API at the same thermodynamic conditions during long-term storage. This result is consistent with the outcome of isothermal crystallization studies carried out around the T_g for 80:20 w/w systems. Unfortunately, we were not able to verify experimentally if the same conclusions may be applied to other BMs (with higher polymer content) since they did not reveal any crystallization tendency over one month of storage at room temperature.

Furthermore, all the simulation data indicated that the dynamics of *star*PVP is closer to the *lin*PVP14k than to the *lin*PVP38k. It means that the dynamics of the branched polymer, which has the highest average mass from all studied self-synthetized systems, reflects the dynamics of short chains (*lin*PVP14k) with a mass comparable to the one arm of the star polymer.

Additionally, keeping in mind that the crystallization of APIs depends on the viscosity of BMs, we performed further simulations to calculate this physical quantity for NAP-PVP 80:20 w/w systems at 314 K. The analysis of the obtained data showed that NAP-*star*PVP and NAP-*lin*PVP38k mixtures are characterized by a viscosity of around 4.2 ± 0.5 and 4.5 ± 0.5 Pa·s, respectively. On the other hand, the NAP-*lin*PVP14k system has a lower viscosity, i.e., 1.1 ± 0.1 Pa·s. Hence, computations indicated that the viscosity of the studied systems close to the T_g is

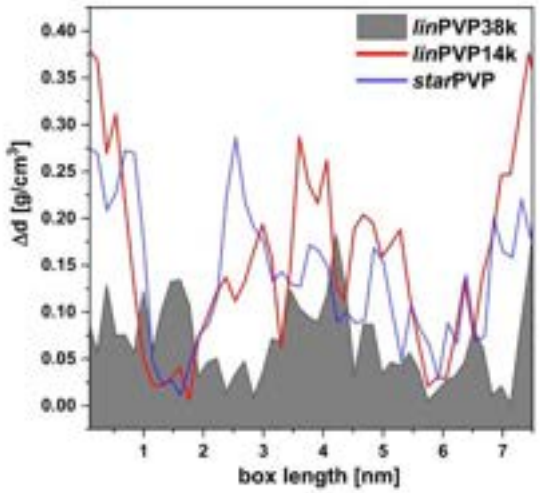

Fig. 12. NAP partial density fluctuation in three NAP-PVP 60:40 w/w systems. Density fluctuation is defined as absolute value from difference between actual and average density.

similar. This finding agrees with the experimental calorimetric data that demonstrated similar T_g of binary mixtures. Consequently, in the vicinity of the T_g, solid dispersions of the same API concentration should have similar viscosities irrespective of the polymer topology. Nevertheless, MD simulations revealed an interesting issue. If the NAP crystallization was governed by the viscosity of the system, the BM containing *lin*PVP14k should crystallize faster compared to the BM with *star*PVP macromolecule. Meanwhile, the isothermal DSC experiments showed a different scenario, i.e., the faster crystallization of NAP in the mixture with *star*PVP than in the system with *lin*PVP14k or *lin*PVP38k. Such observations indicate that the crystallization process is more affected by the polymers' topology than by the system's viscosity. Hence, one can state that the molecular architecture of the polymers used to produce binary formulations plays a key role in inhibiting NAP crystallization.

4. Conclusions

In this article, amorphous BMs composed of NAP and four PVP homopolymers (with linear and star topologies) using DSC, XRD, and FTIR methods were investigated. Three of the matrices used (PVP K30, *lin*PVP38k, and *star*PVP) had similar M_n (~40 000), while M_n of the fourth one (*lin*PVP14k) was close to M_n of one arm of the star polymer (M_n ~ 14 000). Such selection of macromolecules allowed us to thoroughly examine the impact of topology, molecular mass, and dispersity of PVPs on the crystallization kinetics of NAP. In the first step of the study, it was determined that NAP mixes with each polymer matrix in a maximum weight ratio of 60:40 – hence, the following API-PVP systems were selected for the investigations: 95:5, 90:10, 85:15, 80:20, 70:30, and 60:40 w/w. Detailed isothermal DSC studies of the 80:20 w/w BMs allowed us to determine that among the tested polymers, *lin*PVP38k most effectively slows down the crystallization of NAP, while the other three matrices exhibit a similar, weaker ability to inhibit this process. The obtained results also revealed that *star*PVP shows very similar crystallization inhibition effectiveness to the linear PVP with M_n corresponding to one arm of the star polymer. XRD studies indicated that regardless of the topology/M_n of the macromolecule used, NAP crystallizes into the same polymorphic form. Unfortunately, due to the rapid crystallization of the 80:20 w/w systems, it was not possible to determine using this technique, which macromolecule most effectively inhibits the crystallization of the API. However, long-term structural studies showed that the 60:40 w/w mixtures are the most stable (they were amorphous even after a month of storage). Infrared studies revealed clear spectral differences for each NAP-PVP mixture characterized by different polymer content. In turn, the variations between the spectra depending on M_n and the topology of PVP used were very subtle, suggesting no significant differences in the intermolecular interactions between the drug and individual macromolecules. Based on the FTIR results, it was determined that the greatest (even four-month) stability of the 60:40 w/w NAP-PVP mixtures is mainly due to the formation of H-bonds between the API and PVP molecules, as the high polymer content prevents the self-association of NAP molecules, thus significantly affecting the crystallization kinetics. In the final step of the study, MD simulations performed for neat NAP system and 80:20 and 60:40 w/w mixtures of API with various PVPs confirmed the outcomes of infrared studies – i.e., the more PVP used, the more NAP-PVP H-bonding interactions and fewer H-bonded NAP-NAP dimers; consequently, a higher stability of ASDs with a greater amount of the polymer. Additionally, they showed slight differences in the H-bonding interactions depending on the type of PVP polymer in the BM, as well as the greatest homogeneity of the NAP-*lin*PVP38k system, explaining the most effective inhibition of the API crystallization by the polymer with M_n similar to M_n of a commercial PVP, but relatively uniform chain lengths, i.e., low dispersity (which was also deduced from DSC data analysis). Thus, it should be noted that the outcomes of theoretical calculations were in good agreement with the results of experimental studies. The obtained data can be considered extremely crucial from the perspective of designing new pharmaceutical formulations containing polymers with well-defined macromolecular parameters and architecture.

CRediT authorship contribution statement

Luiza Orszulak: Writing – original draft, Writing – review & editing, Visualization, Methodology, Investigation, Funding acquisition, Formal analysis, Conceptualization. **Patryk Włodarczyk:** Investigation, Formal analysis. **Barbara Hachuła:** Investigation. **Taoufik Lamrani:** Investigation. **Karolina Jurkiewicz:** Investigation. **Magdalena Tarnacka:** Investigation. **Marek Hreczka:** Investigation. **Kamil Kamiński:** Supervision, Project administration. **Ewa Kamińska:** Writing – original draft, Writing – review & editing, Funding acquisition, Conceptualization.

Declaration of competing interest

The authors declare that they have no known competing financial interests or personal relationships that could have appeared to influence the work reported in this paper.

Acknowledgment

L.O. is thankful for financial support from the Ministry of Education and Science (Poland) within the Pearls of Science grant (No. PN/01/0078/2022). This research was funded in part by the National Science Centre (Poland), Grant Opus 21 (No. 2021/41/B/NZ7/01654). For the purpose of Open Access, the author has applied a CC-BY public copyright license to any Author Accepted Manuscript (AAM) version arising from this submission.

Appendix A. Supplementary material

Supplementary data to this article can be found online at https://doi.org/10.1016/j.ejpb.2024.114581.

Data availability

Data will be made available on request.

References

[1] D. Sun, W. Gao, H. Hu, S. Zhou, Why 90% of clinical drug development fails and how to improve it? Acta Pharm. Sin. B 12 (2022) 3049–3062, https://doi.org/10.1016/j.apsb.2022.02.002.

[2] S. Abbasi, H. Higashino, Y. Sato, K. Mizumi, M. Kataoka, S. Yamashita, H. Harashima, Maximizing the oral bioavailability of poorly water-soluble drugs using novel oil like materials in lipid based formulations, Mol. Pharm. 18 (2021) 3281–3289, https://doi.org/10.1021/acs.molpharmaceut.1c00197.

[3] D. Hasa, B. Perissutti, C. Cepek, S. Bhardwaj, E. Carlino, M. Grassi, S. Invernizzi, D. Voinovich, Drug salt formation via mechanochemistry: The case study of vinpocetine, Mol. Pharm. 10 (2013) 211–224, https://doi.org/10.1021/mp300371f.

[4] E. Reverchon, R. Adami, F. Campardelli, G. Della Porta, I. De Marco, M. Scognamiglio, Supercritical fluids based techniques to process pharmaceutical products difficult to micronize: Palmitoylethanolamide, J. Supercrit. Fluids 102 (2015) 24–31, https://doi.org/10.1016/j.supflu.2015.04.005.

[5] K. Laitinen, K. Löbmann, C.J. Strachan, H. Grohganz, T. Rades, Emerging trends in the stabilization of amorphous drugs, Int. J. Pharm. 453 (2013) 65–79. https://doi.org/10.1016/j.ijpharm.2012.04.066.

[6] N.A. Vasilev, A.O. Surov, A.P. Voronin, K.V. Drozd, G.L. Perlovich, Novel cocrystals of itraconazole: Insights from phase diagrams, formation thermodynamics and solubility, Int. J. Pharm. 599 (2021) 120441, https://doi.org/10.1016/j.ijpharm.2021.120441.

[7] K.L. Yeh, T. Lee, Intensified crystallization processes for 1:1 Drug-drug cocrystals of sulfadiazine theophylline, and sulfathiazole sulfanilamide, Cryst. Growth Des. 18 (2018) 1339–1349, https://doi.org/10.1021/acs.cgd.7b01197.

[8] D.A. Snider, W. Addicks, W. Owens, Polymorphism in generic drug product development, Adv. Drug Deliv. Rev. 56 (2004) 391–395, https://doi.org/10.1016/j.addr.2003.10.010.

[9] Y. He, C. Ho, Amorphous solid dispersions: Utilization and challenges in drug discovery and development, J. Pharm. Sci. 104 (2015) 3237–3258, https://doi.org/10.1002/jps.24541.

[10] M. Rams-Baron, R. Jachowicz, E. Boldyreva, D. Zhou, W. Jamroz, M. Paluch, Amorphous drugs: Benefits and challenges, 2018. https://doi.org/10.1007/978-3-319-72002-9.

[11] K. Kaveshani, M.J. Pikal, Calorimetric investigation of the structural relaxation of amorphous materials: Evaluating validity of the methodologies, J. Pharm. Sci. 94 (2005) 948–965, https://doi.org/10.1002/jps.20298.

[12] C. Brough, R.O. Williams, Amorphous solid dispersions and nano crystal technologies for poorly water-soluble drug delivery, Int. J. Pharm. 453 (2013) 157–166, https://doi.org/10.1016/j.ijpharm.2013.05.040.

[13] Y. Huang, W. G. Dai, Fundamental aspects of solid dispersion technology for poorly soluble drugs, Acta Pharm. Sin. B 4 (2014) 18–25, https://doi.org/10.1016/j.apsb.2013.11.001.

[14] S. Baghel, H. Cathcart, N.J. O'Reilly, Polymeric amorphous solid dispersions: a review of amorphization, crystallization, stabilization, solid-state characterization, and aqueous solubilization of biopharmaceutical classification system class II drugs, J. Pharm. Sci. 105 (2016) 2527–2544, https://doi.org/10.1016/j.xphs.2015.10.008.

[15] J. Zhang, M. Guo, M. Luo, T. Cai, Advances in the development of amorphous solid dispersions: The role of polymeric carriers, Asian J. Pharm. Sci. 18 (2023) 100834, https://doi.org/10.1016/j.ajps.2023.100834.

[16] C. Baig, V.G. Mavrantzas, Tension thickening, molecular shape, and flow birefringence of an H-shaped polymer melt in steady shear and planar extension, J. Chem. Phys. 132 (2010) 14904, https://doi.org/10.1063/1.3271831.

[17] J.M. Kim, C. Baig, Communication: Role of short chain branching in polymer structure and dynamics, J. Chem. Phys. 144 (2016) 81101, https://doi.org/10.1063/1.4942351.

[18] A.M. Granville, W.J. Brittain, Recent Advances in Polymer Brush Synthesis, in: Polym. Brushes, John Wiley & Sons, Ltd, 2004: pp. 33–50. https://doi.org/https://doi.org/10.1002/3527603824.ch3.

[19] X. Zhu, Y. Zhou, D. Yan, Influence of branching architecture on polymer properties, J. Polym. Sci. Part B Polym. Phys. 49 (2011) 1277–1286, https://doi.org/10.1002/polb.22320.

[20] B.I. Voit, A. Lederer, Hyperbranched and highly branched polymer architectures—synthetic strategies and major characterization aspects, Chem. Rev. 109 (2009) 5924–5973, https://doi.org/10.1021/cr900068q.

[21] M. Calderón, M.A. Quadir, S.K. Sharma, R. Haag, Dendritic polyglycerols for biomedical applications, Adv. Mater. 22 (2010) 190–218, https://doi.org/10.1002/adma.200902244.

[22] C. Gabriel, H. Münstedt, Influence of long-chain branches in polyethylenes on linear viscoelastic flow properties in shear, Rheol. Acta 41 (2002) 232–244, https://doi.org/10.1007/s003970100194.

[23] D. Choe, S.H. Jeong, C. Baig, Structural, topological, and rheological characteristics of entangled short chain branched polymer melts under shear flow in comparison with the linear analog, J. Rheol. (N. Y. N. Y). 68 (2024) 591–601. https://doi.org/10.1122/8.0000844.

[24] B. Ramachandran, G. Beaucage, A.S. Kulkarni, D. McFaddin, J. Merrick Mack, V. Galiatsatos, Persistence length of short chain branched polyethylene, Macromolecules 41 (2008) 9802–9806, https://doi.org/10.1021/ma801775n.

[25] K. Löbmann, K. Laitinen, H. Grohganz, K.C. Gordon, C. Strachan, T. Rades, Coamorphous drug systems: Enhanced physical stability and dissolution rate of indomethacin and naproxen, Mol. Pharm. 8 (2011) 1919–1928, https://doi.org/10.1021/mp200297x.

[26] J. Sibik, K. Löbmann, T. Rades, J.A. Zeitler, Predicting crystallization of amorphous drugs with terahertz spectroscopy, Mol. Pharm. 12 (2015) 3062–3068, https://doi.org/10.1021/acs.molpharmaceut.5b00356.

[27] A.E. Wiącek, K. Przykaza, Wettability and stability of naproxen, ibuprofen and/or cyclosporine A/Silica delivery systems, Colloids and Interfaces 6 (2022), https://doi.org/10.3390/colloids6010011.

[28] C. Xing, T. Chen, L. Wang, Q. An, Y. Jin, D. Yang, L. Zhang, G. Du, Y. Lu, Two novel co-crystals of naproxen: Comparison of stability, solubility and intermolecular interaction, Pharmaceuticals 15 (2022) 1–14, https://doi.org/10.3390/ph15070807.

[29] T. Tang, K. Yang, S. Zhao, Q. Chen, L. Qin, B. Qin, Evaluation of solubility, physicochemical properties, and cytotoxicity of naproxen-based ionic liquids, ACS Omega 8 (2023) 8332–8340, https://doi.org/10.1021/acsomega.2c07944.

[30] J.S. Song, Y.T. Sohn, Crystal forms of naproxen, Arch. Pharm. Res. 34 (2011) 87–90, https://doi.org/10.1007/s12272-011-0110-7.

[31] N. Tumanova, N. Tumanov, F. Fischer, F. Morelle, V. Ban, K. Robeyns, Y. Filinchuk, J. Wouters, F. Emmerling, T. Leyssens, Exploring polymorphism and stoichiometric diversity in naproxen/proline cocrystals, CrystEngComm 20 (2018) 7308–7321, https://doi.org/10.1039/C8CE01336B.

[32] E. Kamińska, O. Madejczyk, M. Tarnacka, K. Jurkiewicz, K. Kamiński, M. Paluch, Studying of crystal growth and overall crystallization of naproxen from binary mixtures, Eur. J. Pharm. Biopharm. 113 (2017) 75–87, https://doi.org/10.1016/j.ejpb.2016.12.014.

[33] A. Minecka, M. Tarnacka, K. Jurkiewicz, B. Hachuła, R. Wrzalik, K. Kamiński, M. Paluch, E. Kamińska, Impact of the chain length and topology of the acrylated oligosaccharide on the crystallization tendency of naproxen from amorphous binary mixtures, Mol. Pharm. 18 (2021) 347–358, https://doi.org/10.1021/acs.molpharmaceut.0c00983.

[34] Q. Zhu, S.J. Toth, G.J. Simpson, H. Y. Han, L.S. Taylor, M.T. Harris, Crystallization and dissolution behavior of naproxen/polyethylene glycol solid dispersions, J. Phys. Chem. B 117 (2013) 1494–1500, https://doi.org/10.1021/jp3106716.

[35] M. Teodorescu, M. Bercea, S. Morariu, Biomaterials of PVA and PVP in medical and pharmaceutical applications: perspectives and challenges, Biotechnol. Adv. 37 (2019) 109–131, https://doi.org/10.1016/j.biotechadv.2018.11.008.

[36] M. Bejenari, H. Gulei, F. Tonoli, S. Kouass, Multifunctional Roles of PVP as a Versatile Biomaterial in Solid State, in: U. Ahmad (Ed.), Dos. Forms, IntechOpen, Rijeka, 2021. https://doi.org/10.5772/intechopen.99431.

[37] F. Haaf, A. Sanner, F. Straub, Polymers of n-vinylpyrrolidone: synthesis, characterization and uses, Polym. J. 17 (1985) 143–152, https://doi.org/10.1295/polymj.17.143.

[38] A. Nuber, S. Lang, A. Sanner, G. Schroeder, Preparation of polyvinylpyrrolidone, 1985 (1988) 3–5.

[39] J. Pawlak, M. Rams-Baron, B. Chrząszcz, R. Jachowicz, M. Paluch, Effect of polymer chain length on the physical stability of amorphous drug-polymer blends at ambient pressure, Mol. Pharm. 15 (2018) 2807–2815, https://doi.org/10.1021/acs.molpharmaceut.8b00313.

[40] S. Mohapatra, S. Samanta, K. Kothari, P. Mistry, R. Suryanarayanan, Effect of polymer molecular weight on the crystallization behavior of indomethacin amorphous solid dispersions, Cryst. Growth Des. 17 (2017) 3143–3150, https://doi.org/10.1021/acs.cgd.7b00096.

[41] U.S. Kestur, H. Lee, D. Santiago, C. Rinaldi, T.Y. Won, L.S. Taylor, Effects of the molecular weight and concentration of polymer additives, and temperature on the melt crystallization kinetics of a small drug molecule, Cryst. Growth Des. 10 (2010) 3565–3595, https://doi.org/10.1021/cg1004053.

[42] A. Sahoo, R. Suryanarayanan, P.A. Siegel, Stabilization of amorphous drugs by polymers: The role of overlap concentration (C*), Mol. Pharm. 17 (2020) 4401–4406, https://doi.org/10.1021/acs.molpharmaceut.0c00575.

[43] Z. Ayenew, A. Paudel, G. Van den Mooter, Can compression induce demixing in amorphous solid dispersions? A case study of naproxen-PVP K25, Eur. J. Pharm. Biopharm. 81 (2012) 207–213, https://doi.org/10.1016/j.ejpb.2012.01.007.

[44] K. Lehmkemper, S.O. Kyeremateng, O. Heinzerling, M. Degenhardt, G. Sadowski, Long Term physical stability of PVP- and PVPVA Amorphous solid dispersions, Mol. Pharm. 14 (2017) 157–171, https://doi.org/10.1021/acs.molpharmaceut.6b00763.

[45] L. Orszulak, T. Lazarski, M. Tarnacka, B. Hachuła, K. Jurkiewicz, P. Zioła, A. Mrozek Wilczkiewicz, E. Kamińska, K. Kamiński, The Impact of Various Poly (vinylpyrrolidone) polymers on the crystallization process of metronidazole, Pharmaceutics 16 (2024) 136, https://doi.org/10.3390/pharmaceutics16010136.

[46] L. Orszulak, T. Lazarski, E. Bernat, M. Tarnacka, D. Żakowiecki, K. Jurkiewicz, P. Zioła, A. Mrozek Wilczkiewicz, A. Ziyba, K. Kamiński, E. Kamińska, The Influence of PVP Polymer topology on the liquid crystalline order of itraconazole in binary systems, Mol. Pharm. 21 (2024) 3027–3039, https://doi.org/10.1021/acs.molpharmaceut.4c00215.

[47] B. Hess, C. Kutzner, D. van der Spoel, E. Lindahl, GROMACS 4: algorithms for highly efficient, load-balanced, and scalable molecular simulation, J. Chem. Theory Comput. 4 (2008) 435–447, https://doi.org/10.1021/ct700301q.

[48] M.J. Abraham, T. Murtola, R. Schulz, S. Páll, J.C. Smith, B. Hess, E. Lindah, Gromacs: high performance molecular simulations through multi-level parallelism from laptops to supercomputers, SoftwareX 1–2 (2015) 19–25, https://doi.org/10.1016/j.softx.2015.06.001.

[49] D. Van Der Spoel, E. Lindahl, B. Hess, G. Groenhof, A.E. Mark, H.J.C. Berendsen, GROMACS: Fast, flexible, and free, J. Comput. Chem. 26 (2005) 1701–1718, https://doi.org/10.1002/jcc.20291.

[50] E. Lindahl, B. Hess, D. van der Spoel, GROMACS 3.0: A package for molecular simulation and trajectory analysis, J. Mol. Model. 7 (2001) 306–317. https://doi.org/10.1007/s008940100045.

[51] P. Schlord, M. Abraham, G. Kutzner, B. Hess, E. Lindahl, Tackling Exascale Software Challenges in Molecular Dynamics Simulations with GROMACS, 2015. https://doi.org/10.1007/978-3-319-15976-8_1.
[52] H.J.C. Berendsen, D. van der Spoel, R. van Drunen, GROMACS: A message passing parallel molecular dynamics implementation, Comput. Phys. Commun. 91 (1995) 43–56, https://doi.org/10.1016/0010-4655(95)00042-E.
[53] J. Wang, W. Wang, P.A. Kollman, D.A. Case, Automatic atom type and bond type perception in molecular mechanical calculations, J. Mol. Graph. Model. 25 (2006) 247–260, https://doi.org/10.1016/j.jmgm.2005.12.005.
[54] J. Wang, R.M. Wolf, J.W. Caldwell, P.A. Kollman, D.A. Case, Development and testing of a general amber force field, J. Comput. Chem. 25 (2004) 1157–1174, https://doi.org/10.1002/jcc.20035.
[55] M. Huang, C.F. Abrams, HTPolyNet: A general system generator for all atom molecular simulations of amorphous crosslinked polymers, SoftwareX 21 (2023) 101303, https://doi.org/10.1016/j.softx.2022.101303.
[56] A. Kozyra, N.A. Mogheirbi, K.J. Paluch, G. Garbacz, L. Tajber, Phase Diagrams of Polymer-dispersed liquid crystal systems of itraconazole/component immiscibility induced by molecular anisotropy, Mol. Pharm. 15 (2018) 5192–5206, https://doi.org/10.1021/acs.molpharmaceut.8b00724.
[57] K. Chmiel, J. Knapik-Kowalczuk, E. Kamińska, L. Tajber, M. Paluch, High-Pressure dielectric studies – a way to experimentally determine the solubility of a drug in the polymer matrix at low temperatures, Mol. Pharm. 18 (2021) 3050–3062, https://doi.org/10.1021/acs.molpharmaceut.1c00264.
[58] H.E. Kissinger, Variation of Peak Temperature With Heating Rate in DTA- Kissinger 1956.pdf, 57 (1956) 217–221.
[59] R.L. Blaine, H.E. Kissinger, Homer Kissinger and the kissinger equation, Thermochim. Acta 540 (2012) 1–6, https://doi.org/10.1016/j.tca.2012.04.008.
[60] R.M.F. Wellen, E.L. Canedo, On the Kissinger equation and the estimate of activation energies for non-isothermal cold crystallization of PET, Polym. Test. 40 (2014) 33–38, https://doi.org/10.1016/j.polymertesting.2014.08.008.
[61] D. Heczko, B. Hachuła, P. Maksym, K. Kamiński, A. Ziąba, L. Orszulok, M. Paluch, E. Kamińska, The effect of various poly (N-vinylpyrrolidone) (PVP) polymers on the crystallization of flutamide, Pharmaceuticals 15 (2022) 971, https://doi.org/10.3390/ph15080971.
[62] E. Schulz, B. Wunderlich, Macromolecular physics, vol. 2 crystal nucleation, growth, annealing, Academic Press New York 1976, Preis $ 46, 50, Krist. Und Tech. 12 (1977) K11–K12. https://doi.org/https://doi.org/10.1002/crat.19770120121.
[63] N. Coburn, P. Douglas, D. Keys, J. Gupta, T. McNally, Isothermal and non-isothermal crystallization kinetics of composites of poly(propylene) and MWCNTs, Adv. Ind. Eng. Polym. Res. 1 (2018) 99–110, https://doi.org/10.1016/j.aiepr.2018.06.001.
[64] D.R. Nelson, Phase transitions in solids, Nature 275 (1978) 258, https://doi.org/10.1038/275258b0.
[65] D.R. Uhlmann, On the internal nucleation of melting, J. Non. Cryst. Solids 41 (1980) 347–357, https://doi.org/10.1016/0022-3093(80)90180-5.
[66] Y.H. Li, C. Yang, L.M. Kang, H.D. Zhao, S.G. Qu, X.Q. Li, W.W. Zhang, Y.Y. Li, Non-isothermal and isothermal crystallization kinetics and their effect on microstructure of sintered and crystallized TiNbZrTaSi bulk alloys, J. Non. Cryst. Solids 432 (2016) 440–452, https://doi.org/10.1016/j.jnoncrysol.2015.11.005.
[67] M. Safandowska, A. Rozanski, Ring banded spherulites in polylactide and its blends, Polym. Test. 100 (2021) 107230, https://doi.org/10.1016/j.polymertesting.2021.107230.
[68] M.B. Alawajy, B. Ozdemir, M. Nofar, A. Ozmen, Isothermal and non-isothermal cold crystallization kinetics of polylactide/cellulose nanocrystal (PLA/CNC) nanocomposites, J. Therm. Anal. Calorim. 147 (2022) 14211–14227, https://doi.org/10.1007/s10973-022-11598-9.
[69] Y. Bouzerzour, A. Layachi, A. Cherfia, F. Lauzrid, H. Safsa, Non-Isothermal crystallization kinetics and activation energy for crystal growth of polyamide 66/Short Glass Fiber/Carbon black composites, Materials (Basel) 16 (2023) 7073, https://doi.org/10.3390/ma16227073.
[70] A. Apelblat, Dissertation and continuous association including formation of cyclic dimers, Can. J. Chem. 69 (1991) 638–647, https://doi.org/10.1139/v91-097.
[71] A. Paudel, E. Nies, G. Van den Mooter, Relating hydrogen bonding interactions with the phase behavior of naproxen/PVP K 25 solid dispersions: evaluation of solution cast and quench cooled films., Mol. Pharm. 9 11 (2012) 3301–3317. https://api.semanticscholar.org/CorpusID:39531237.
[72] L.S. Taylor, G. Zografi, Spectroscopic characterization of interactions between PVP and indomethacin in amorphous molecular dispersions, Pharm. Res. 14 (1997) 1691–1698, https://doi.org/10.1023/A:1012167411087.

Supplementary Material

Inhibition of naproxen crystallization by polymers: The role of topology and chain length of polyvinylpyrrolidone macromolecules

Luiza Orszulak[1*], Patryk Włodarczyk[2], Barbara Hachuła[1], Taoufik Lamrani[3], Karolina Jurkiewicz[3], Magdalena Tarnacka[3], Marek Hreczka[2,4], Kamil Kamiński[3], Ewa Kamińska[5*]

[1] *Institute of Chemistry, Faculty of Science and Technology, University of Silesia in Katowice, Szkolna 9, 40-007 Katowice, Poland*

[2] *Institute of Non Ferrous Metals, Sowinskiego 5, 44-100 Gliwice, Poland*

[3] *Institute of Physics, Faculty of Science and Technology, University of Silesia in Katowice, 75 Pułku Piechoty 1A, 41-500 Chorzow, Poland*

[4] *Department of Mechatronics, Silesian University of Technology, Akademicka 10A, 44-100 Gliwice, Poland*

[5] *Department of Pharmacognosy and Phytochemistry, Faculty of Pharmaceutical Sciences in Sosnowiec, Medical University of Silesia in Katowice, Jagiellonska 4, 41-200 Sosnowiec, Poland*

*Corresponding author: luiza.orszulak@us.edu.pl, ekaminska@sum.edu.pl

Molecular Dynamics Simulations data

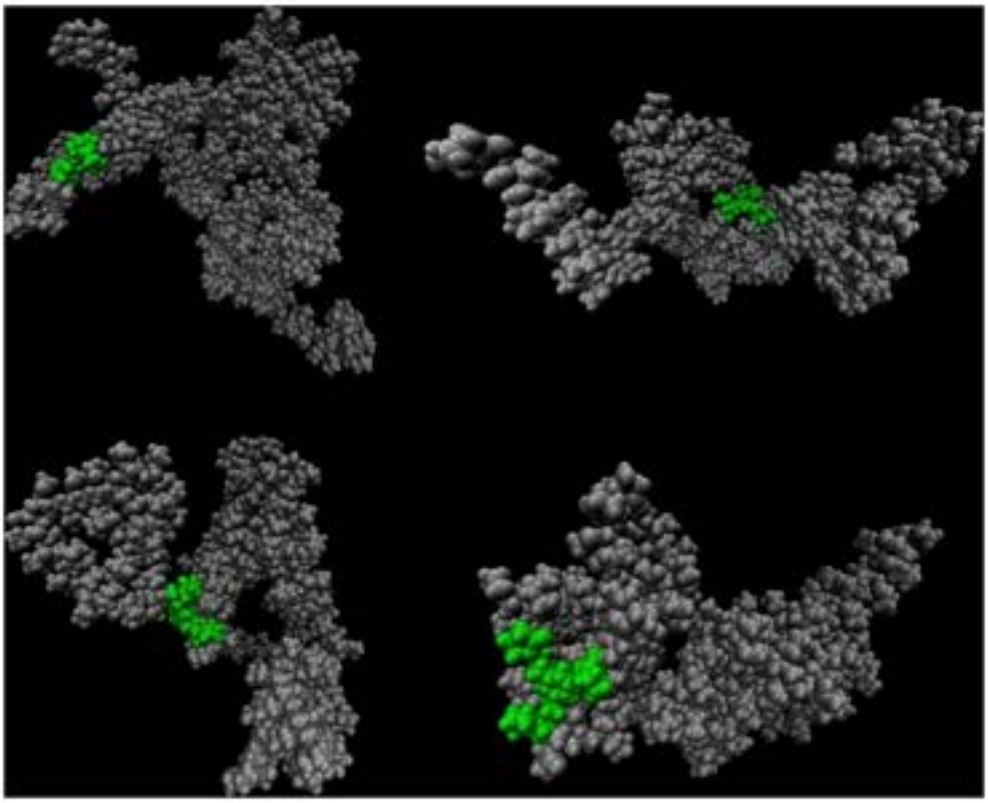

Fig. S1 The structures of simulated star-shaped PVPs. The green areas indicate the centers of the star-shaped macromolecules.

DSC data

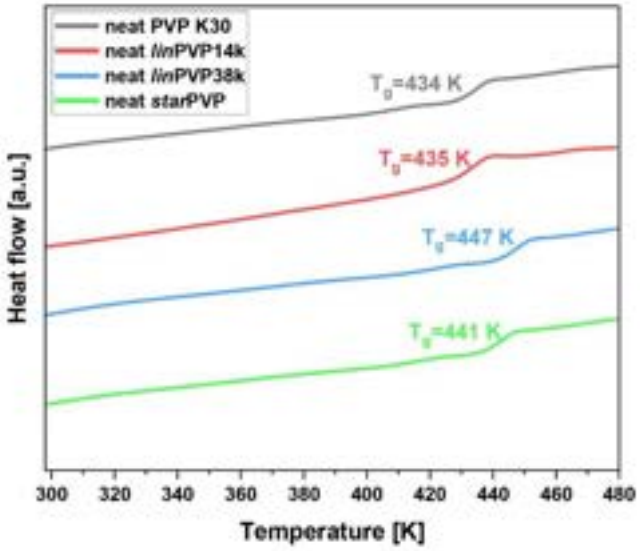

Fig. S2 DSC thermograms (heating rate, ϕ =10 K/min) collected for neat amorphous PVPs. T_g was determined as the midpoint of the heat capacity increment.

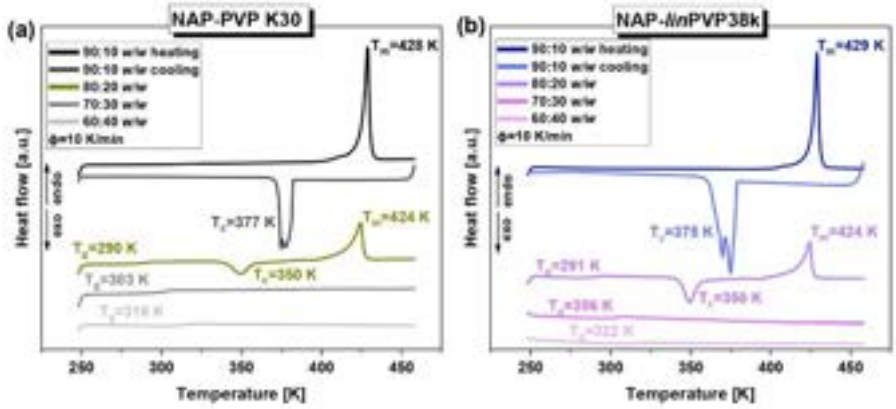

Fig. S3 DSC thermograms (ϕ = 10 K/min) of **(a)** NAP-PVP K30, and **(b)** NAP-*lin*PVP38k mixtures with different weight ratios (90:10, 80:20, 70:30, 60:40 *w/w*). The thermograms for NAP-PVP 90:10 *w/w* systems were collected on heating and subsequent cooling, while the thermograms for other BMs were collected on heating (after previous heating and cooling).

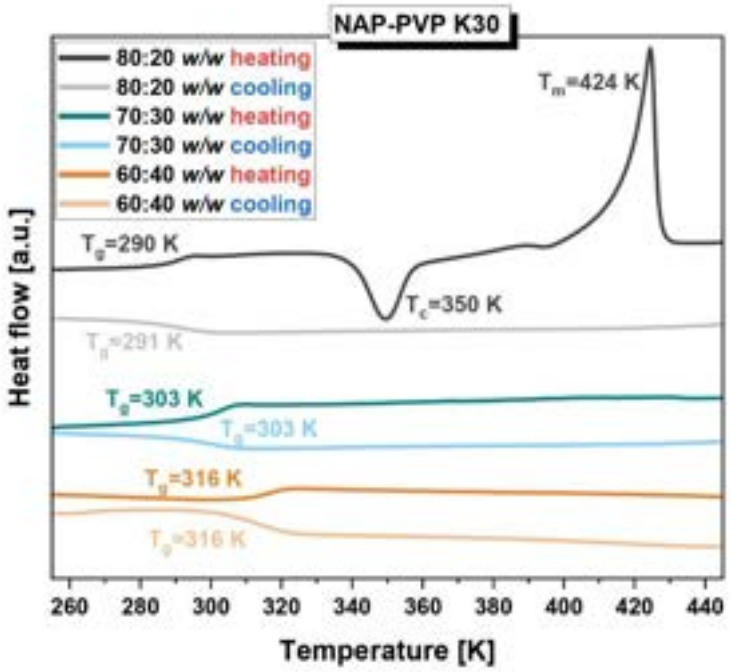

Fig. S4 DSC thermograms (ϕ =10 K/min) collected for NAP-PVP K30, 80:20, 70:30 and 60:40 *w/w* mixtures during the heating and cooling procedures.

Table S1. The values of the calorimetric glass transition temperature (ϕ =10 K/min) as well as heat capacity changes at T_g (ΔC_p) for the examined NAP-PVP binary mixtures in various weight ratios and neat PVPs.

Binary mixture, *w/w*	NAP-PVP K30		NAP-*lin*PVP14k		NAP-*lin*PVP38k		NAP-*star*PVP	
	T_g [K]	ΔC_p [J/gK]	T_g [K]	ΔC_p [J/gK]	T_g [K]	ΔC_p [J/gK]	T_g [K]	ΔC_p [J/gK]
90:10	-	-	-	-	-	-	-	-
80:20	290	0.31	290	0.35	291	0.32	290	0.35
70:30	303	0.35	305	0.31	306	0.24	302	0.34
60:40	316	0.31	315	0.24	322	0.25	318	0.29
neat polymer	434	0.26	435	0.28	447	0.25	441	0.30

Table S2. Values of the calorimetric melting temperatures, T_m, and melting enthalpies, ΔH_m (determined upon ϕ =10 K/min) for neat NAP and the examined NAP-PVP binary mixtures in various weight ratios.

Binary mixture, *w/w*	neat NAP		NAP-PVP K30		NAP-*lin*PVP14k		NAP-*lin*PVP38k		NAP-*star*PVP	
	T_m [K]	ΔH_m [J/g]	T_m [K]	ΔH_m [J/g]	T_m [K]	ΔH_m [J/g]	T_m [K]	ΔH_m [J/g]	T_m [K]	ΔH_m [J/g]
100:0	431	142.8	-	-	-	-	-	-	-	-
95:5	–	–	430	–	430	–	430	–	430	–
90:10	-	-	428	95.9	427	88.5	429	101.6	428	91.9
85:15	–	–	427	–	427	–	428	–	428	–
80:20	-	-	424	53.2	422	51.4	424	57.0	423	55.6
70:30	-	-	–	-	–	-	–	-	–	-
60:40	-	-	–	-	–	-	–	-	–	-

Table S3. The crystallization temperature values for NAP-PVP 80:20 *w/w* mixtures depending on the heating rate (ϕ).

NAP-PVP 80:20 *w/w* mixtures				
ϕ [K/min]	T_c [K]			
	NAP-PVP K30	NAP-*lin*PVP14k	NAP-*lin*PVP38k	NAP-*star*PVP
5	338.8	341.4	341.1	338.2
7.5	342.8	346.4	346.6	343.6
10	345.6	350.0	350.2	347.2
12.5	348.2	353.0	353.8	350.2
15	350.8	355.2	356.6	352.8
17.5	352.8	357.2	358.8	355.2
20	354.4	358.8	360.8	357.2
25	357.4	361.8	363.8	360.2
30	359.8	364.2	366.6	362.8
35	362.0	366.8	368.6	365.2
40	364.0	369.2	371.0	367.4

XRD data

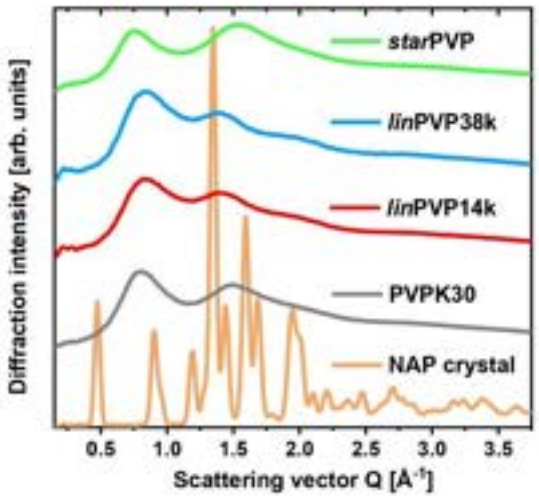

Fig. S5 Comparison of XRD patterns obtained for neat crystalline NAP and neat PVP polymers.

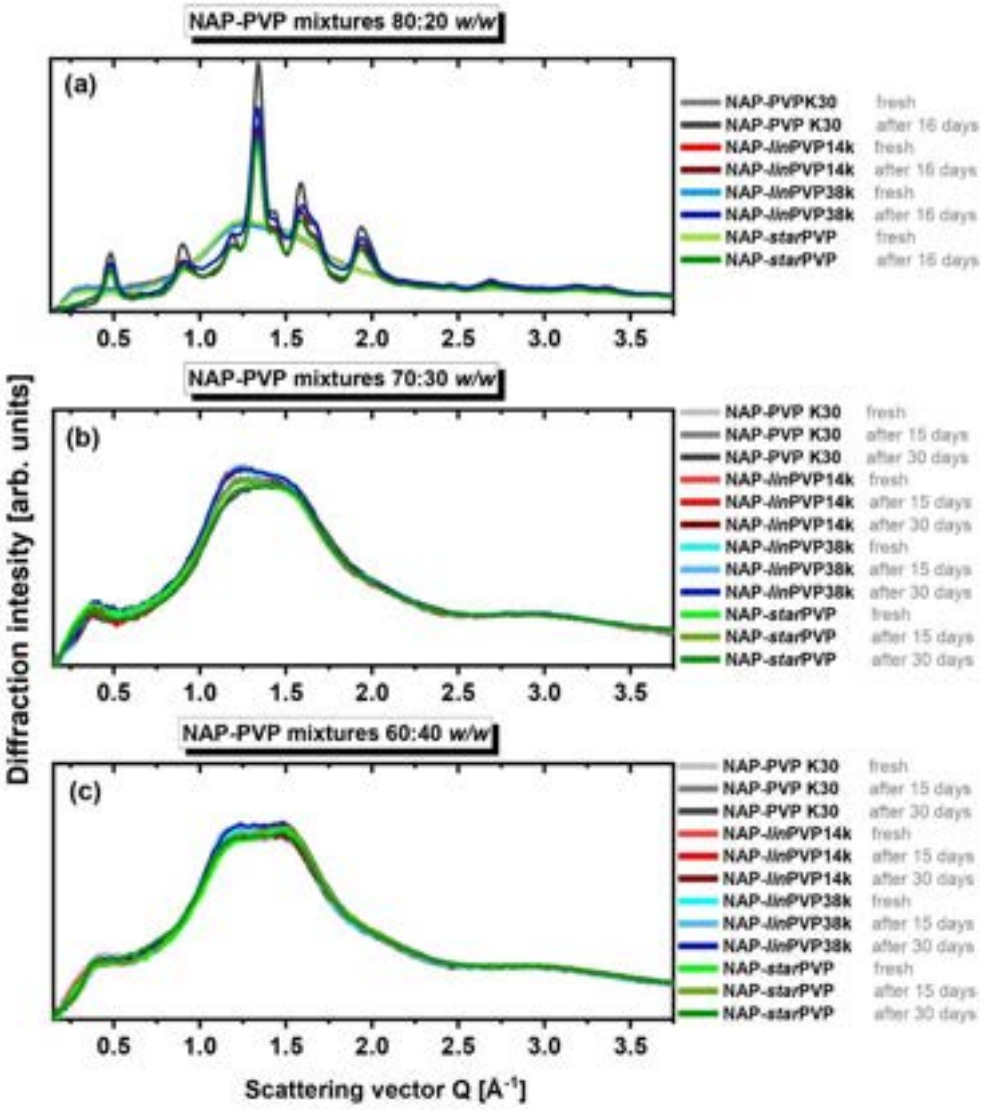

Fig. S6 The temporal evolution of diffraction patterns for NAP-PVP mixtures at different weight ratios **(a)** 80:20, **(b)** 70:30 and **(c)** 60:40.

FT-IR data

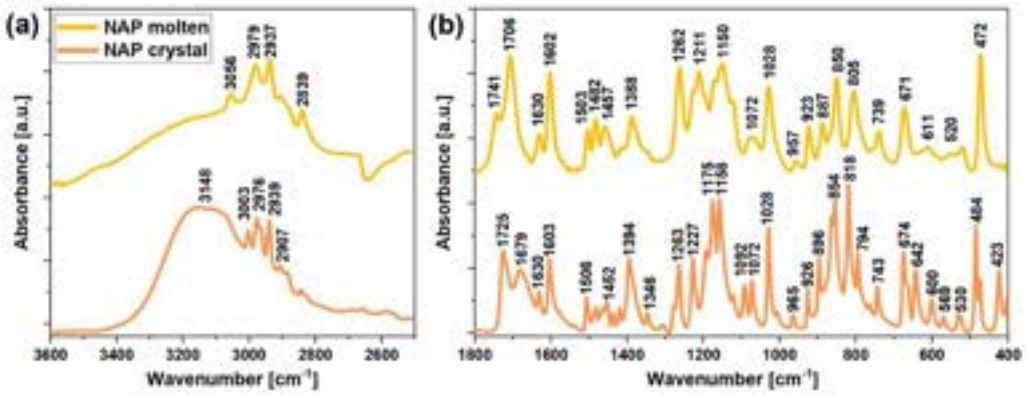

Fig. S7 FTIR spectra of molten NAP and neat crystalline NAP, measured in two wavenumber ranges of **(a)** 3600-2500 and **(b)** 1800-400 cm^{-1}.

As reported in the literature, crystalline NAP molecules are connected through O-H···O H-bonds involving the oxygen atoms from the carboxylic groups, leading to the creation of a one-dimensional helix chain.[1] Consequently, the stretching vibration band of H-bonded OH groups (ν_{OH}) in this API form, occurring from 3450 to 2700 cm^{-1}, is broad and intense. In contrast, the ν_{OH} band of molten NAP is even further widened towards the higher wavenumbers, and the intensity of its higher-wavenumber component (3550-3100 cm^{-1}) is more prominent. Moreover, the weak band contour assigned to the stretching vibrations of non-H-bonded ("free") OH groups is detected in the 3550-3400 cm^{-1} range. These facts clearly indicate the existence of completely different types of H-bonding interactions between API molecules in both phases, molten and crystalline. It should be noted that the spectrum of molten NAP mimics that of NAP diluted in a CCl_4 liquid mixture, showing that NAP molecules exist as H-bonded dimers in the liquid phase.[2] The difference in the association process of crystalline and molten phases is also reflected in the lower wavenumber region connected with the stretching vibrations of the carbonyl group ($\nu_{C=O}$). For crystalline NAP, the $\nu_{C=O}$ signal involves two overlapping peaks located at 1725 cm^{-1} and 1679 cm^{-1}, whereas, in the case of the molten NAP, the $\nu_{C=O}$ band exhibits two peaks at 1741 and 1706 cm^{-1} with inverse intensity ratio. The other bands located in the lower wavenumber range of 1800-400 cm^{-1} exhibit similar positions for both studied forms; however, for molten NAP, the signals are broadened and blurred compared to the sharper and split peaks of crystalline NAP. Thus, the signal located at 1603 cm^{-1} for crystalline NAP is assigned to symmetric ring stretch, while that at 1452 cm^{-1} corresponds to

the CH_3 asymmetric bend.[3] The C-C-OH antisymmetric bend/stretch occurs at 1394 cm^{-1}, and the C–C–O antisymmetric bend/stretch is observed at 1263 cm^{-1}.[3] A peak at 1227 cm^{-1} is related to the C–O–C asymmetric stretch of the methoxy group, whereas a signal located at 1028 cm^{-1} is connected with the C–O–C symmetric stretch of the methoxy group.[3] At 926 cm^{-1}, the band assigned to the out-of-plane OH bending vibration is found.

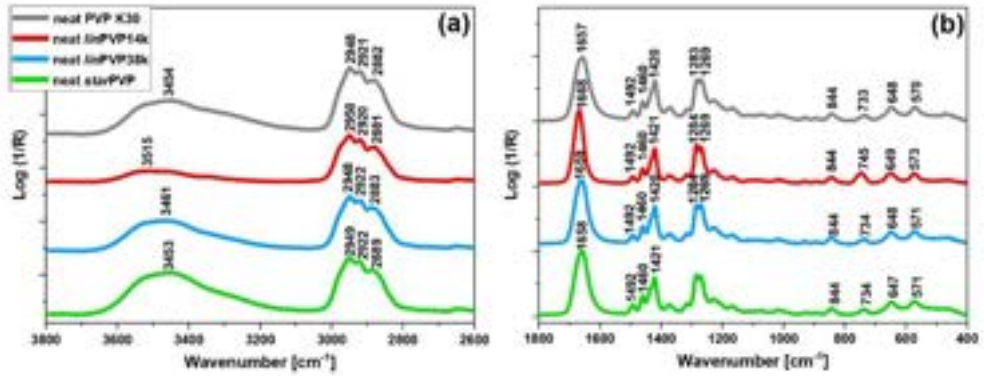

Fig. S8 FTIR spectra of neat PVP K30, *lin*PVP14k, *lin*PVP38k, and *star*PVP, measured in two wavenumber ranges of **(a)** 3750-2500 and **(b)** 1800-400 cm^{-1}.

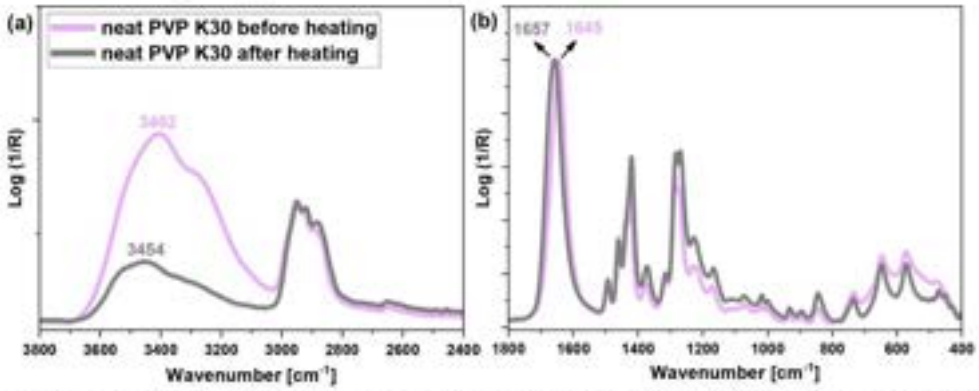

Fig. S9 FTIR spectra of neat PVP K30, measured before and after heating at 393 K for 20 hours in two wavenumber ranges of **(a)** 3800-2600 and **(b)** 1800-400 cm^{-1}.

As mentioned in the main manuscript, PVP is a highly hygroscopic polymer, hence the analysis of FT-IR data for binary mixtures can be difficult, especially in the ranges of 1650 and 3400 cm^{-1}. As can be observed in **Fig. S9** for the exemplary PVP K30 polymer, PVP macromolecules have a lot of absorbed water (see light violet line) - about 13 wt%, as shown by independent TGA measurements. However, after sample annealing (dark grey line), a significant amount of water is lost from the system, and its content is then 2-3%. Considering

that the samples were prepared at T=433 K (see section 2.2. "*The procedure of preparing amorphous NAP-PVP formulations*" in the main manuscript), it can be assumed that the share of water in the studied BMs is small, as evidenced by the very low intensity of the band around 3400 cm^{-1} in the presented spectra (for example, see **Fig. S10**). In addition, it is worth noting that the thermograms recorded for NAP-PVP systems also do not show an endothermic peak that could indicate water evaporation from the sample during measurement (see **Fig. 2** in the main manuscript and **Fig. S3**). Based on the above, it can be assumed that neat polymers certainly contain a significant amount of water, but the method used to prepare binary mixtures (melt-cooling) allows for the majority of water to be removed from macromolecules and thus does not interfere with the interpretation of FT-IR spectra. It should also be recalled that, according to the literature, PVP is a material that is extremely difficult to completely dry and the amount of water contained in samples usually oscillates around 5%.[4,5]

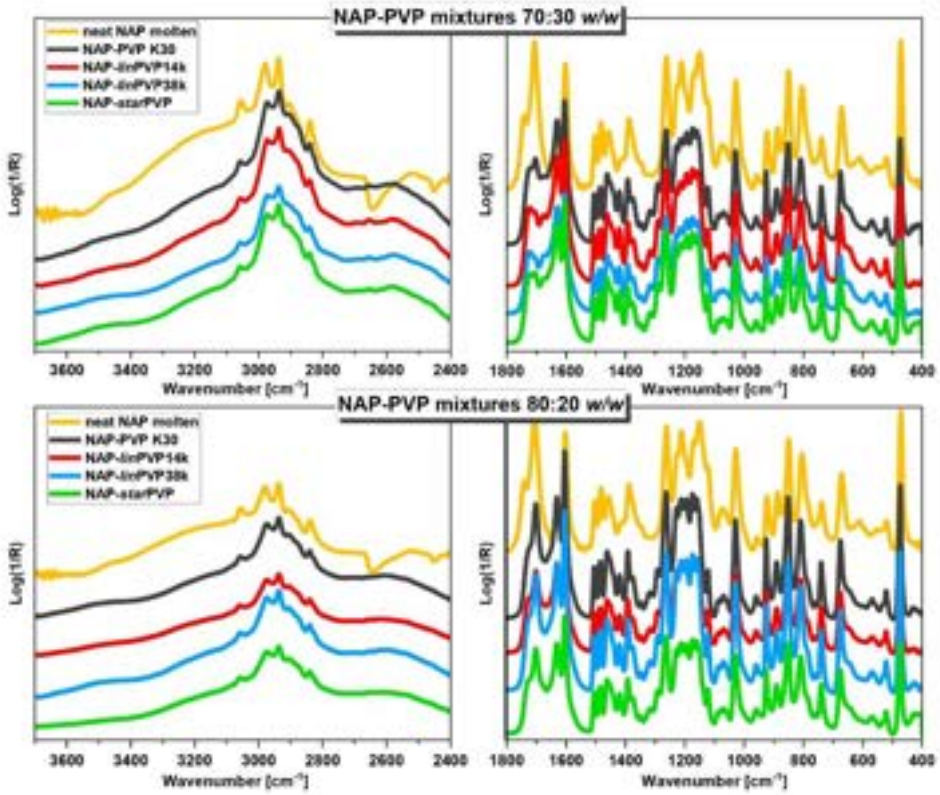

Fig. S10 FTIR spectra of binary mixtures containing NAP and PVP of different topologies at two API–polymer weight ratios: 70:30 *w/w*, and 80:20 *w/w*, measured in the supercooled liquid/or glassy states, and that of neat molten NAP.

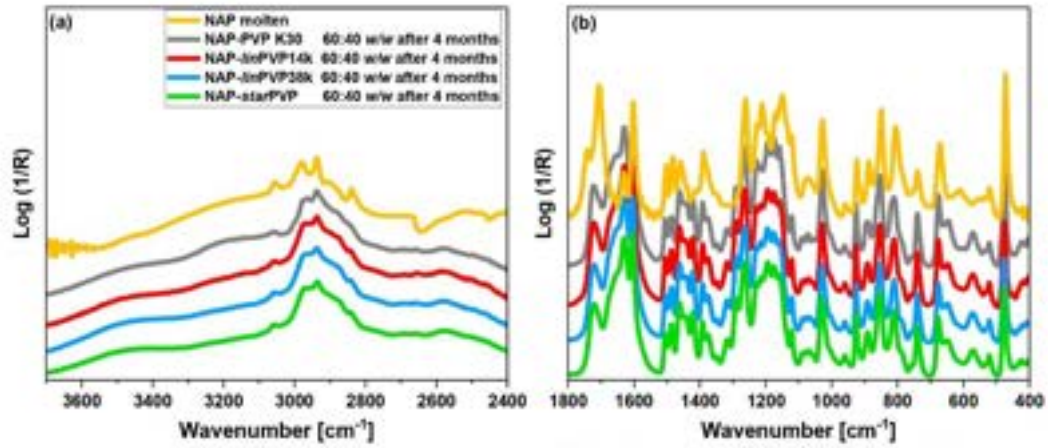

Fig. S11 FTIR spectra of NAP-PVP 60:40 *w/w* BMs: NAP-PVP K30, NAP-*lin*PVP14k, NAP-*lin*PVP38k and NAP-*star*PVP, measured after 4 months of storage in two wavenumber ranges of **(a)** 3700-2400 and **(b)** 1800-400 cm^{-1}. The spectrum of molten NAP was drawn for comparison.

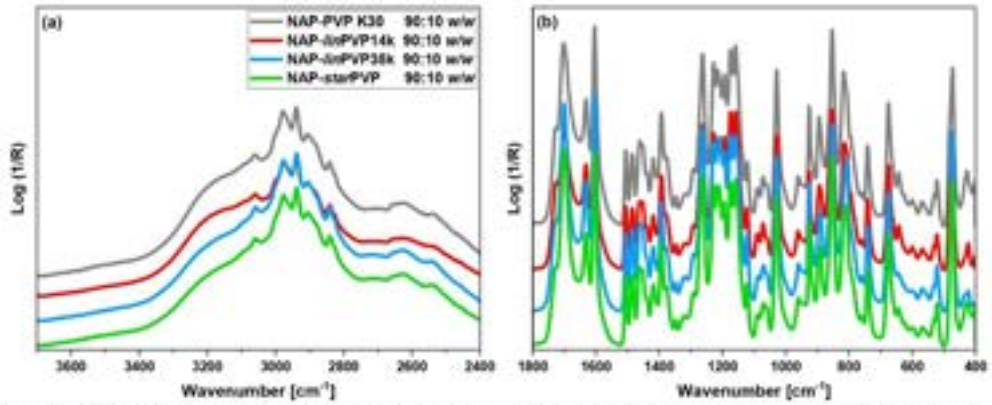

Fig. S12 FTIR spectra of NAP-PVP 90:10 *w/w* BMs: NAP-PVP K30, NAP-*lin*PVP14k, NAP-*lin*PVP38k, and NAP-*star*PVP, measured immediately after preparation/vitrification in two wavenumber ranges of **(a)** 3700-2400 and **(b)** 1800-400 cm^{-1}.

511

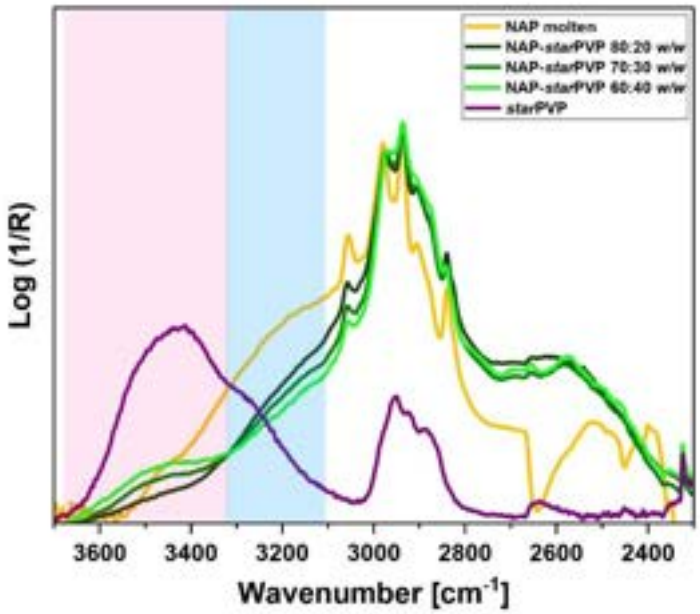

Fig. S13 FTIR spectra of amorphous NAP-*star*PVP BMs with different weight ratios, measured in the region 3700-2300 cm^{-1}. The spectra of molten NAP and neat *star*PVP were also drawn for comparison. An increase in peak intensity as the concentration of *star*PVP increases in the mixture is highlighted in red and a decrease in blue, respectively.

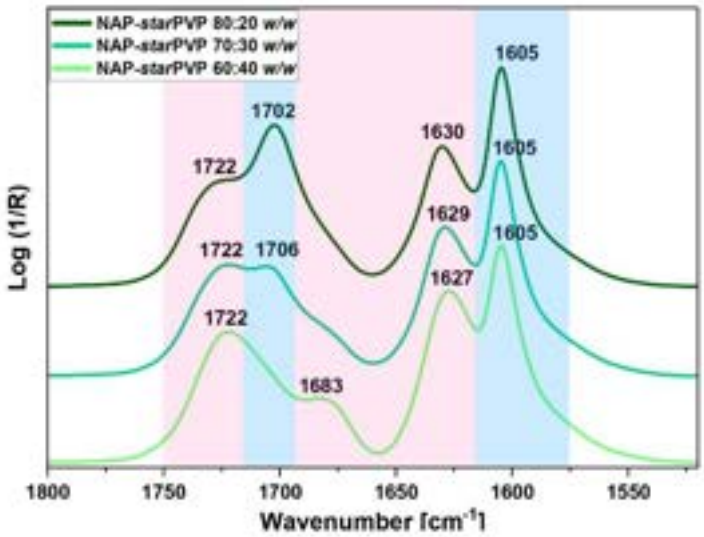

Fig. S14 FTIR spectra of amorphous NAP-*star*PVP BMs with different weight ratios, measured in the region 1800-1520 cm^{-1} after subtracting the C=O band of neat *star*PVP. An increase in peak intensity as the concentration of starPVP increases in the mixture is highlighted in red and a decrease in blue, respectively.

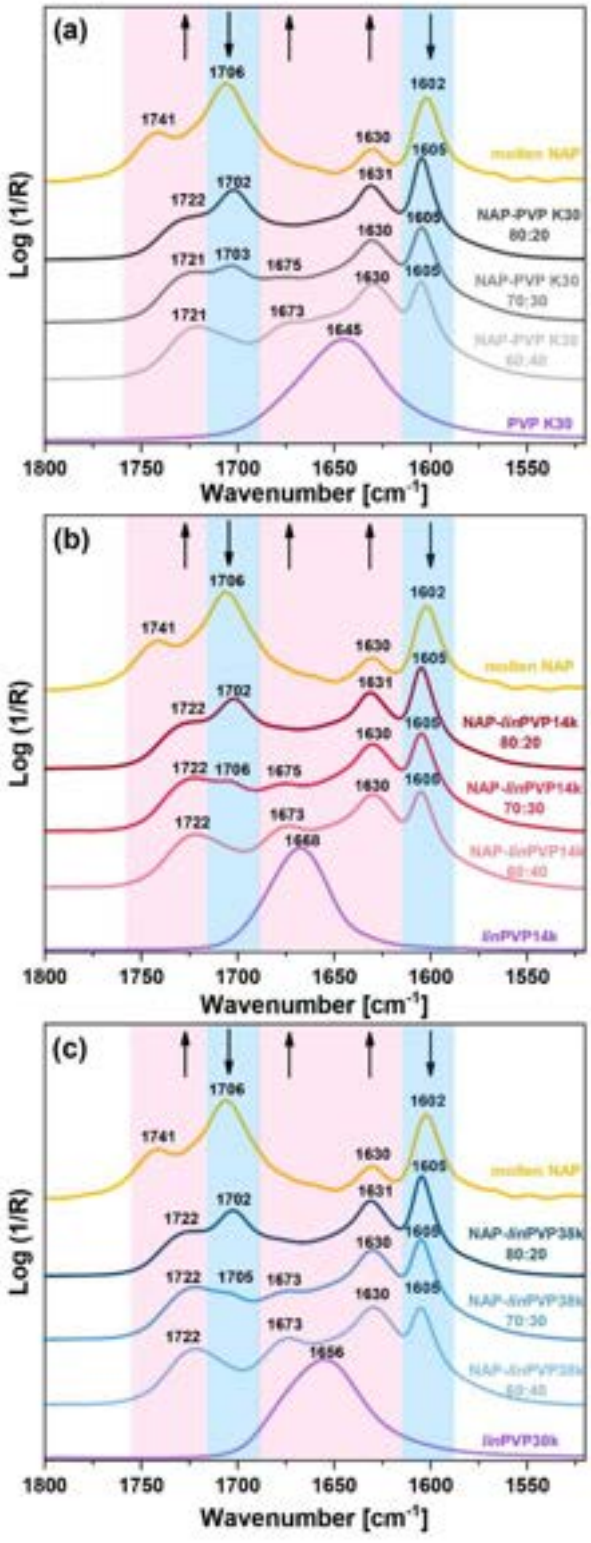

513

Fig. S15 FTIR spectra of amorphous BMs of NAP with **(a)** PVP K30, **(b)** *lin*PVP14k, and **(c)** *lin*PVP38k, with different weight ratios, measured in the region 1800-1520 cm^{-1}. The spectra of molten NAP and neat PVP samples were also drawn for comparison. An increase in peak intensity as the concentration of PVP increases in the mixture is highlighted in red and a decrease in blue, respectively.

References:

[1] B. Hachuła, The nature of hydrogen-bonding interactions in nonsteroidal anti-inflammatory drugs revealed by polarized IR spectroscopy., Spectrochim. Acta. A. Mol. Biomol. Spectrosc. 188 (2018) 189–196. https://doi.org/10.1016/j.saa.2017.07.005.

[2] A. Apelblat, Dimerization and continuous association including formation of cyclic dimers, Can. J. Chem. 69 (1991) 638–647. https://doi.org/10.1139/v91-097.

[3] L. Liu, H. Gao, Quantum chemistry study of molecular structure and vibrational spectrum of naproxen, Spectrochim. Acta Part A Mol. Biomol. Spectrosc. 86 (2012) 131–138. https://doi.org/https://doi.org/10.1016/j.saa.2011.10.018.

[4] T.L. Lebedeva, M.M. Feldstein, S.A. Kuptsov, N.A. Plate, Structure of stable H-linked complexes of poly-N-vinylpyrrolidone with water, Polym. Sci. Ser. A 42 (2000) 989–1005.

[5] S. V. Kurmaz, N. V. Fadeeva, V.M. Ignat'ev, V.A. Kurmaz, S.A. Kurochkin, N.S. Emel'yanova, Structure and State of Water in Branched N-Vinylpyrrolidone Copolymers as Carriers of a Hydrophilic Biologically Active Compound, Molecules 25 (2020) 6015. https://doi.org/10.3390/MOLECULES25246015.

4.3. The influence of PVP polymer topology on the liquid crystalline order of itraconazole in binary systems (P3)

Autorzy: L. Orszulak, T. Lamrani, R. Bernat, M. Tarnacka, D. Żakowiecki, K. Jurkiewicz, P. Zioła, A. Mrozek-Wilczkiewicz, A. Zięba, K. Kamiński, E. Kamińska

Referencja: *Molecular Pharmaceutics*, 2024, 21 (6), 3027−3039

DOI: 10.1021/acs.molpharmaceut.4c00215

Impact Factor czasopisma: 4.5

Liczba punktów ministerialnych MNiSW czasopisma: 140 (2024)

Mój udział w pracy polegał na zsyntezowaniu matryc polimerowych, ich pełnej charakterystyce spektroskopowej i chromatograficznej, tworzeniu mieszanin binarnych metodą witryfikacji, pomiarach dielektrycznych, analizie i wizualizacji danych, dyskusji wyników, przygotowywaniu tekstów manuskryptów, opracowywaniu odpowiedzi dla recenzentów i edytora, pozyskaniu finansowania w ramach kierowania grantem *„Perły Nauki”*.

molecular pharmaceutics

pubs.acs.org/molecularpharmaceutics

Article

The Influence of PVP Polymer Topology on the Liquid Crystalline Order of Itraconazole in Binary Systems

Published as part of Molecular Pharmaceutics virtual special issue "Pharmaceutical Sciences and Drug Delivery Research from Early Career Scientists".

Luiza Orszulak,* Taoufik Lamrani, Roksana Bernat, Magdalena Tarnacka, Daniel Żakowiecki, Karolina Jurkiewicz, Patryk Zioła, Anna Mrozek-Wilczkiewicz, Andrzej Zięba, Kamil Kamiński, and Ewa Kamińska

Cite This: Mol. Pharmaceutics 2024, 21, 3027−3039

Read Online

ACCESS | Metrics & More | Article Recommendations | Supporting Information

ABSTRACT: This study presents a novel approach by utilizing poly(vinylpyrrolidone)s (PVPs) with various topologies as potential matrices for the liquid crystalline (LC) active pharmaceutical ingredient itraconazole (ITZ). We examined amorphous solid dispersions (ASDs) composed of ITZ and (*i*) self-synthesized linear PVP, (*ii*) self-synthesized star-shaped PVP, and (*iii*) commercial linear PVP K30. Differential scanning calorimetry, X-ray diffraction, and broad-band dielectric spectroscopy were employed to get a comprehensive insight into the thermal and structural properties, as well as global and local molecular dynamics of ITZ−PVP systems. The primary objective was to assess the influence of PVPs' topology and the composition of ASD on the LC ordering, changes in the temperature of transitions between mesophases, the rate of their restoration, and finally the solubility of ITZ in the prepared ASDs. Our research clearly showed that regardless of the PVP type, both LC transitions, from smectic (Sm) to nematic (N) and from N to isotropic (I) phases, are effectively suppressed. Moreover, a significant difference in the miscibility of different PVPs with the investigated API was found. This phenomenon also affected the solubility of API, which was the greatest, up to 100 μg/mL in the case of *star*PVP 85:15 *w*/*w* mixture in comparison to neat crystalline API (5 μg/mL). Obtained data emphasize the crucial role of the polymer's topology in designing new pharmaceutical formulations.

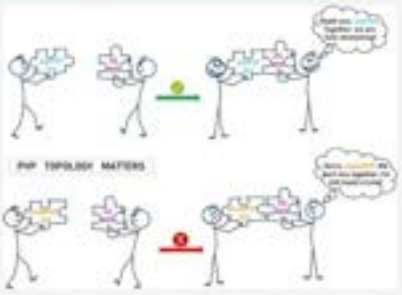

KEYWORDS: *itraconazole, poly(vinylpyrrolidone), star-shaped polymer, binary mixtures, amorphous solid dispersions, nematic phase, smectic phase, liquid crystalline order*

INTRODUCTION

The pharmaceutical industry is a rapidly evolving sector of the economy. However, despite its dynamic development, bringing new pharmaceutical products to the market encounters several serious problems. One of them is the very poor solubility of a large number of active pharmaceutical ingredients (APIs) and, consequently, their low bioavailability.[1] Hence, in recent years, many scientific groups have been working on various strategies to increase the solubility and therapeutic effectiveness of APIs.[2−4] In this context, one can mention several methods, e.g., salt formation,[5] cocrystallization,[6,7] micronization,[8] or amorphization.[9] The latter technique, i.e., the transformation of the crystalline active substance into the fully disordered (amorphous) form, is a highly promising research direction.[9] Numerous experimental and theoretical studies have indicated that amorphous pharmaceuticals due to higher entropy and free energy than their crystalline counterparts exhibit greater solubility and bioavailability.[10] On the other hand, the amorphous phase is thermodynamically unstable, which creates a high possibility of spontaneous crystallization under storage and processing conditions.[11,12] Nevertheless, this example clearly shows that it is quite easy to enhance both the physicochemical and pharmacokinetic properties of pharmaceuticals by a simple manipulation of the degree of molecular order/disorder. Considering this fact, special attention is paid to looking for materials characterized by various kinds of molecular ordering, which can be tuned by employing different external factors, such as pressure, temperature, solvent, pH, etc. Among all studied systems until now, liquid crystals (LCs) are looming as the best candidates, satisfying the above criteria.[13]

Received: February 27, 2024
Revised: May 2, 2024
Accepted: May 3, 2024
Published: May 17, 2024

These materials exhibit features of both three-dimensionally ordered solid crystals and conventional liquids[14] and are characterized by the abundance of phases differing in structural order. Two of the most common liquid crystalline (LC) mesophases are the nematic (N) and smectic (Sm) phases. In the former, rodlike molecules are arranged parallel to each other, with their long axes pointing in approximately the same direction. At the same time, their centers of mass are arranged randomly; thus, only the orientational order is maintained. In the Sm phase, the molecules located within layers are arranged in planes—hence, besides the orientational order, there is also a positional order.[14−16] Moreover, it should be emphasized that there are two main types of LCs: thermotropic and lyotropic liquid crystals (TLCs and LLCs), where LC phases can be induced by changing the temperature (heating or cooling) or dissolving mesogens in a suitable solvent, respectively.[13] Therefore, it is possible to obtain various states of molecular order. Consequently, due to the change in the spatial organization of molecules and higher Gibbs energy, the dissolution rate and bioavailability of LC API's can be optimized.[10,14,17−19] Hence, studies aimed at in-depth characterization of pharmaceuticals forming LC phases are entirely justified.

Certainly, among thermotropic LC APIs, an extremely interesting example is itraconazole (ITZ). It is a broad-spectrum antifungal medication belonging to the triazole antifungals.[20,21] According to the biopharmaceutics classification system, ITZ is considered a class II drug due to its extremely low aqueous solubility (merely 1 ng/mL), which increases to 5 μg/mL in an acid solution.[22] The first measurements of ITZ using differential scanning calorimetry (DSC) were performed by Six et al.[23] They observed two additional endothermic phase transitions in thermograms, at T = 346 and 363 K, located above the glass-transition temperature (T_g = 332 K). The peak occurring at 363 K was interpreted as the transition from the isotropic liquid to the chiral nematic mesophase, while the transition at a lower T (= 346 K) was considered as most likely caused by a restriction in the rotation of molecules. Further studies on the molecular dynamics of ITZ carried out by Tarnacka et al.[24] clearly indicated that the observed endothermic events are indeed associated with the formation of the nematic N (363 K) and smectic Sm (346 K) phases. Since that time, ITZ has been thoroughly studied by different research groups.[25−34] Furthermore, new reports still continue to emerge, shedding light on their remarkably intriguing LC properties and the possibilities for their modification. Herein, one can mention a paper by Teerekapibal et al., who investigated the influence of the cooling rate (ϕ) of liquid ITZ on the occurrence of mesophases.[35] The experiments have demonstrated that when ϕ is equal to 20 K/s, the transition from N to Sm phase is completely suppressed, while at the standard ϕ (10 K/min), the latter phase is formed. Moreover, a recent study by Heczko et al. has shown that the rapid compression of liquid API has an effect similar to fast cooling—an effective suppression of the N−Sm transition.[26] As a result, in both cases (rapid cooling and compression), only the nematic order was preserved in the glassy phase. Another interesting approach to tuning molecular order in ITZ was presented by Ediger's group, where the authors in a series of articles indicated that by varying temperature and the rate of vapor deposition of ITZ on a substrate, one can modify the molecular arrangement in this system.[31,32] Finally, it should be mentioned that Knapik-Kowalczuk et al.[33] and Mierzwa et al.[34] demonstrated that another external force, i.e., mechanical shearing, influences ITZ spatial alignment.

Herein, it is worth noting that apart from the physical factors affecting the LC ordering of ITZ, the role of the addition of low- and high-molecular-weight compounds is extensively studied. In the paper by Kaminska et al., it was demonstrated that in the ITZ-acetylated maltose amorphous solid dispersions (ASDs) with various API contents, both LC transitions are effectively suppressed.[35] In another work, Amponsah-Efah et al. reported that the addition of glycerol has a significant effect on the phase behavior of this LC pharmaceutical. Interestingly, they observed a spectacular change in the phase sequence and the order of phase transitions in the considered ITZ-glycerol binary mixture.[36] Another intriguing research showed the impact of various konazoles on the LC properties of ITZ. The authors indicated that with an increasing content of three of the used APIs, i.e., ketonazole, fluconazole, and voriconazole, both the Sm and N ordering in ITZ are suppressed.[37] Furthermore, there are reports depicting the effect of polymer addition on the LC order of ITZ. Cruz et al. revealed that the type of poly(ethylene glycol) used has a significant impact on the suppression or enhancement of the Sm phase in API particles, thereby contributing to the improvement or deterioration of the drug's solubility, respectively.[38] It is also worth noting that in the majority of articles addressing formulations of API−polymer systems, researchers predominantly used commercially available macromolecules. In particular, there are many works focused on ASDs of ITZ with Soluplus (poly(vinyl caprolactam)−poly(vinyl acetate)−poly(ethylene glycol) graft copolymer),[39] KollidonVA64 (vinylpyrrolidone−vinyl acetate copolymer),[40] Kollicoat IR (polyethylene glycol−poly(vinyl alcohol) graft copolymer),[41] or EudragitE100 (poly(methacrylate)s derivative).[40] However, in the mentioned papers, the authors noted only that polymers partially suppress the Sm and/or N order of ITZ but do not cause their complete and permanent disappearance. Only DiNunzio et al. showed that the preparation of fully amorphous binary mixtures of ITZ with poly(vinyl acetate phthalate) by ultrarapid freezing leads to a significant improvement in ITZ bioavailability. Unfortunately, in this work, the authors did not discuss whether LC phases reconstruct with time.[42]

Furthermore, in the literature, there are no reports that show directly how the polymer structure affects the solubility and LC ordering of ITZ. There is also a general interest in understanding how other macromolecules (beyond commercial polymers) influence the formation of mesophases in this API. Thus, to cover this intriguing research gap, we performed pioneering studies on the impact of poly(vinylpyrrolidone) (PVP) topology on the disruption/suppression of the LC order of ITZ, a possible reconstruction of smectic or nematic order, as well as the solubility of this active substance.

MATERIALS AND METHODS

Materials. 1-Vinyl-2-pyrrolidone (VP, >99%, Sigma-Aldrich, Poznan, Poland) was passed through an alumina column before use to remove the inhibitor. 2,2′-Azobis(2-methylpropionitrile) solution (AIBN, 0.2 M in toluene, Sigma-Aldrich, Poznan, Poland), cyanomethyl methyl(4-pyridyl) carbamodithioate (CTA1, 98%, Sigma-Aldrich, Poznan, Poland), 1,3,5-tris(bromomethyl)benzene (97%, Sigma-Aldrich, Poznan, Poland), sodium diethyldithiocarbamate trihydrate

https://doi.org/10.1021/acs.molpharmaceut.4c00215
Mol. Pharmaceutics 2024, 21, 3027−3039

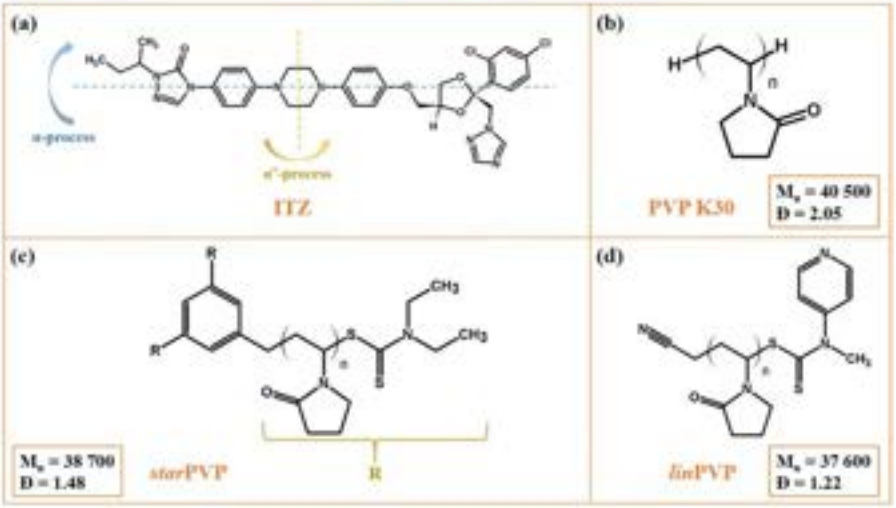

Figure 1. Chemical structure of (a) ITZ with marked motions being the source of two relaxation processes (α and α'), (b) commercially available PVP K30, (c) self-synthesized *star*PVP, and (*d*) self-synthesized *lin*PVP.

(Sigma-Aldrich, Poznan, Poland), diethyl ether (pure for analysis, Chempur, Piekary Slaskie, Poland), methanol (99.85%, PureLand, Stargard, Poland), dichloromethane (DCM, 99%, Karpinex, Warszawa, Poland), chloroform-*d* (99.8% D, contains 0.03% *v*/*v* TMS, Sigma-Aldrich, Poznan, Poland), PVP K30 (M_n = 40 500, $Đ$ = 2.05, Sigma-Aldrich, Poznan, Poland), and neat ITZ (IUPAC name: (2*R*,4*S*)- rel-1-(butan-2-yl)-4-{4-[4-(4-{[(2*R*,4*S*)-2-(2,4-dichlorophenyl)-2-(1*H*1,2,4-triazol-1-ylmethyl)-1,3-dioxolan-4yl]methoxy}-phenyl)piperazin-1-yl]phenyl}-4,5-dihydro-1*H*-1,2,4-triazol-5-one, 99%, Sigma-Aldrich, Poznan, Poland) were used as received. The polymorphic form of the commercial ITZ was the stable form I (triclinic space group P1 with 4 molecules per unit cell and lattice parameters: $a \approx 8.62$ Å, $b \approx 20.15$ Å, $c \approx 21.04$ Å, $\alpha \approx 73.49°$, $\beta \approx 89.07°$, $\gamma \approx 79.78°$).[43,44] The same polymorphic form was observed after the recrystallization of ITZ from binary mixtures with PVP.

Procedure of Preparing ITZ−PVP Mixtures. Amorphous solid dispersions (ASDs) composed of ITZ and PVP polymers, including a commercial PVP K30, self-synthesized linear, and star-shaped PVP samples (see Figure 1), were obtained using the melt-cooling method. The ITZ−PVP systems were prepared at the same weight ratio of API to polymer, i.e., 95:5 *w*/*w*. In the case of ITZ−*star*PVP, the 90:10 and 85:15 *w*/*w* systems were also examined. To determine a homogeneous mixture, appropriate amounts of neat ITZ and PVP were weighed, carefully transferred to a metal plate, and preliminarily mixed using a spatula. Subsequently, the plate with the API−polymer system was transferred to a hot plate heated to a temperature of 453 K. After a while, ITZ began to melt and the entire binary mixture was stirred until the complete mixing of PVP in the API. Once homogeneity of the system was ensured, the sample was vitrified by rapidly transferring it to a precooled copper substrate. Herein, it is worth noting that the same melt-cooling procedure was used to obtain the amorphous form of neat ITZ.

Fourier-Transform Infrared Spectroscopy (FTIR). FTIR spectra were collected on a Nicolet iS50 FTIR spectrometer (Thermo Scientific) with a built-in diamond iS50 ATR sampling station in the range of 4000−400 cm^{-1} with a resolution of 4 cm^{-1}. Sixteen scans were averaged for each spectrum.

Differential Scanning Calorimetry (DSC). Differential scanning calorimetry measurements were performed using a Mettler−Toledo DSC apparatus (Mettler−Toledo International, Inc., Greifensee, Switzerland) equipped with a liquid nitrogen cooling accessory and an HSS8 ceramic sensor (heat flux sensor with 120 thermocouples). Temperature and enthalpy calibrations were performed using indium and zinc standards. All investigated samples (neat PVP polymers and ITZ−PVP, 95:5 and 85:5 *w*/*w* systems) were scanned at a rate of 10 K/min over a temperature range from 298 to 480 K. Moreover, additional DSC studies at heating rates of 5 and 20 K/min were conducted for ITZ−PVP 95:5 *w*/*w* mixtures.

X-ray Diffraction (XRD). X-ray diffraction experiments were carried out using a Rigaku D/Max Rapid II diffractometer equipped with a rotating Ag anode and an incident beam (002) graphite monochromator (wavelength of the incident beam λ = 0.56 Å). Samples were measured in borosilicate glass capillaries with the Debye−Scherrer geometry. The diffraction patterns were collected in a single shot using a two-dimensional (2D) image plate detector and transferred to the function of the scattering vector $Q = 4\pi \sin\theta/\lambda$, where 2θ is the scattering angle. The background intensity from the empty capillary was subtracted from the data collected for the samples. The temperature during the measurements was 298 K. The samples were closed and long-term stored in capillaries at 323 K. Before XRD measurements, each sample was dried in a vacuum desiccator for at least 1 h to remove any moisture.

Broad-Band Dielectric Spectroscopy (BDS). Isobaric measurements of the dielectric permittivity were performed using the Novo-Control α dielectric spectrometer (Novocontrol Technologies GmbH & Co., KG, Hundsangen, Germany) over a frequency (f) range from 1×10^{-2} to 1×10^{6} Hz. The samples were placed between two stainless steel electrodes (diameter: 15 mm, gap: 0.052 mm) and mounted on a

https://doi.org/10.1021/acs.molpharmaceut.4c00215
Mol. Pharmaceutics 2024, 21, 3027−3039

cryostat. During measurement, each sample was maintained under a dry nitrogen gas flow. The temperature was controlled by a Quatro System using a nitrogen gas cryostat, with stability better than 0.1 K. The dielectric measurements of all examined samples were carried out in a wide temperature range (both above and below the T_g) from 173 to 363 K.

Solubility Studies. Before the dissolution tests, the sample was pulverized using a mortar and pestle and the resulting powder was sifted between 45 and 150 μm screens. The study examined the dissolution rate of itraconazole in a 0.1 M hydrochloric acid solution (pH = 1) at 37 °C using a USP apparatus II PTWS 820D (PharmaTest Apparatebau AG, Hainburg, Germany). Around 300 mg of each sample was placed in 300 mL of medium and stirred at 150 rpm for 120 min. The concentration of the dissolved drug substance was determined by the ultraviolet/visible (UV/vis) method at 255 nm using a T70 UV/vis split-beam spectrophotometer equipped with flow-through quartz cuvettes with a path length of 10 mm (PharmaTest AG, Hainburg, Germany). Measurements were taken every minute until 10 min of the test, then every 5 min, and beyond 60 min every 15 min until the end of the test.

RESULTS AND DISCUSSION

Innovative Polymeric Materials. First, we briefly outline the motivation and the importance of this study. For many years, PVP has been widely used in the medical, cosmetic, and food industries due to its unique chemical and biological properties: it is nontoxic to humans, biocompatible, and highly water-soluble.[45] Other properties, such as film-forming ability, chemical and thermal resistance, and its amorphous character, are also desirable and widely utilized in the above-mentioned industrial sectors.[46,47] Hence, there are numerous works in the literature where the influence of this macromolecule on improving the solubility of APIs by forming ASDs is considered. Unfortunately, despite the great importance of this polymer, scientists still only examine the role of molecular weights (M_n) of commercially available PVP,[48−51] while the impact of other factors, such as polymer topology or dispersity ($Đ$) on the pharmacokinetic properties of numerous pharmaceuticals, is not described at all. Herein, it should be stressed that this is most likely because the large-scale PVP synthesis is based on an uncontrolled free radical process.[52,53] As a result, the obtained linear macromolecules consist of both long and short chains, ultimately leading to high $Đ$ values (most often above 2, which means poorly defined macrostructural parameters). Moreover, free radical polymerization is mainly employed to produce high-M_n PVP, posing a potential threat of accumulation in the human body or the environment.[54,55] It should also be kept in mind that for special applications (e.g., in pharmaceutical formulation designing), strict control of polymer parameters is highly required. Therefore, searching for new methods to obtain PVP with precisely desired parameters appears entirely justified.

Herein, it is important to emphasize that although many macromolecules available on the market can improve the pharmacokinetic properties of poorly soluble drugs, PVP appears to be particularly important. The main motivation behind the selection of exactly this polymer for our studies was a unique opportunity to synthesize macromolecules of various topologies and low dispersities, which is far more complicated in the case of other commercially available polymers. Consequently, it was possible to probe the impact of polymer topology on the physicochemical properties, spatial molecular organization, and API solubility in an amorphous solid dispersion.

Recognizing such an extremely intriguing research gap, we have recently developed new polymeric materials with linear (*lin*PVP) and star-shaped (*star*PVP) topologies, employing thermally initiated reversible addition−fragmentation chain-transfer (RAFT) polymerization. Utilizing this method allowed us to gain control over the polymerization process and obtain well-defined polymers characterized by excellent macrostructural parameters in comparison to the commercial sample. Moreover, the chain-end functionalization of polymers synthesized *via* RAFT allows for further modifications of the macromolecules as needed (for example, through copolymerization), contrary to the commercially available PVP (see Figure 1). So far, we have used these PVPs only once to study their influence on the physical stability of amorphous metronidazole and the rate of its recrystallization from ASDs.[56] Therefore, a highly interesting scientific issue would be to investigate how these innovative self-synthesized materials will affect the properties of a completely different API, namely, ITZ, classified as a liquid crystal, and thereby exhibiting interesting molecular ordering that further influences its solubility. The detailed synthesis procedures, ^{1}H and ^{13}C NMR spectra confirming the structures of the obtained polymers, and SEC traces allowing the determination of the macrostructural parameters (M_n, $Đ$) can be found in our previous publication.[50] However, as a reminder, all key information regarding the synthesis of well-defined PVPs with various topologies is also provided in the Supporting Information, SI of this work (see Figures S1−S7 and the description).

Preparation of ITZ−PVP Binary Formulations and FTIR Studies. First, it is worth noticing that before preparing ASDs with ITZ, we performed cytotoxicity tests on normal human dermal fibroblasts (NHDFs) for both synthesized samples: *lin*PVP and *star*PVP, as well as a reference sample—PVP K30 (see Figure S8 in the SI). The results of these tests, described in detail in the SI, confirmed that the obtained macromolecules exhibit high neutrality and can be successfully utilized as additives in medicinal products. Moreover, terminal groups in the macromolecules obtained via RAFT and star initiator do not affect the biocompatibility of the newly synthesized polymers in any way.

Hence, with the results of cytotoxicity tests, we proceeded to prepare ASDs by the melt-cooling method. Note that a detailed description of this experimental technique can be found in the Materials and Methods Section. The created binary mixtures consisted of ITZ (known for its liquid crystalline character) and three different polymeric materials: (i) commercial PVP K30 (M_n = 40,500, $Đ$ = 2.05), (ii) self-synthesized linear PVP, *lin*PVP (M_n = 37,600, $Đ$ = 1.22), and (iii) self-synthesized three-armed star-shaped PVP, *star*PVP (M_n = 38,700, $Đ$ = 1.48).[50] While preparing ASDs, we noticed an extremely intriguing relationship. Both linear polymeric matrices (PVP K30, *lin*PVP) are mixed with ITZ in a polymer amount of up to 5 wt %, whereas *star*PVP exhibits a significantly better capability for homogeneous mixing with the API (even up to 15 wt %). At this point, it is essential to emphasize that all used macromolecules have a similar molecular weight (M_n ∼ 40,000). Therefore, the observed effect of better miscibility of *star*PVP with ITZ cannot be attributed to M_n but rather to the topology of the applied

https://doi.org/10.1021/acs.molpharmaceut.4c00215
Mol. Pharmaceutics 2024, 21, 3027−3039

macromolecules (see Figure 1). To better understand this phenomenon, infrared measurements were conducted for neat active substance (ITZ) and polymers (PVP K30, *lin*PVP, and *star*PVP), as well as ITZ−PVP 95:5 *w*/*w* ASDs (see Figure S9 in the SI). Interestingly, no differences in the shape or position of individual bands/peaks throughout the spectral range were observed for neat macromolecules and binary formulations with different PVPs. The obtained results suggest that, in this case, the polymer topology does not affect the type of API−PVP intermolecular interactions. Thus, it can be assumed that the observed differences in miscibility are rather related to how ITZ molecules are localized/distributed along the polymer chains of different matrices, which consequently may lead to differences in improvement in the pharmacokinetic properties of API depending on the type and amount of macromolecule used in binary mixtures.

Differential Scanning Calorimetry (DSC) Data. Subsequently, we carried out calorimetric measurements to characterize the thermal properties and phase transitions of both neat substances (ITZ, PVP K30, *lin*PVP, *star*PVP) and API−PVP binary systems. DSC thermograms collected for neat polymers are shown in Figure S10 in the SI, while the data obtained for amorphous ITZ and ITZ−PVP mixtures were compiled in a single graph (see Figure 2). As can be seen,

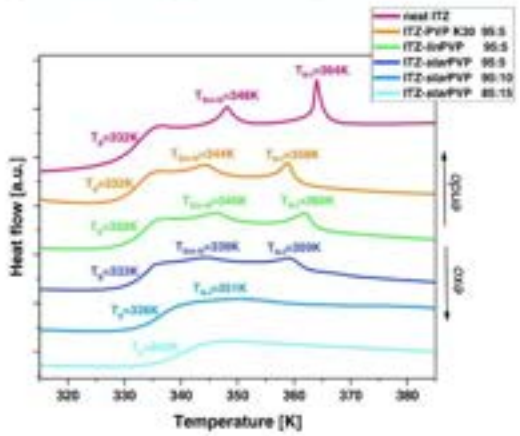

Figure 2. DSC thermograms (ϕ = 10 K/min) collected for neat glassy/amorphous ITZ and ITZ−PVP ASDs with different weight ratios (*w*/*w*) of both components.

during the heating of neat ITZ (the second scan after initial melting of the crystalline sample and supercooling) at a rate of 10 K/min, three distinct endothermic events are visible. The first phenomenon occurring at the lowest temperature (T) is associated with the glass-transition phenomenon (at T_g = 332 K). Meanwhile, the two remaining endothermic peaks at higher T are linked to the LC ordering of ITZ. More precisely, the thermal event at 348 K corresponds to the transition of API from the smectic (Sm) to nematic (N) phase (T_{Sm-N}), while that at 364 K is related to a transition from the N to isotropic (I) phase (T_{N-I}). Herein, it is worth noting that the obtained thermogram of neat ITZ and the determined phase transitions are in good agreement with the data reported in previous works.[10,19,26−33,35]

Next, we registered thermograms of ITZ−PVP 95:5 *w*/*w* ASDs. As can be observed in Figure 2, regardless of the type of polymer applied in the binary system, the T_g remains unchanged with respect to neat API, while the temperatures of both LC transitions shift toward lower values of T: to 339 K (T_{Sm-N}) and 359 K (T_{N-I}). It is also worth noting that compared to neat API, the peak intensities representing liquid crystalline transitions have decreased, with the most significant intensity reduction observed for the ITZ−*star*PVP mixture.

As mentioned above, due to the possibility of obtaining homogeneous ITZ−*star*PVP systems with a higher content of the polymer, calorimetric studies were also performed on ASDs, where the weight ratios of API to PVP were 90:10 and 85:15, respectively. The analysis of the obtained thermograms showed that in the case of the ITZ−*star*PVP 90:10 *w*/*w* mixture, there is a distinct glass transition, but it is slightly shifted toward higher T (T_g = 336 K) due to the higher polymer concentration in the sample. What is particularly interesting, the Sm−N transition is completely suppressed, while the N−I transition has very low intensity and is strongly shifted toward lower T (T_{N-I} = 351 K). For the ITZ−*star*PVP 85:15 *w*/*w* system, only one transition corresponding to the glass-transition phenomenon is visible at T_g = 340 K. In turn, both LC transitions are completely suppressed. It means that the ITZ−*star*PVP 85:15 *w*/*w* mixture is fully amorphous, which is not possible to achieve in the case of binary systems containing linear polymers (PVP K30 and *lin*PVP); see Figures 2 and S11 in the SI showing DSC curves for ITZ−PVP K30 and ITZ−*lin*PVP, 85:15 *w*/*w* mixtures. The data presented in the SI clearly demonstrated that the increasing content of *lin*PVP and PVP K30 does not change the T_g of the whole system, indicating the lack of homogeneity of the binary mixtures for this composition. Hence, the novel star-shaped PVP material appears to be unique compared to both linear polymers. It should be stressed that the obtained results seem to be among the few, where such a small macromolecule content (even 5 wt %) significantly suppresses LC transitions. Moreover, the newly obtained star-shaped macromolecule (unavailable commercially) effectively damps the Sm−N and N−I transitions even at a 15 wt % concentration, imparting a fully amorphous character to ITZ.

It should also be mentioned that we carried out additional DSC measurements with lower and higher ϕ values (i.e., 5 and 20 K/min) on the studied systems. As expected, subtle shifts in the temperatures of all three phase transitions (T_g, T_{Sm-N}, T_{N-I}) toward higher values were observed with increasing heating rates (see Figure S12 in the SI).

X-ray Diffraction (XRD) Data. Noticing exceptionally intriguing results from calorimetric studies, we decided to perform further structural investigations of neat ITZ and analogous ITZ−PVP binary systems (the diffraction patterns of neat PVP polymers and ITZ−PVP K30 and ITZ−*lin*PVP, 85:15 *w*/*w* ASDs can be found in the SI). As illustrated in Figure 3, XRD patterns of ITZ and its ASDs with various PVP (95:5 *w*/*w*) samples show characteristic peaks in the small-*Q* range related to the LC order. Generally, in the case of API molecules arranged in Sm layers, a sequence of diffraction peaks at $Q \sim 0.2$, 0.4, and 0.6 Å^{-1} is usually reported.[30,34] For the N phase, these peaks are heavily suppressed. Here, significantly higher amplitudes of these small-*Q* peaks are visible for the neat ITZ sample compared to those of ASDs. This can be seen better in the inset in Figure 3a, where all diffractograms were set together. It should be pointed out that

https://doi.org/10.1021/acs.molpharmaceut.4c00215
Mol. Pharmaceutics 2024, 21, 3027−3039

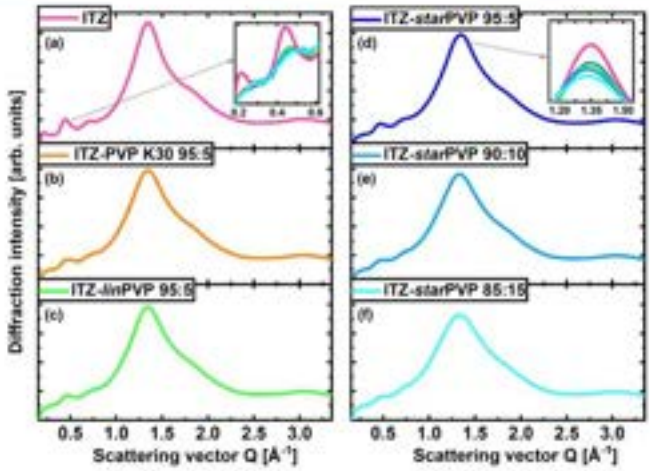

Figure 3. Diffraction patterns of (a) neat ITZ glass and indicated ASDs, (b) ITZ−PVP K30 95:5 w/w; (c) ITZ−*lin*PVP 95:5 w/w; (d) ITZ−*star*PVP 95:5 w/w; (e) ITZ−*star*PVP 90:10 w/w; and (f) ITZ−*star*PVP 85:15 w/w. The first inset (in panel a) shows the zoomed-in view of the compared diffractograms in the small-Q range, while the second inset (in panel d) presents the comparison of the main diffraction peak amplitude.

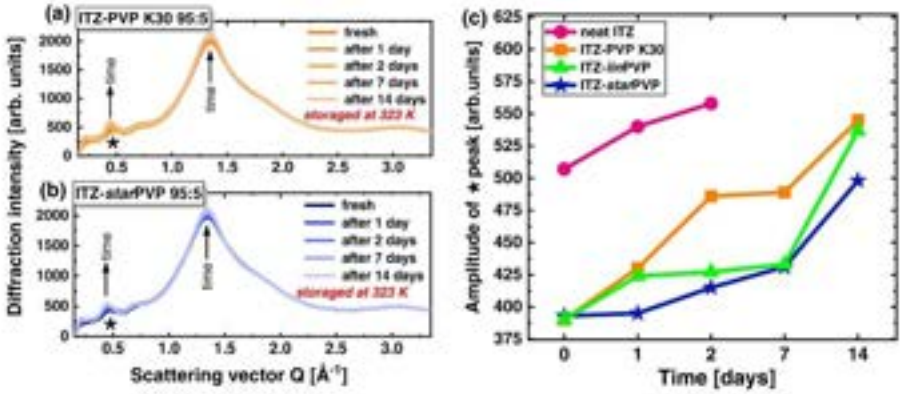

Figure 4. Temporal evolution of the diffraction patterns for (a) ITZ−PVP K30 and (b) ITZ−*star*PVP 95:5 w/w systems. The peak at $Q \sim 0.47$ Å^{-1} marked with an asterisk * was taken for the quantification of the degree of the smectic order. Panel (c) presents the temporal evolution of the amplitude of the * maximum at $Q \sim 0.47$ Å^{-1} for all studied samples.

the presence of PVP does not practically influence the diffraction data of ASDs in this small-Q range. Thus, the suppression of Sm order in these binary systems seems to be due to changes in the ITZ structure caused by the polymer. The inset in Figure 3d shows that also the main diffraction peak of ITZ gets smaller by the presence of PVP, indicating that the nearest-neighbor organization of molecules is also more disordered. However, no big differences in the XRD patterns for various ITZ−PVP 95:5 w/w systems were noted. Nevertheless, the data for ASDs of API with varying wt % of *star*PVP demonstrate that with increasing polymer content, there is an evident suppression and a slight shift of the main diffraction peak toward lower Q-values (see the inset in Figure 3d), indicating a stronger disordering of the intermolecular structure of ITZ. Moreover, the low-Q peaks are smaller in 90:10 w/w ASD, suggesting that only the N order is preserved in this system, while in the 85:15 w/w mixture, the low-Q peaks practically totally disappear, so the structure of ITZ in this system resembles that of isotropic liquid.

Herein, it should be mentioned that additional XRD studies carried out for ITZ−PVP K30 and ITZ−*lin*PVP at 85:15 w/w ASDs confirmed the results of DSC measurements, indicating that these binary systems in contrast to PVP−*star*PVP 85:5 w/w ASD are nonhomogeneous. For more details, see Figure S13 and the description given in the SI.

Additionally, the differences between ITZ and various PVP 95:5 w/w systems were observed for the samples stored at 323 K, which is slightly below the T_g. Panels (a and b) in Figure 4 show the temporal evolution of the XRD patterns for the stored ITZ−PVP K30 and ITZ−*star*PVP 95:5 w/w ASDs, respectively. Similar data were collected for neat ITZ and the ITZ−*lin*PVP 95:5 w/w system. The results of these long-term structural studies indicated a gradual recovery of the Sm order in time for all samples. The degree of this order was quantified

https://doi.org/10.1021/acs.molpharmaceut.4c00215
Mol. Pharmaceutics 2024, 21, 3027−3039

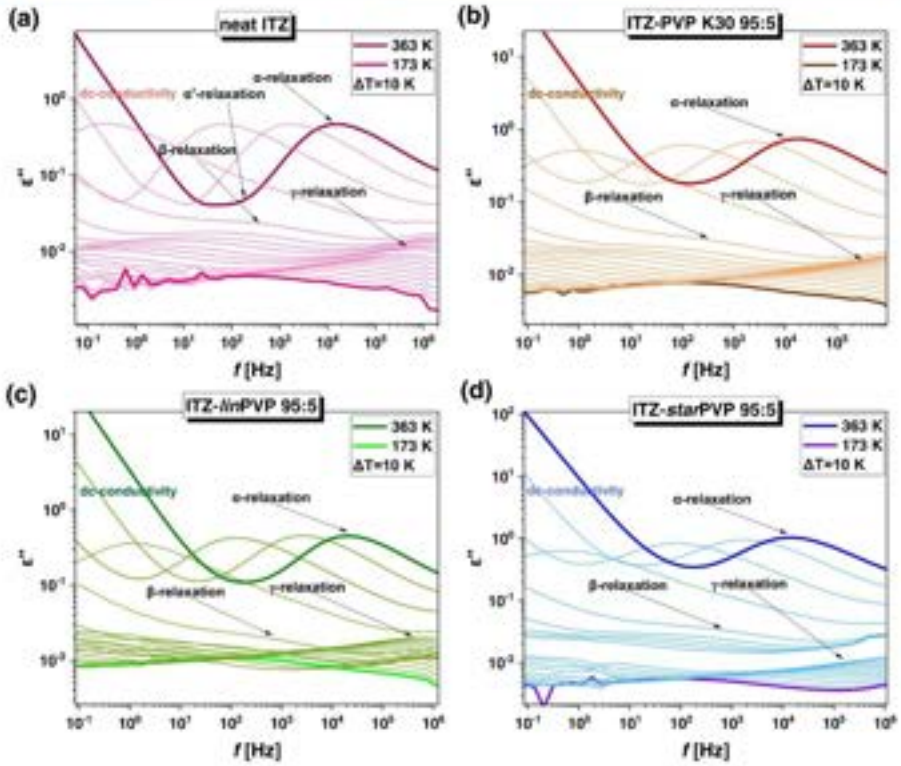

Figure 5. Dielectric loss spectra of (a) neat ITZ[17] and (b) ITZ−PVP K30, (c) ITZ−*lin*PVP, (d) ITZ−*star*PVP 95:5 *w*/*w* binary mixtures.

based on the amplitude of the peak maximum located at $Q \sim 0.47$ Å^{-1} (marked with an asterisk *), and the changes in the amplitude of this peak in time are presented in Figure 4c. The neat ITZ recrystallized after 2 days. Therefore, the data points for the neat API were limited to 2 days. In turn, the ITZ−PVP 95:5 *w*/*w* ASDs exhibited a gradual recovery of the Sm order with time, manifested by an increase in the amplitude of the * peak and no sign of recrystallization over 14 days. Interestingly, the rate of this structural transformation was different depending on the polymer—the ITZ−PVP K30 system was the least stable, and after 14 days, it recovered almost the same amplitude of the diffraction peak as neat ITZ after 2 days. Meanwhile, the ITZ−*star*PVP ASD was the most stable and had a lower amplitude of this peak after 14 days compared to the ITZ−PVP K30 and ITZ−*lin*PVP systems. The variations in the peak amplitude with time were also accompanied by a shift of the peak position toward $Q \sim 0.45$ Å^{-1}, so toward the position where this peak is located for neat ITZ. This suggests that the addition of PVP polymers may tilt the ITZ molecules by an angle with respect to the layer normal. However, the annealing causes returning of molecules to a more parallel alignment to the layer normal. Nevertheless, it should be noted that these results are related to the annealing of neat ITZ and binary mixtures at 323 K. At room temperature, the rate of restoring Sm phase in API is significantly reduced and it takes months or even years to reach the order characteristic for the vitrified ITZ sample.

Broad-Band Dielectric Spectroscopy (BDS) Data. Having the results from DSC and XRD experiments, we carried out molecular dynamics studies of ITZ−PVP ASDs using the BDS method. Dielectric data for neat API were taken from our previous paper.[17] The measurements were conducted at ambient pressure over a wide range of temperatures, both above and below the glass-transition temperature (T_g). The spectra of dielectric loss obtained for neat API and all API−polymer 95:5 *w*/*w* ASDs are presented in Figure 5. Note that BDS spectra were also collected for the ITZ−*star*PVP 85:15 *w*/*w* mixture (see Figure S15 in the SI). As can be observed in Figure 5, at $T > T_g$, two well-visible processes, which shift toward lower f with decreasing T, can be identified in the spectra of each examined sample. The first one is the direct-current (dc) conductivity associated with the transport of ionic impurities, which are always present in the liquid. Meanwhile, the second process located at higher frequencies (f) is the structural relaxation (α) originating from cooperative movements of all molecules in the sample and responsible for the glass transition. Herein, it is worth noting that in the case of ITZ (a compound exhibiting liquid crystalline character), the α-relaxation is associated with complex fluctuations of rotating molecules around its long axis (see Figure 1a, blue arrow). Moreover, in the spectra of neat API (Figure 5a), at f lower than those where the α-process occurred, an additional dielectric response, called the α'-process or flip−flop rotation, can be observed. According to the literature data, this relaxation mode is closely related to the rotational motions

https://doi.org/10.1021/acs.molpharmaceut.4c00215
Mol. Pharmaceutics 2024, 21, 3027−3039

of the ITZ molecule around its short axis (see Figure 1a, yellow arrow).[17,37,57] Unfortunately, it is not directly discernible in the spectra of each studied ITZ−PVP 95:5 *w*/*w* ASDs.

In turn, the dielectric spectra of neat ITZ and ITZ−PVP systems measured in the glassy state ($T < T_g$) revealed the presence of two well-separated secondary relaxations, i.e., the slower β and the faster γ. As demonstrated in our previous papers concerning ITZ and its ASDs with various low-molecular-weight excipients (i.e., acetylated maltose and other APIs from konazole groups), the former one (called β) is a Johari−Goldstein (JG) process having an intermolecular origin, while the latter one (called γ) is a non-JG relaxation of intramolecular character, i.e., a non-JG type.[15,17]

As mentioned above, the α'-process is visible in dielectric spectra of neat ITZ, while for ITZ−PVP 95:5 *w*/*w* mixtures, this relaxation is not directly observed. To confirm whether the flip−flop rotation (connected directly with the LC ordering in ITZ) indeed occurs in the case of investigated ASDs, we performed the dc-conductivity cutting procedure for each sample (also for ITZ−*star*PVP 85:15 *w*/*w* system) and then compared the shapes of the peaks. The obtained results are presented in Figure 6. As can be seen, for neat API, the α-

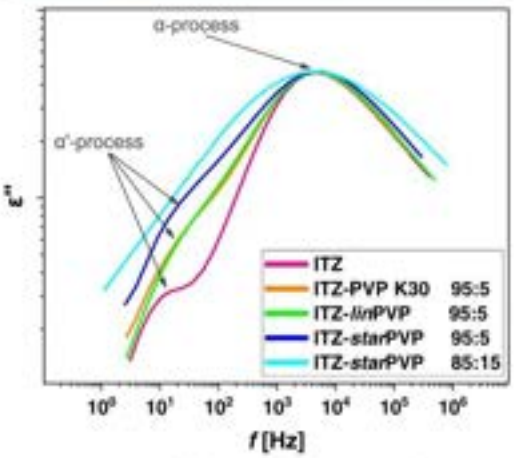

Figure 6. Comparison of dielectric loss spectra measured for neat ITZ and ITZ−PVP binary mixtures (at indicated weight ratios) at T = 347 K.

dispersion is the narrowest and the α'-mode is separated. In turn, for each ITZ−PVP 95:5 *w*/*w* ASD, the α-peak is significantly broadened and the α'-process is less resolved compared to that of neat API. Importantly, for the ITZ−*star*PVP 85:15 *w*/*w* sample, the α-dispersion is the widest, and the α'-mode is completely undetectable (see Figure 6, light blue line). This indicates that in all binary formulations, despite the low polymer content (only 5%), there is a strong damping of the liquid crystalline order of ITZ. Furthermore, a complete suppression of both LC phase transitions occurs in the case of the ITZ−*star*PVP 85:15 *w*/*w* system. Thus, the obtained outcomes of dielectric measurements perfectly correspond to those determined from calorimetric and structural experiments. Herein, it should be noted that a similar scenario, i.e., suppression of LC order by other excipients (acetylated maltose and several APIs: ketoconazole, fluconazole, voriconazole), confirmed also by the decreased amplitude/or even the absence of α'-mode in dielectric spectra, has been reported in our previous works.[35,57]

To get a complete overview of the relaxation processes occurring in all investigated samples (neat API and API−PVP ASDs) and characterize their molecular dynamics, the dielectric loss spectra were analyzed using the Havriliak−Negami (HN) function with an additional term describing the dc-conductivity[59]

$$\varepsilon(\tilde{\omega})'' = \frac{\sigma_{dc}}{\varepsilon_0 \tilde{\omega}} + Im \sum_{i=1}^{2} \left(\varepsilon_\infty \frac{\Delta\varepsilon_i}{[1 + (i\tilde{\omega}\tau_{HN})^{\alpha_{HN}}]^{\beta_{HN}}} \right) \quad (1)$$

where σ_{dc} is the dc-conductivity, ε_0 is the vacuum permittivity, $\tilde{\omega}$ is an angular frequency ($\tilde{\omega} = 2\pi f$), ε_∞ is the high-frequency limit permittivity, $\Delta\varepsilon$ is the dielectric relaxation strength, τ_{HN} is the HN relaxation time, and α_{HN} and β_{HN} are the shape parameters representing the breadth and asymmetry of the given relaxation peaks, respectively.

Next, the relaxation times of α- and α'- ($T > T_g$), as well as the β- and γ- ($T < T_g$) processes were calculated from τ_{HN} using the following formula[60]

$$\tau = \tau_{HN} \left[\sin \frac{\alpha_{HN}\pi}{2 + 2\beta_{HN}} \right]^{-1/\alpha_{HN}} \left[\sin \frac{\alpha_{HN}\beta_{HN}\pi}{2 + 2\beta_{HN}} \right]^{1/\alpha_{HN}} \quad (2)$$

Figure 7a presents τ_α and $\tau_{\alpha'}$ plotted as functions of the inverse temperature for neat API and investigated ITZ−PVP ASDs. Interestingly, one can notice clear changes in the dependence of $\tau_{\alpha'}$ versus $1/T$, which are evident at temperatures close to the two LC phase transitions (Sm−N and N−I; see dashed black lines in Figure 7a). It indicates a strong disruption of the molecular order of ITZ, to which the primary α'-process is exceptionally sensitive. However, regardless of the type of polymer used, α-relaxation times for each ITZ−PVP 95:5 *w*/*w* system and their temperature dependences are very similar and differ only slightly from those determined for neat API. This is in accordance with calorimetric data showing the same values of T_g (= 332 K) for neat ITZ and 95:5 *w*/*w* ASDs. It should also be observed that there is a divergence between τ_α vs $1/T$ plots for the ITZ−*star*PVP 85:15 *w*/*w* formulation compared to other, i.e., 95:5 *w*/*w* mixtures. The reason for that is a difference in T_g (see Figure 2, ΔT_g = 8 K) for these samples.

We also characterized the molecular dynamics of neat ITZ and its ASDs with various PVPs at T below T_g. As mentioned earlier, two secondary relaxations (β and γ) can be detected in the dielectric spectra of each examined system (Figure 5). The relaxation times of both processes obtained from the analysis of the loss spectra using eq 1, plotted vs $1/T$, are shown in Figure 7b. To calculate the activation energy barrier (E_a) for these relaxations, the presented data were fitted to the Arrhenius equation

$$\tau_x = \tau_{\infty,x} \exp\left(\frac{E_a}{RT}\right); \; x = \beta, \gamma \quad (3)$$

where R is a gas constant. The determined values are listed in Table 1. As can be seen, E_β for neat API is equal to 93.8 kJ/mol, while for ITZ−PVP systems, it ranges from 76.1 to 103.8 kJ/mol depending on the type of polymer matrix and its content in ASDs. It indicates significant fluctuations in the molecular order of ITZ under the influence of various

https://doi.org/10.1021/acs.molpharmaceut.4c00215
Mol. Pharmaceutics 2024, 21, 3027−3039

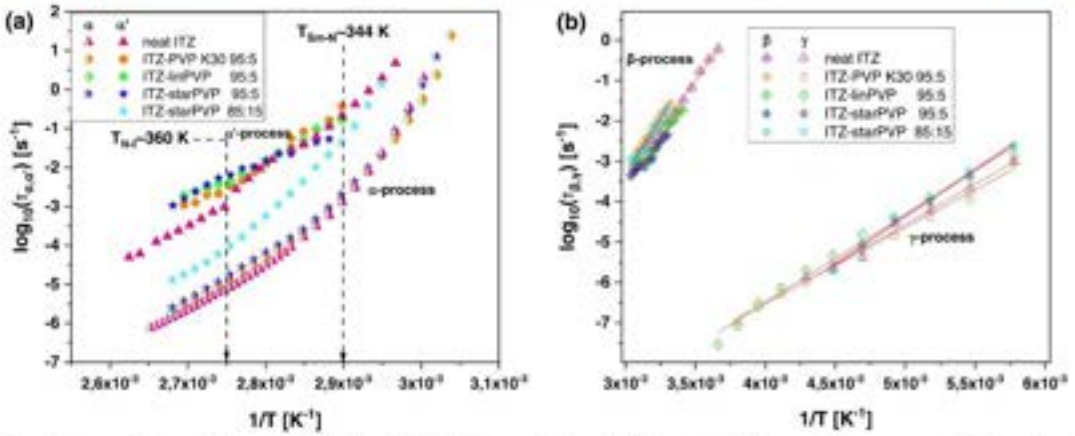

Figure 7. Dependencies of (a) $\log_{10}\tau_{\alpha}$ (half-filled symbols) and $\log_{10}\tau_{\alpha'}$ (filled symbols) as well as (b) $\log_{10}\tau_{\beta}$ and $\log_{10}\tau_{\gamma}$ versus $1/T$ for neat ITZ and ITZ−PVP ASDs with different weight ratios. Solid red lines represent Arrhenius fits. The data for neat ITZ, shown in both panels, were taken from ref. 37

Table 1. Values of Activation Energies of β- and γ-Secondary Relaxations Obtained from Dielectric Measurements for Neat API and ITZ−PVP Binary Mixtures

sample	E_{β} [kJ/mol]	E_{γ} [kJ/mol]
neat ITZ	93.8 ± 1.5[a]	38.1 ± 1.9[a]
ITZ−PVP K30 95:5 w/w	103.8 ± 3.1	35.8 ± 1.0
ITZ−*lin*PVP 95:5 w/w	90.6 ± 3.0	41.8 ± 1.5
ITZ−*star*PVP 95:5 w/w	76.1 ± 5.2	44.6 ± 1.3
ITZ−*star*PVP 85:15 w/w	99.7 ± 4.6	44.6 ± 1.8

[a]The data were taken from ref. 37

macromolecules, which consequently affects the dynamics of the slower β-relaxation (a JG type). On the other hand, the activation barrier for the γ-process (a non-JG relaxation) does not show large variations in the studied systems (i.e., E_{γ} varies from 35.8 to 44.6 kJ/mol, E_{γ} = 38.1 kJ/mol for neat ITZ). It is worth noting that in the case of ITZ−*star*PVP mixtures, the calculated E_{γ} was the highest. However, regardless of the weight percentage of the star-shaped polymer in the formulation, it remained unchanged (i.e., E_{γ} = 44.6 kJ/mol for ASDs with 5 and 15 wt % of the polymer). It implies that the γ-process is slightly sensitive to the type of macromolecule but not to its content in ASD. In summary, the sensitivity of

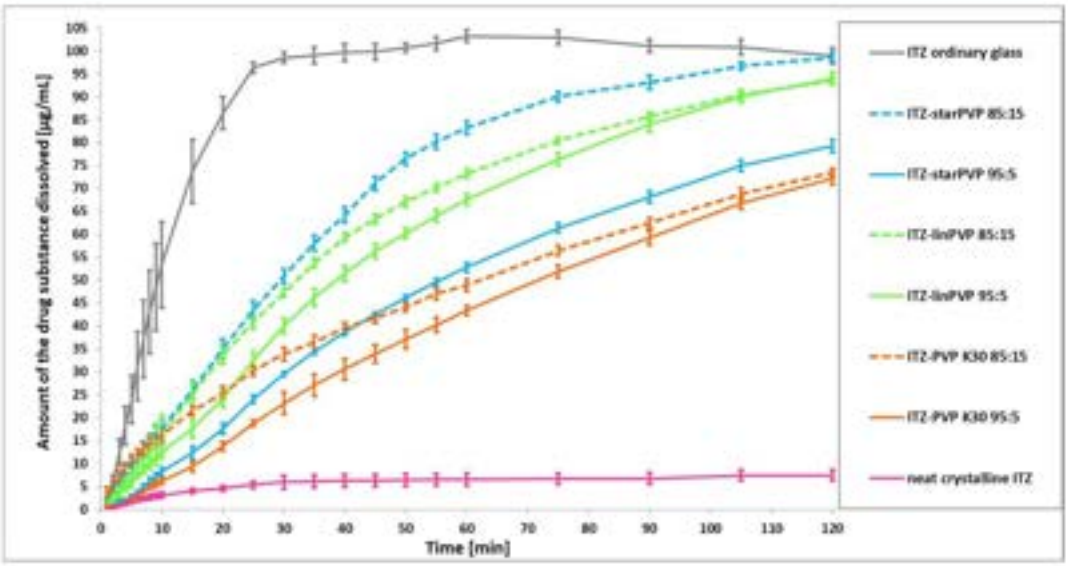

Figure 8. Dissolution kinetics of ITZ and ASDs of ITZ with various PVPs (95:5 and 85:15 w/w) in 0.1 M HCl.

https://doi.org/10.1021/acs.molpharmaceut.4c00215
Mol. Pharmaceutics 2024, 21, 3027−3039

the β-relaxation to the molecular ordering of ITZ in binary systems is greater compared to that of the γ-relaxation. Herein, it should be recalled that in the case of ASDs of ITZ with other konazoles prepared in various weight ratios, we also observed a similar scenario (i.e., the LC ordering was mainly affected by the dynamics of the β-process, not the γ-mode).[37]

Solubility Studies. In the final part of our work, we have conducted solubility studies on neat ITZ, as well as API dispersed in three different polymeric matrices (PVP K30, *lin*PVP, and *star*PVP). The dissolution tests of itraconazole were performed using a hydrochloric acid solution with a pH of 1 as a medium representing the fasted human stomach. It is generally assumed that the gastric emptying time on an empty stomach is usually around 0.5−2 h.[6,1,62] Therefore, in our study, we have assumed a measurement time of approximately 120 min.

The outcomes of the experiments are listed in Figure 8. As can be seen, neat crystalline ITZ exhibits very poor solubility in an acidic medium, at a level of around 5 μg/mL, which is fully consistent with the data reported in the literature.[22,23] The amorphization, as also indicated in our previous paper,[35] results in a clear improvement of API solubility (~100 μg/mL after around 30 min). At this time, the drug substance is rapidly dissolved until a supersaturated state is achieved. However, after about 60 min of the test, the amount of dissolved amorphous ITZ begins to decrease slightly, suggesting the beginning of precipitation (the so-called spring and parachute effect).

For each of the ITZ−PVP systems tested, a significant increase in the solubility of the drug substance compared to that of the neat crystalline form was observed. Moreover, in contrast to amorphous ITZ, the dissolution rate is slower in all binary systems. However, a steady increase in the concentration of the dissolved API is visible over a 120 min period with no signs of precipitation. This supposition finds confirmation in the XRD pattern obtained for the representative 95:5 *w*/*w* binary system recovered from dissolution measurements. As shown in Figure S14 in the SI, in the tested ASD, ITZ did not recrystallize and, during the dissolution process, the smectic order was restored in the sample.

Interestingly, for ITZ−PVP 95:5 *w*/*w* ASDs, the greatest improvement in solubility was noted for the API dispersed in *lin*PVP. After approximately 120 min of the experiment, the released API from PVP K30, *lin*PVP, and *star*PVP matrices reached the following concentrations: 70, 90, and 75 μg/mL, respectively. Moreover, even though only *star*PVP exhibits the ability to create a homogeneous mixture with a polymer content of 15 wt %, we decided to prepare 85:15 *w*/*w* binary formulations containing each examined polymer for solubility measurements. Interestingly, as shown in Figure 8, for ITZ−PVP K30 and PVP−*lin*PVP systems, regardless of the API to polymer ratio, the solubility curves have a very similar course. However, the situation is entirely different for the ITZ−*star*PVP system. Namely, the solubility of ITZ−*star*PVP 85:5 *w*/*w* (100 μg/mL) is significantly improved in comparison to the same binary systems with 5 wt % of the polymer (75 μg/mL). These observations are related to the fact that the API does not form any LC phases in the ASD with 15 wt % of *star*PVP, which was confirmed before based on outcomes of DSC, XRD, and BDS studies.

The study clearly showed that the choice of polymer type is crucial for improving the solubility of the drug substance. Here, of all of the ASDs tested, the lowest enhancement was determined for the ITZ−PVP K30 systems (95:5 and 85:15 *w*/*w*), while the best was obtained for the API−*star*PVP 85:15 *w*/*w* mixture. A probable reason for the highest dissolution rate of API incorporated into a star-shaped PVP compared with linear polymeric matrices is the complete amorphization of the ITZ−*star*PVP 85:15 *w*/*w* system (the lack of LC ordering). Finally, one should comment on the slowing down of the dissolution rate of ITZ from binary mixtures with respect to neat amorphous API. We suppose that it might be related to the occurrence of some weak intermolecular interactions between both components. Moreover, one can also assume that PVP molecules although well soluble in water may limit access diffusion of solvent to ITZ. Alternatively, the change in the molecular organization of API molecules in the tested systems cannot be ruled out as well. However, these are just hypotheses that should be clarified in the future.

■ CONCLUSIONS

In this work, calorimetric, diffraction, dielectric, and solubility studies were carried out on ASDs composed of a liquid crystalline API itraconazole and three polymer matrices differing in (macro)structure: commercially available PVP K30, self-synthesized *lin*PVP, and self-synthesized three-armed *star*PVP. Special research attention was paid to examining the impact of polymer topology on changes in the LC order of examined API and the potential improvement of its pharmacokinetic properties. In the initial step of our research, we discovered a highly intriguing relationship. Namely, linear homopolymers (PVP K30, *lin*PVP) exhibited miscibility with the API only at a level of 5 wt %, while the star-shaped PVP mixed with ITZ up to 15 wt %. Calorimetric measurements revealed that each polymer matrix strongly influences both LC (Sm−N and N−I) transition temperatures in ITZ, while the glass-transition temperature remained unchanged compared to T_g of neat API. Importantly, for each ITZ−PVP 95:5 *w*/*w* ASD, a significant damping of the mentioned LC transitions was observed. Moreover, ITZ in the ASDs with 10 and 15 wt % of *star*PVP exhibited stronger suppression and destruction of LC order, respectively. Further structural studies confirmed this finding. Moreover, long-term XRD experiments demonstrated the greatest stability of ITZ−*star*PVP systems, indicating the slowest mesophase rebuilding compared with other ASDs. Additionally, dielectric measurements revealed changes in the temperature dependences of $\tau_{\alpha'}$ in the vicinity of calorimetric T_{Sm-N} and T_{N-I}, which meant that the α'-process is more sensitive to disruptions in the LC order than the α-one. It was also demonstrated that the fluctuations in molecular ordering affect the dynamics of the slower secondary β-process, while they have practically no impact on the faster γ-mode. Finally, dissolution rate measurements showed that the solubility of all examined ITZ−PVP ASDs in an acidic medium is significantly enhanced compared to neat crystalline API, and, contrary to the amorphous sample, the dissolution curves do not increase as rapidly, preventing saturation and the onset of ITZ precipitation. Importantly, the most significant improvement in solubility was observed for ITZ−*star*PVP 85:15 *w*/*w*, i.e., approximately 100 μg/mL—representing a 20-fold increase with respect to the neat crystalline API.

It can be assumed that the use of new star-shaped polymeric matrices as novel drug carriers is an interesting perspective. This may contribute to the improvement of ITZ as well as other poorly soluble APIs' dissolution, ultimately increasing the bioavailability of these drugs. Therefore, from the

https://doi.org/10.1021/acs.molpharmaceut.4c00215
Mol. Pharmaceutics 2024, 21, 3027−3039

pharmaceutical sector's perspective, the results of the performed studies are extremely promising. We believe that they open up a new pathway in scientific discussion regarding the influence of the topology of a relatively well-known polymer, PVP, on the molecular ordering of poorly soluble drugs and the desired improvement in their bioavailability.

■ ASSOCIATED CONTENT

Supporting Information

The Supporting Information is available free of charge at https://pubs.acs.org/doi/10.1021/acs.molpharmaceut.4c00215.

Synthesis of trifunctional CTA, *lin*PVP, *star*PVP, including ^{1}H NMR and ^{13}C NMR spectra and SEC traces of PVP samples; description of cell culture and cytotoxicity tests; infrared spectra of ITZ−PVP (K30, *lin*PVP and *star*PVP), 95:5 *w*/*w*, in the amorphous state; DSC data for neat PVP polymers, as well as ITZ−PVP K30 and ITZ−*lin*PVP 95:5 and 85:15 *w*/*w* systems measured at ϕ = 10 K/min; DSC thermograms collected for amorphous ITZ−PVP 95:5 *w*/*w* mixtures at ϕ = 5 and 20 K/min; XRD data for neat PVP polymers and nonhomogeneous ITZ−PVP K30 and ITZ−*lin*PVP 85:15 *w*/*w* mixtures; XRD patterns of ITZ−PVP K30 95:5 *w*/*w* ASD before and after dissolution studies, and dielectric spectra measured in a wide temperature range for ITZ−*star*PVP 85:15 *w*/*w* system (PDF)

■ AUTHOR INFORMATION

Corresponding Author

Luiza Orszulak − *Institute of Chemistry, Faculty of Science and Technology, University of Silesia in Katowice, 40-007 Katowice, Poland;* orcid.org/0000-0002-7709-5867; Email: luiza.orszulak@us.edu.pl

Authors

Taoufik Lamrani − *Institute of Physics, Faculty of Science and Technology, University of Silesia in Katowice, 41-500 Chorzow, Poland*

Roksana Bernat − *Department of Pharmacognosy and Phytochemistry, Faculty of Pharmaceutical Sciences in Sosnowiec, Medical University of Silesia in Katowice, 41-200 Sosnowiec, Poland; Institute of Materials Engineering, Faculty of Science and Technology, University of Silesia in Katowice, 41-500 Chorzow, Poland*

Magdalena Tarnacka − *Institute of Physics, Faculty of Science and Technology, University of Silesia in Katowice, 41-500 Chorzow, Poland;* orcid.org/0000-0002-9444-3114

Daniel Żakowiecki − *Chemische Fabrik Budenheim KG, 55257 Budenheim, Germany*

Karolina Jurkiewicz − *Institute of Physics, Faculty of Science and Technology, University of Silesia in Katowice, 41-500 Chorzow, Poland;* orcid.org/0000-0002-4289-7827

Patryk Ziola − *Institute of Physics, Faculty of Science and Technology, University of Silesia in Katowice, 41-500 Chorzow, Poland*

Anna Mrozek-Wilczkiewicz − *Institute of Physics, Faculty of Science and Technology, University of Silesia in Katowice, 41-500 Chorzow, Poland; Biotechnology Centre, Silesian University of Technology, 44-100 Gliwice, Poland*

Andrzej Zięba − *Department of Organic Chemistry, School of Pharmacy with the Division of Laboratory Medicine in Sosnowiec, Medical University of Silesia in Katowice, 41-200 Sosnowiec, Poland*

Kamil Kamiński − *Institute of Physics, Faculty of Science and Technology, University of Silesia in Katowice, 41-500 Chorzow, Poland;* orcid.org/0000-0002-5871-0203

Ewa Kamińska − *Department of Pharmacognosy and Phytochemistry, Faculty of Pharmaceutical Sciences in Sosnowiec, Medical University of Silesia in Katowice, 41-200 Sosnowiec, Poland;* orcid.org/0000-0001-9725-8654

Complete contact information is available at: https://pubs.acs.org/10.1021/acs.molpharmaceut.4c00215

Notes

The authors declare no competing financial interest.

■ ACKNOWLEDGMENTS

L.O. is thankful for financial support from the Ministry of Education and Science (Poland) within the Pearls of Science grant (No. PN/01/0078/2022). This research was funded, in part, by the National Science Centre (Poland), Grant Opus 21 (No. 2021/41/B/NZ7/01654). R.B. gratefully acknowledges support from the Foundation for Polish Science (FNP). For the purpose of Open Access, the author has applied a CC-BY public copyright license to any author accepted manuscript (AAM) version arising from this submission. We would like to thank prof. B. Hachula for infrared measurements.

■ REFERENCES

(1) Elder, D. P.; Kuentz, M.; Holm, R. Pharmaceutical Excipients - Quality, Regulatory and Biopharmaceutical Considerations. *Eur. J. Pharm. Sci.* **2016**, *87*, 88−99.

(2) Kumari, L.; Choudhari, Y.; Patel, P.; Gupta, G. D.; Singh, D.; Rosenholm, J. M.; Bansal, K. K.; Kurmi, B. D. Advancement in Solubilization Approaches: A Step towards Bioavailability Enhancement of Poorly Soluble Drugs. *Life* **2023**, *13* (5), No. 1099.

(3) Bhalani, D. V.; Nutan, B.; Kumar, A.; Chandel, A. K. S. Bioavailability Enhancement Techniques for Poorly Aqueous Soluble Drugs and Therapeutics. *Biomedicines* **2022**, *10* (9), No. 2055.

(4) Rams-Baron, M.; Jachowicz, R.; Boldyreva, E.; Zhou, D.; Jamroz, W.; Paluch, M.*Amorphous Drugs: Benefits and Challenges*; Springer, 2018.

(5) Hasa, D.; Perissutti, B.; Cepek, C.; Bhardwaj, S.; Carlino, E.; Grassi, M.; Invernizzi, S.; Voinovich, D. Drug Salt Formation via Mechanochemistry: The Case Study of Vincamine. *Mol. Pharmaceutics* **2013**, *10* (1), 211−224.

(6) Vasilev, N. A.; Surov, A. O.; Voronin, A. P.; Drozd, K. V.; Perlovich, G. L. Novel Cocrystals of Itraconazole: Insights from Phase Diagrams, Formation Thermodynamics and Solubility. *Int. J. Pharm.* **2021**, *599*, No. 120441.

(7) Yeh, K. L.; Lee, T. Intensified Crystallization Processes for 1:1 Drug-Drug Cocrystals of Sulfathiazole-Theophylline, and Sulfathiazole-Sulfanilamide. *Cryst. Growth Des.* **2018**, *18* (3), 1339−1349.

(8) Reverchon, E.; Adami, R.; Campardelli, R.; Della Porta, G.; De Marco, I.; Scognamiglio, M. Supercritical Fluids Based Techniques to Process Pharmaceutical Products Difficult to Micronize: Palmitoylethanolamide. *J. Supercrit. Fluids* **2015**, *102*, 24−31.

(9) Laitinen, R.; Lobmann, K.; Strachan, C. J.; Grohganz, H.; Rades, T. Emerging Trends in the Stabilization of Amorphous Drugs. *Int. J. Pharm.* **2013**, *453* (1), 65−79.

(10) Yu, L. Amorphous Pharmaceutical Solids: Preparation, Characterization and Stabilization. *Adv. Drug Delivery Rev.* **2001**, *48* (1), 27−42.

(11) Hancock, B. C.; Zografi, G. Characteristics and Significance of the Amorphous State in Pharmaceutical Systems. *J. Pharm. Sci.* **1997**, *86* (1), 1−12.

(12) Zallen, R.*The Physics of Amorphous Solids*; Wiley, 1998; Vol. 93.

(13) Gray, G. W.Introduction and Historical Development. In *Handbook of Liquid Crystals*; Wiley, 1998; pp 1−16.
(14) Bunjes, H.; Rades, T. Thermotropic Liquid Crystalline Drugs. *J. Pharm. Pharmacol.* **2010**, *57* (7), 807−816.
(15) Mukherjee, P. K. Advances of Isotropic to Smectic Phase Transitions. *J. Mol. Liq.* **2021**, *340*, No. 117227.
(16) Rams-Baron, M.; Musial, M.; Kramarczyk, D.; Paluch, M. Insight from High-Pressure Dielectric Studies into Molecular Dynamics of the Itraconazole-Glycerol Mixture in Smectic and Isotropic Phases. *J. Chem. Phys.* **2022**, *156* (15), No. 154501.
(17) Patterson, J.; Bary, A.; Rades, T. Physical Stability and Solubility of the Thermotropic Mesophase of Fenoprofen Calcium as Pure Drug and in a Tablet Formulation. *Int. J. Pharm.* **2002**, *247* (1−2), 147−157.
(18) Serajuddin, A. T. Solid Dispersion of Poorly Water-Soluble Drugs: Early Promises, Subsequent Problems, and Recent Breakthroughs. *J. Pharm. Sci.* **1999**, *88* (10), 1058−1066.
(19) Kozyra, A.; Maghsoubi, N. A.; Paluch, K. J.; Garbacz, G.; Tajber, L. Phase Diagrams of Polymer-Dispersed Liquid Crystal Systems of Itraconazole/Component Immiscibility Induced by Molecular Anisotropy. *Mol. Pharmaceutics* **2018**, *15* (11), 5192−5206.
(20) Campoy, S.; Adrio, J. L. Antifungals. *Biochem. Pharmacol.* **2017**, *133*, 86−96.
(21) Denning, D. W.; Hope, W. W. Therapy for Fungal Diseases: Opportunities and Priorities. *Trends Microbiol.* **2010**, *18* (5), 195−204.
(22) Peeters, J.; Neeskens, P.; Tollenaere, J. P.; Van Remoortere, P.; Brewster, M. E. Characterization of the Interaction of 2-Hydroxypropyl-β-Cyclodextrin With Itraconazole at PH 2, 4, and 7. *J. Pharm. Sci.* **2002**, *91* (6), 1414−1422.
(23) Six, K.; Verreck, G.; Peeters, J.; Binnemans, K.; Berghmans, H.; Augustijns, P.; Kinget, R.; Van den Mooter, G. Investigation of Thermal Properties of Glassy Itraconazole: Identification of a Monotropic Mesophase. *Thermochim. Acta* **2001**, *376* (2), 175−181.
(24) Tarnacka, M.; Adrjanowicz, K.; Kaminska, E.; Kaminski, K.; Grzybowska, K.; Kolodziejczyk, K.; Wlodarczyk, P.; Hawelek, L.; Garbacz, G.; Kocot, A.; Paluch, M. Molecular Dynamics of Itraconazole at Ambient and High Pressure. *Phys. Chem. Chem. Phys.* **2013**, *15* (47), 20742−20752.
(25) Rams-Baron, M.; Kramarczyk, D.; Knapik-Kowalczuk, J.; Hachuła, B.; Kocot, A.; Paluch, M. Broadband-dielectric-spectroscopy study of molecular dynamics in a mixture of itraconazole and glycerol in glassy, smectic-A, and isotropic phases. *Phys. Rev. E* **2022**, *104* (3), No. 034702.
(26) Heczko, D.; Kamińska, E.; Tarnacka, M.; Jurkiewicz, K.; Dulski, M.; Bębenek, A.; Garbacz, G.; Kamiński, K.; Paluch, M. Varying Thermodynamic Conditions as a New Way to Tune the Molecular Order in Glassy Itraconazole. *J. Mol. Liq.* **2019**, *286*, No. 110920.
(27) Heczko, D.; Jurkiewicz, K.; Grelska, J.; Kamiński, K.; Paluch, M.; Kamińska, E. Influence of High Pressure on the Local Order and Dynamical Properties of the Selected Azole Antifungals. *J. Phys. Chem. B* **2020**, *124* (52), 11949−11961.
(28) Tarnacka, M.; Madejczyk, O.; Adrjanowicz, K.; Pionteck, J.; Kaminska, E.; Kamiński, K.; Paluch, M. Thermodynamic Scaling of Molecular Dynamics in Supercooled Liquid State of Pharmaceuticals: Itraconazole and Ketoconazole. *J. Chem. Phys.* **2015**, *142* (22), No. 224507.
(29) Mapesa, E. U.; Tarnacka, M.; Kamińska, E.; Adrjanowicz, K.; Dulski, M.; Kossack, W.; Tress, M.; Kipnusu, W. K.; Kamiński, K.; Kremer, F. Molecular Dynamics of Itraconazole Confined in Thin Supported Layers. *RSC Adv.* **2014**, *4* (54), 28432−28438.
(30) Teerakapibal, R.; Huang, C.; Gujral, A.; Ediger, M. D.; Yu, L. Organic Glasses with Tunable Liquid-Crystalline Order. *Phys. Rev. Lett.* **2018**, *120* (5), No. 55502.
(31) Gujral, A.; Gómez, J.; Ruan, S.; Toney, M. F.; Bock, H.; Yu, L.; Ediger, M. D. Vapor-Deposited Glasses with Long-Range Columnar Liquid Crystalline Order. *Chem. Mater.* **2017**, *29* (21), 9110−9119.
(32) Bishop, C.; Gujral, A.; Toney, M. F.; Yu, L.; Ediger, M. D. Vapor-Deposited Glass Structure Determined by Deposition Rate-Substrate Temperature Superposition Principle. *J. Phys. Chem. Lett.* **2019**, *10* (13), 3536−3542.
(33) Knapik-Kowalczuk, J.; Kramarczyk, D.; Jachowicz, R.; Paluch, M. Effect of Shear Strain on the Supercooled Itraconazole. *J. Pharm. Sci.* **2023**, *112* (6), 1644−1652.
(34) Mierzwa, M.; Rams-Baron, M.; Capaccioli, S.; Pawlus, S.; Paluch, M. How to Align a Nematic Glassy Phase − Different Conditions − Different Results. *J. Mol. Liq.* **2019**, *280*, 314−318.
(35) Kaminska, E.; Tarnacka, M.; Kolodziejczyk, K.; Dulski, M.; Zakowiecki, D.; Hawelek, L.; Adrjanowicz, K.; Zych, M.; Garbacz, G.; Kaminski, K. Impact of Low Molecular Weight Excipient Octaacetylmaltose on the Liquid Crystalline Ordering and Molecular Dynamics in the Supercooled Liquid and Glassy State of Itraconazole. *Eur. J. Pharm. Biopharm.* **2014**, *88* (3), 1094−1104.
(36) Amponsah-Efah, K. K.; Glorieux, C.; Thoen, J.; Suryanarayanan, R. Effect of Glycerol on the Order of the Mesophase Transitions of Supercooled Itraconazole. *J. Mol. Liq.* **2020**, *320*, No. 114222.
(37) Heczko, D.; Kamińska, E.; Jurkiewicz, K.; Tarnacka, M.; Merkel, K.; Kamiński, K.; Paluch, M. The Impact of Various Azole Antifungals on the Liquid Crystalline Ordering in Itraconazole. *J. Mol. Liq.* **2020**, *307*, No. 112959.
(38) Cruz, R. M.; Santos-Martinez, M. J.; Tajber, L. Impact of Polyethylene Glycol Polymers on the Physicochemical Properties and Mucoadhesivity of Itraconazole Nanoparticles. *Eur. J. Pharm. Biopharm.* **2019**, *144*, 57−67.
(39) Kalepu, S.; Nekkanti, V. Insoluble Drug Delivery Strategies: Review of Recent Advances and Business Prospects. *Acta Pharm. Sin. B* **2015**, *5* (5), 442−453.
(40) Sarode, A. L.; Sandhu, H.; Shah, N.; Malick, W.; Zia, H. Hot Melt Extrusion (HME) for Amorphous Solid Dispersions: Predictive Tools for Processing and Impact of Drug-Polymer Interactions on Supersaturation. *Eur. J. Pharm. Sci.* **2013**, *48* (3), 371−384.
(41) Janssens, S.; de Armas, H. N.; Remon, J. P.; Van den Mooter, G. The Use of a New Hydrophilic Polymer, Kollicoat IR, in the Formulation of Solid Dispersions of Itraconazole. *Eur. J. Pharm. Sci.* **2007**, *30* (3−4), 288−294.
(42) DiNunzio, J. C.; Miller, D. A.; Yang, W.; McGinity, J. W.; Williams, R. O. Amorphous Compositions Using Concentration Enhancing Polymers for Improved Bioavailability of Itraconazole. *Mol. Pharmaceutics* **2008**, *5* (6), 968−980.
(43) Peeters, O. M.; Blaton, N. M.; De Ranter, C. J. Cis-2-Sec-Butyl-4-{4-[4-(4-{[2-(2,4-Dichlorophenyl)-2-(1H-1,2,4-Triazol-1- Ylmethyl)-1,3-Dioxolan-4-Yl]Methoxy}phenyl)-1-Piperazinyl]Phenyl}-2,4-Dihydro- 3H-1,2,4-Triazol-3-One (Itraconazole). *Acta Crystallogr., Sect. C: Cryst. Struct. Commun.* **1996**, *52* (9), 2225−2229.
(44) Lee, S.-K.; Ha, E.-S.; Park, H.; Jeong, J.-S.; Kim, J.-S.; Baek, I.; Yoon, I.-S.; Yun, H.; Yoo, J.-W.; Ryong Moon, H.; Kim, M.-S. Synergistic Solvation Effect and Modeling of Itraconazole Solubility in Eight Binary Mixtures (Dichloromethane and Chloroform + Primary Alcohol) at the Range of 288.15 to 308.15 K. *J. Chem. Thermodyn.* **2023**, *185*, No. 107115.
(45) Awasthi, R.; Manchanda, S.; Das, P.; Valu, V.; Malipeddi, H.; Pabreja, K.; Pinto, T. D. J. A.; Gupta, G.; Dua, K. Poly-(vinylpyrrolidone). In *Engineering of Biomaterials for Drug Delivery Systems*; Parambath, A., Ed.; Woodhead Publishing, 2018; pp 255−272.
(46) Franco, P.; De Marco, I. The Use of Poly(N-Vinyl Pyrrolidone) in the Delivery of Drugs: A Review. *Polymers* **2020**, *12* (5), No. 1114.
(47) Roka, N.; Kokkorogianni, O.; Kontoes-Georgoudakis, P.; Choinopoulos, I.; Pitsikalis, M. Recent Advances in the Synthesis of Complex Macromolecular Architectures Based on Poly(N-Vinyl Pyrrolidone) and the RAFT Polymerization Technique. *Polymers* **2022**, *14* (4), No. 701.
(48) Pacult, J.; Rams-Baron, M.; Chrzanez, R.; Jachowicz, R.; Paluch, M. Effect of Polymer Chain Length on the Physical Stability of Amorphous Drug-Polymer Blends at Ambient Pressure. *Mol. Pharmaceutics* **2018**, *15* (7), 2807−2815.

(49) Mohapatra, S.; Samanta, S.; Kothari, K.; Mistry, P.; Suryanarayanan, R. Effect of Polymer Molecular Weight on the Crystallization Behavior of Indomethacin Amorphous Solid Dispersions. *Cryst. Growth Des.* **2017**, *17* (6), 3142−3150.
(50) Kestur, U. S.; Lee, H.; Santiago, D.; Rinaldi, C.; Won, Y. Y.; Taylor, L. S. Effects of the Molecular Weight and Concentration of Polymer Additives, and Temperature on the Melt Crystallization Kinetics of a Small Drug Molecule. *Cryst. Growth Des.* **2010**, *10* (8), 3585−3595.
(51) Sahoo, A.; Suryanarayanan, R.; Siegel, R. A. Stabilization of Amorphous Drugs by Polymers: The Role of Overlap Concentration (C*). *Mol. Pharmaceutics* **2020**, *17* (11), 4401−4406.
(52) Devasia, R.; Bindu, R. L.; Borsali, R.; Mougin, N.; Gnanou, Y. Controlled Radical Polymerization of *N*-Vinylpyrrolidone by Reversible Addition-Fragmentation Chain Transfer Process. *Macromol. Symp.* **2005**, *229*, 8−17.
(53) Bielas, R.; Maksym, P.; Tarnacka, M.; Minecka, A.; Jurkiewicz, K.; Talik, A.; Geppert-Rybczyńska, M.; Grelska, J.; Mielańczyk, Ł.; Bernat, R.; Kamiński, K.; Paluch, M.; Kamińska, E. Synthetic Strategy Matters: The Study of a Different Kind of PVP as Micellar Vehicles of Metronidazole. *J. Mol. Liq.* **2021**, *332*, No. 115789.
(54) Vanharova, L.; Julinova, M.; Slavik, R. PVP Based Materials: Biodegradation in Different Environments. *Ecol. Chem. Eng. S* **2017**, *24* (2), 299−309.
(55) Julinova, M.; Kupec, J.; Slavik, R.; Vaskova, M. Initiating Biodegradation of Polyvinylpyrrolidone in an Aqueous Aerobic Environment: Technical Note. *Ecol. Chem. Eng. S* **2013**, *20* (1), 199−208.
(56) Orzeluk, L.; Lamrani, T.; Tarnacka, M.; Hachuła, B.; Jurkiewicz, K.; Ziola, P.; Mrozek-Wilczkiewicz, A.; Kamińska, E.; Kamiński, K. The Impact of Various Poly(Vinylpyrrolidone) Polymers on the Crystallization Process of Metronidazole. *Pharmaceutics* **2024**, *16* (1), No. 136.
(57) Heczko, D.; Kamińska, E.; Tarnacka, M.; Koperwas, K.; Dzienia, A.; Chorążewski, M. A.; Kamiński, K.; Paluch, M. The Impact of Liquid Crystalline Phase Ordering on the Thermodynamic Scaling of Itraconazole. *J. Phys. Chem. C* **2019**, *123* (7), 4558−4566.
(58) Chen, Z.; Yu, J.; Teerakapibal, R.; Meerpoel, L.; Richert, R.; Yu, L. Organic Glasses with Tunable Liquid-Crystalline Order through Kinetic Arrest of End-over-End Rotation: The Case of Saperconazole. *Soft Matter* **2020**, *16* (8), 2025−2030.
(59) Havriliak, S.; Negami, S. A Complex Plane Analysis of α-Dispersions in Some Polymer Systems. *J. Polym. Sci., Part C: Polym. Symp.* **1966**, *14* (1), 99−117.
(60) Kremer, F.; Schönhals, A. *Broadband Dielectric Spectroscopy*; Springer: Berlin, 2003.
(61) Schneider, F.; Koziolek, M.; Weitschies, W. In Vitro and in Vivo Test Methods for the Evaluation of Gastroretentive Dosage Forms. *Pharmaceutics* **2019**, *11* (8), No. 416.
(62) Rangaraj, N.; Sampathi, S.; Junnuthula, V.; Kolimi, P.; Mandati, P.; Narala, S.; Nyavanandi, D.; Dyawanapelly, S. Fast-Fed Variability: Insights into Drug Delivery, Molecular Manifestations, and Regulatory Aspects. *Pharmaceutics* **2022**, *14* (9), No. 1807.

https://doi.org/10.1021/acs.molpharmaceut.4c00215
Mol. Pharmaceutics 2024, 21, 3027−3039

Supporting Information

The influence of PVP polymer topology on the liquid crystalline order of itraconazole in binary systems

Luiza Orszulak[1]*, Taoufik Lamrani[2], Roksana Bernat[3,4], Magdalena Tarnacka[2], Daniel Żakowiecki[5], Karolina Jurkiewicz[2], Patryk Zioła[2], Anna Mrozek-Wilczkiewicz[2,6], Andrzej Zięba[7], Kamil Kamiński[2], Ewa Kamińska[3]

[1] *Institute of Chemistry, Faculty of Science and Technology, University of Silesia in Katowice, Szkolna 9, 40-007 Katowice, Poland*

[2] *Institute of Physics, Faculty of Science and Technology, University of Silesia in Katowice, 75 Pulku Piechoty 1A, 41-500 Chorzow, Poland*

[3] *Department of Pharmacognosy and Phytochemistry, Faculty of Pharmaceutical Sciences in Sosnowiec, Medical University of Silesia in Katowice, Jagiellonska 4, 41-200 Sosnowiec, Poland*

[4] *Institute of Materials Engineering, Faculty of Science and Technology, University of Silesia in Katowice, 75 Pulku Piechoty 1A, 41-500 Chorzow, Poland*

[5] *Chemische Fabrik Budenheim KG, Rheinstrasse 27, 55257 Budenheim, Germany*

[6] *Biotechnology Centre, Silesian University of Technology, Boleslawa Krzywoustego 8, 44-100 Gliwice, Poland*

[7] *Department of Organic Chemistry, School of Pharmacy with the Division of Laboratory Medicine in Sosnowiec, Medical University of Silesia in Katowice, Jagiellonska 4, 41-200 Sosnowiec, Poland*

**Corresponding author:* luiza.orszulak@us.edu.pl

Experimental

Synthesis of trifunctional chain transfer agent (CTA2)

Trifunctional chain transfer agent (1,3,5-benzyl tri(diethyldithiocarbamate), CTA2) was prepared in a single-step route by the reaction of 1,3,5-tribromomethyl benzene with sodium diethyldithiocarbamate according to the following procedure. In a 100 mL two-neck round-bottom flask equipped with a magnetic stirrer, inlet-outlet nitrogen, and dropping funnel, sodium diethyldithiocarbamate trihydrate (2 g, 8.88 mmol) was dissolved in methanol (40 mL) under a nitrogen atmosphere and cooled to 273 K. A solution of 1,3,5-tribromomethyl benzene (1 g, 2.80 mmol) in methanol (10 mL) was added dropwise over a 30 min period. The reaction was gradually warmed to room temperature and remained under magnetic stirring for a further 72 h. Then, the yellowish precipitate was filtered, washed with cold methanol, and left to dry to constant mass. The structure of the obtained 1,3,5-benzyl tri(diethyldithiocarbamate) was confirmed by ^{1}H NMR spectrum (see **Figure S2**).

Synthesis of PVP with linear topology (linPVP)

Thermally-initiated Reversible Addition Fragmentation Chain Transfer (RAFT) polymerization of N-vinylpyrrolidone (VP) using CTA1 as a chain transfer agent and 2,2'-azobis(2-methylpropionitrile) (AIBN) as an initiator with molar ratios $[VP]_0/[CTA1]_0/[AIBN]_0$ = 500/1/0.25) was carried out as follows. Prior to polymerization, VP was passed through an alumina column to remove the inhibitor. CTA1 (33.5 mg, 0.15 mmol) and VP (8 mL, 74.86 mmol) were placed in a Schlenk flask with a magnetic stirring bar. The solution was purged under nitrogen and purified by three freeze-pump-thaw cycles. Then, the solution of AIBN (187 µL, 0.037 mmol) was added to the reaction mixture and the flask was immersed in an oil bath thermostated at 60 °C to start the reaction. The polymerization was quenched after a predetermined time (t = 3.5 h) by cooling and exposing the reaction mixture to air. The product was precipitated with cold diethyl ether and re-dissolved in chloroform and this cycle was repeated twice. The polymer was isolated, filtered, and then dried under vacuum to a constant mass. The structure of the obtained linear PVP was confirmed by ^{1}H and ^{13}C NMR spectra (see **Figures S3 and S4**). The molecular weight and dispersity of the produced *lin*PVP were determined by size exclusion chromatography (SEC) (see **Figure S7**).

Synthesis of PVP with star topology (starPVP)

Thermally-initiated RAFT polymerization of VP using previously synthesized CTA2 as a chain transfer agent and AIBN as an initiator with molar ratios $[VP]_0/[CTA2]_0/[AIBN]_0$ =

400/5/1) was carried out as follows. Before polymerization, VP was passed through an alumina column to remove the inhibitor. CTA2 (0.13148 g, 0.23 mmol), VP (2 mL, 18.72 mmol) and DCM (4 mL, 200% *v/v* in relation to the monomer) were placed in a Schlenk flask with a magnetic stirring bar. The solution was purged under nitrogen and purified by three freeze-pump-thaw cycles. Then, the solution of AIBN (234 µL, 0.047 mmol) was added to the reaction mixture and the flask was immersed in an oil bath thermostated at 60 °C to start the reaction. The polymerization was quenched after a predetermined time (t = 8 h) by cooling and exposing the reaction mixture to air. The product was precipitated with cold diethyl ether and re-dissolved in chloroform, and this cycle was repeated twice. The polymer was isolated, filtered, and then dried under vacuum to a constant mass. The structure of the obtained three-arm star-shaped PVP was confirmed by ^{1}H and ^{13}C NMR spectra (see **Figures S5 and S6**). The molecular weight and dispersity of the produced *star*PVP were determined by SEC (see **Figure S7**).

Nuclear Magnetic Resonance (NMR)

Nuclear magnetic resonance (^{1}H and ^{13}C NMR) spectra were collected using a Bruker Ascend 500 MHz spectrometer in $CDCl_3$ as a solvent. Standard experimental conditions and the standard Bruker program were used.

Size Exclusion Chromatography (SEC)

Molecular weights (M_n) and dispersity (Đ) of linear and star-shaped PVP homopolymers were determined by size exclusion chromatography (SEC). Viscotek GPC Max VE 2001 and a Viscotek TDA 305 triple detection system (refractometer, viscosimeter and low angle laser light scattering) was used for data collection and OmniSec 5.12 for data processing. Two T6000M general mixed columns were used for separation. The measurements were carried out in DMF/LiBr (0.01M) as an eluent at 303 K with a flow rate of 0.7 mL/min.

Cell culture

Normal human dermal fibroblasts (NHDF) were purchased from PromoCell. The cell line was cultured in Dulbecco's Modified Eagle's Medium (DMEM) supplemented with 15% non-inactivated FBS (*Sigma Aldrich*) and penicillin/streptomycin antibiotics (1% *v/v*; Gibco, Waltham, MA USA). The cells were kept under standard conditions at 37 °C in a humid atmosphere with 5% CO_2 and passed as required by the manufacturer. Additionally, cells were tested against *Mycoplasma* contamination using the PCR technique with specific primers.

Cytotoxicity studies

The cells were seeded in 96-well transparent plates (Nunc, Waltham, MA USA) at a density of 4000 cells per well and incubated for 24 h at 37 °C. Approximately 24 h after seeding, the medium was removed from wells and 200 µL of various concentrations (from 1 to 0.001 mg/mL) of tested compounds (dissolved in DMEM) were added to the plate and incubated for 72 h at 37 °C. Next, compound solutions were exchanged with 100 µL of DMEM without phenol red and 20 µL of CellTiter 96®AQueous One Solution-MTS (Promega, Madison, USA) and incubated for 1 h at 37 °C. After that time, the absorbance of the samples was measured at 490 nm using a multi-plate reader (Varioskan LUX, Thermo Scientific, Waltham, MA USA). The results were normalized to a control consisting of untreated cells. Compounds were tested in triplicate in a single experiment, each repeated three times.

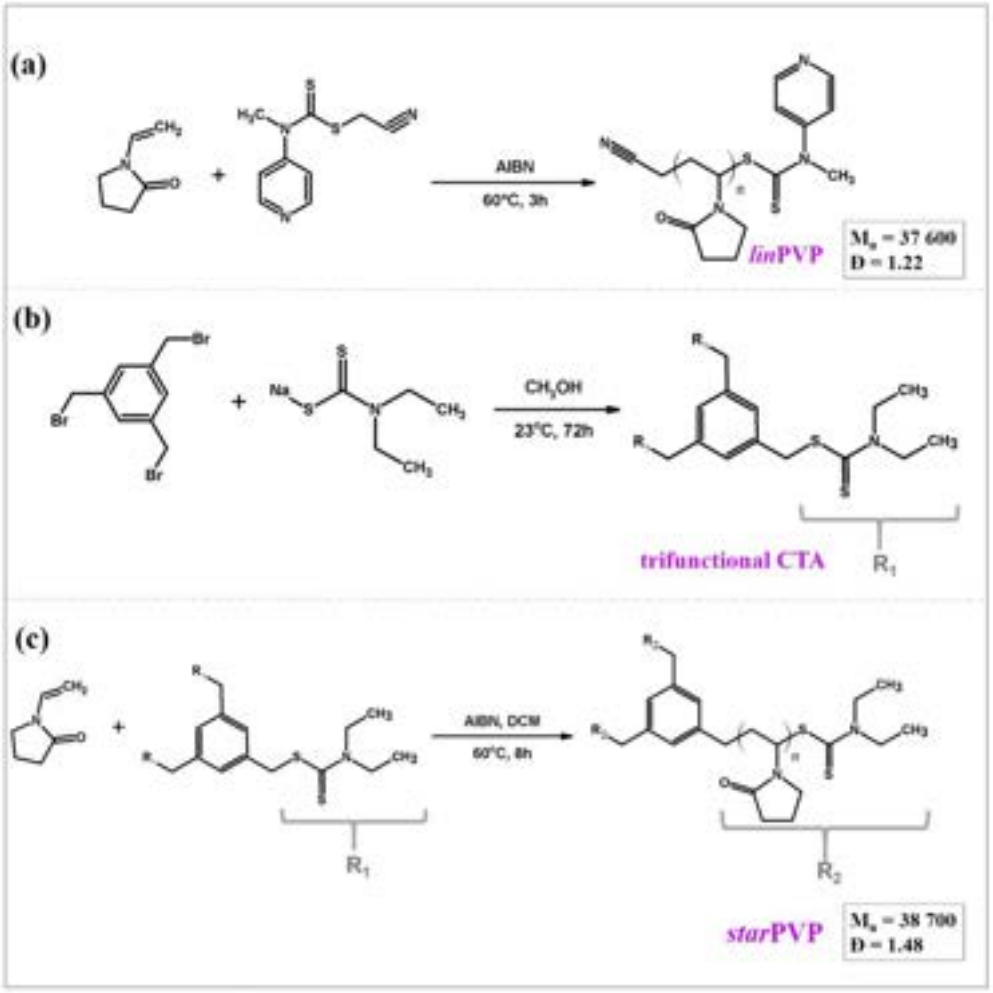

Figure S1. Synthetic pathways for obtaining: (**a**) *lin*PVP, (**b**) trifunctional CTA and (**c**) *star*PVP.

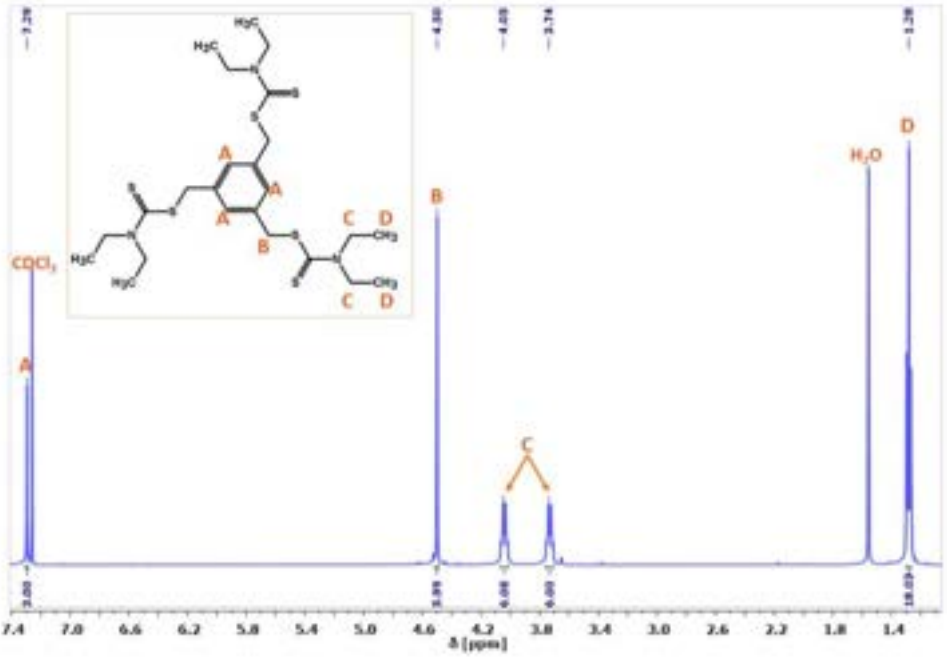

Figure S2. ^{1}H NMR spectrum of trifunctional CTA2 in $CDCl_3$ (500 MHz).

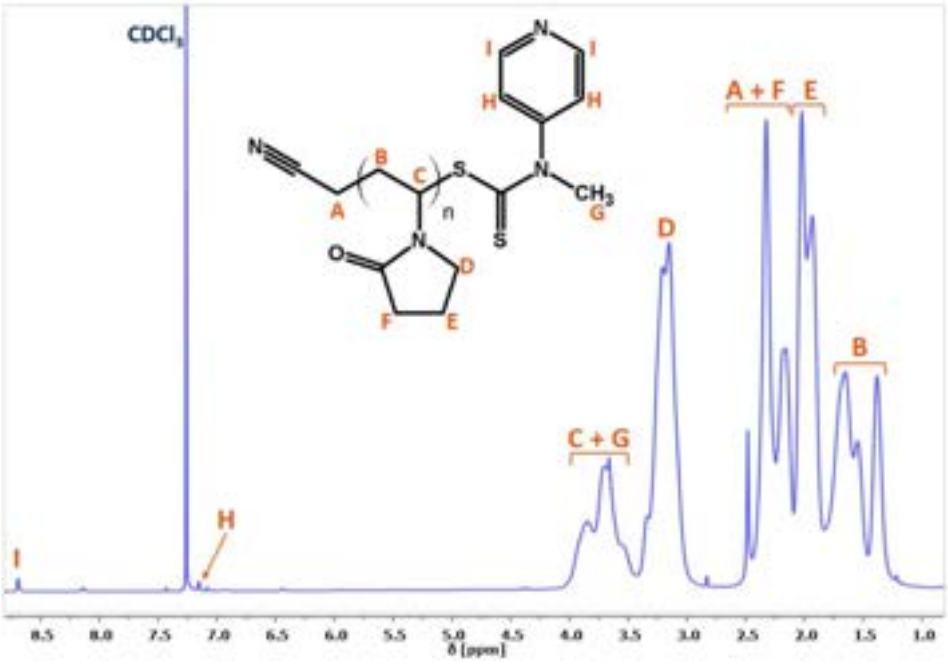

Figure S3. ^{1}H NMR spectrum of *lin*PVP in $CDCl_3$ (600 MHz).

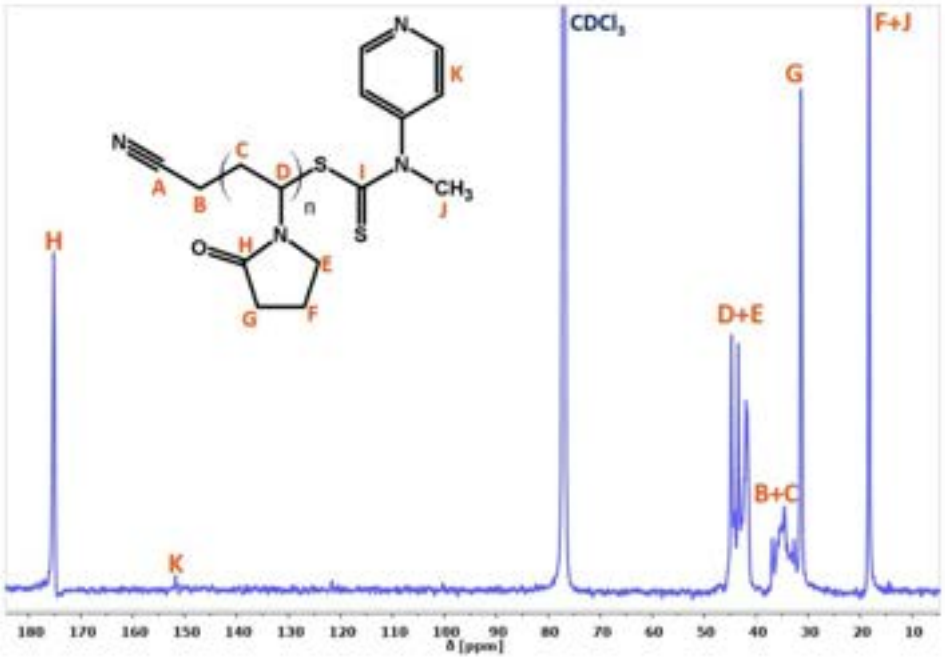

Figure S4. ^{13}C NMR spectrum of *lin*PVP in $CDCl_3$ (600 MHz).

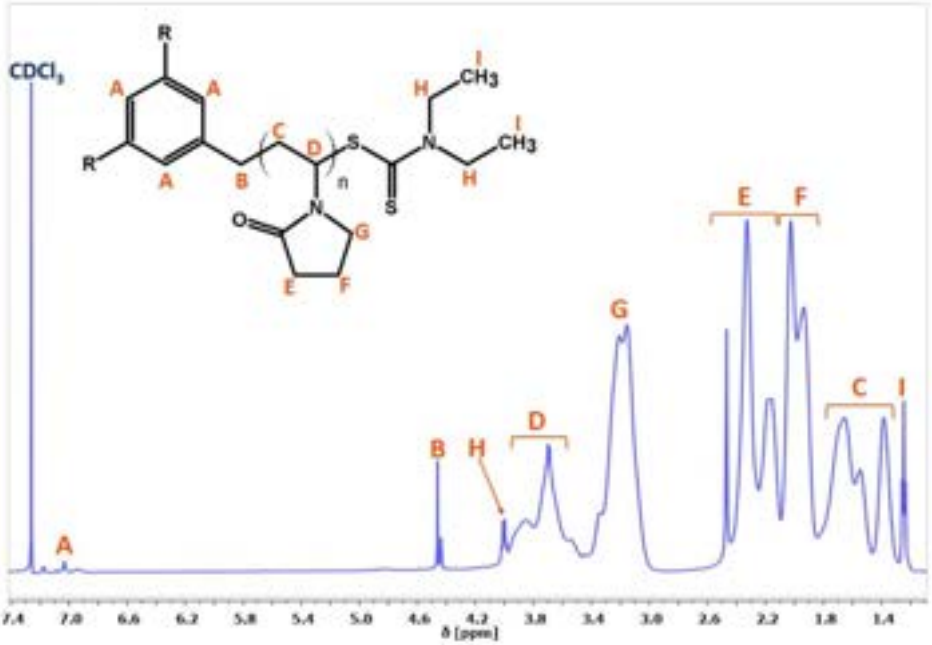

Figure S5. ^{1}H NMR spectrum of *star*PVP in $CDCl_3$ (600 MHz).

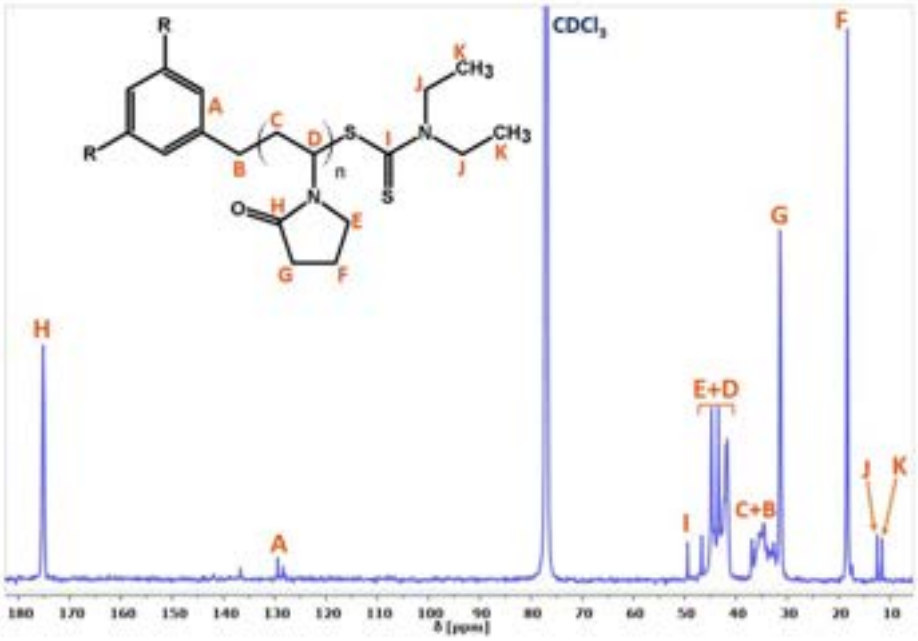

Figure S6. ^{13}C NMR spectrum of *star*PVP in $CDCl_3$ (600 MHz).

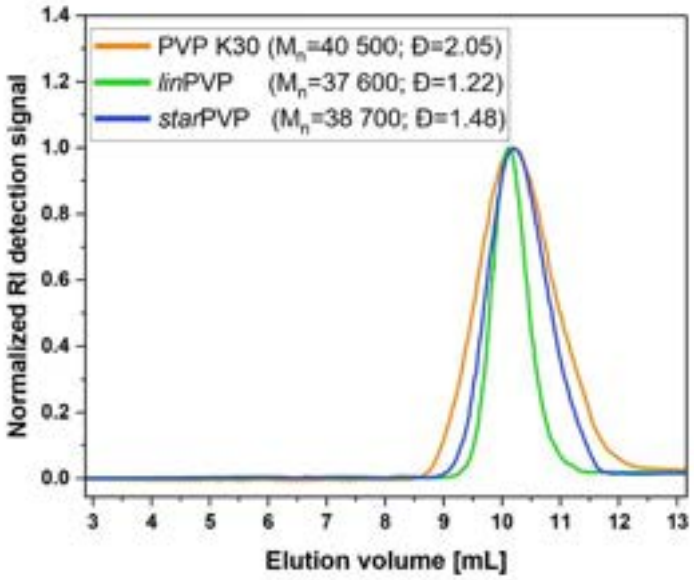

Figure S7. SEC traces of PVP samples: commercial (PVP K30 - orange line) and self-synthesized (*lin*PVP - green line, *star*PVP - blue line).

Results

Cytotoxicity studies

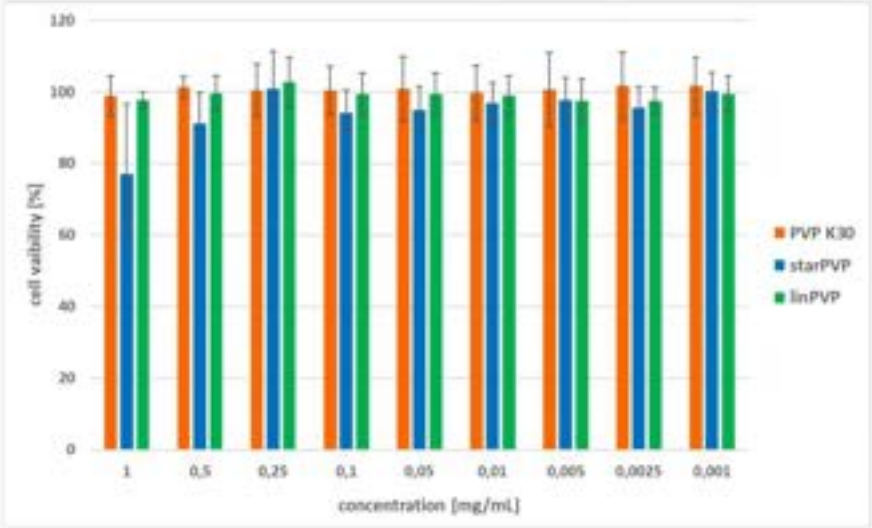

Figure S8. Cell viability seeded onto various PVP samples.

Cytotoxicity tests were conducted for the newly synthesized polymers (*lin*PVP and *star*PVP) prior to the preparation of binary mixtures. The collected data were then compared with the results obtained for PVP K30 (as a reference sample) because it is a fully neutral macromolecule, widely used in the pharmaceutical and cosmetic sectors. As shown in **Figure S8**, the tested compounds exhibit no cytotoxicity towards NHDF cells. The survival fraction in all cases did not drop below 90 %, except *star*PVP, for which a decrease not exceeding 75% was recorded, indicating a neutral impact of the newly synthesized PVP homopolymers on the proliferation of the selected cell line. Herein, it is worth mentioning that we initially selected concentrations for testing that are commonly reported in the literature (i.e., below 0.05 mg/mL). However, upon noticing that the samples showed no cytotoxicity at these concentrations (see our previous paper),[1] we decided to investigate higher concentrations (>0.05 mg/mL). It was revealed that the newly synthesized polymeric materials do not demonstrate harmful effects on the NHDF cell line, even at a concentration of 1 mg/mL.

Infrared data

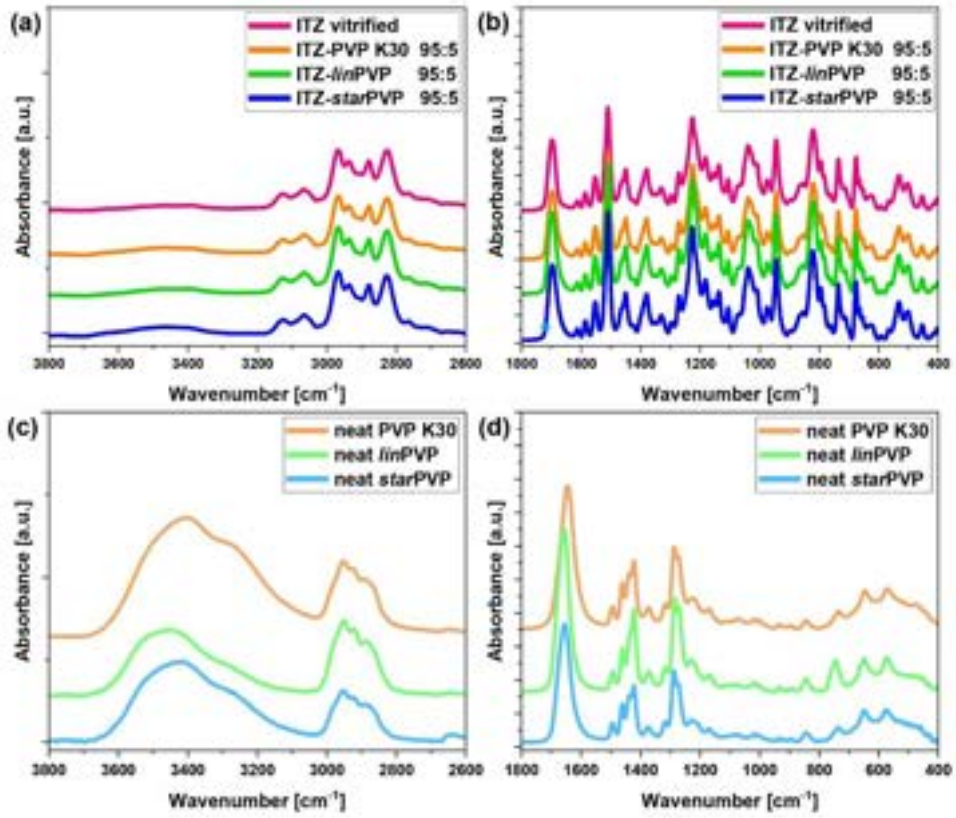

Figure S9. Infrared spectra of binary mixtures of ITZ with three PVP samples (K30, *lin*PVP and *star*PVP) in the weight ratio of 95:5, in the amorphous state, presented in the ranges of **(a)** 3800–2600 cm^{-1} and **(b)** 1800–400 cm^{-1} as well as infrared spectra of neat PVP samples (K30, *lin*PVP and *star*PVP) in the ranges of **(c)** 3800–2600 cm^{-1} and **(d)** 1800–400 cm^{-1}.

DSC data

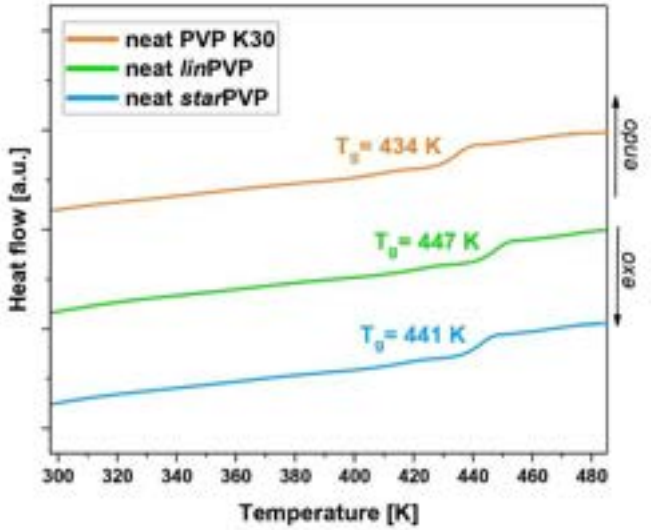

Figure S10. DSC thermograms (ϕ =10 K/min) collected for neat PVPs.

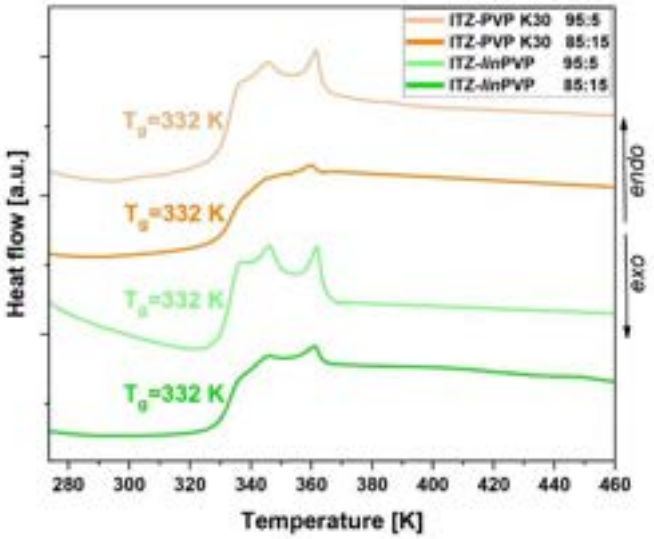

Figure S11. DSC thermograms (ϕ =10 K/min) collected for ITZ-PVP K30 and ITZ-*lin*PVP mixtures prepared at various weight ratios (95:5 and 85:15 *w/w*).

To confirm the limitation in the miscibility of linear polymer matrices with the drug, DSC studies were also conducted for non-homogeneous API formulations with PVP K30 and *lin*PVP (85:15 *w/w*). The collected data were plotted on a single graph alongside their homogeneous counterparts, i.e., 95:5 *w/w* (see **Figure S11**). Analysis of the thermograms obtained for ITZ-PVP K30 and ITZ-*lin*PVP, 95:5 and 85:15 *w/w* systems showed the same glass transition temperatures T_g=332 K regardless of the polymer content in ASDs. It is worth recalling that for ITZ-*star*PVP mixtures, a clear change in phase transition temperatures was detected with increasing polymer matrix content in the binary mixture (the higher the weight fraction of *star*PVP polymer, the higher T_g, **Figure 2** in the main manuscript). Such behavior was not observed in the case of ITZ-PVP K30 and ITZ-*lin*PVP systems, which further reinforces the conviction that there is a limitation in the miscibility of linear polymers with the tested drug at a 5 wt% level. Thus, amongst the tested macromolecules, only *star*PVP exhibits exceptional behavior and miscibility with the API at a 15 wt% level.

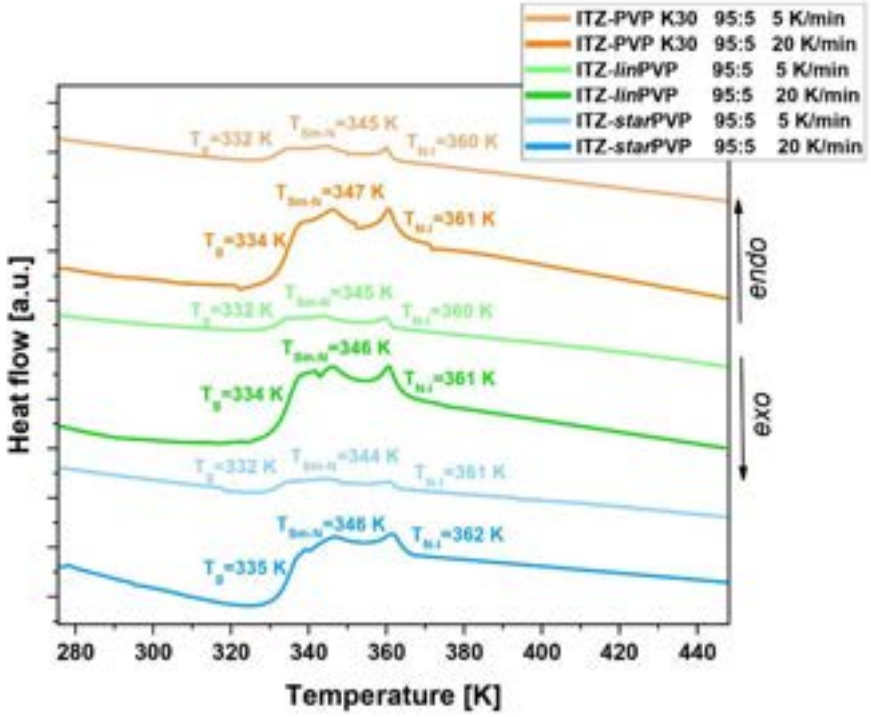

Figure S12. DSC thermograms collected for amorphous ITZ-PVP 95:5 *w/w* mixtures at various heating rates (ϕ =5 and 20 K/min).

X-ray diffraction data

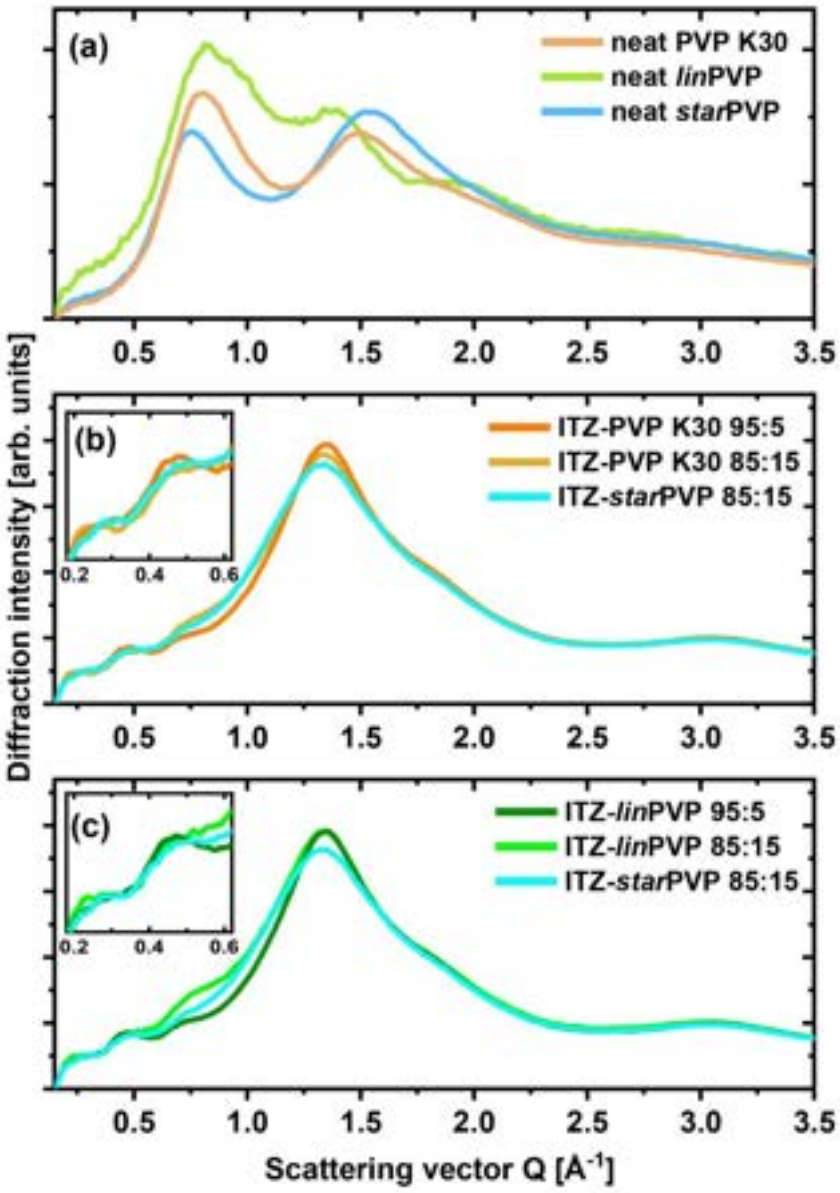

Figure S13. XRD patterns of **(a)** neat PVPs, **(b)** non-homogenous ITZ-PVP K30 85:15 *w/w* compared with its homogeneous counterpart ITZ-PVP K30 95:5 *w/w* as well as ITZ-*star*PVP 85:15 *w/w*, **(c)** non-homogenous ITZ-*lin*PVP 85:15 *w/w* compared with its homogeneous counterpart ITZ-*lin*PVP 95:5 *w/w*, as well as ITZ-*star*PVP 85:15 *w/w*.

In addition to the calorimetric measurements conducted and presented above (see **Figure S11**), we also performed structural investigations for heterogeneous ITZ-PVP K30 and ITZ-*lin*PVP 85:15 *w/w* systems (see **Figure S13**). It turned out that the difference in miscibility could also be successfully observed in the XRD patterns. First, we compared XRD data for neat PVPs. As seen in **Figure S13a**, all utilized polymer matrices distinctly differ in the intensity of the first diffraction peak (around $Q = 0.5 - 1.0\ \text{Å}^{-1}$). Subsequently, X-ray diffraction measurements were carried out for heterogeneous ITZ-PVP K30 and ITZ-*lin*PVP 85:15 *w/w* systems, and they were compared with their homogeneous counterparts (95:5 *w/w*), as well as with a system showing the highest degree of homogeneous mixing, i.e., ITZ-*star*PVP 85:15 *w/w* (see **Figure S13b,c**). As can be observed, for the weight ratio of 85:15, the obtained XRD patterns of the mixtures differ. It is especially noticeable in the range, where PVP exhibits the first diffraction peaks. This peak in the ITZ-*lin*PVP system shows the highest intensity because neat *lin*PVP polymer has the highest peak intensity, indicating that a part of the polymer is not solved in this formulation. On the other hand, the ITZ-PVP K30 85:5 *w/w* mixture exhibits lower intensity in the range of $Q = 0.5 - 1.0\ \text{Å}^{-1}$ compared to the ITZ-*lin*PVP 85:5 *w/w* mixture but slightly higher than the ITZ-*star*PVP mixture because neat commercial PVP K30 has an intensity between linear and star-shaped PVP matrices in this Q range. However, for all investigated mixtures in a ratio of 95:5 (see **Figure 3** in the main manuscript). XRD data show no difference in the analyzed range, confirming the hypothesis that PVP molecules are well miscible with ITZ.

Results of XRD studies obtained for non-homogeneous systems perfectly match the data determined from DSC measurements and additionally confirm the miscibility of ITZ with linear matrices at a weight ratio of 95:5, while ITZ with *star*PVP demonstrates the maximum miscibility at a ratio of 85:15 *w/w*.

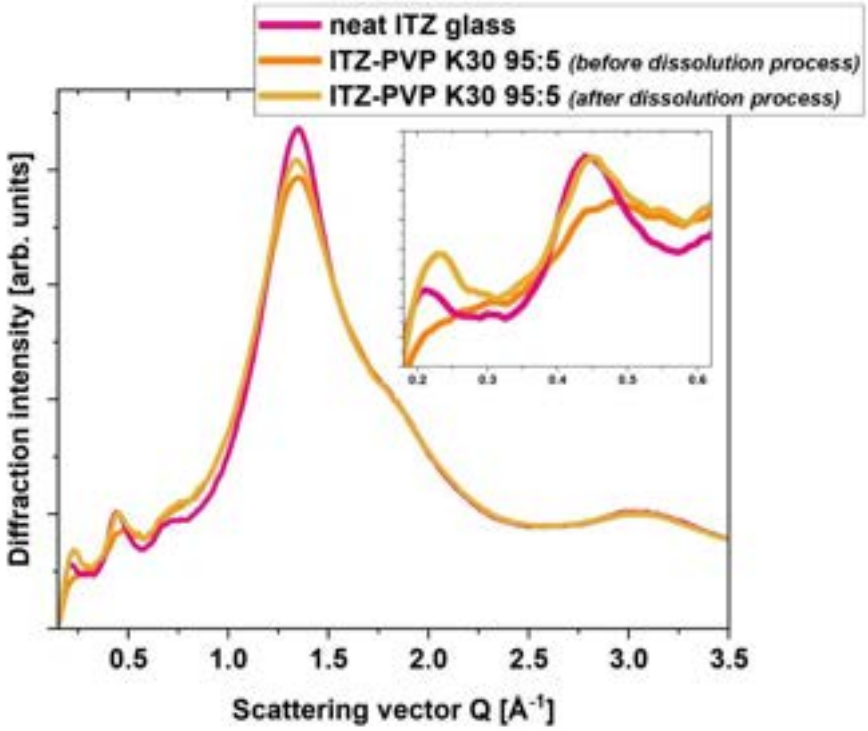

Figure S14. XRD patterns of neat ITZ glass (pink line), as well as ITZ-PVP K30 95:5 *w/w* mixtures before (orange line) and after (yellow line) dissolution process.

Dielectric data

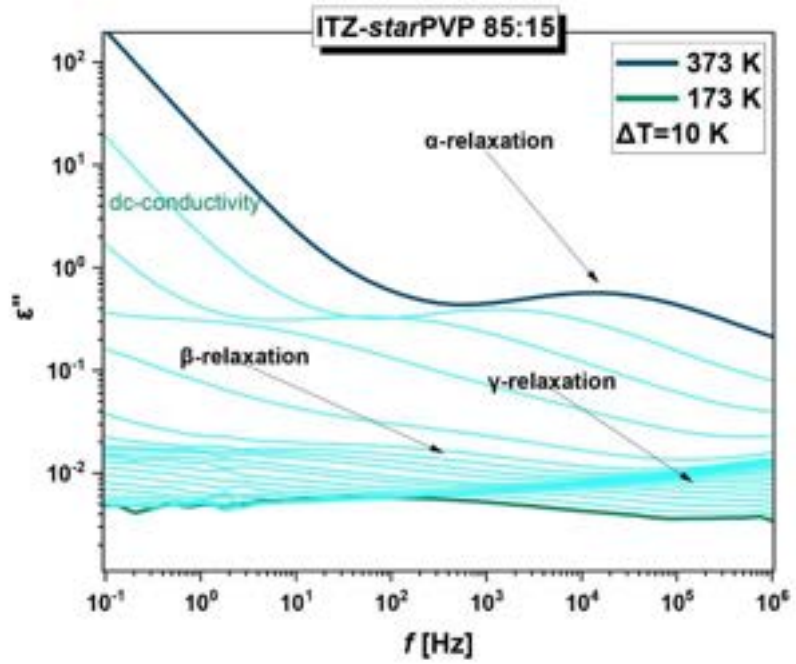

Figure S15. Dielectric loss spectra of ITZ-*star*PVP 85:15 *w/w* mixture.

References:

(1) Orszulak, L.; Lamrani, T.; Tarnacka, M.; Hachuła, B.; Jurkiewicz, K.; Zioła, P.; Mrozek-Wilczkiewicz, A.; Kamińska, E.; Kamiński, K. The Impact of Various Poly(Vinylpyrrolidone) Polymers on the Crystallization Process of Metronidazole. *Pharmaceutics* **2024**, *16* (1), 136. https://doi.org/10.3390/pharmaceutics16010136.

4.4. Hydrophilic and amphiphilic macromolecules as modulators of the physical stability and bioavailability of piribedil: A study on binary mixtures and micellar systems (P4)

Autorzy: L. Orszulak, A. Minecka, R. Bernat, T. Lamrani, K. Jurkiewicz, B. Hachuła, M. Tarnacka, M. Geppert-Rybczyńska, M. Zubko, M. Staniszewska, M. Smoleński, J. Dobosz, G. Garbacz, K. Kamiński, E. Kamińska

Referencja: *Molecular Pharmaceutics*, 2025, 22 (8), 4708−4730

DOI: 10.1021/acs.molpharmaceut.5c00276

Impact Factor czasopisma: 4.5

Liczba punktów ministerialnych MNiSW czasopisma: 140 (2025)

Mój udział w pracy polegał na zsyntezowaniu matryc polimerowych, ich pełnej charakterystyce spektroskopowej i chromatograficznej, tworzeniu mieszanin binarnych metodą witryfikacji, tworzeniu układów micelarnych, przeprowadzeniu badań uwalniania leku z nośnika polimerowego, przeprowadzeniu badań dielektrycznych, analizie i wizualizacji danych, dyskusji wyników, przygotowywaniu tekstów manuskryptów, opracowywaniu odpowiedzi dla Recenzentów i Edytora, pozyskaniu finansowania w ramach kierowania grantem *„Perły Nauki”*.

molecular pharmaceutics

pubs.acs.org/molecularpharmaceutics

Article

Hydrophilic and Amphiphilic Macromolecules as Modulators of the Physical Stability and Bioavailability of Piribedil: A Study on Binary Mixtures and Micellar Systems

Luiza Orszulak,* Aldona Minecka, Roksana Bernat, Taoufik Lamrani, Karolina Jurkiewicz, Barbara Hachuła, Magdalena Tarnacka, Monika Geppert-Rybczyńska, Maciej Zubko, Marcela Staniszewska, Michał Smoleński, Justyna Dobosz, Grzegorz Garbacz, Kamil Kamiński, and Ewa Kamińska

Cite This: Mol. Pharmaceutics 2025, 22, 4708−4730

Read Online

ACCESS | Metrics & More | Article Recommendations | Supporting Information

ABSTRACT: This study presents an innovative approach that utilizes polymers with different topologies and properties as potential matrices for the poorly water-soluble active pharmaceutical ingredient piribedil (PBD). We investigated amorphous solid dispersions (ASDs) as well as micellar systems composed of PBD and (*i*) the commercial amphiphilic copolymer Soluplus, (ii) self-synthesized hydrophilic linear PVP (*lin*PVP), and (iii) self-synthesized hydrophilic star-shaped PVP (*star*PVP). Differential scanning calorimetry, X-ray diffraction, Fourier-transform infrared, and broadband dielectric spectroscopy were applied to gain comprehensive insights into the thermal and structural properties, intermolecular interactions, global molecular dynamics, and recrystallization of the API from the amorphous PBD−polymer ASDs. The primary objective was to evaluate the impact of the type and topology of macromolecules, as well as the composition of binary formulations, on the physical stability of PBD in the amorphous form, phase transition temperatures, the API's recrystallization rate, and ultimately, the release of drug in the prepared ASDs and micelles. Most importantly, our research led to the discovery of new polymorphic form (II) of PBD that has not been previously described in the scientific literature. We also revealed that ASDs containing hydrophilic PVP polymers exhibit the best performance in stabilizing the amorphous form of the API, with the *star*PVP systems showing the highest stabilization effect. In contrast, for micellar systems, Soluplus turned out to be the most suitable candidate in terms of forming the self-assembles of the lowest size distribution among all systems. The long-term stability of the amorphous drug in PBD−Soluplus micelles was higher compared to PBD−*star*PVP ASD. Moreover, an improvement in the bioavailability of the API contained in all tested formulations (binary and micellar systems) was observed, with PBD−*star*PVP micelles exhibiting the most desirable drug release profile within the polymer matrix, as well as the highest concentration of released drug. The obtained data highlight the crucial role of the type and topology/architecture of the polymer in the design of novel pharmaceutical formulations.

KEYWORDS: *Soluplus copolymer, polyvinylpyrrolidone, piribedil, amorphous solid dispersions, micellar systems, topology of polymers, drug delivery system, solubility, bioavailability*

1. INTRODUCTION

The pharmaceutical industry is considered to be one of the fastest-growing sectors of the economy. However, despite this, it still struggles with a significant challenge—the poor water solubility (and consequently low bioavailability) of many active substances (APIs)/drugs available on the market, which results in their unsatisfactory therapeutic effect.[1−4] Moreover, patients have often to take higher doses of pharmaceuticals, leading to undesirable side effects.[5] One way to overcome these problems and improve the bioavailability of APIs is amorphization, i.e., the transformation of the initial crystalline substances into amorphous ones. The resulting material is characterized by a lack of long-range order compared to the crystalline form, which leads to improved solubility and bioavailability of APIs.[6,7] However, amorphous substances are thermodynamically unstable, possess a high Gibbs free energy, and, as a result, show a high tendency to recrystallization, i.e., return to their energetically favorable crystalline form during storage or use of

Received: March 1, 2025
Revised: June 14, 2025
Accepted: June 16, 2025
Published: June 30, 2025

the products.[7,8] To stabilize these systems, various excipients, EXCs (both low- and high-molecular-weight compounds) are widely applied. Among them, polymers are gaining popularity as innovative pharmaceutical additives.

It should be emphasized that polymers are considered as one of the most effective EXCs for stabilizing the labile amorphous form of APIs, due to numerous favorable properties.[9−13] The key benefits of using them in pharmaceutical formulations include: *(i)* a high glass transition temperature (T_g), which significantly increases T_g of the entire drug-polymer system,[13] *(ii)* reduction of the molecular mobility of the drug,[14,15] *(iii)* an increase in the activation energy of API nucleation,[16,17] *(iv)* the ability to synthesize "tailor-made" macromolecules adapted to specific types of drugs through various controlled polymerization methods, i.e., polymers with targeted molecular weights (M_w) and low dispersity ($Đ$),[18] *(v)* the possibility of modifying polymer chain ends to build subsequent polymer blocks and produce (co)polymers, thereby fine-tuning macromolecular properties to suit specific applications.[19] Given these unique features, polymers can significantly influence the dissolution, distribution, and transport of drugs within the human body. However, it is crucial to ensure that the polymer matrix is carefully selected for the specific API, the expected/desired properties, and also the used drug delivery system (DDS).

Among advanced DDSs, micellar systems and amorphous binary mixtures (BMs), also known as amorphous solid dispersions (ASDs), stand out as promising approaches for targeted therapy and controlled release.[20] However, as mentioned earlier, for these new formulations to work effectively, the polymer matrix must be carefully selected for the specific DDS.[21] Micellar DDSs primarily utilize amphiphilic polymers, which contain both hydrophilic and hydrophobic segments. Such a structure enables them to self-assemble in aqueous environments, forming micelles with cores capable of solubilizing hydrophobic APIs.[22] These systems offer several advantages, such as enhanced drug stability, controlled release, and the ability to modify the micelle surface for tissue specificity. As a result, they are widely applied in formulations of APIs with low water solubility and targeted DDSs, including cancer therapies and vaccines.[23,24] On the other hand, in amorphous BMs/ASDs, mostly hydrophilic polymers, due to their strong affinity to water, are primarily used to enhance the drug bioavailability by improving wettability, solubility, and dissolution rate. These systems may reduce or completely damp the crystalline order and stabilize disordered APIs, preventing their recrystallization and maintaining higher concentrations in solution.[12,25] Among the well-known amphiphilic polymers, a copolymer Soluplus, deserves attention. There are increasingly frequent reports indicating its significant ability to enhance the solubility of hydrophobic APIs.[26−28] Consequently, it has been proposed as a carrier for oral drug administration,[29,30] ocular,[31,32] and topical applications,[33,34] as well as intravenous injections in cancer treatment.[27,35] Due to amphiphilic properties, it can self-assemble into micelles with a hydrophilic outer shell and a hydrophobic core that entraps the hydrophobic drug, thereby facilitating its dissolution.[22] Applying Soluplus in micellar DDSs with chosen APIs has been reported in several papers.[36−38] There are also works that describe the impact of this polymer on the physical stability of amorphous APIs prepared by various methods,[39,40] and even the liquid crystalline order of some pharmaceuticals, e.g., itraconazole.[41] In turn, among hydrophilic macromolecules, one can mention polyvinylpyrrolidone (PVP), which is frequently used in various pharmaceutical formulations due to several exceptional properties (high T_g, excellent water solubility, biocompatibility, nontoxicity, chemical stability, good adhesion, and emulsifying properties).[42,43] It acts as an effective stabilizer for many amorphous APIs by reducing their molecular mobility through e.g., enhanced intermolecular interactions.[43,44] Importantly, both approaches—micellar formulations and amorphous BMs, with the appropriate selection of polymer carriers—form the foundation of modern, advanced therapeutic systems, which not only enhance treatment efficacy but also minimize side effects, opening new possibilities in the design of effective medications.

It is important to highlight that, despite ongoing investigations into new polymeric-based pharmaceutical formulations, scientists still predominantly focus on applying various polymer matrices without delving into more complex aspects, such as polymer topology (linear and branched). However, it is well-known that macromolecules with the same chemical composition but differing in architecture/structure can exhibit distinct properties (e.g., various phase transition temperatures, hydrodynamic radius, degree of crystallinity, solubility, or number of functional groups at the chain ends).[45−48] This suggests that such polymers might also cause varied effects on the bioavailability of active substances in drug-polymer formulations. Recognizing this overlooked scientific area, our research group has undertaken detailed research into the impact of macromolecular topology on the physicochemical and pharmacokinetic parameters of poorly bioavailable APIs. Preliminary studies on metronidazole-PVP systems demonstrated that the polymer topology influences drug-polymer interactions and miscibility (the branched polymer was miscible with the active substance in a wider range of concentrations compared to the linear macromolecules).[49] Additionally, we revealed that the dispersity of the polymer is crucial for stabilizing amorphous forms of APIs.[50−52] For instance, investigations on ASDs of the rapidly crystallizing drug—naproxen—and PVPs of varying topologies showed that macromolecules with tightly controlled parameters (targeted M_w, and low $Đ$) effectively suppress the recrystallization of API from the amorphous form. In contrast, a commercially available PVP with high $Đ$ (containing both high- and low-molecular-weight fractions) was the weakest inhibitor of the recrystallization process.[52] Moreover, research on ASDs based on the extremely poorly water-soluble drug itraconazole demonstrated a significant improvement in API solubility (up to 20-fold) when dispersed in a star-shaped polymer matrix compared to a linear one.[51] This clearly indicates that strict control over macromolecular parameters (such as M_w, $Đ$) and architecture is crucial for designing advanced API-polymer formulations.

Inspired by previous intriguing results and aiming to further explore this fascinating scientific area, we developed new ASDs and micellar DDSs based on piribedil (PBD) − a poorly water-soluble and rapidly recrystallizing drug − and polymers with various architectures. As matrices, a commercially available amphiphilic graft copolymer known as Soluplus, composed of three distinct polymer blocks (polyvinyl caprolactam−polyvinyl acetate−polyethylene glycol, PCL−PVAc−PEG), as well as innovative, self-synthesized PVP matrices with linear (*lin*PVP) and three-arm star-shaped (*star*PVP) topologies, were selected. Applying PBD and the polymers described above, we created amorphous BMs and micellar systems in various API to EXC weight ratios, which were subsequently investigated using various experimental techniques. It should be clearly emphasized that just in this paper, using macromolecules of very similar

https://doi.org/10.1021/acs.molpharmaceut.5c00376
Mol. Pharmaceutics 2025, 22, 4708−4730

molecular weight and different composition and topology, we have touched on all key aspects related to *(i)* the character of the polymer matrix (amphiphilic vs. hydrophilic), *(ii)* macromolecular topology (linear vs. branched), and *(iii)* the type of DDS (micelles vs. binary mixtures) to precisely determine which factors are important for improving the physical stability of API, drug release and consequently the bioavailability of the examined API. By closely following the results presented in this work, important conclusions can be drawn regarding the deliberate design of new drug-polymer pharmaceutical systems.

2. MATERIALS AND METHODS

2.1. Materials. 1-vinyl-2-pyrrolidone (VP, > 99%, *Sigma-Aldrich*) was passed through an alumina column before use to remove the inhibitor. 2,2′-Azobis(2-methylpropionitrile) solution (AIBN, 0.2 M in toluene, *Sigma-Aldrich*), cyanomethyl methyl(4-pyridyl) carbamodithioate (CTA1, 98%, *Sigma-Aldrich*), 1,3,5-tris(bromomethyl)benzene (97%, *Sigma-Aldrich*), sodium diethyldithiocarbamate trihydrate (*Sigma-Aldrich*), diethyl ether (pure for analysis, Chempur), methanol (99.85%, *PureLand*), dichloromethane (DCM, 99%, *Honeywell*), chloroform-d (99.8% D, contains 0.03% *v/v* TMS, *Sigma-Aldrich*), Soluplus (M_w∼118 000 g/mol, $Đ$ = 2.05, *BASF*), crystalline PBD (IUPAC name 2-[4-(benzo[1,3]dioxol-5-ylmethyl)piperazin-1-yl]pyrimidine, 98%, *Angene*) were used as received. Acetonitrile for HPLC, ammonium acetate, sodium chloride, and anhydrous sodium dihydrogen phosphate were purchased from Th. Geyer Ingredients GmbH & Co. KG (Höxter-Stahle, Germany). Sodium hydroxide was purchased from VWR Chemicals (Leuven, Belgium). 3F Powder was obtained from the biorelevant.com LTD (London, United Kingdom). Pronoran (Les Laboratoires Servier, France) was purchased from the local pharmacy. Ultrapure water was self-produced from Hydrolab Ultra UV (Hydrolab Sp z o.o., Straszyn, Poland).

2.2. Methods. *2.2.1. Amorphous Binary Mixtures' Preparation.* Amorphous binary mixtures (BMs) composed of PBD and PVP polymers with different topologies, as well as commercial Soluplus polymer, were obtained by melt cooling method. They were prepared at different weight ratios of API to polymer, i.e., 90:10, 80:20, 70:30, and 60:40 *w/w*. To obtain a homogeneous mixture, appropriate amounts of crystalline PBD and polymer were weighed, carefully transferred to a metal plate, and preliminarily mixed using a spatula. Then, the plate with the API-polymer mixture was moved to a hot plate heated to a temperature of 403 K. After a while, PBD began to melt and the entire BM was stirred until complete dissolution of the macromolecule in the API. After determining a homogeneous system, each sample was vitrified by rapidly transferring it to a precooled copper plate.

2.2.2. Drug Loading and Micelle Preparation. PVP or Soluplus and PBD were dissolved in chloroform $CHCl_3$ with the following API-polymer weight ratios: 1:1 and 1:2. Solutions were added dropwise into deionized water and stirred overnight to evaporate the organic solvent. An excess of nonencapsulated drug was removed via filtration (using medium-graded filters with a pore size of 8−12 μm). In the final step, aqueous solutions were lyophilized (freeze-dried). More precisely, the obtained filtrate was frozen in liquid nitrogen for 10 min, then placed in a freeze-dryer (Labconco FreeZone 4.5 L) and lyophilized at 189 K and 0.1 mbar for 48 h.

2.2.3. Thermogravimetric Analysis (TGA). The degradation of the drug (PBD) as well as the pure excipients (Soluplus, *lin*PVP, and *star*PVP) was investigated using a Mettler TG 50 thermogravimetric analyzer coupled with a Mettler MT5 balance (Mettler Toledo, Switzerland). The powders were placed in aluminum pans and heated in a furnace under a nitrogen flow (30 mL/min) at a heating rate of 10 K/min, from room temperature up to T = 873 K. Degradation temperatures of the samples were determined based on the percentage of mass loss.

2.2.4. Differential Scanning Calorimetry (DSC). Preliminary calorimetric measurements of BMs containing PBD and various polymers (i.e., Soluplus, *lin*PVP, and *star*PVP) with different weights ratios (90:10, 80:20, 70:30, 60:40 *w/w*), as well as neat PBD were performed using a Mettler-Toledo DSC system, which is equipped with a liquid nitrogen cooling accessory and an HSS8 ceramic sensor. Temperature and enthalpy were calibrated using indium and zinc standards. Samples were placed in aluminum crucibles (40 μL). The examined PBD-Soluplus 90:10, 80:20, 70:30, and 60:40 *w/w* binary mixtures, as well as neat API were heated from 293 to 393 K, then cooled to 222 K, and reheated to 393 K. An analogous procedure (heating−cooling−heating) was applied in the case of PBD−PVPs 90:10, 80:20, 70:30, and 60:40 *w/w* binary mixtures, but within a different temperature range (they were heated in the T-range of 293−381 K, then cooled to 250 K, and reheated to 381 K). In turn, neat polymers (Soluplus, *lin*PVP, and *star*PVP) were heated from 293 to 483 K, next cooled to 230 K, and heated again to 425 K (Soluplus) or 483 K (PVPs). Measurements were performed at a constant heating/cooling rate (ϕ) of 10 K/min. In turn, nonisothermal studies at a ϕ from 2 to 20 K/min were carried out over a temperature range of 220 to 410 K. Additionally, the amorphous PBD-Soluplus and PBD-*lin*PVP binary mixtures (90:10, 80:20, 70:30, 60:40 *w/w*), as well as the molten API, were left to recrystallize at room temperature, after which each sample was scanned using a slow heating rate of 2 K/min within the temperature range of 298 to 413 K. The data collected in this manner were used to confirm the miscibility of the systems. For one representative sample, PBD-*lin*PVP 60:40 *w/w*, calorimetric measurements were performed at a standard heating rate (ϕ = 10 K/min) over three thermal cycles (heating from 298 to 473 K, cooling to 223 K, and reheating to 473 K). Furthermore, the PBD-*lin*PVP 80:20 *w/w* formulation was subjected to calorimetric analysis both before and after the release process, with heating conducted from 298 to 403 K at a standard rate (10 K/min). Each measurement at a given ϕ was repeated 2 times. For each experiment, a new sample was prepared. It should be mentioned that all described calorimetric measurements for the PBD−PVPs systems were performed immediately after sample preparation to avoid water absorption by the hygroscopic PVP.

The values of the calorimetric glass transition temperature (T_g) for all samples were determined as the midpoint of the heat capacity increment. In turn, the crystallization and melting temperatures (T_c and T_m) were obtained from the maximum of the exothermic and endothermic peaks in the thermograms, respectively.

2.2.5. X-ray Diffraction (XRD). XRD patterns of neat PBD, polymers, their BMs, and micellar systems were collected using a D/Max Rapid II diffractometer (Rigaku, Tokyo, Japan) equipped with a rotating Ag anode X-ray tube powered by 12 kW, a graphite (002) monochromator, and a two-dimensional curved image-plate detector. The powdered samples were probed in borosilicate glass capillaries of 1.5 mm diameter. The size of the collimated incident X-ray beam on the probed sample

https://doi.org/10.1021/acs.molpharmaceut.5c00276
Mol. Pharmaceutics 2025, 22, 4708−4730

was 0.3 mm, and the wavelength was 0.5608 Å (Ag K_α line). The background from empty capillary was also measured and subtracted from the patterns collected for samples. All measurements were performed at a temperature of 293 K. Before XRD measurements, each sample was vacuum-dried in a desiccator for a minimum of 1 h to eliminate any moisture.

2.2.6. Fourier-Transform Infrared (FT-IR) Spectroscopy. FTIR spectra were measured on the Nicolet iS50 spectrometer (Thermo Fisher Scientific, Massachusetts, USA) in the ATR (attenuated total reflectance) mode in the range of 4000−400 cm^{-1} at 293 K. The data were recorded at a spectral resolution of 4 cm^{-1}, taking 16 scans. The high-temperature FTIR spectrum of PBD (at T = 393 K) was measured using a GladiATR accessory (Pike Technologies) coupled with an FTIR spectrometer in the range 4000−400 cm^{-1} (32 scans; spectral resolution of 4 cm^{-1}). All examined binary mixtures were measured immediately after preparation to avoid water absorption by hygroscopic PVP polymers.

2.2.7. Broadband Dielectric Spectroscopy (BDS). Complex dielectric permittivity measurements ($\varepsilon^*(\omega) = \varepsilon'(\omega) - i\varepsilon''(\omega)$) of binary mixtures composed of PBD and various polymers (90:10 and 80:20 w/w) were performed using the Novocontrol Alpha dielectric spectrometer (Novocontrol Technologies GmbH & Co. KG, Hundsangen, Germany), with temperature control provided by a Quatro system, employing a nitrogen gas cryostat with a stability better than 0.1 K. The data were collected over a frequency range from 10^{-1} to 10^6 Hz. The sample was placed between two stainless steel electrodes of a capacitor (diameter: 15 mm, gap: 0.15 mm) and mounted on a cryostat.

Molecular dynamics studies of PBD-Soluplus BMs were conducted within the T-range of 228−397 K. In turn, PBD-*lin*PVP and PBD-*star*PVP systems were measured in the T-range of 173−353 K.

Crystallization kinetics studies (neat PBD and PBD-polymer 90:10 and 80:20 w/w systems) were performed at a frequency of 10^4 Hz, which corresponded to different temperatures depending on the system (please see Table 1 in the main manuscript). Each sample, after preparation, was heated to T = 373 K (above the melting point of the API), subsequently cooled well below the glass transition temperature (approximately T = 173 K), and then heated to the planned crystallization temperature. Spectra were collected until complete crystallization occurred.

Table 1. Parameters of the Avrami Formula Used to Describe the Kinetics of Isothermal Crystallization Monitored Using BDS for Neat PBD and PBD-Polymer Systems

No.	Sample/ System	Weight ratio API:polymer	T_c [K]	k [s^{-n}]	n-value	$t_{1/2}$ [s]
1.	neat PBD	–	268	1.81×10^{-4}	2.55	4 800
2.	PBD-Soluplus	90:10	328	2.57×10^{-4}	3.00	3 400
3.	PBD-*lin*PVP		333	2.66×10^{-4}	2.92	3 400
4.	PBD-*star*PVP		333	1.79×10^{-4}	3.67	5100
5.	PBD-Soluplus	80:20	333	1.56×10^{-4}	1.85	5 300
6.	PBD-*lin*PVP		345	6.37×10^{-5}	2.74	13 800
7.	PBD-*star*PVP		341	5.21×10^{-5}	3.85	17 700

2.2.8. Critical Micelle Concentration (CMC). The surface tension (γ) at 25 °C ± 0.1 °C was measured by the pendant drop technique with a Krüss DSA 100 tensiometer (using Advanced software). There is a direct method, in which γ is determined by fitting the Young−Laplace equation (eq 1) to the drop's contour.

$$\Delta P = P_{in} - P_{out} = \gamma\left(\frac{1}{R_1} + \frac{1}{R_2}\right) \quad (1)$$

where P_{in}, P_{out} are pressures inside and outside of curved liquid surface/interface, respectively, γ is the surface tension, and R_1 and R_2 are the main radii of curvature.

The drop's size and shape are related to the liquid's surface tension when the drop is hanging freely from the tip of the needle (in equilibrium with the cohesive and gravitational forces). The resolution and the accuracy of the surface tension measurements declared by the manufacturer are 0.01 and 0.3 mN/m, respectively. The critical micelle concentration (CMC) of the surfactants in aqueous solution can be calculated from the analysis of the concentration (c) dependence of γ (as γ (c) or γ (logc)). It is determined as a cross-point of two straight lines representing lower and higher concentration dependences of γ for the surfactant (before and after CMC). It is well-known that for higher concentrations, after CMC, the surface tension changes only slightly since all aggregation processes occurring in the bulk solutions have a minimal influence on the surface.

2.2.9. UV−Vis Spectrophotometry. All measurements were performed using Agilent Technologies Cary 60 UV−Vis spectrophotometer and Cary WinUV software for data processing. PBD solutions in ethanol of different concentration were measured to determine calibration curve (see **Figures S16 and S17** in the Supporting Information, SI).

Drug loading efficiency (DLE) and drug loading content (DLC) were determined for the prepared micellar systems dissolved in ethanol and calculated from the following eqs (eq 2) and (eq 3):

$$DLE = \frac{m_{DM}}{m_D} \cdot 100\% \quad (2)$$

where m_{DM} is the amount of drug in micelles, while m_D is the amount of drug used for preparing micellar systems.

$$DLC = \frac{m_{DM}}{m_{DLM}} \cdot 100\% \quad (3)$$

where m_{DLM} is the amount of drug-loaded micelles used for measurement.

For drug release studies, API-polymer micellar systems (30 mg) were dissolved in 1 mL of the Fasted State Simulated Intestinal Fluid (FaSSIF) solution, prepared before use according to the procedure described in the HPLC section. The solution was introduced into a dialysis cellulose membrane bag (MWCO 3.5 kDa), which was placed into a glass vial with 30 mL of FaSSIF solution and stirred at 37 °C in an oil bath. The dialysis was carried out for 24 h. The solution samples (100 μL) were taken from the release medium at appropriate time intervals (5, 15, 30, 60, 120, 180, 1200, and 1460 min) and dissolved in ethanol (1 mL) to determine the concentration of released drug by UV−Vis spectroscopy. Due to different DLC in each micellar system, the results were calculated referring to the equivalent of API used in HPLC studies to enable comparison of the drug release profiles performed utilizing these two methods (UV−Vis spectroscopy and HPLC).

https://doi.org/10.1021/acs.molpharmaceut.5c00376
Mol. Pharmaceutics 2025, 22, 4708−4730

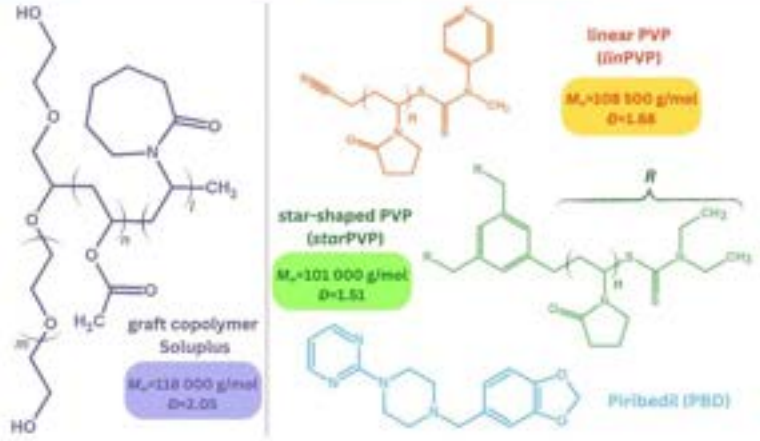

Figure 1. Chemical structures of PBD and different polymeric matrices (commercially available Soluplus and self-synthesized macromolecules – *lin*PVP and *star*PVP) along with their macrostructural parameters (M_w, $Đ$).

2.2.10. Dynamic Light Scattering (DLS). Hydrodynamic diameters (d_h) and zeta potentials (ZP) of polymer particles were measured on Malvern Zetasizer Nano-ZS (4 mW Hesingle bondNe ion laser, λ = 633 nm) for samples in deionized water (1 mg/mL) at 25 °C ± 0.1 °C.

2.2.11. Transmission Electron Microscopy (TEM). Microstructure analysis was carried out using JEOL JEM-3010 high-resolution transmission electron microscope (TEM, JEOL Ltd., Tokyo, Japan) with 300 kV acceleration voltage, equipped with a Gatan 2k × 2k Orius 833 SC200D CCD camera (Gatan Inc., Pleasanton, CA, USA). The studied micelles were suspended in isopropanol and deposited on a Cu grid with an amorphous carbon film standardized for TEM observations. Micelles' size distribution was characterized based on the image analysis performed using free-of-charge, open ImageJ software (1.54k).

2.2.12. Preparation of FaSSIF Solution. Fasted State Simulated Intestinal Fluid (FaSSIF, biorelevant.com LTD, United Kingdom) was prepared using 3F Powder (FFF-02) according to the instructions of the manufacturer. Briefly, 0.42 g of sodium hydroxide, 3.438 g of anhydrous sodium dihydrogen phosphate, and 6.186 g of sodium chloride were weighed and dissolved in 900 mL of ultrapure water. The pH was adjusted to 6.5 with 1 M hydrochloric acid or 1 M sodium hydroxide and the volume was made up to 1000 mL. Then 2.24 g of 3F Powder was added. For equilibration, the solution was left at room temperature for 2 h.

2.2.13. HPLC Method. The determination of PBD concentration in the micellar samples was determined using the RP-HPLC (Reverse Phase – High-Performance Liquid Chromatography) method adapted from Uppuluri et al.[57] The analysis was performed on a Shimadzu LC-2050C system (Shimadzu U.S.A Manufacturing Inc., Canby, OR, USA) with a DAD detector, equipped with Phenomenex Kinetex EVO C18 (250 × 4.6 mm, 5 μm) chromatographic column. The mobile phase consisted of 10 mM ammonium acetate, pH 4.0, and acetonitrile (75:25) and the elution was isocratic. The flow rate was 1.5 mL/min. The column was thermostated at 40 °C. The retention time was 2.6 min, while the wavelength was 286 nm. The method was characterized by good linearity (R^2 = 0.9999).

2.2.14. Determination of Saturation Solubility and Solubility Kinetics. Determination of the saturation concentration and solubility kinetics of PBD was performed in a small-scale dissolution system (Physiolution Poland). The device consisted of a magnetic stirrer with a precise thermostat, allowing the test to be carried out simultaneously in nine 25 mL glass vessels. An amount of sample equivalent to 25 mg of neat PBD was weighed into the vessel each time. In the Pronoran tablets test (50 mg of PBD, Les Laboratoires Servier, France) it was previously crushed in a mortar. Then 25 mL of FaSSIF preheated to 37 °C was added. The samples were stirred constantly, and the temperature was maintained at 37 °C.

Samples were withdrawn at the following time points: 5 min, 15 min, 30 min, 1, 2, 3, 4, 23, and 24 h. The sample was withdrawn through a 1 μm polyethylene cannula filter (ProSense B.V., Oosterhout, Netherlands) and then filtered into a centrifuge tube through a syringe filter (RC 0.2 μm, J.T. Baker). Subsequently, the sample was diluted with acetonitrile at a 1:1 volume ratio and analyzed by HPLC.

3. RESULTS AND DISCUSSION

3.1. Results of Experimental Studies on ASDs Composed of PBD and Different Polymers. At the outset, it should be emphasized that herein we explore new-synthesized hydrophilic PVP matrices with various topologies (linear vs. branched) in different pharmaceutical formulations (binary systems and micelles) and compare them to a commercial amphiphilic copolymer (Soluplus) in the context of their impact on physical and pharmacokinetic properties of a hydrophobic drug, piribedil (PBD) used in the treatment of Parkinson's disease. It is worth mentioning that the detailed procedures for obtaining PVPs with various topologies have been outlined in our previous publications.[49,51] However, for the purpose of this work, we synthesized new linear PVP (*lin*PVP) and star-shaped PVP (*star*PVP) macromolecules with M_w comparable to the commercial copolymer Soluplus, using the same synthetic procedures but modifying the reagent ratios, temperature, and reaction time (please see the SI). Such an approach allowed us to evaluate the influence of structure (linear vs. branched) and properties (hydrophilic vs. amphiphilic) of the polymer

https://doi.org/10.1021/acs.molpharmaceut.5c00276
Mol. Pharmaceutics 2025, 22, 4708−4730

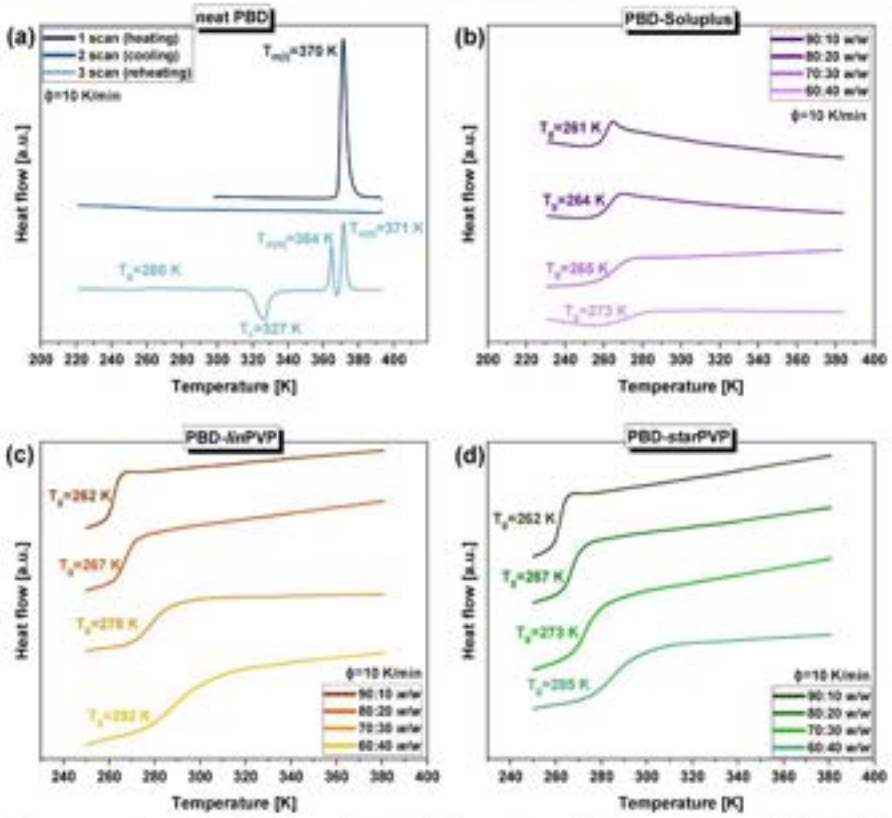

Figure 2. DSC thermograms (ϕ = 10 K/min) of (a) neat drug-PBD and binary mixtures with different weight ratios, (b) PBD-Soluplus, (c) PBD-*lin*PVP, and (d) PBD-*star*PVP (90:10, 80:20, 70:30, 60:40 *w*/*w*).

exclusively on the physical stability and the release (hence bioavailability) of PBD, eliminating the effect of EXC's molecular weight on the behavior of the API. The chemical structures of PBD and the applied polymers, along with their macromolecular parameters, are presented in Figure 1.

Initially, before proceeding with the preparation of API−polymer mixtures, TGA analyses were performed for all pure substances to exclude the possibility of drug or polymer degradation during formulation using the high-temperature melt method (at T = 403 K). As clearly shown in **Figure S1** in the SI, the degradation temperatures of each compound significantly exceed 500 K, which clearly indicates that the melt-cooling method, described in detail in the Materials and Methods section, can be successfully applied for the preparation of binary formulations. Subsequently, for the self-synthesized polymeric matrices (*lin*PVP, *star*PVP), we conducted NMR measurements to confirm the chemical structure and purity of the obtained compounds (**Figures S2 and S3** in the SI). With the molecular structure of the synthesized macromolecules determined and individual degradation temperatures established, the preparation of binary mixtures was initiated. During multiple formulation attempts using the vitrification method, we found that PBD can mix freely with the excipients at a maximum weight ratio of 60:40 *w*/*w*. However, to verify this experimentally, NMR spectra were recorded for both physical mixtures and binary systems at the highest tested mass ratio (i.e., 60:40 *w*/*w*). As shown in **Figures S4** and **S5** in the SI, both physical mixtures and binary systems exhibit identical chemical shifts and comparable signal intensities, which confirms that the intended drug-to-polymer ratio was preserved during the preparation of binary mixtures. Next, DSC measurements were performed up to 473 K (i.e., above the T_g of the neat polymer) for a selected representative PBD−*lin*PVP 60:40 *w*/*w* mixture. As seen on the representative thermogram (**Figure S6** in the SI), no signal corresponding to unmixed/free polymer is observed, suggesting the formation of a homogeneous binary mixture.

Nevertheless, to further confirm drug−polymer miscibility, a Flory−Huggins analysis was carried out. According to this approach, the interaction parameter (χ) can quantitatively describe miscibility from a thermodynamic perspective by using the melting point depression method.[54,55] Typically, in miscible systems, due to the exothermic nature of mixing, a decrease in the melting point of the drug is expected, whereas the opposite trend indicates immiscibility. The determined χ values were negative, which indicates that the polymers used (Soluplus and PVPs) can be homogeneously mixed with the drug up to a 60:40 weight ratio. This analysis is presented and described in detail in

https://doi.org/10.1021/acs.molpharmaceut.5c00276
Mol. Pharmaceutics 2025, 22, 4708−4730

the SI (**Figures S7** and **S8**). As a result, amorphous PBD−Soluplus and PBD−PVPs systems at 90:10, 80:20, 70:30, and 60:40 *w*/*w* were selected for further detailed analysis.

3.1.1. DSC Data. At the beginning, we performed calorimetric measurements on the neat macromolecules (**Figure S9** in the SI) and API. As seen in Figure 2a, during the heating of crystalline PBD (ϕ = 10 K/min), a strong endothermic peak at T = 370 K corresponding to the melting of the substance, is visible in the thermogram (dark blue line). After cooling the molten sample (at the same ϕ = 10 K/min; navy blue line) and reheating it, four thermal events can be detected (light blue line). The first, occurring at lower T, might be attributed to the glass transition at T_g = 260 K. Additionally, at higher temperatures, exothermic and endothermic processes, corresponding to the crystallization (at T_c = 327 K) and melting (at $T_{m(1)}$ = 371 K, and $T_{m(2)}$ = 364 K), respectively, are observed. The presence of the two melting peaks is an interesting observation that may indicate the formation of two polymorphic forms of PBD during the second heating run (Figure 2a, light blue line). To the best of our knowledge, only one polymorphic form of PBD (form I) with a melting point at $T_{m(I)}$ = 370 K[58] has been reported in the literature so far. There are no mentions of the other polymorphs. This issue will be elaborated in the further part of this paper. Additionally, before proceeding with the calorimetric studies of the binary mixtures, it is important to highlight one crucial aspect. During the cooling of neat PBD from the molten state at a rate of ϕ = 10 K/min (Figure 2a, second scan, navy blue line), no signs of crystallization were observed. However, in the subsequent heating cycle (Figure 2a, third scan, light blue line), recrystallization of the API can be observed. This observation is important for correctly classifying PBD within the appropriate Glass-Forming Ability (GFA) group. The GFA classification system is based on the tendency of a drug to recrystallize during cooling and heating cycles.[57] GFA class I refers to compounds that recrystallize during cooling of the melt at a rate of 20 K/min. Class II compounds do not recrystallize during cooling at 20 K/min but recrystallize during the subsequent heating cycle at 10 K/min. Finally, GFA class III compounds do not recrystallize during either cooling at 20 K/min or reheating at 10 K/min.[58] The GFA classes (I, II, and III) represent poor, moderate, and good glass formers, respectively. Based on this classification, the studied drug should be assigned to GFA class II, indicating that PBD exhibits moderate stability of its amorphous form upon heating above its T_g.

Intrigued by the above results, subsequent calorimetric measurements were carried out on PBD-polymer systems (also at the standard ϕ = 10 K/min) to check how the addition of EXCs affects the crystallization process of API and the formation of different polymorphs. As shown in Figure 2b−d, PBD in each mixture, even with a small amount of the excipient (10 wt %), could be vitrified regardless of the type of polymer matrix used. In every case, attempts to prepare ASDs were successful, and the DSC curves of these formulations showed only a single thermal event. Specifically, the thermograms of API-polymer systems reveal only the glass transition event without any signs of recrystallization, indicating their amorphous nature and the suppression of PBD crystallization. Values of T_g determined for the individual BMs are presented in Figure 2 and additionally summarized in tabular form (please see **Table S1** in the SI).

They were also plotted as a function of the weight fraction of PBD in Figure 3. As expected, the lower X_{PBD} (and consequently, the greater $X_{polymer}$ in the mixtures), the higher T_g of the system.

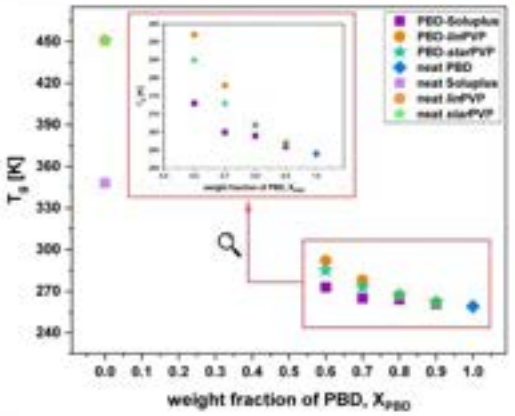

Figure 3. Dependency of calorimetric T_g vs. X_{PBD} for the examined ASDs (ϕ = 10 K/min).

A similar scenario was reported in numerous works devoted to various API-EXC systems, both containing low-molecular-weight[59−62] and high-molecular-weight[50−52,63,64] additives. Therefore, the result obtained for the examined PBD-Soluplus and PBD-lin/starPVP BMs is not particularly surprising, but another aspect should be noted. Namely, the progressive addition of both PVP polymers (linear and branched) significantly influences the T_g, while mixing PBD with Soluplus (10−30 wt % of the polymer) results in a minor variation in the T_g (up to 4 K; see the purple squares in Figure 3). Only the larger amount of this macromolecule (40 wt %) causes a more pronounced increase in the glass transition temperature (up to 273 K), though still not as strong as in the case of the BMs with various PVPs. The observed effect is most likely related to the significant differences in the T_g values of two PVPs and Soluplus polymers (see **Table S1** in the SI). At this point, it is worth highlighting an interesting observation − namely, despite the pronounced differences in the T_g values of the pure polymers Soluplus and PVPs (approximately 100 K, see **Figure S9** in the SI), the binary mixtures (especially at the 90:10 *w*/*w* ratio) do not exhibit such striking discrepancies in T_g. This phenomenon suggests a lack of specific intermolecular interactions between the polymers and the API, which was confirmed by infrared spectroscopy studies (description below). However, it should be noted that the absence of significant differences between the T_g of BMs was mainly observed at low/moderate polymer concentrations (10 and 20 wt %). In contrast, as the polymer content increases, the T_g values of individual ASDs begin to diverge more clearly, which corresponds well with the variations in T_g observed for the pure excipients.

Taking into account the preliminary DSC measurements at a standard heating rate of 10 K/min, which demonstrated rather good physical stability and lack of crystallization of all tested BMs during heating, in the next step we conducted non-isothermal DSC studies at ϕ = 2, 4, 8, and 20 K/min for PBD and at ϕ = 2, 4, 6, and 8 K/min for the selected PBD-polymer BMs (Figure 4).

As shown in Figure 4a, the DSC curve of neat API reveals three/or four thermal events depending on the applied ϕ. As previously mentioned, the heat capacity jump at the lowest T corresponds to the glass transition (at T_g). It is followed by a strong nonsymmetric exothermic signal attributed to the PBD

https://doi.org/10.1021/acs.molpharmaceut.5c00276
Mol. Pharmaceutics 2025, 22, 4708−4730

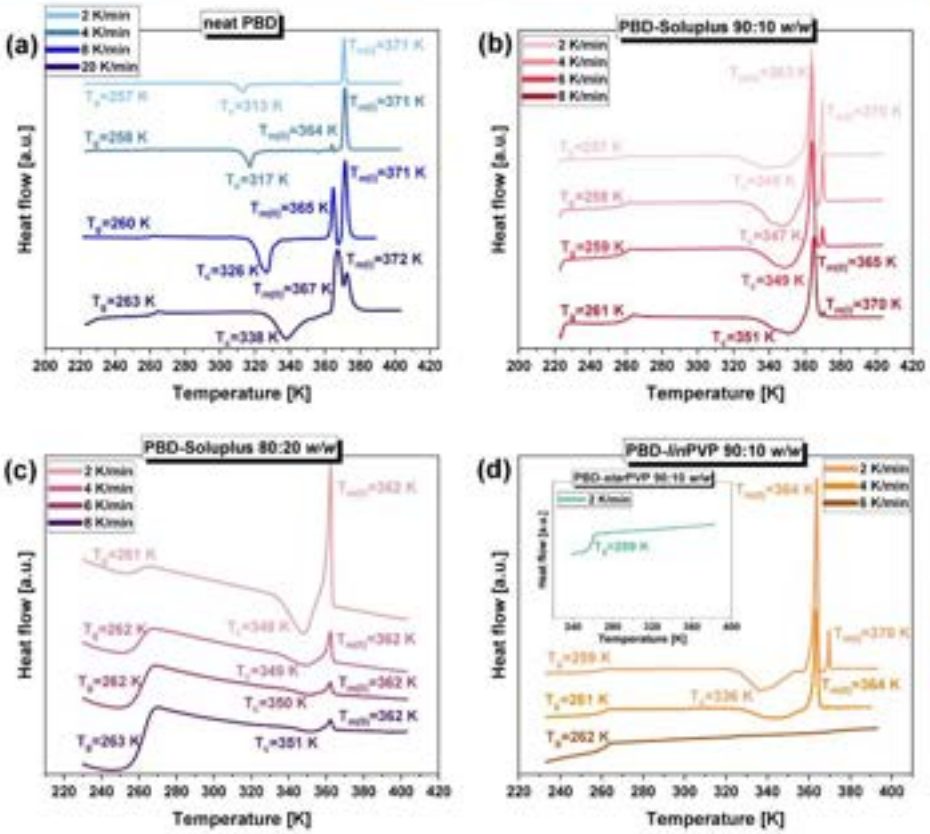

Figure 4. DSC thermograms obtained from nonisothermal measurements of (a) neat PBD, as well as different BMs: (b) PBD-Soluplus 90:10 *w*/*w*, (c) PBD-Soluplus 80:20 *w*/*w*, (d) PBD-*lin*PVP 90:10 *w*/*w* (in the inset, the thermogram of PBD-*star*PVP 90:10 *w*/*w* system collected at ϕ = 2 K/min is presented).

crystallization (at T_c), and an endothermic peak/or peaks related to the melting of API. In agreement with other reports on the nonisothermal studies,[63−67] it can be observed that at higher ϕ, T_g and T_c shift to higher values. Importantly, even at the highest ϕ (20 K/min), a strong exothermic peak (consisting of the two components) is well visible, which clearly suggests a great tendency of PBD to recrystallization. Moreover, at the slowest rate (ϕ = 2 K/min), only a single sharp and intense endothermic peak is noticeable at $T_{m(I)}$ = 371 K. Conversely, as the ϕ increases (4, 8, and 20 K/min), an additional thermal event begins to appear (and becomes more pronounced in the thermogram) at a slightly lower T ($T_{m(II)}$ = 364−367 K), Figure 4a. This leads to the conclusion that by modulating the heating rate of the neat PBD, it is relatively straightforward to alter the proportion of the two polymorphic forms (I and II) presented in the sample.

The outcomes of the nonisothermal calorimetric measurements for PBD-Soluplus, 90:10 and 80:20 *w*/*w* mixtures, as well as PBD−PVP 90:10 *w*/*w* systems are shown in panels **b**−**d** of Figure 4. As can be observed, PBD-Soluplus 90:10 *w*/*w* BM, similar to the neat PBD, exhibits four distinct thermal events (at T_g, T_c, $T_{m(I)}$ and $T_{m(II)}$). Interestingly, unlike the neat API, in this mixture, the recrystallization to the polymorphic form II with the lower melting temperature ($T_{m(II)}$) is favored. Moreover, the amount of polymorph I with the higher $T_{m(I)}$ gradually decreases with increasing ϕ. Another intriguing observation is that a higher Soluplus content in the mixture (20 wt %) results in recrystallization exclusively to the polymorphic form II of PBD with $T_{m(II)}$ = 362 K, as is seen in Figure 4c. In turn, a *lin*PVP appears to be a better candidate for effective suppression of PBD recrystallization. Specifically, the thermogram of PBD-*lin*PVP 90:10 *w*/*w* BM exhibits a wide (double) exothermic peak assigned to the crystallization only at the slowest ϕ = 2 and 4 K/min, whereas at a slightly greater ϕ (6 K/min), only a glass transition event is observed, indicating a fully disordered nature of the material (Figure 4d). In the case of PBD-*star*PVP system, even just a 10 wt % of the polymer at the slowest ϕ (2 K/min) significantly suppresses the drug crystallization, as evidenced by the occurrence of only heat capacity jump at T_g = 259 K in the DSC curve (see the inset in Figure 4d). It is worth adding that in PBD-*lin*PVP 90:10 *w*/*w* BM, the API recrystallized to both polymorphic forms: I and II with the predominance of the latter one. The content of both polymorphs is clearly reduced at ϕ = 4 K/min with respect to ϕ = 2 K/min. Note that the crystallization temperatures for the studied samples are summarized in **Table S2** in the SI. It should also be mentioned that the nonisothermal

https://doi.org/10.1021/acs.molpharmaceut.5c00376
Mol. Pharmaceutics 2025, 22, 4708−4730

calorimetric data for the PBD-*lin*PVP and PBD-*star*PVP, 80:20 *w*/*w* BMs were not presented in Figure 4 due to the lack of recrystallization tendency even at the slowest ϕ (=2 K/min).

All the above observations lead to the conclusion that PVP matrices more effectively (in comparison to Soluplus) inhibit undesired recrystallization of the API from the binary mixtures. Furthermore, besides the type of polymer, its topology (linear and branched) plays a crucial role in controlling the crystallization of PBD. It is also worth stressing that, by selecting an appropriate polymer and adjusting the heating rate of the system, it is possible to obtain (upon recrystallization) one or two polymorphic forms of API of various content in the sample. This provides a unique opportunity to relatively easily modulate the stability of PBD depending on the specific needs.

Subsequently, based on the obtained nonisothermal DSC data, a Kissinger analysis was performed to determine the activation energy for the crystallization of the examined API (E_a). It should be added that in the case of API-PVP BMs, using such an approach (which is based on the variation of T_c, i.e., the crystallization peak temperature, with ϕ) was not feasible due to the absence of crystallization phenomenon in the collected thermograms (this process was detected only for PBD-*lin*PVP, 90:10 *w*/*w* system at ϕ = 2 and 4 K/min - such data were insufficient to accurate analysis). Moreover, the PBD-*star*PVP BM at any weight ratio of both components and heating rate showed no signs of this process. Therefore, we applied the Kissinger method (eq 4)[48] exclusively for PBD-Soluplus mixtures (see Figure 5)

$$\ln\left(\frac{\phi}{T_c^2}\right) = C_4 - \frac{E_a}{RT_c} \tag{4}$$

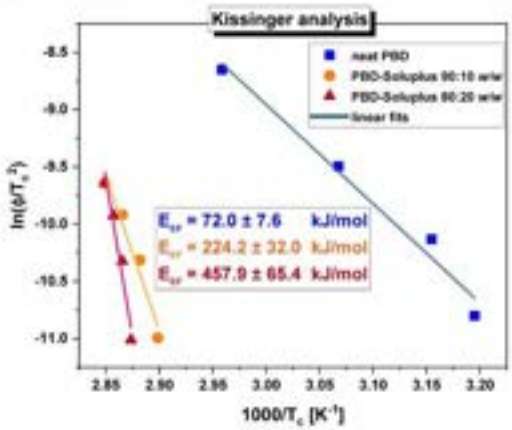

Figure 5. Kissinger plots for the exothermic crystallization peaks in neat PBD, as well as PBD-Soluplus 90:10 and 80:20 *w*/*w* systems (the solid lines represent linear fits).

where C_4 is fitting parameter and R is gas constant.

As can be clearly observed in Figure 5, the activation barrier for the crystallization of PBD in BMs with Soluplus increases significantly compared to the neat API (E_a = 72 kJ/mol). Even a 10 wt % of the polymer leads to a substantial increase in the E_a value (up to 224 kJ/mol). For the PBD-Soluplus 80:20 *w*/*w* mixture, E_a reaches up 458 kJ/mol. Such results indicate that this polymer (and its amount in the BM) has a significant impact on the activation barrier for the nonisothermal crystallization of PBD. At this point, it is important to emphasize that in the case of other API-polymer and API-oligosaccharide systems (with various amounts of EXC), such high E_a values determined from the Kissinger analysis are rarely reported. The calculated activation energies for the drug crystallization are usually at a low/moderate level, e.g.,: for naproxen-various PVPs (E_a = 68−77 kJ/mol),[52] for metronidazole-PVPs (E_a = 65−71 kJ/mol),[49] and for metronidazole-cyclodextrins (E_a = 51−68 kJ/mol).[61] Higher values were determined for naproxen-oligosaccharides (E_a = 64−109 kJ/mol),[62] and flutamide-PVPs, 90:10 *w*/*w* ASDs (E_a = 170−200 kJ/mol).[50] Importantly, in the latter systems, in contrast to PBD-polymer ones, all macromolecules decreased slightly the activation barrier for flutamide crystallization in comparison to the neat API. To the best of our knowledge, only one study on the aspirin−poly(vinyl alcohol-*co*-ethylene) revealed a great increase of E_a (~ 500 kJ/mol) compared to the neat drug (E_a = 156 kJ/mol).[69] The authors explained this finding as related to the inhibition of API crystal growth due to strong interactions between aspirin clusters and the polymer matrix.

In one of the further subsections, the outcomes of infrared studies, which were conducted to verify whether PBD-matrix interactions play a key role in inhibiting API crystallization, will be discussed.

3.1.2. XRD Data. To specify the nature of the PBD phase structure in the studied binary systems with polymers as well as its stability and recrystallization behavior, we performed XRD studies. Figure 6 presents the comparison of the diffraction patterns for PBD-Soluplus (**panels a, d, g, j**), PBD-*lin*PVP (**panels b, e, h, k**), and PBD-*star*PVP (panels **c, f, i, l**) mixtures at different weight ratios: 90:10, 80:20, 70:30, and 60:40 *w*/*w*, measured as fresh samples − just after preparation, and over time − over the course of days. All the experiments were carried out at room temperature (T = 293 K) and the samples were stored during this experiment in room conditions as well, in closed glass capillaries. The XRD patterns of neat PBD and polymers were also presented for reference. As one can see, the diffraction patterns of all BMs collected just after their preparation exhibit only a broad halo, confirming their amorphous character. However, in the case of the PBD-Soluplus system, the appearance of sharp Bragg peaks in the XRD data in the time scale of days is noted. PBD in ASD with the lowest concentration of Soluplus, 90:10 *w*/*w*, recrystallized after 1 day of storage, while for the higher Soluplus concentrations, there was a clear trend in the increase of the physical stability of the amorphous state with the higher fraction of the polymer. For the system with the highest loading of Soluplus (60:40 *w*/*w*), the recrystallization of PBD proceeded only after 2 weeks.

Regarding the polymorphic form of the PBD recrystallized from PBD-Soluplus ASDs, from the XRD patterns presented in panels **a, d, g, j** of Figure 6, one can see that the pattern of Bragg peaks for this recrystallized mixture is different from that reported for the neat PBD. For the 90:10 *w*/*w* system, the pattern for the recrystallized system was composed of Bragg peaks typical for polymorphic form I of the neat PBD as well as additional Bragg peaks (in the predominant fraction), which confirm the formation of another polymorphic phase (form II). Further calorimetric investigations on this BM recrystallized at room temperature confirmed this. However, a much different situation was found for the binary systems with the lower API content. XRD investigations supported by the further DSC

https://doi.org/10.1021/acs.molpharmaceut.5c00276
Mol. Pharmaceutics 2025, 22, 4708−4730

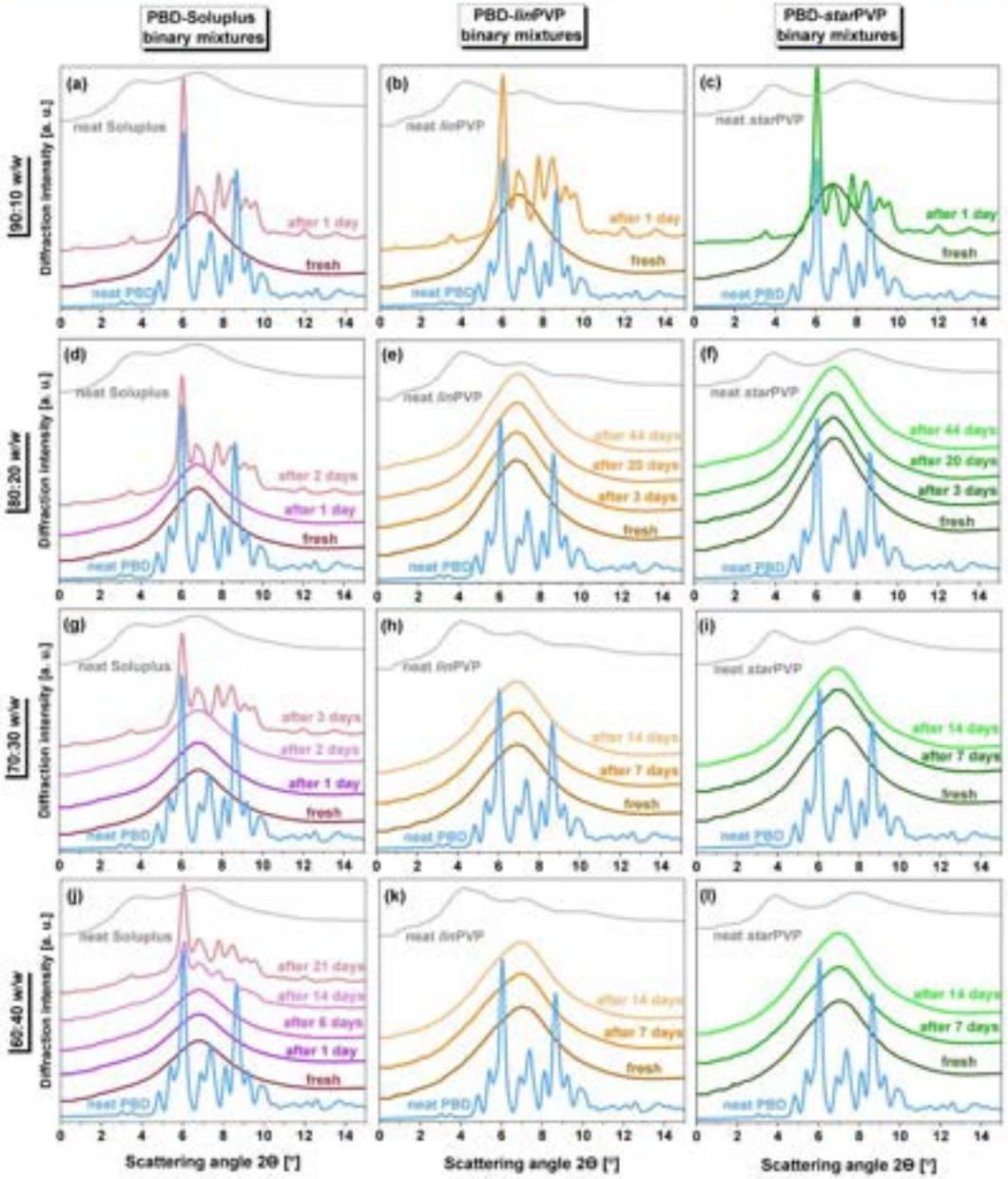

Figure 6. Temporal evolution of diffraction patterns for (**a, d, g, j**) PBD-Soluplus, (**b, e, h, k**) PBD-linPVP and (**c, f, i, l**) PBD-*star*PVP mixtures at different weight ratios 90:10, 80:20, 70:30 and 60:40 w/w.

studies on the recrystallized samples with the amount of Soluplus ≥ 20 wt %) indicated only one melting at $T_{m(II)}$ = 360−361 K (see **Figure S10** in the SI). Therefore, we could conclude that the diffraction patterns collected for the BMs with the higher polymer content are strictly related to the sole presence of the polymorph II of PBD not described before in the literature.

To verify the stability of PBD in ASDs with PVP polymers (*lin*PVP and *star*PVP) in room conditions, their diffraction data measured at different time points were analyzed. As can be seen from **panels b** and **c** in Figure 6, the recrystallization of PBD in the systems with the lowest PVP content (90:10 w/w) was visible after 1 day of storage, regardless of the PVP architectures,

https://doi.org/10.1021/acs.molpharmaceut.5c00276
Mol. Pharmaceutics 2025, 22, 4708−4730

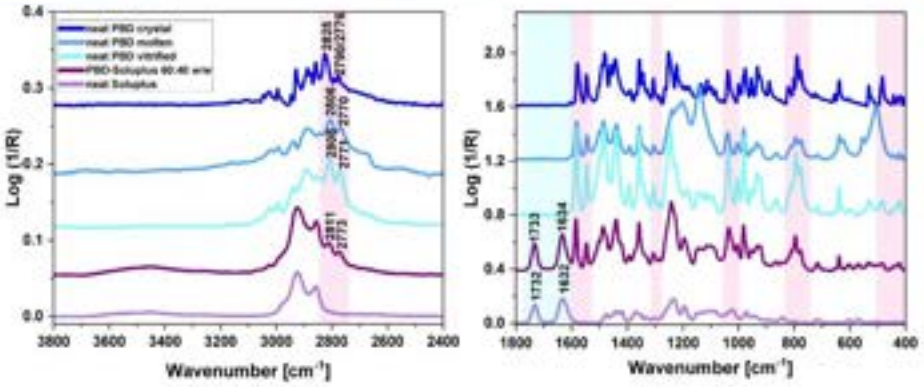

Figure 7. FTIR spectra of neat supercooled, crystal, and molten PBD as well as neat Soluplus and PBD-Soluplus 60:40 *w*/*w* BM, presented in the ranges of (left) 3800−2400 cm^{-1} and (right) 1800−400 cm^{-1}. The spectral regions characteristic for neat PBD and neat polymer (not overlapped by the signals of the second compound) are highlighted in light pink and light blue, respectively.

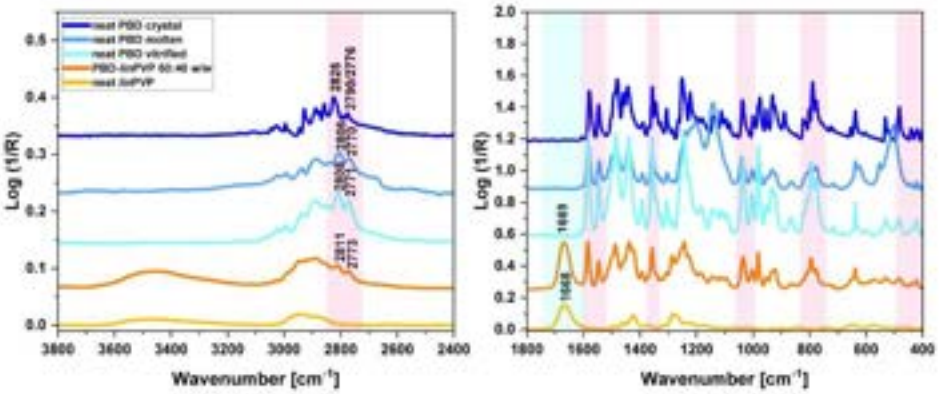

Figure 8. FTIR spectra of neat supercooled, crystal, and molten PBD as well as neat *lin*PVP and PBD-*lin*PVP 60:40 *w*/*w* BM, presented in the ranges of (left) 3800−2400 cm^{-1} and (right) 1800−400 cm^{-1}. The spectral regions characteristic for neat PBD and neat polymer (not overlapped by the signals of the second compound) are highlighted in light pink and light blue, respectively.

similar to the behavior of the PBD in the system with Soluplus polymer of the same weight ratio. Moreover, the recrystallized systems were primarily composed of polymorphic form II, which agrees with the results of calorimetric investigations. In contrast, for ASDs with higher PVP concentrations (80:20, 70:30, and 60:40 *w*/*w*), no fingerprints of PBD recrystallization were observed up to 44 days. Thus, compared to the mixtures with Soluplus, the PBD−PVP BMs were much more physically stable.

3.1.3. FTIR Data. The next step of our research was FTIR spectroscopy measurements. Their purpose, as previously mentioned, was to determine whether any specific interactions exist between the API and the polymers that could influence the different crystallization behaviors of PBD. The experiments were performed on the two representative BMs, namely PBD-Soluplus and PBD-*lin*PVP, at the highest possible weight ratio of the API and the polymer, 60:40 *w*/*w* (characterized by the greatest T_g), for which potential intermolecular interactions should be most evident. At this point, it should also be explained that the PBD-*star*PVP 60:40 *w*/*w* system exhibits exactly the same spectral band pattern as the PBD-*lin*PVP 60:40 *w*/*w* mixture, which can be clearly observed in **Figure S11** in the SI. Therefore, in the following FTIR spectra figures, the comparisons mainly focus on the PBD-Soluplus and PBD-*lin*PVP 60:40 *w*/*w* BMs (as a representative of the PBD−PVP systems), ensuring good clarity and readability of the figures.

First, spectroscopic investigations were done on the neat substances (PBD, Soluplus, and *lin*PVP). In **Figure S12** in the SI, FTIR spectra of the individual components, with a detailed assignment of the spectral bands, are presented. To better identify the intermolecular interactions occurring between PBD molecules, the IR spectra of the API in the three different phases, i.e., the crystalline, glass (vitrified), and liquid (molten), were measured. These data, along with the spectra of API-*lin*PVP and API-Soluplus 60:40 *w*/*w* BMs in the supercooled liquid/or glassy states, were recorded at room temperature (T = 293 K) in the wavenumber regions of 3800−2400 and 1800−400 cm^{-1}, see Figures 7 and 8.

As depicted in Figures 7 and 8, the characteristic PBD peaks in PBD−polymer (Soluplus, *lin*PVP) mixtures exhibited only minor shifts in both the high- and low-wavenumber regions (highlighted in light pink). Specifically, the CH stretching peaks

https://doi.org/10.1021/acs.molpharmaceut.5c00276
Mol. Pharmaceutics 2025, 22, 4708−4730

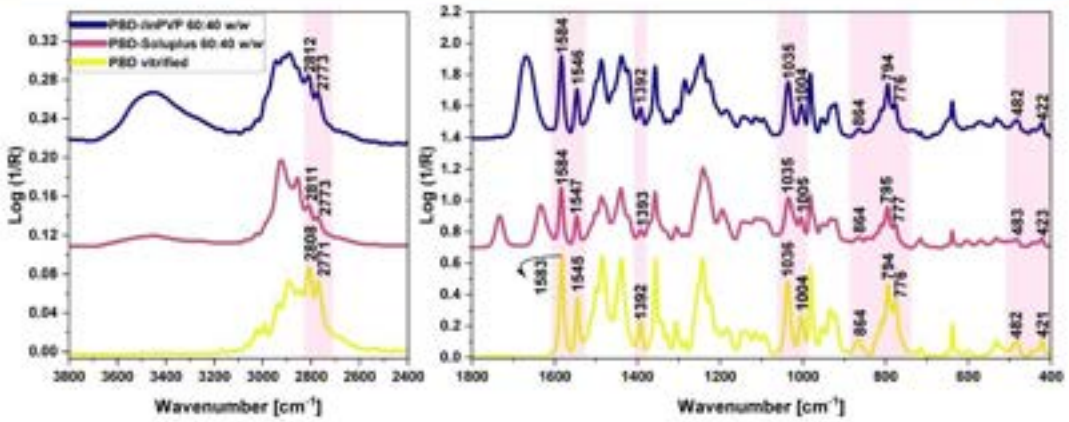

Figure 9. FTIR spectra of neat supercooled PBD as well as PBD-Soluplus and PBD-linPVP 60:40 *w/w* BMs (fresh amorphous systems), presented in the ranges of (left) 3800−2400 cm^{-1} and (right) 1800−400 cm^{-1}. The spectral regions characteristic for neat PBD (not overlapped by the signals of the polymer) are highlighted in light pink.

(ν_{C-H}) of 1,3-dioxolane ring of the neat PBD, located at 2808 and 2771 cm^{-1}, are shifted to the higher wavenumbers (blue-shift) by approximately 2−4 cm^{-1} in the mixtures. Moreover, other PBD bands, located at lower wavenumber ranges of BMs, showed only slight shifts (ca. 1 cm^{-1}) compared to those in neat vitrified API, as presented in Figure 9.

Notably, both Soluplus and linPVP contain functional groups capable of interacting with the drug. Soluplus includes both proton-donating (−OH) and proton-accepting groups (ester carbonyl and tertiary amide carbonyl), while PVP contains a proton-accepting group (ester carbonyl). Therefore, the changes in peak positions associated with these functional groups of polymers after mixing with the neat API might suggest possible interactions between them. It is also worth mentioning that in the crystal, the C−H atoms of the PBD molecule (from the aliphatic $-CH_2$ group and 1,3-dioxolane and pyrimidine rings) are involved in the weak C−*H*···π hydrogen bonds (HBs) with the pyrimidine and benzene rings as acceptors.[56] These intermolecular interactions result in the blue shifts of the C−H bands of crystalline PBD compared to the corresponding CH peak positions in the molten PBD sample ($\Delta\nu$ = ca. + 20 cm^{-1}), Figures 7 and 8.

To further verify this hypothesis, we analyzed the spectra of BMs, particularly in the regions corresponding to the stretching vibrations of the C=O groups ($\nu_{C=O}$) of the studied polymers. As shown in Figure 7, the $\nu_{C=O}$ bands of neat Soluplus located at 1732 cm^{-1} (the ester group, see **Figure S12** in the SI) and 1632 cm^{-1} (the tertiary amide group) exhibit minimal blue shift (shifted to higher wavenumbers) in the examined BMs (1733 cm^{-1}, $\Delta\nu$ = +1 cm^{-1}; 1634 cm^{-1}, $\Delta\nu$ = +2 cm^{-1}). Similarly, a very minor (insignificant) blue-shift is observed in the case of the $\nu_{C=O}$ band in the API-linPVP system (from 1668 cm^{-1} to 1669 cm^{-1}, $\Delta\nu$ = +1 cm^{-1}), Figure 8. These experimental facts indicate a lack of specific interactions (HBs or significant dipole−dipole interactions) occurring between the carbonyl groups of the studied polymers and API.

Overall, the most prominent shifts in the IR spectra of the BMs were observed for the C−H stretching bands of PBD (max +4 cm^{-1}). Interestingly, the C−H peak position values of the API in BMs were essentially close to those detected in the IR spectrum of molten or vitrified PBD, in which some of the HBs involving weak C−*H*···π interactions were broken/disrupted. Thus, this observation implies that, in the studied binary systems, certain H-bonds between PBD molecules were destroyed by the introduction of PVP or Soluplus molecules (the steric hindrance). However, at the accuracy of our investigations, we can state that there are no differences in the intermolecular interactions between the API and the applied polymers. Hence, an argument that the higher physical stability of PBD in the BM composed of star or linear PVP, as deduced from DSC and XRD investigations, is related to the stronger intermolecular interactions between both components with respect to those occurring in the solid dispersions formed by Soluplus, can be easily rejected.

3.1.4. BDS Data. According to previous DSC and XRD investigations, the self-synthesized PVP polymer matrices (both linear and branched) more effectively inhibit the recrystallization of PBD compared to the commercial Soluplus. As shown by FTIR studies, such differences in the crystallization behavior are not related to significant or specific interactions between the API and three examined macromolecules. Considering the results of XRD investigations, one can suppose that a greater physical stability of API-PVP BMs at room temperature with respect to API-Soluplus formulations is probably due to higher viscosities (η) related to greater T_g's of these systems (Figure 2). To confirm or exclude the effect of η on various stability of PBD-polymer mixtures, we decided to examine the molecular dynamics of all considered ASDs, especially to find such a T, at which the crystallization process will occur relatively fast and the viscosity of all systems will be constant. For this purpose, broadband dielectric spectroscopy (BDS) measurements in a wide temperature range, both above and below the T_g, were carried out.

The loss spectra obtained for representative API-polymer 90:10 *w/w* ASDs are presented in Figure 10. Analogous data for PBD-polymer 80:20 *w/w* binary systems are illustrated in **Figure S13** in the SI. As shown in both figures, at $T > T_g$, two processes can be identified in the spectra of each examined sample, both shifting toward lower frequencies (f) with decreasing T. The first one is a direct-current (dc) conductivity, associated with the

https://doi.org/10.1021/acs.molpharmaceut.5c00376
Mol. Pharmaceutics 2025, 22, 4708−4730

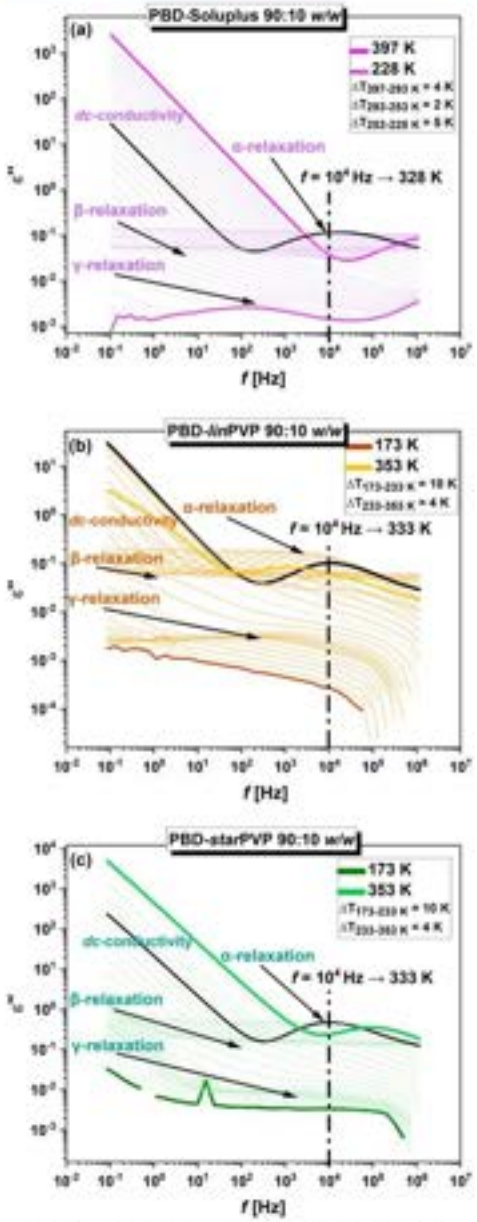

Figure 10. Dielectric loss spectra of (a) PBD-Soluplus, (b) PBD-linPVP, and (c) PBD-starPVP 90:10 *w/w* binary mixtures collected at ambient *p* and in the indicated *T*-ranges.

transport of ionic impurities that are always present in the liquid. Meanwhile, the second process, located at higher *f*, is a structural (α) relaxation, originating from the cooperative motions of all molecules in the sample and responsible for the glass transition. At higher *T*, a decrease (subtle or more clear) in the amplitude of the α-peak can be detected, indicating the ongoing crystallization. On the other hand, in the glassy state ($T < T_g$), two secondary relaxations (β and γ) with lower amplitudes dominate the spectra of ASDs. In all studied 90:10 and 80:20 *w/w* BMs, β- and γ- processes are fairly well separated from each other.

It should be emphasized that the primary goal of molecular dynamics studies using BDS was not the in-depth analysis of the relaxation processes detected in the loss spectra of PBD-polymer systems (e.g., the estimation of T_g or activation barrier for both secondary relaxations) but, as mentioned above, the determination of temperatures, at which different BMs exhibit similar viscosities. Herein, it is worth noting that according to Maxwell's relationship,[70,71] for a given/constant structural relaxation time ($\tau_\alpha = 1/(2\pi f_\alpha)$), a similar system viscosity (η) can be assumed. Based on this, we chose *T*, at which the maxima of α-peaks occur at $f = 10^4$ Hz (see Figure 10 and **S13** in the SI, black spectra and black dash-dotted lines), hence τ_α is nearly the same. Next, isothermal crystallization studies at these temperatures (given in Table 1) and constant η/τ_α (isochoric conditions) were carried out for the examined binary formulations. Furthermore, it should be emphasized that to ensure comparable degrees of undercooling across all mixtures and to allow the analysis of crystallization kinetics based solely on the differences in the type of polymer used, the crystallization temperatures (T_c) of each system had to be appropriately selected. **Table S3** in the SI presents the $T_{g(DSC)}$ values for the 90:10 and 80:20 *w/w* ASDs, as well as the $T_{c(BDS)}$ values for the corresponding systems. The $\frac{T_{c(BDS)}}{T_{g(DSC)}}$ ratios were then calculated, and it was found that they fall within a narrow range of 1.26−1.29 for all tested mixtures. This indicates that very similar degrees of undercooling were achieved. This is not surprising since all the crystallization studies were performed at isochronal conditions (the same viscosity). Therefore, differences in crystallization kinetics can be attributed to variations in the type and architecture of the polymer used in the ASD.

It should be added that to measure the progress of crystallization using the BDS method, we employed a standard approach − API and BMs were melted in the apparatus, supercooled, and then reheated to the appropriate crystallization temperatures (T_c). The dielectric loss spectra obtained during the isothermal crystallization of PBD from representative 90:10 *w/w* systems are presented in Figure 11. The same data for PBD-polymer 80:20 *w/w* mixtures are given in **Figure S14** in the SI. As shown, in all cases, the amplitude of the α-relaxation process systematically decreases over time. A reason for this is the freezing of the molecular mobility during the ongoing crystallization.[72,73]

To analyze the progress of this process in the studied BMs and neat API system, we followed the time dependency of the imaginary part of the complex dielectric permittivity (ε^*) measured at the frequency corresponding to the maximum of the α-peak. Next, ε'' was normalized using the following equation

$$\varepsilon_n''(t) = \frac{\varepsilon''(0) - \varepsilon''(t)}{\varepsilon''(0) - \varepsilon''(\infty)} \quad (5)$$

where $\varepsilon''(0)$ is the ε'' at the beginning of the crystallization, $\varepsilon''(\infty)$ is the long-time limiting value, and $\varepsilon''(t)$ is the value at the time, *t*.

In Figure 12, the values of ε_n'' are presented as a function of time. To analyze these data, the Avrami equation was applied

$$\varepsilon_n'' = 1 - \exp(-kt^n) \quad (6)$$

https://doi.org/10.1021/acs.molpharmaceut.5c00276
Mol. Pharmaceutics 2025, 22, 4709−4730

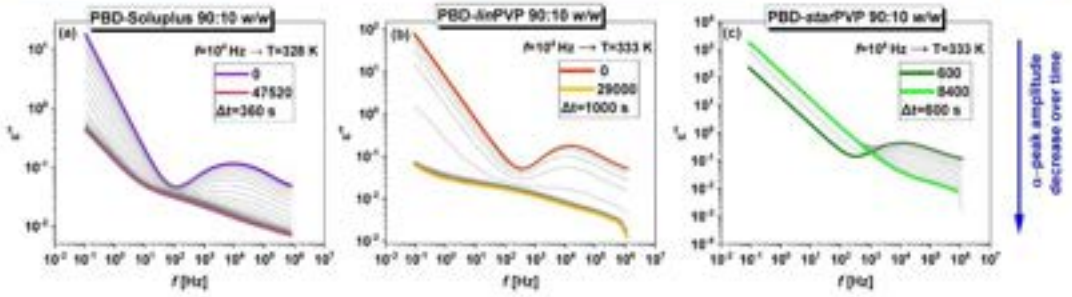

Figure 11. Time evolution of the imaginary (ε'') part of the complex dielectric permittivity plotted versus frequency during the isothermal crystallization of (a) PBD-Soluplus 90:10 *w*/*w*, (b) PBD-linPVP 90:10 *w*/*w*, and (c) PBD-*star*PVP 90:10 *w*/*w* at indicated temperatures ($f = 10^3$ Hz).

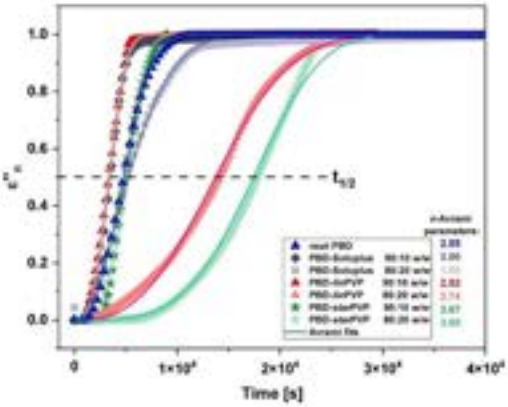

Figure 12. Time dependence of normalized permittivity ε''_n for neat PBD and API-polymer BMs in various ratios (90:10 and 80:20 *w*/*w*). The solid lines represent Avrami fits.

where k is the rate constant of crystallization and n is the Avrami exponent (it is generally assigned to a dimension of growing crystals).[74]

The solid lines in Figure 12 represent the best fits of eq 6 to experimental data, and as shown, the Avrami model describes them satisfactorily. The values of the parameters k and n are given in Table 1. From the analysis of k, it can be determined that the slowest crystallizing systems are PBD-linPVP and PBD-*star*PVP 80:20 *w*/*w* ($k = 6.37 \times 10^{-5}$ and 5.21×10^{-5} s^{-1}, respectively), while the fastest crystallizing ASDs are PBD-Soluplus 80:20 *w*/*w* and PBD-*star*PVP 90:10 *w*/*w* ($k = 1.56 \times 10^{-4}$ and 1.79×10^{-4} s^{-1}, respectively). However, it should be remembered that the parameter k gives information on the crystallization rate, whereas the time scale of this process is also an extremely important aspect. To have insight into this property, we also analyzed the crystallization half-time ($t_{1/2}$), which is the time required to reach 50% of the final crystallinity. It can be seen (Table 1) that the shortest $t_{1/2}$ equal to 3 400 s was determined for both PBD-Soluplus and PBD-linPVP 90:10 *w*/*w* mixtures. In contrast, PBD-linPVP and PBD-*star*PVP 80:20 *w*/*w* mixtures were characterized by the longest $t_{1/2}$ (≈13 800 and 17 700 s, respectively), as well as the longest crystal nucleation time. The latter result corresponds well with those obtained from the analysis of k parameter (eq 6) as well as the outcomes of calorimetric and structural investigations.

In summary, the conducted studies showed that the differences observed in the stability of the amorphous PBD-polymer BMs are not related to the variations in the viscosity of the systems but rather to the architecture of the macromolecules. This conclusion is supported by dielectric studies performed at a constant η, which revealed entirely different crystallization behaviors of PBD depending on the polymer matrix used. Therefore, it can be stated that the type and topology of the polymer play a crucial role in PBD crystallization. Notably, hydrophilic PVP polymers, especially those with branched topologies and controlled macromolecular parameters, seem to be the most effective inhibitors of undesired API recrystallization from the amorphous form. However, it should be noted that once crystallization begins, it proceeds more rapidly in the BM (80:20 *w*/*w*) containing *star*PVP, as evidenced by the analysis of the crystallization rate constant.

3.2. Results of Experimental Studies on Micelles Composed of PBD and Various Polymers. Having comprehensively characterized the amorphous binary mixtures, the next step was to investigate in detail the impact of various polymer matrices on the physical stability of PBD and its release, which is directly related to its bioavailability and therapeutic effectiveness, using micellar systems.

3.2.1. Micelle Formation and the Determination of Their Key Parameters. In the first step, before the preparation of PBD-

Table 2. Parameters Describing the Tested Micellar Systems

No.	Micellar systems	CMC [μg/mL]	DLC [%]	DLE [%]	d_h (TEM) [nm]	d_h (DLS) [nm]	ZP [mV]
1.	PBD-Soluplus 1:1 (5:95)	95	4.26	3.72	162.41	67.09	−9.20
2.	PBD-Soluplus 1:2 (5:95)		4.57	8.31	164.70	61.82	−7.23
3.	PBD-linPVP 1:1 (2:98)	105	2.06	1.74	104.07	46.02	−16.17
4.	PBD-linPVP 1:2 (2:98)		2.17	3.46	86.03	39.47	−12.60
5.	PBD-*star*PVP 1:1 (5:95)	65	4.84	4.36	684.70	174.75	−13.53
6.	PBD-*star*PVP 1:2 (10:90)		9.76	16.21	660.80	134.40	−11.90

https://doi.org/10.1021/acs.molpharmaceut.5c00376
Mol. Pharmaceutics 2025, 22, 4708−4730

polymer micelles, an important parameter - critical micelle concentration (CMC) - was determined for each polymer matrix. The CMC measurement is traditionally performed before micellar system formation to determine the exact macromolecule concentration at which micelles begin to form in solution. This concentration is crucial, as it marks the transition from the individual molecules to self-assembling aggregates (micelles), which exhibit significantly different physicochemical properties.[30] The study of this key parameter was conducted for aqueous polymer solutions at various concentrations by analyzing changes in the surface tension as a function of solution concentration (see **Figure S15** in the SI). The detailed measurement procedure is described in the Materials and Methods section, while the determined CMC values for each polymer matrix are presented in Table 2. At this point, it is also important to highlight the structural differences among the studied polymers. The commercial macromolecule Soluplus is a typical amphiphilic polymer, containing both hydrophilic (PEG, PVAc) and hydrophobic (PCL) domains. In contrast, PVP polymers are distinctly hydrophilic; however, their structure is quite intriguing. Their main aliphatic carbon backbone is hydrophobic, while the cyclic butyrolactam groups (due to the presence of oxygen and nitrogen) exhibit strong hydrophilic properties.[75] Therefore, despite the lack of typical amphiphilicity (i.e., the absence of two distinct hydrophilic and hydrophobic polymer segments), PVP polymers may still have a good tendency to form micellar systems. Thus, determining the CMC value is an important and highly interesting aspect, as its value can vary significantly depending on factors such as polymer topology and chain length (due to steric effects), as well as the presence of (non)polar domains (structural effects).[76] As presented in Table 2, the CMC values follow the trend: *star*PVP < Soluplus < *lin*PVP. Scientific data report that the CMC is generally lower for compounds with a higher degree of hydrophobicity and higher for substances with greater hydrophilicity. Additionally, the longer the hydrophilic block, the higher the CMC values, indicating a lower tendency to form micelles. This is because, as the polymer chain length increases, the number of hydrogen bonds between the repeating units of the hydrophilic block and water molecules also increases, resulting in greater water solubility and a higher CMC value.[77,78] Thus, it should be noted that our data correspond well with literature reports. The macromolecule *lin*PVP (with the longest hydrophilic chain) exhibits a slightly higher CMC value compared to the commercial copolymer Soluplus, which has a somewhat shorter hydrophilic segment. On the other hand, when comparing linear and star-shaped samples, the *star*PVP demonstrates a significantly lower CMC value than its linear counterpart. This is likely due to the presence of three shorter hydrophilic arms/blocks, leading to a higher density of PVP segments that facilitate the self-assembly process. Therefore, it has been concluded that star-shaped polymers are more prone to micelle and aggregate formation than linear ones, which is also consistent with findings from other literature reports.[79]

After determining the CMC parameter, micelles were prepared at two weight ratios (1:1 and 1:2) following a well-described and widely used method in the literature.[80] The procedure for obtaining micellar systems based on PBD and various macromolecules (Soluplus, *lin*PVP, *star*PVP) is detailed in the Materials and Methods section. After successful preparation, UV−Vis measurements were performed on the neat API (see **Figures S16** and **S17** in the SI) as a reference sample. This step was essential to subsequently assess the encapsulation efficiency of PBD and determine two parameters − drug loading efficiency (DLE) and drug loading content (DLC), which are crucial in the design, evaluation, and optimization of DDSs. DLE (often also called encapsulation efficiency) represents the percentage of drug successfully incorporated into the DDS compared to the total amount of the drug initially used during the formulation process. On the other hand, DLC describes the amount of API present in the DDS relative to the total weight of the drug carrier.[81] DLE and DLC values for all tested micellar systems, calculated according to eqs 1 and 2, respectively, in the Materials and Methods section, are shown in Table 2. As can be seen, the values of DLE remain relatively low in all cases, ranging from 1.74% to 16.21%. Similarly, the values of DLC also fluctuate at relatively low levels, not exceeding 10%. For instance, in the PBD-Soluplus and PBD-*lin*PVP micellar systems, they were approximately 4% and 2%, respectively, indicating that only a small fraction of the added PBD was successfully encapsulated. In contrast, the PBD-*star*PVP system exhibited a slightly higher DLC compared to the other systems. Moreover, a noticeable difference was observed between the 1:1 (4.84%) and 1:2 (9.76%) formulations. Additionally, the PBD-*star*PVP 1:2 system demonstrated the highest DLE of 16%. Therefore, it was concluded that the micellar system incorporating the star-shaped polymer matrix exhibits the most favorable DLC and DLE parameters. It should be noted that the initial amounts of drug and polymers used differ significantly from the actual amount of drug encapsulated in the polymeric matrix. Therefore, due to the considerable discrepancies between the initial and final drug−polymer ratios in the micellar systems, both the initial ratio and (in brackets) the actual content of API and polymer in each formulation are provided throughout the following sections of this study. These two ratios are also presented in Table 2 (outside the brackets − initial ratio; in brackets − actual drug-polymer ratio after the micellization process).

The obtained drug-loaded micellar systems were further analyzed using Dynamic Light Scattering (DLS). This technique is used to determine the hydrodynamic diameter (d_h) of micelles, providing insight into their size distribution and aggregation behavior in solution.[82,83] As observed in **Figure S18** in the SI, and based on the d_h values presented in Table 2, the micelles' hydrodynamic diameters vary depending on the polymer matrices used, following the trend: PBD-*lin*PVP < PBD-Soluplus < PBD-*star*PVP. Furthermore, as can be clearly observed in Figure S18a, Soluplus seems to be the best candidate to form micelles with PBD since the size distribution of the self-assembles in this case was the lowest of all studied systems. In contrast, in the remaining cases (PVP-based micelles), two fractions of micellar systems with different sizes can be observed (Figure S18bc). Additionally, DLS measurements allowed for the determination of the Zeta Potential (*ZP*), which helps assess the surface charge of micelles and its impact on their colloidal stability. A low negative *ZP* value indicates strong electrostatic repulsion between particles, preventing aggregation.[84] Values closer to zero suggest lower stability, as weaker repulsive forces increase the likelihood of micelle coalescence or precipitation. Thus, measuring the *ZP* provides insight into the colloidal stability and shelf life of micellar systems. Based on our data analysis, the most stable micellar systems were PBD-*lin*PVP and PBD-*star*PVP, exhibiting similar *ZP* values of approximately −12 mV. In turn, the PBD-Soluplus system was less stable and exhibited a higher *ZP* value (−7.23 mV).

https://doi.org/10.1021/acs.molpharmaceut.5c00276
Mol. Pharmaceutics 2025, 22, 4708−4730

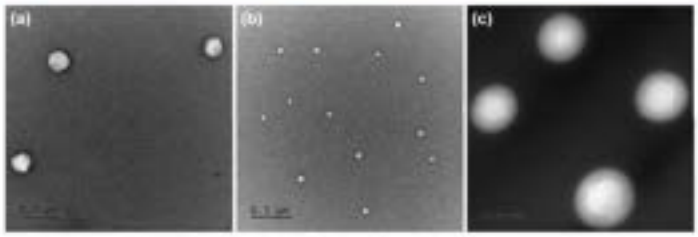

Figure 13. TEM images of (a) PBD-Soluplus micelles 1:2(5:95), (b) PBD-*lin*PVP micelles 1:2(2:98), and (c) PBD-*star*PVP micelles 1:2(10:90). Scale = 0.5 μm.

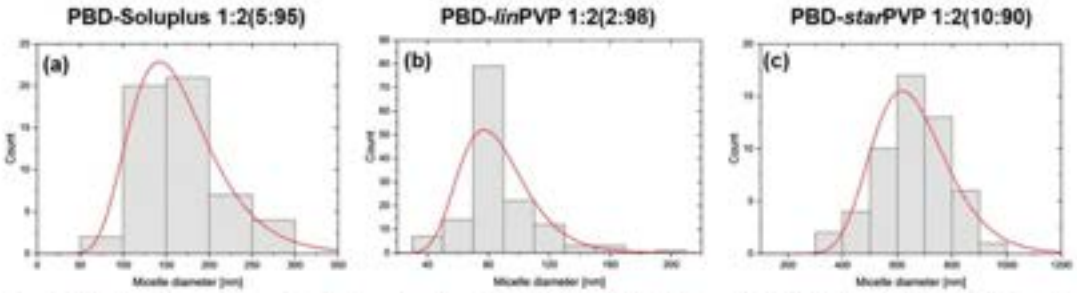

Figure 14. Size distribution of obtained micelles based on collected TEM data for (a) PBD-Soluplus, (b) PBD-*lin*PVP, and (c) PBD-*star*PVP micellar systems.

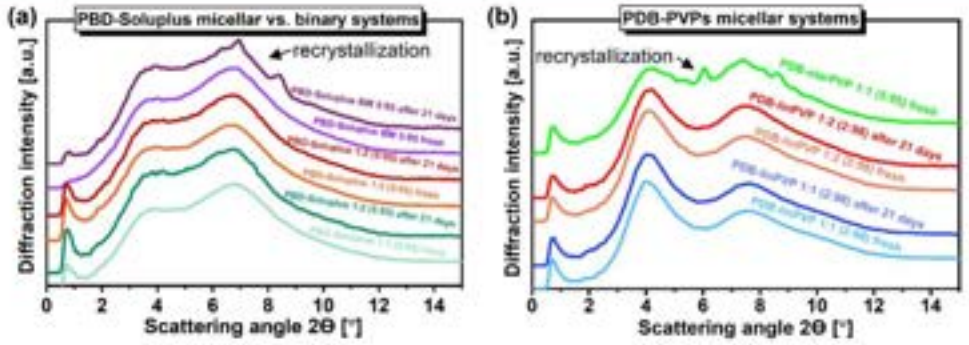

Figure 15. XRD patterns of (a) freshly prepared and stored by 3 weeks PBD-Soluplus micellar systems and PBD-Soluplus 5:95 *w*/*w* amorphous binary mixture as well as (b) PBD−PVPs micellar systems.

In this study, we also visualized the microstructure of the investigated micellar systems using Transmission Electron Microscopy (TEM). As seen in Figure 13, the obtained structures are well-defined and suggest that the drug migrates into the core of the formed particles, surrounded by polymer chains. The observed spherical structures further confirm the micellar architecture. It is worth noting that the three different micellar systems vary in d_v, as determined by TEM. Therefore, in the next step, micellar particle size statistics were conducted (Figure 14), and the average d_v values are presented in Table 2. Based on TEM measurements, a similar trend was observed as in DLS measurements, i.e., the PBD-*lin*PVP system exhibited the smallest d_v values, while PBD-*star*PVP − the largest. However, a significant discrepancy in d_v parameters was noted between the two independent methods (DLS vs. TEM). This difference may result from the sample preparation process for TEM measurements. Indeed, solvent evaporation can considerably increase the material concentration, potentially leading to aggregation or forming of larger particles. It is important to highlight that similar phenomena have also been observed in other micelle-related studies.[76]

3.2.2. XRD Data. Subsequently, to characterize the stability of PBD in its amorphous form when encapsulated in polymeric micellar systems, structural (XRD) measurements were performed. Figure 15, respectively, show the XRD patterns of PBD-Soluplus BMs and PBD−PVP micellar systems (both freshly prepared samples and those stored for 21 days at room temperature). Moreover, in Figure 15a, the structural data determined for the amorphous PBD-Soluplus 5:95 *w*/*w* BM, which contains approximately the same amount of loaded API as

https://doi.org/10.1021/acs.molpharmaceut.5c00276
Mol. Pharmaceutics 2025, 22, 4708−4730

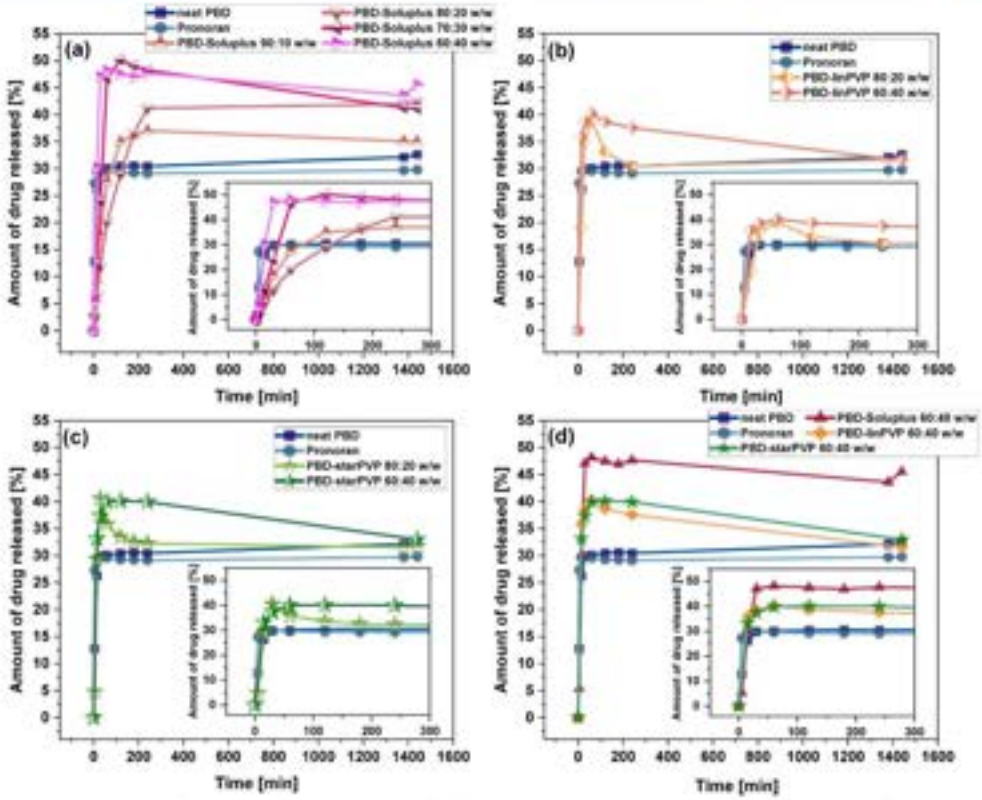

Figure 16. Drug release profile (percentage of drug released vs. time) from various polymer matrices in BMs: (a) PBD-Soluplus, (b) PBD-*lin*PVP, and (c) PBD-*star*PVP. Panel (d) presents a comparison of drug release profiles from various polymer matrices for 60:40 *w*/*w* BMs. Each panel contains two reference samples: neat crystalline PBD and the API Pronoran. The insets in each panels present the API release profiles over a shorter time (up to 300 min), which highlights the differences in the release kinetics.

the PBD-Soluplus 1:2 micellar system, are presented. As can be seen, both PBD-Soluplus (1:1(5:95) and 1:2(5:95)) and PBD-*lin*PVP (1:1(2:98) and 1:2(2:98)) were amorphous just after preparation and remained stable in this form after 3 weeks of storage at 293 K. In turn, the active substance in PBD-*star*PVP micellar systems (1:1(5:95)) recrystallized immediately (to the polymorphic form I), hence it was impossible to obtain it in the stable amorphous form.

Moreover, when we compare the ASD and the micellar system with the same PBD content (PBD-Soluplus 5:95 *w*/*w* and 1:2(5:95), respectively), one can state that (*i*) both fresh samples were amorphous, (*ii*) the more stable was the latter, i.e., the micellar system, (*iii*) in the case of 5:95 ASD, the recrystallization of PBD during 3 weeks of storage was observed. However, the recrystallized phase may be a new polymorphic form since the system of Bragg peaks is different than that for polymorphic form I.

3.3. Drug Release Studies. At the final stage, we carried out the studies of PBD release from various API-polymer ASDs and micelles. It is important to emphasize that such investigations are crucial in the aspect of developing new macromolecules as effective drug carriers and, consequently, more efficient DDSs. It is also worth noting the significant challenges related to the bioavailability of the given pharmaceutical. In this context, it should be stressed that the use of PBD is significantly limited by its very low (<10%) oral bioavailability due to extensive first-pass hepatic metabolism and a short biological half-life. As a result, the drug is prescribed with a high dosing frequency of 3−5 tablets per day.[63,64] Nevertheless, it should be clearly emphasized that although first-pass hepatic metabolism is the main factor contributing to the poor bioavailability of PBD, approximately 50% of the drug is eliminated from the body within 24 h (according to Servier − Summary of Product Characteristics for Pronoran). Therefore, improving the solubility of PBD using appropriate excipients may potentially increase the amount of API absorbed in the intestines and subsequently entering systemic circulation. A higher absorbed drug dose could enhance therapeutic efficacy, as hepatic enzymes would require more time to metabolize a larger amount of the active substance. Moreover, research performed over the past two decades has shown that, in addition to improving motor symptoms, PBD has the unique advantage of alleviating nonmotor symptoms, such as apathy, or cognitive impairment. This has renewed interest in this API, which may enhance its clinical application in the future.[65−69] Due to the highly inefficient current oral route for PBD delivery,[65] the

https://doi.org/10.1021/acs.molpharmaceut.5c00276
Mol. Pharmaceutics 2025, 22, 4709−4730

ongoing search for novel polymer matrices and their application in various DDSs represents a very important and intriguing area of research.

The PBD release tests were carried out using a special FaSSIF medium at pH = 6.5. At this point, it is important to justify the selection of the dissolution medium. PBD exhibits pH-dependent solubility – it is highly soluble under gastric (acidic) conditions but poorly soluble under intestinal (near-neutral) conditions (pK_a = 6.94).[90] However, the intestines are the primary site of drug absorption. Therefore, evaluating the solubility of PBD under intestinal conditions appears to be a rational strategy for properly assessing the potential improvement in drug absorption. The aim of the dissolution studies was primarily to assess how various excipients in the formulations influence both the drug release kinetics and the saturation solubility. Since saturation solubility must be determined under stable conditions where the drug remains in equilibrium, a 24-h time frame is commonly used, although longer periods may be applied for drugs with slower dissolution rates. In our study, we adopted a measurement time of up to 24 h. Under these conditions, it was assumed that both the drug and the polymeric matrices were in a stable state. According to forced degradation studies by Kumar et al., PBD is not susceptible to acid, base, or water hydrolysis.[91] Moreover, HPLC analysis (used to determine the concentration of released drug) did not reveal any additional peaks that could be attributed to degradation products of API. On the other hand, the applied PVP polymers are not pH-sensitive, and the FaSSIF medium used for the release studies is a buffered solution. This allows us to reasonably assume that the pH of the medium remained largely stable throughout the dissolution process, with only minimal potential fluctuations.

The first tests involved the release of the API from ASDs (Figure 16). It should be noted that the release profiles presented in Figures 16 and 17 refer to the percentage of drug released, whereas in the SI, we showed the drug concentration (mg/mL) vs time (Figures S19 and S20). As can be observed in Figure 16, neat crystalline PBD achieves a drug release level of about 30% after 60 min of the test, and then the solubility changes (increases) only slightly with time. Moreover, there are small differences in the release profiles of crystalline PBD and that used in the commercial formulation (called Pronoran, which mainly contains the API, commercial PVP/Povidone and talc). However, as clearly seen, for each investigated API-polymer ASD, a noticeable improvement in the API release from the matrix compared to the neat crystalline PBD can be observed. Increasing the macromolecules' content generally results in a higher amount of released drug. Note that similar conclusions were drawn in our previous studies on itraconazole-PVP BMs.[51] It is also worth noting that all conducted release tests showed similar behavior: for approximately 60−100 min (or ~ 200 min in the case of PBD-Soluplus 80:20 w/w), an intense release of the API from the polymer matrices was observed. During this period, the drug was rapidly released and dissolved until reaching a supersaturated state. However, after this time, most tests revealed a decrease in the amount of dissolved amorphous PBD, suggesting the onset of precipitation. Such observations suggest the presence of the so-called "parachute effect". Initially, the drug dissolves relatively quickly, but then there is a tendency for it to precipitate due to exceeding its equilibrium solubility. However, thanks to the stabilizing properties of the polymers, PBD remains in a metastable supersaturated state, preventing or delaying crystallization – effectively slowing down the "fall" (precipitation). This effect is often considered highly beneficial, as it can extend the absorption window in the gastrointestinal tract, thereby potentially increasing the oral bioavailability of poorly water-soluble drugs.[92−94] Additionally, Figure 16d compares the release profiles for the 60:40 w/w ASDs containing different polymer matrices. This comparison clearly indicated that the most favorable formulation (showing the highest amount of released drug, ~ 50%) is the PBD-Soluplus 60:40 w/w ASD. Moreover, keeping in mind the discovery of a new polymorphic form of PBD, an interesting aspect was to verify whether the polymorph II remains stable during the drug release studies from the binary formulations. Therefore, additional calorimetric measurements were performed to identify the existing polymorphic forms of the drug in one selected, representative formulation (PBD−linPVP 80:20 w/w), both before and after the release process. As clearly shown in Figure S21 in the SI, the sample prior to the release exhibited two endothermic peaks assigned to melting at $T_{m(II)}$ = 362 K and $T_{m(I)}$ = 369 K, indicating the presence of both polymorphs (I and II). In contrast, the same sample analyzed after the release process revealed only a single, strong endothermic event corresponding to the melting of polymorphic form I of PBD ($T_{m(I)}$ = 371 K). Thus, the calorimetric studies demonstrated that new polymorph II of the API converts to the primary polymorph I upon contact with the release medium/solution.

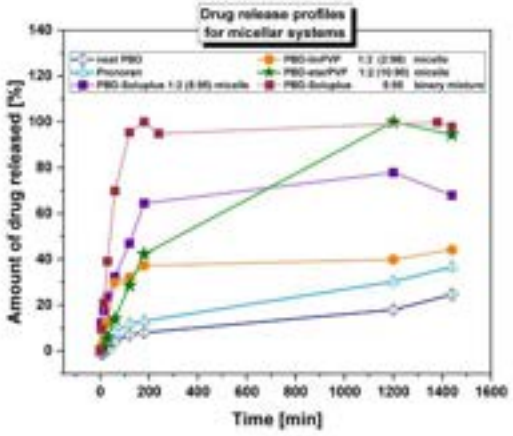

Figure 17. Drug release profiles (percentage of drug released vs time) for micellar systems with various polymer matrices, as well as for the reference samples: neat PBD and the Pronoran tablet.

Analogous release tests were then conducted for the 1:2 API-polymer micellar systems. Notably, despite the relatively small amounts of drug successfully encapsulated (see DLC values in Table 2), it was possible to precisely determine the API release profile, as shown in Figure 17. At this point, it is worth adding that alongside the micellar systems, the PBD-Soluplus 5:95 w/w BM was also tested, which, as mentioned earlier, in terms of the API content, is similar/analogous to the PBD-Soluplus micellar system. As can be observed, the most desirable release profile is exhibited by the PBD-*star*PVP 1:2 (10:90) micelle. In contrast to other systems, where a rapid API release (for around 200 min) and then slow changes up to the end of the test are observed, herein a gradual API release (up to 99%, ~ 1 mg/mL) over 1200

https://doi.org/10.1021/acs.molpharmaceut.5c00376
Mol. Pharmaceutics 2025, 22, 4708−4730

min/20 h, which represents the most favorable sustained release behavior, is visible. On the other hand, it is important to highlight the comparison between the micellar system and the binary mixture with approximately the same API content (~5 wt %). The noticeably higher drug release (~99%, ~ 1 mg/mL) from the PBD-Soluplus 5:95 *w*/*w* BM compared to the PBD-Soluplus 1:2 (5:95) micellar system (~70%, ~ 0.7 mg/mL) clearly indicates better bioavailability of the API contained in the ASD. Such findings emphasize the very important aspect of these studies, i.e., the testing of new polymeric drug carriers in various types of formulations.

Summarizing, the formation of all PBD-polymer ASDs resulted in improving API release in the FaSSIF medium with respect to the crystalline substance (30%). The most visible effect was observed for the BMs with Soluplus (an increase even up to 50%). Moreover, the PBD-Soluplus 1:2 (5:95) micellar system was characterized by better solubility in FaSSIF than the ASD with the same polymer content (5:95 *w*/*w*). Among all 1:2 micelles, the best/the more favorable release profile (a gradual API release over 20 h up to 99%) was determined for the formulation with *star*PVP. In other cases, we observed a fast dissolution of the sample (within the first 200 min of the test), followed by small changes in the API content. In the case of PBD-polymer (90:10−60:40 *w*/*w*) ASDs, a large amount of PBD was released during the first 60−100 min of the experiment.

4. CONCLUSIONS

In this paper, several experimental techniques were applied to study ASDs and micellar systems composed of the low water-soluble and bioavailable API − piribedil and three polymer matrices differing in structure and properties: the commercially available Soluplus, self-synthesized linear PVP (*lin*PVP), and self-synthesized three-arm star-shaped PVP (*star*PVP). Particular attention was devoted to examining the influence of polymer type, topology, and its amount in the system on inhibiting the recrystallization of PBD from the amorphous BMs, changes in phase transition temperatures, and the potential enhancement of API's pharmacokinetic properties.

A highly intriguing discovery was made at the initial stage of our research. Specifically DSC and XRD studies revealed that in PBD−polymer ASDs, the API recrystallizes primarily (API-PVP) or solely (API-Soluplus BMs with the polymer content ≥ 20) into a completely new polymorphic form II exhibiting $T_{m(II)}$ ~ 363 K, which is lower than the melting temperature of polymoeph I ($T_{m(I)}$ ~ 370 K). Furthermore, XRD, non-isothermal DSC and isothermal BDS measurements indicated that the amorphous PBD is the most physically stable in ASDs with hydrophilic self-synthesized PVP macromolecules. However, among the PVP matrices, the star-shaped polymer demonstrated a slightly stronger ability to suppress the recrystallization of PBD from the amorphous phase compared to its linear counterpart. FTIR and BDS studies confirmed that there are no specific API-polymer interactions and variations in the system viscosity which can influence the observed differences in the crystallization behavior of PBD−PVP and PBD−Soluplus ASDs. It was stated that the factor affecting the physical stability of the examined binary systems is the architecture/topology of macromolecules.

We also showed that the commercially available amphiphilic copolymer Soluplus is more suitable for forming micellar systems. Only in the case of PBD−Soluplus micelles, a low/homogeneous particle size distribution was observed. Moreover, as revealed by XRD studies, in these micellar systems (and in those with *lin*PVP), PBD remained in the amorphous form for a longer period than in the micelles containing *star*PVP. What is more, PBD-Soluplus 1:2(5:95) micelle in comparison to PBD-Soluplus ASD with the same API content (5:95 *w*/*w*) was more physically stable.

Finally, drug release measurements indicated that the amount of PBD released from all tested formulations in a mildly acidic environment (FaSSIF medium, pH = 6.5) is clearly enhanced compared to the neat crystalline API (~30%). Notably, the most significant improvement in solubility was observed for PBD−Soluplus 60:40 *w*/*w* ASD (~50%) and the PBD−*star*PVP 1:2 (10:90) micellar system (~99%). Importantly, for the latter formulation, the most desirable release profile (a gradual API release over 20 h instead of a fast API release within the first 1−3.5 h) was observed. Therefore, it can be assumed that the use of different polymer matrices as novel drug carriers in various types of formulations is an interesting perspective. Macromolecules can significantly contribute to improving the solubility of PBD as well as other poorly soluble APIs, ultimately increasing their bioavailability. From the pharmaceutical sector's perspective, the results of our studies are highly promising. We believe they open a new pathway in the scientific discussion regarding the search for new polymorphic forms of APIs and the impact of polymer type, topology, as well as the kind of formulation, in the context of the enhancement of the bioavailability of numerous drugs.

■ ASSOCIATED CONTENT

Supporting Information

The Supporting Information is available free of charge at https://pubs.acs.org/doi/10.1021/acs.molpharmaceut.5c00276.

Information on the synthetic pathways of *lin*PVP and *star*PVP together with the description of Size Exclusion Chromatography (SEC) and Nuclear Magnetic Resonance (NMR); TGA traces of neat API and polymers; ^{1}H NMR spectra of *lin*PVP and *star*PVP; A comparison of ^{1}H NMR spectra of the binary and physical PBD-Soluplus and PBD-*lin*PVP 60:40 *w*/*w* mixtures; The calorimetric T_g values (ϕ = 10 K/min) for the examined PBD-polymer BMs as well as neat polymers in various weight ratios; The calorimetric T_c values for neat PBD and PBD-polymer 90:10 and 80:20 *w*/*w* mixtures depending on the ϕ; DSC thermogram (ϕ = 10 K/min) for PBD-*lin*PVP 60:40 *w*/*w* BM heated up to 473 K; DSC thermograms of PBD-Soluplus and PBD-linPVP BMs (90:10, 80:20, 70:30, 60:40 *w*/*w*) at a heating rate of 2 K/min; Graphs of $\left(\frac{1}{T_m^{mix}} - \frac{1}{T_m^{pure}}\right)\left(\frac{\Delta H_{2m}}{-R}\right) - \ln \phi_{drug} - \left[1 - \left(\frac{1}{m}\right)\right]\phi_{polymer}$ vs. $\phi_{polymer}^2$ to determine the χ values for PBD-Soluplus and PBD-linPVP systems; a brief description of the F−H theory and the method of determining the miscibility of binary systems; DSC thermograms collected at ϕ = 10 K/min for neat polymers as well as for PBD-Soluplus 80:20 and 70:30 *w*/*w* systems after recrystallization at room temperature; FTIR spectra of PBD-*lin*PVP and PBD-*star*PVP 60:40 *w*/*w* BMs, presented in the ranges of 3800−400 cm^{-1}; FTIR spectra of crystalline PBD as well as Soluplus and linPVP samples, measured in the spectral regions 3800−2400 cm^{-1} and 1800−400 cm^{-1} and their short description; Dielectric loss spectra of PBD-Soluplus,

https://doi.org/10.1021/acs.molpharmaceut.5c00276
Mol. Pharmaceutics 2025, 22, 4708−4730

PBD-linPVP, and PBD-starPVP 80:20 w/w BMs; Time evolution of ε'' plotted versus f during the isothermal crystallization of the examined PBD-polymer 80:20 w/w systems at indicated temperatures ($f = 10^4$ Hz); Determination of CMC by measuring the surface tension of serial dilutions of Soluplus, linPVP, and starPVP; UV−Vis spectra for PBD at different concentrations (in the range of 2−15 μg/mL; solutions in ethanol solvent); the calibration curve for PBD in ethanol; Hydrodynamic diameters of the obtained PBD-Soluplus, PBD-linPVP, and PBD-starPVP 1:2 micellar systems; Drug release profile (drug concentration vs. time) from various polymer matrices in binary mixtures and micellar systems; and DSC thermograms ($\phi = 10$ K/min) for the PBD−linPVP 80:20 w/w BM before and after the release process (PDF)

AUTHOR INFORMATION

Corresponding Author

Luiza Orszulak − *Institute of Chemistry, Faculty of Science and Technology, University of Silesia in Katowice, 40-006 Katowice, Poland;* orcid.org/0000-0002-7709-5867; Email: luiza.orszulak@us.edu.pl

Authors

Aldona Minecka − *Department of Pharmacognosy and Phytochemistry, Faculty of Pharmaceutical Sciences in Sosnowiec, Medical University of Silesia in Katowice, 41-200 Sosnowiec, Poland;* orcid.org/0000-0001-5603-032X

Roksana Bernat − *Institute of Materials Engineering, University of Silesia in Katowice, 41-500 Chorzow, Poland*

Taoufik Lamrani − *Institute of Physics, Faculty of Science and Technology, University of Silesia in Katowice, 41-500 Chorzow, Poland*

Karolina Jurkiewicz − *Institute of Physics, Faculty of Science and Technology, University of Silesia in Katowice, 41-500 Chorzow, Poland;* orcid.org/0000-0002-4289-7827

Barbara Hachuła − *Institute of Chemistry, Faculty of Science and Technology, University of Silesia in Katowice, 40-006 Katowice, Poland*

Magdalena Tarnacka − *Institute of Physics, Faculty of Science and Technology, University of Silesia in Katowice, 41-500 Chorzow, Poland;* orcid.org/0000-0002-9444-3114

Monika Geppert-Rybczyńska − *Institute of Chemistry, Faculty of Science and Technology, University of Silesia in Katowice, 40-006 Katowice, Poland;* orcid.org/0000-0002-7112-9624

Maciej Zubko − *Institute of Materials Engineering, University of Silesia in Katowice, 41-500 Chorzow, Poland; Department of Physics, Faculty of Science, University of Hradec Králové, 500 03 Hradec Králové, Czech Republic*

Marcela Staniszewska − *Physiolution Polska sp. z o.o., 53-025 Wroclaw, Poland;* orcid.org/0000-0002-6865-5471

Michał Smoleński − *Physiolution Polska sp. z o.o., 53-025 Wroclaw, Poland;* orcid.org/0000-0002-6075-9866

Justyna Dobosz − *Physiolution Polska sp. z o.o., 53-025 Wroclaw, Poland*

Grzegorz Garbacz − *Physiolution Polska sp. z o.o., 53-025 Wroclaw, Poland*

Kamil Kamiński − *Institute of Physics, Faculty of Science and Technology, University of Silesia in Katowice, 41-500 Chorzow, Poland;* orcid.org/0000-0002-5871-0203

Ewa Kamińska − *Department of Pharmacognosy and Phytochemistry, Faculty of Pharmaceutical Sciences in Sosnowiec, Medical University of Silesia in Katowice, 41-200 Sosnowiec, Poland;* orcid.org/0000-0001-9725-8654

Complete contact information is available at: https://pubs.acs.org/10.1021/acs.molpharmaceut.5c00276

Notes

The authors declare no competing financial interest.

ACKNOWLEDGMENTS

A.M. is grateful for the financial support from the National Center for Research and Development (Poland) within the framework of the Lider XII project (No. LIDER/28/0152/L-12/20/NCBR/2021). This research was funded in part by the National Science Centre (Poland), grant number: Opus 21 No. 2021/41/B/NZ7/01654. For the purpose of Open Access, the author has applied a CC-BY public copyright license to any Author Accepted Manuscript (AAM) version arising from this submission.

REFERENCES

(1) Elder, D. P.; Kuentz, M.; Holm, R. Pharmaceutical Excipients - Quality, Regulatory and Biopharmaceutical Considerations. *Eur. J. Pharm. Sci.* **2016**, *87*, 88−99.

(2) Kumari, L.; Choudhari, Y.; Patel, P.; Gupta, G. D.; Singh, D.; Rosenholm, J. M.; Bansal, K. K.; Kurmi, B. D. Advancement in Solubilization Approaches: A Step towards Bioavailability Enhancement of Poorly Soluble Drugs. *Life* **2023**, *13* (5), 1099.

(3) Bhalani, D. V.; Nutan, B.; Kumar, A.; Singh Chandel, A. K. Bioavailability Enhancement Techniques for Poorly Aqueous Soluble Drugs and Therapeutics. *Biomedicines* **2022**, *10* (9), 2055.

(4) Erike, T. C.; Okpala, U. S.; Onoja, U. L.; Nwike, C. P.; Ezeako, E. C.; Okpara, O. J.; Okoroafor, C. C.; Eze, S. C.; Kalu, O. L.; Odoh, E. C.; Nwadike, U. G.; Ogbodo, J. O.; Umeh, B. U.; Ossai, E. C.; Nwanguma, B. C. Advances in Drug Delivery Systems, Challenges and Future Directions. *Heliyon* **2023**, *9* (6), No. e17488.

(5) Daughton, C. G.; Ruhoy, I. S. Lower-Dose Prescribing: Minimizing "Side Effects" of Pharmaceuticals on Society and the Environment. *Sci. Total Environ.* **2013**, *443*, 324−337.

(6) Williams, H. D.; Trevaskis, N. L.; Charman, S. A.; Shanker, R. M.; Charman, W. N.; Pouton, C. W.; Porter, C. J. H. Strategies to Address Low Drug Solubility in Disc. *Pharmacol. Rev.* **2013**, *65* (1), 315−499.

(7) Rams-Baron, M.; Jachowicz, R.; Boldyreva, E.; Zhou, D.; Jamroz, W.; Paluch, M. *Amorphous Drugs: Benefits and Challenges*; 2018, DOI: 10.1007/978-3-319-72002-9.

(8) Kawakami, K.; Pikal, M. J. Calorimetric Investigation of the Structural Relaxation of Amorphous Materials: Evaluating Validity of the Methodologies. *J. Pharm. Sci.* **2005**, *94* (5), 948−965.

(9) Brough, C.; Williams, R. O. Amorphous Solid Dispersions and Nano-Crystal Technologies for Poorly Water-Soluble Drug Delivery. *Int. J. Pharm.* **2013**, *453* (1), 157−166.

(10) Huang, Y.; Dai, W.-G. Fundamental Aspects of Solid Dispersion Technology for Poorly Soluble Drugs. *Acta Pharm. Sin. B* **2014**, *4* (1), 18−25.

(11) Baghel, S.; Cathcart, H.; O'Reilly, N. J. Polymeric Amorphous Solid Dispersions: A Review of Amorphization, Crystallization, Stabilization, Solid-State Characterization, and Aqueous Solubilization of Biopharmaceutical Classification System Class II Drugs. *J. Pharm. Sci.* **2016**, *105* (9), 2527−2544.

(12) Zhang, J.; Guo, M.; Luo, M.; Cai, T. Advances in the Development of Amorphous Solid Dispersions: The Role of Polymeric Carriers. *Asian J. Pharm. Sci.* **2023**, *18* (4), No. 100834.

(13) Lappe, S.; Mulac, D.; Langer, K. Polymeric Nanoparticles − Influence of the Glass Transition Temperature on Drug Release. *Int. J. Pharm.* **2017**, *517* (1), 338−347.

(14) Xiang, T.-X.; Anderson, B. D. Effects of Molecular Interactions on Miscibility and Mobility of Ibuprofen in Amorphous Solid Dispersions With Various Polymers. *J. Pharm. Sci.* **2019**, *108* (1), 178−186.
(15) Sharma, J.; Singh, B.; Agrawal, A. K.; Bansal, A. K. Correlationship of Drug-Polymer Miscibility, Molecular Relaxation and Phase Behavior of Dipyridamole Amorphous Solid Dispersions. *J. Pharm. Sci.* **2021**, *110* (4), 1470−1479.
(16) Yang, J.; Grey, K.; Doney, J. An Improved Kinetics Approach to Describe the Physical Stability of Amorphous Solid Dispersions. *Int. J. Pharm.* **2010**, *384* (1), 24−31.
(17) Boucenna, Y.; Layachi, A.; Cherfia, A.; Laoutid, F.; Satha, H. Non-Isothermal Crystallization Kinetics and Activation Energy for Crystal Growth of Polyamide 66/Short Glass Fiber/Carbon Black Composites. *Materials (Basel)* **2023**, *16* (22), 7073.
(18) Zhao, W.; Li, C.; Chang, J.; Zhou, H.; Wang, D.; Sun, J.; Liu, T.; Peng, H.; Wang, Q.; Li, Y.; Whittaker, A. K. Advances and Prospects of RAFT Polymerization-Derived Nanomaterials in MRI-Assisted Biomedical Applications. *Prog. Polym. Sci.* **2023**, *146*, No. 101739.
(19) Kim, J.; Jung, H. Y.; Park, M. J. End-Group Chemistry and Junction Chemistry in Polymer Science: Past, Present, and Future. *Macromolecules* **2020**, *53* (3), 746−763.
(20) Ding, L.; Agrawal, P.; Singh, S. K.; Chhonker, Y. S.; Sun, J.; Murry, D. J. Polymer-Based Drug Delivery Systems for Cancer Therapeutics. *Polymers* **2024**, *16*, 843.
(21) Ulbrich, K.; Holá, K.; Šubr, V.; Bakandritsos, A.; Tuček, J.; Zbořil, R. Targeted Drug Delivery with Polymers and Magnetic Nanoparticles: Covalent and Noncovalent Approaches, Release Control, and Clinical Studies. *Chem. Rev.* **2016**, *116* (9), 5338−5431.
(22) Ghezzi, M.; Pescina, S.; Padula, C.; Santi, P.; Del Favero, E.; Cantù, L.; Nicoli, S. Polymeric Micelles in Drug Delivery: An Insight of the Techniques for Their Characterization and Assessment in Biorelevant Conditions. *J. Controlled Release* **2021**, *332*, 312−336.
(23) Lu, Y.; Zhang, E.; Yang, J.; Cao, Z. Strategies to Improve Micelle Stability for Drug Delivery. *Nano Res.* **2018**, *11* (10), 4985−4998.
(24) Assiri, A. A.; Glover, K.; Mishra, D.; Waite, D.; Vora, L. K.; Thakur, R. R. S. Block Copolymer Micelles as Ocular Drug Delivery Systems. *Drug Discovery Today* **2024**, *29* (8), No. 104098.
(25) Van Duong, T.; Van den Mooter, G. The Role of the Carrier in the Formulation of Pharmaceutical Solid Dispersions. Part II: Amorphous Carriers. *Expert Opin. Drug Delivery* **2016**, *13* (12), 1681−1694.
(26) Linn, M.; Collnot, E.-M.; Djuric, D.; Hempel, K.; Fabian, E.; Kolter, K.; Lehr, C.-M. Soluplus® as an Effective Absorption Enhancer of Poorly Soluble Drugs in Vitro and in Vivo. *Eur. J. Pharm. Sci.* **2012**, *45* (3), 336−343.
(27) Bonde, G. V.; Ajmal, G.; Yadav, S. K.; Mittal, P.; Singh, J.; Bakde, B. V.; Mishra, B. Assessing the Viability of Soluplus® Self-Assembled Nanocolloids for Sustained Delivery of Highly Hydrophobic Lapatinib (Anticancer Agent): Optimisation and in-Vitro Characterisation. *Colloids Surfaces B Biointerfaces* **2020**, *185*, No. 110611.
(28) Mateos, H.; Gentile, L.; Mergia, S.; Colafemmina, G.; Collu, M.; Smets, J.; Palazzo, G. Understanding the Self-Assembly of the Polymeric Drug Solubilizer Soluplus®. *J. Colloid Interface Sci.* **2022**, *611*, 224−234.
(29) Xia, D.; Yu, H.; Tao, J.; Zeng, J.; Zhu, Q.; Zhu, C.; Gan, Y. Supersaturated Polymeric Micelles for Oral Cyclosporine A Delivery: The Role of Soluplus-Sodium Dodecyl Sulfate Complex. *Colloids Surfaces B Biointerfaces* **2016**, *141*, 301−310.
(30) Alopaeus, J. F.; Hagesæther, E.; Tho, I. Micellisation Mechanism and Behaviour of Soluplus®−Furosemide Micelles: Preformulation Studies of an Oral Nanocarrier-Based System. *Pharmaceutics* **2019**, *12* (1), 15.
(31) Alvarez-Rivera, F.; Fernández-Villanueva, D.; Concheiro, A.; Alvarez-Lorenzo, C. α-Lipoic Acid in Soluplus® Polymeric Nanomicelles for Ocular Treatment of Diabetes-Associated Corneal Diseases. *J. Pharm. Sci.* **2016**, *105* (9), 2855−2863.
(32) Varela-Garcia, A.; Concheiro, A.; Alvarez-Lorenzo, C. Soluplus Micelles for Acyclovir Ocular Delivery: Formulation and Cornea and Sclera Permeability. *Int. J. Pharm.* **2018**, *552* (1), 39−47.
(33) Salah, I.; Shamat, M. A.; Cook, M. T. Soluplus Solutions as Thermothickening Materials for Topical Drug Delivery. *J. Appl. Polym. Sci.* **2019**, *136* (1), 1−9.
(34) Taveira, S. F.; Varela-Garcia, A.; dos Santos Souza, B.; Marreto, R. N.; Martin-Pastor, M.; Concheiro, A.; Alvarez-Lorenzo, C. Cyclodextrin-Based Poly(Pseudo)Rotaxanes for Transdermal Delivery of Carvedilol. *Carbohydr. Polym.* **2018**, *200* (May), 278−288.
(35) Jin, X.; Zhou, B.; Xue, L.; Sun, W. Soluplus® Micelles as a Potential Drug Delivery System for Reversal of Resistant Tumor. *Biomed. Pharmacother.* **2015**, *69*, 388−395.
(36) Pignatello, R.; Corsaro, R.; Bonaccorso, A.; Zingale, E.; Carbone, C.; Musumeci, T. Soluplus® Polymeric Nanomicelles Improve Solubility of BCS-Class II Drugs. *Drug Delivery Transl. Res.* **2022**, *12* (8), 1991−2006.
(37) Attia, M. S.; Elshahat, A.; Hamdy, A.; Fathi, A. M.; Emad-Eldin, M.; Ghazy, F.-E. S.; Chopra, H.; Ibrahim, T. M. Soluplus® as a Solubilizing Excipient for Poorly Water-Soluble Drugs: Recent Advances in Formulation Strategies and Pharmaceutical Product Features. *J. Drug Delivery Sci. Technol.* **2023**, *84*, No. 104519.
(38) Kaur, D.; Rathee, A.; Krishna, V.; Nagpal, M. Soluplus-Based Polymeric Micelles: A Promising Carrier System for Challenging Drugs. *Int. J. Pharm. Sci. Rev. Res.* **2024**, *84*, 83−93.
(39) Liu, P.; Zhou, J. Y.; Chang, J. H.; Liu, X. G.; Xue, H. F.; Wang, R. X.; Li, Z. S.; Li, C. S.; Wang, J.; Liu, C. Z. Soluplus-Mediated Diosgenin Amorphous Solid Dispersion with High Solubility and High Stability: Development, Characterization and Oral Bioavailability. *Drug Des. Devel. Ther.* **2020**, *14*, 2959−2975.
(40) Li, S.; Zhang, Z.; Gu, W.; Gallas, M.; Jones, D.; Boulet, P.; Johnson, L. M.; de Margerie, V.; Andrews, G. P. Hot Melt Extruded High-Dose Amorphous Solid Dispersions Containing Lumefantrine and Soluplus. *Int. J. Pharm.* **2024**, *665*, No. 124676.
(41) Singh, A.; Bharati, A.; Frederiks, P.; Verkinderen, O.; Goderis, B.; Cardinaels, R.; Moldenaers, P.; Van Humbeeck, J.; Van den Mooter, G. Effect of Compression on the Molecular Arrangement of Itraconazole−Soluplus Solid Dispersions: Induction of Liquid Crystals or Exacerbation of Phase Separation? *Mol. Pharmaceutics* **2016**, *13* (6), 1879−1893.
(42) Bejaoui, M.; Galai, H.; Touati, F.; Kouass, S. Multifunctional Roles of PVP as a Versatile Biomaterial in Solid State. In *Dosage Forms*; Ahmad, U., Ed.; IntechOpen: Rijeka, 2021. DOI: 10.5772/intechopen.99431.
(43) Kurakula, M.; Rao, G. S. N. K. Pharmaceutical Assessment of Polyvinylpyrrolidone (PVP): As Excipient from Conventional to Controlled Delivery Systems with a Spotlight on COVID-19 Inhibition. *J. Drug Delivery Sci. Technol.* **2020**, *60* (August), No. 102046.
(44) Franco, P.; De Marco, I. The Use of Poly(N-Vinyl Pyrrolidone) in the Delivery of Drugs: A Review. *Polymers (Basel)* **2020**, *12* (5), 1114.
(45) Kim, J. M.; Baig, C. Communication: Role of Short Chain Branching in Polymer Structure and Dynamics. *J. Chem. Phys.* **2016**, *144* (8), 81101.
(46) Gabriel, C.; Münstedt, H. Influence of Long-Chain Branches in Polyethylenes on Linear Viscoelastic Flow Properties in Shear. *Rheol. Acta* **2002**, *41* (3), 232−244.
(47) Ramachandran, R.; Beaucage, G.; Kulkarni, A. S.; McFaddin, D.; Merrick-Mack, J.; Galiatsatos, V. Persistence Length of Short-Chain Branched Polyethylene. *Macromolecules* **2008**, *41* (24), 9802−9806.
(48) Choe, D.; Jeong, S. H.; Baig, C. Structural, Topological, and Rheological Characteristics of Entangled Short-Chain Branched Polymer Melts under Shear Flow in Comparison with the Linear Analog. *J. Rheol. (N. Y. N. Y).* **2024**, *68* (4), 591−601.
(49) Orszulak, L.; Lamrani, T.; Tarnacka, M.; Hachuła, B.; Jurkiewicz, K.; Ziola, P.; Mroczek-Wiczkiewicz, A.; Kamińska, E.; Kamiński, K. The Impact of Various Poly(Vinylpyrrolidone) Polymers on the Crystallization Process of Metronidazole. *Pharmaceutics* **2024**, *16* (1), 136.

https://doi.org/10.1021/acs.molpharmaceut.5c00276
Mol. Pharmaceutics 2025, 22, 4708−4730

(50) Heczko, D.; Hachuła, B.; Maksym, P.; Kamiński, K.; Zięba, A.; Orszulak, L.; Paluch, M.; Kamińska, E. The Effect of Various Poly (N-Vinylpyrrolidone) (PVP) Polymers on the Crystallization of Flutamide. *Pharmaceuticals* **2022**, *15* (8), 971.
(51) Orszulak, L.; Lamrani, T.; Bernat, R.; Tarnacka, M.; Żakowiecki, D.; Jurkiewicz, K.; Ziola, P.; Mrozek-Wilczkiewicz, A.; Zięba, A.; Kamiński, K.; Kamińska, E. The Influence of PVP Polymer Topology on the Liquid Crystalline Order of Itraconazole in Binary Systems. *Mol. Pharmaceutics* **2024**, *21* (6), 3027−3039.
(52) Orszulak, L.; Włodarczyk, P.; Hachuła, B.; Lamrani, T.; Jurkiewicz, K.; Tarnacka, M.; Heczka, M.; Kamiński, K.; Kamińska, E. Inhibition of Naproxen Crystallization by Polymers: The Role of Topology and Chain Length of Polyvinylpyrrolidone Macromolecules. *Eur. J. Pharm. Biopharm.* **2025**, *207*, No. 114581.
(53) Uppuluri, C. T.; Dalvi, A. V.; Bommireddy, E. P.; Ravi, P. R. Development and Validation of Rapid and Sensitive LC Methods with PDA and Fluorescence Detection for Determination of Piribedil in Rat Plasma and Brain Tissues and Their Pharmacokinetic Application. *Biomed. Chromatogr.* **2018**, *32* (10), 1−10.
(54) Meng, F.; Dave, V.; Chauhan, H. Qualitative and Quantitative Methods to Determine Miscibility in Amorphous Drug-Polymer Systems. *Eur. J. Pharm. Sci. Off. J. Eur. Fed. Pharm. Sci.* **2015**, *77*, 106−111.
(55) Bansal, K.; Baghel, U. S.; Thakral, S. Construction and Validation of Binary Phase Diagram for Amorphous Solid Dispersion Using Flory-Huggins Theory. *AAPS PharmSciTech* **2016**, *17* (2), 318−327.
(56) Wu, C.; Li, J.; Wei, H.; Hang, Y.; Jiang, Y. 2-[4-[(1,3-Benzodioxol-5-Yl)Methyl]Piperazin-1-Yl]pyrimidine. *Acta Crystallogr. Sect. E Struct. Reports Online* **2013**, *69* (7), o1140.
(57) Baird, J. A.; Van Eerdenbrugh, B.; Taylor, L. S. A Classification System to Assess the Crystallization Tendency of Organic Molecules from Undercooled Melts. *J. Pharm. Sci.* **2010**, *99* (9), 3787−3806.
(58) Blaabjerg, L. I.; Lindenberg, E.; Löbmann, K.; Grohganz, H.; Rades, T. Is There a Correlation between the Glass Forming Ability of a Drug and Its Supersaturation Propensity? *Int. J. Pharm.* **2018**, *538* (1−2), 243−249.
(59) Kaminska, E.; Tarnacka, M.; Włodarczyk, P.; Jurkiewicz, K.; Kołodziejczyk, K.; Dulski, M.; Haznar-Garbacz, D.; Hawelek, L.; Kamiński, K.; Włodarczyk, A.; Paluch, M. Studying the Impact of Modified Saccharides on the Molecular Dynamics and Crystallization Tendencies of Model API: Nifedipine. *Mol. Pharmaceutics* **2015**, *12* (8), 3007−3019.
(60) Grzybowska, K.; Grzybowski, A.; Knapik-Kowalczuk, J.; Chmiel, K.; Wojnа-Orlewicz, K.; Szafraniec-Szczęsny, J.; Antosik-Rogóż, A.; Jachowicz, R.; Kowalska-Szojda, K.; Lodowski, P.; Paluch, M. Molecular Dynamics and Physical Stability of Ibuprofen in Binary Mixtures with an Acetylated Derivative of Maltose. *Mol. Pharmaceutics* **2020**, *17* (8), 3087−3105.
(61) Minecka, A.; Tarnacka, M.; Jurkiewicz, K.; Hachuła, B.; Wrzalik, R.; Brodka, A.; Kamiński, K.; Kamińska, E. The Impact of the Size of Acetylated Cyclodextrin on the Stability of Amorphous Metronidazole. *Int. J. Pharm.* **2022**, *624*, No. 122025.
(62) Minecka, A.; Tarnacka, M.; Jurkiewicz, K.; Hachuła, B.; Wrzalik, R.; Kamiński, K.; Paluch, M.; Kamińska, E. Impact of the Chain Length and Topology of the Acetylated Oligosaccharide on the Crystallization Tendency of Naproxen from Amorphous Binary Mixtures. *Mol. Pharmaceutics* **2021**, *18* (1), 347−358.
(63) Jayachandra Babu, R.; Brostow, W.; Kalogeras, I. M.; Sathigari, S. Glass Transitions in Binary Drug+polymer Systems. *Mater. Lett.* **2009**, *63* (30), 2666−2668.
(64) Valenti, S.; Del Valle, L. J.; Romanini, M.; Mitjana, M.; Puiggali, J.; Tamarit, J. L.; Macovez, R. Drug-Biopolymer Dispersions: Morphology-and Temperature-Dependent (Anti)Plasticizer Effect of the Drug and Component-Specific Johari−Goldstein Relaxations. *Int. J. Mol. Sci.* **2022**, *23* (5), 2456.
(65) Avramov, I.; Gutzow, I. Heating Rate and Glass Transition Temperature. *J. Non. Cryst. Solids* **1988**, *104* (1), 148−150.
(66) Pries, J.; Wei, S.; Wuttig, M.; Lucas, P. Switching between Crystallization from the Glassy and the Undercooled Liquid Phase in Phase Change Material Ge2Sb2Te5. *Adv. Mater.* **2019**, *31* (39), 1900784.
(67) Hess, K. U.; Schawe, J. E. K.; Wilding, M.; Purgstaller, B.; Goetschl, K. E.; Sturm, S.; Müller-Caspary, K.; Sturm, E. V.; Schmahl, W.; Grieshaber, E.; Bisolbert, T.; Weidendorfer, D.; Dietzel, M.; Dingwell, D. B. Glass Transition Temperatures and Crystallization Kinetics of a Synthetic, Anhydrous, Amorphous Calcium-Magnesium Carbonate. *Philos. Trans. R. Soc. A Math. Phys. Eng. Sci.* **2023**, *381* (2258), 20220356.
(68) Kissinger, H. E. *Variation of Peak Temperature With Heating Rate in DTA- Kissinger* **1956**, *57* (4), 217−221.
(69) Alotaibi, N. M.; Aouak, T. Preparation and Non Isothermal Crystallization Kinetic of Acetylsalicylic Acid-Poly(Vinylalcohol-Co-Ethylene) Blend. Application in Drug Delivery Domain. *Macromol. Res.* **2013**, *21* (7), 747−756.
(70) Maxwell, J. C. *On the Dynamical Theory of Gases* **2003**, *1*, 197−261.
(71) Karra, S.; Průša, V.; Rajagopal, K. R. On Maxwell Fluids with Relaxation Time and Viscosity Depending on the Pressure. *Int. J. Non. Linear. Mech.* **2011**, *46* (6), 819−827.
(72) Kamińska, E.; Minecka, A.; Tarnacka, M.; Hachuła, B.; Kamiński, K.; Paluch, M. Influence of Annealing in the Close Vicinity of Tg on the Reorganization within Dimers and Its Impact on the Crystallization Kinetics of Gemfibrozil. *Mol. Pharmaceutics* **2020**, *17* (3), 990−1000.
(73) Rozwadowski, T.; Noda, H.; Kolek, Ł.; Ito, M.; Yamamura, Y.; Saitoh, H.; Saito, K. Molecular Dynamics and Kinetics of Isothermal Cold Crystallization with Tunable Dimensionality in a Molecular Glass Former, 5′-(2,3-Difluorophenyl)-2′-Ethoxy-4-Pentyloxy-2,3-Difluorotolane. *Phys. Chem. Chem. Phys.* **2022**, *25* (1), 724−735.
(74) Scholz, E. B. Wunderlich. Macromolecular Physics, Vol. 2 Crystal Nucleation, Growth, Annealing. Academic Press New York 1976, Preis $ 46, 50. *Krist. und Technol.* **1977**, *12* (1), K11−K12.
(75) Nair, A. R.; Lakshman, Y. D.; Anand, V. S. K.; Sree, K. S. N.; Bhat, K.; Dengale, S. J. Overview of Extensively Employed Polymeric Carriers in Solid Dispersion Technology. *AAPS PharmSciTech* **2020**, *21* (8), 309.
(76) Bielas, R.; Maksym, P.; Tarnacka, M.; Minecka, A.; Jurkiewicz, K.; Talik, A.; Geppert-Rybczyńska, M.; Grelska, J.; Mielańczyk, Ł.; Bernat, R.; Kamiński, K.; Paluch, M.; Kamińska, E. Synthetic Strategy Matters: The Study of a Different Kind of PVP as Micellar Vehicles of Metronidazole. *J. Mol. Liq.* **2021**, *332*, 115789.
(77) Heinz, D.; Amado, E.; Kressler, J. Polyphilicity-An Extension of the Concept of Amphiphilicity in Polymers. *Polymers (Basel)* **2018**, *10* (9), 960.
(78) Manfredini, N.; Sponchioni, M.; Moscatelli, D. Recoverable Thermo-Responsive Polymeric Surfactants for the Synthesis of Bulk Plastics from Latexes. *ACS Appl. Polym. Mater.* **2022**, *4* (1), 270−279.
(79) Allen, C.; Maysinger, D.; Eisenberg, A. Nano-Engineering Block Copolymer Aggregates for Drug Delivery. *Colloids Surfaces B Biointerfaces* **1999**, *16* (1), 3−27.
(80) Tiwari, D.; Verma, P. Microencapsulation Technique by Solvent Evaporation Method (Study of Effect of Process Variables). *Int. J. Pharm. Life Sci.* **2011**, *2*, 998−1005.
(81) Wallace, S. J.; Li, J.; Nation, R. L.; Boyd, B. J. Drug Release from Nanomedicines: Selection of Appropriate Encapsulation and Release Methodology. *Drug Delivery Transl. Res.* **2012**, *2* (4), 284−292.
(82) Zhou, Y.; Yu, J.; Feng, X.; Li, W.; Wang, Y.; Jin, H.; Huang, H.; Liu, Y.; Fan, D. Reduction-Responsive Core-Crosslinked Micelles Based on a Glycol Chitosan−Lipoic Acid Conjugate for Triggered Release of Doxorubicin. *RSC Adv.* **2016**, *6* (37), 31391−31400.
(83) Mitchell, M. J.; Billingsley, M. M.; Haley, R. M.; Wechsler, M. E.; Peppas, N. A.; Langer, R. Engineering Precision Nanoparticles for Drug Delivery. *Nat. Rev. Drug Discovery* **2021**, *20* (2), 101−124.
(84) Pochapski, D. J.; Carvalho dos Santos, C.; Leite, G. W.; Pulcinelli, S. H.; Santilli, C. V. Zeta Potential and Colloidal Stability Predictions for Inorganic Nanoparticle Dispersions: Effects of Experimental Conditions and Electrokinetic Models on the Interpretation of Results. *Langmuir* **2021**, *37* (45), 13379−13389.

https://doi.org/10.1021/acs.molpharmaceut.5c00376
Mol. Pharmaceutics 2025, 22, 4708−4730

(85) Deleu, D.; Northway, M. G.; Hanssens, Y. Clinical Pharmacokinetic and Pharmacodynamic Properties of Drugs Used in the Treatment of Parkinson's Disease. *Clin. Pharmacokinet.* **2002**, *41* (4), 261−309.
(86) Millan, M. J. From the Cell to the Clinic: A Comparative Review of the Partial D2/D3 Receptor Agonist and A2-Adrenoceptor Antagonist, Piribedil, in the Treatment of Parkinson's Disease. *Pharmacol. Ther.* **2010**, *128* (2), 229−273.
(87) Perez-Lloret, S.; Rascol, O. Piribedil for the Treatment of Motor and Non-Motor Symptoms of Parkinson Disease. *CNS Drugs* **2016**, *30* (8), 703−717.
(88) Uppuluri, C. T.; Ravi, P. R.; Dalvi, A. V. Design, Optimization and Pharmacokinetic Evaluation of Piribedil Loaded Solid Lipid Nanoparticles Dispersed in Nasal in Situ Gelling System for Effective Management of Parkinson's Disease. *Int. J. Pharm.* **2021**, 606, No. 120881.
(89) Demirel, M.; Yazan, Y.; Muller, R. H.; Kilic, F.; Bozan, B. Formulation and in Vitro-in Vivo Evaluation of Piribedil Solid Lipid Micro- and Nanoparticles. *J. Microencapsul.* **2001**, *18* (3), 359−371.
(90) Uppuluri, C. T.; Ravi, P. R.; Dalvi, A. V.; Shaikh, S. S.; Kale, S. R. Piribedil Loaded Thermo-Responsive Nasal in Situ Gelling System for Enhanced Delivery to the Brain: Formulation Optimization, Physical Characterization, and in Vitro and in Vivo Evaluation. *Drug Delivery Transl. Res.* **2021**, *11* (3), 909−926.
(91) Kumar, S. K.; Ganesan, V.; Riggleman, R. A. Perspective: Outstanding Theoretical Questions in Polymer-Nanoparticle Hybrids. *J. Chem. Phys.* **2017**, *147* (2), 020901.
(92) Fujita, M.; Goto, S.; Chatani, H.; Otsuka, Y.; Shimada, Y.; Terada, H.; Inoo, K. The Function of Oxybuprocaine: A Parachute Effect That Sustains the Supersaturated State of Anhydrous Piroxicam Crystals. *RSC Adv.* **2020**, *10* (3), 1572−1579.
(93) Fujita, M.; Tsuchida, T.; Kataoka, H.; Tsunoda, C.; Moritake, K.; Goto, S. Spring and Parachute Approach for Piroxicam Dissolution; Its Phenomenological Model on the Thermodynamics of Irreversible Processes. *Int. J. Pharm.* **2024**, 667, No. 124886.
(94) Real, D. A.; Gaghano, A.; Orzan, L.; Leonardi, D.; Salomon, C. J. Amorphous Solid Dispersions of Triclabendazole: Keeping the Supersaturated Drug Solution Using Poloxamers. *J. Drug Delivery Sci. Technol.* **2024**, *91*, No. 105223.

Supporting Information

Hydrophilic and Amphiphilic Macromolecules as Modulators of the Physical Stability and Bioavailability of Piribedil: A Study on Binary Mixtures and Micellar Systems

Luiza Orszulak[1]*, Aldona Minecka[2], Roksana Bernat[3], Taoufik Lamrani[4], Karolina Jurkiewicz[4], Barbara Hachuła[1], Magdalena Tarnacka[4], Monika Geppert-Rybczyńska[1], Maciej Zubko[3,5], Marcela Staniszewska[6], Michał Smoleński[6], Justyna Dobosz[6], Grzegorz Garbacz[6], Kamil Kamiński[4], Ewa Kamińska[2]

[1] *Institute of Chemistry, Faculty of Science and Technology, University of Silesia in Katowice, Szkolna 9, 40-006 Katowice, Poland*

[2] *Department of Pharmacognosy and Phytochemistry, Faculty of Pharmaceutical Sciences in Sosnowiec, Medical University of Silesia in Katowice, Jagiellonska 4, 41-200 Sosnowiec, Poland*

[3] *Institute of Materials Engineering, University of Silesia in Katowice, 75 Pulku Piechoty 1A, 41-500 Chorzow, Poland*

[4] *Institute of Physics, Faculty of Science and Technology, University of Silesia in Katowice, 75 Pulku Piechoty 1A, 41-500 Chorzow, Poland*

[5] *Department of Physics, Faculty of Science, University of Hradec Králové, Rokitanského 62, 500 03, Hradec Králové, Czech Republic*

[6] *Physiolution Polska sp. z o.o., Skarbowcow 81/7, 53-025 Wroclaw, Poland*

**Corresponding author:* luiza.orszulak@us.edu.pl

Experimental

1. Synthetic pathway of PVP with linear topology (linPVP)

Thermally-initiated Reversible Addition Fragmentation Chain Transfer (RAFT) polymerization of *N*-vinylpyrrolidone (VP) using CTA1 (cyanomethyl methyl(4-pyridyl) carbamodithioate) as a chain transfer agent and 2,2'-azobis(2-methylpropionitrile) (AIBN) as an initiator with molar ratios $[VP]_0/[CTA1]_0/[AIBN]_0 = 1300/1/0.25$) was carried out as follows. Prior to polymerization, VP was passed through an alumina column to remove the inhibitor. CTA1 and VP were placed in a Schlenk flask with a magnetic stirring bar. The solution was purged under nitrogen and purified by three freeze-pump-thaw cycles. Then, the solution of AIBN was added to the reaction mixture and the flask was immersed in an oil bath thermostated at 70 °C to start the reaction. The polymerization was quenched after a predetermined time (t = 21 h) by cooling and exposing the reaction mixture to air. The product was precipitated with cold diethyl ether and re-dissolved in chloroform and this cycle was repeated twice. The polymer was isolated, filtered, and then dried under vacuum to a constant mass.

2. Synthetic pathway of PVP with star topology (starPVP)

Thermally-initiated RAFT polymerization of VP using previously synthesized 1,3,5-benzyl tri(diethyldithiocarbamate), CTA2 (please see the synthetic pathway in our previous papers[1,2]) as a chain transfer agent, and AIBN as an initiator with molar ratios $[VP]_0/[CTA2]_0/[AIBN]_0 = 1200/5/1$) was carried out as follows. Before polymerization, VP was passed through an alumina column to remove the inhibitor. CTA2, VP, and dichloromethane (DCM) were placed in a Schlenk flask with a magnetic stirring bar. The solution was purged under nitrogen and purified by three freeze-pump-thaw cycles. Then, the solution of AIBN was added to the reaction mixture and the flask was immersed in an oil bath thermostated at 70 °C to start the reaction. The polymerization was quenched after a predetermined time (t = 10 h) by cooling and exposing the reaction mixture to air. The product was precipitated with cold diethyl ether and re-dissolved in chloroform, and this cycle was repeated twice. The polymer was isolated, filtered, and then dried under vacuum to a constant mass.

3. Size Exclusion Chromatography (SEC)

Molecular weights (M_n) and dispersities ($Đ$) of *lin*PVP and *star*PVP homopolymers were determined by size exclusion chromatography (SEC). Viscotek GPC Max VE 2001 and a Viscotek TDA 305 triple detection system (refractometer, viscosimeter, and low angle laser light scattering) were used for data collection, and OmniSec 5.12 for data processing. Two

T6000M general mixed columns were applied for separation. The measurements were carried out in DMF/LiBr (0.01M) as an eluent at 323 K with a flow rate of 0.5 mL/min.

4. Nuclear Magnetic Resonance (NMR)

Nuclear magnetic resonance (^{1}H NMR) spectra were collected using a Bruker Ascend 600 MHz spectrometer for the samples in $CDCl_3$ as a solvent with TMS internal standard. Standard experimental conditions and the standard Bruker program were used.

TGA data

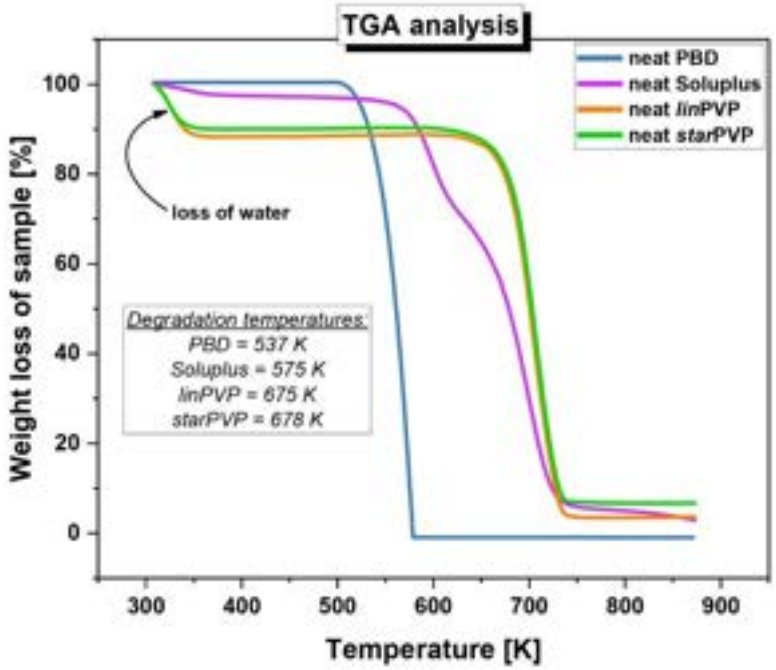

Figure S1. TGA traces of neat API and polymers (Soluplus, *lin*PVP, *star*PVP). The figure also presents the precise degradation temperatures of the individual compounds.

NMR data

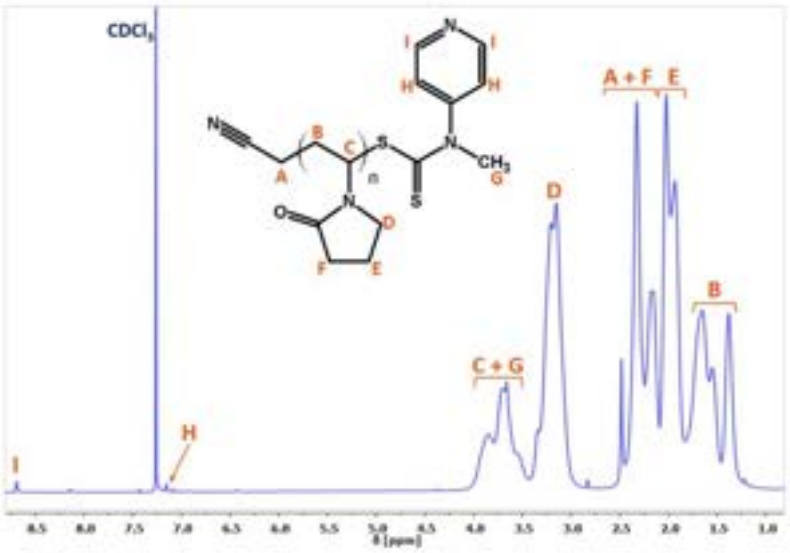

Figure S2. ^{1}H NMR spectrum of *lin*PVP in $CDCl_3$ (600 MHz).

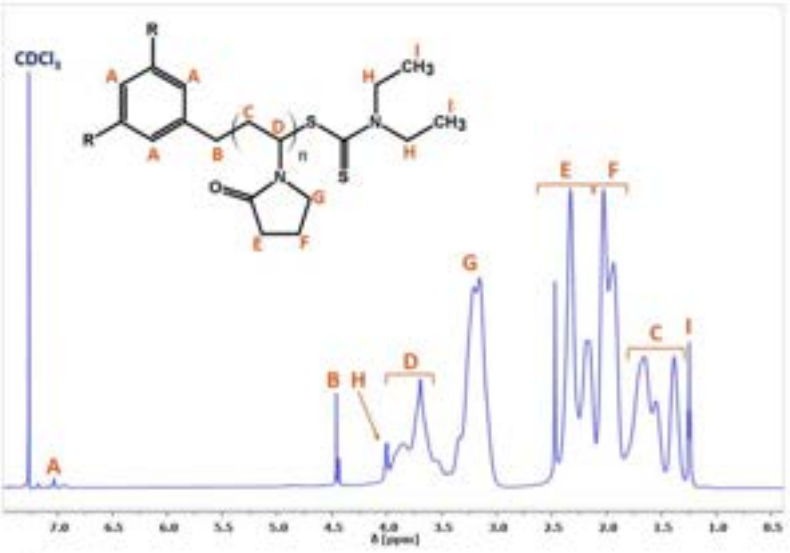

Figure S3. ^{1}H NMR spectrum of *star*PVP in $CDCl_3$ (600 MHz).

The ^{1}H NMR spectra confirm the structure of the synthesized macromolecules, i.e., *lin*PVP (**Figure S2**) and *star*PVP (**Figure S3**). In both figures, the chemical structures of the polymers are presented, and each signal is assigned to the corresponding proton group. Moreover, it is worth noting that a large amount of diethyl ether was used to purify the polymer

matrices after the polymerization process. However, as shown in **Figures S2** and **S3**, no signal is observed at the chemical shift of 1.21 ppm (which corresponds to the protons of diethyl ether),[3] indicating effective drying of the polymers after purification and the absence of residual solvents. Furthermore, **Figure S6** below shows the thermogram of a binary mixture with a high polymer content (40 wt%), where only the glass transition of the binary mixture is observed (T_g = 288 K), with no signs of solvent evaporation processes. A similar scenario was observed during the calorimetric measurements of the pure polymers (**Figure S9**), where a single, clearly visible signal corresponding to the glass transition of the polymers was detected, with no phase transitions that could indicate the presence of residual solvents. Thus, the calorimetric studies further confirm the purity of the obtained macromolecular compounds.

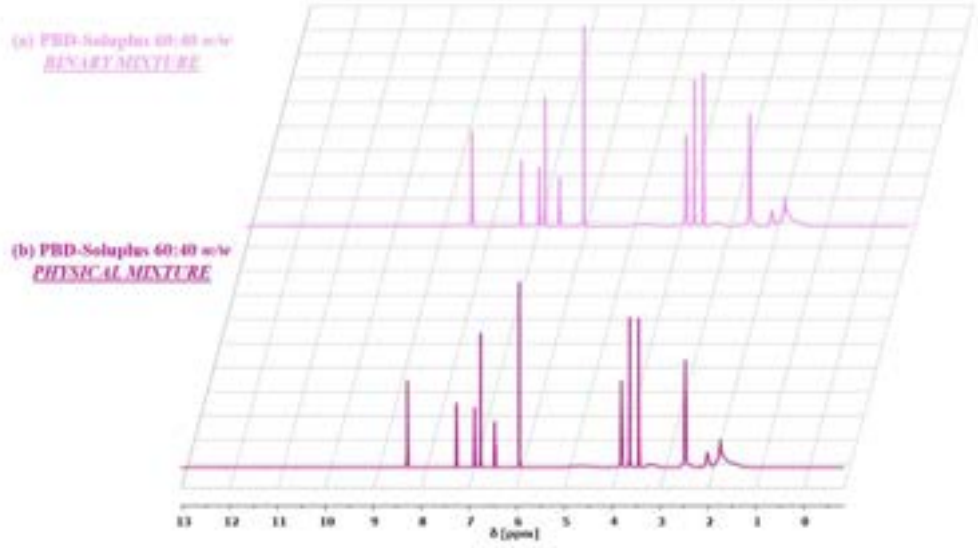

Figure S4. Comparison of ^{1}H NMR spectra of the PBD-Soluplus 60:40 *w/w* system: **(a)** binary and **(b)** physical mixtures.

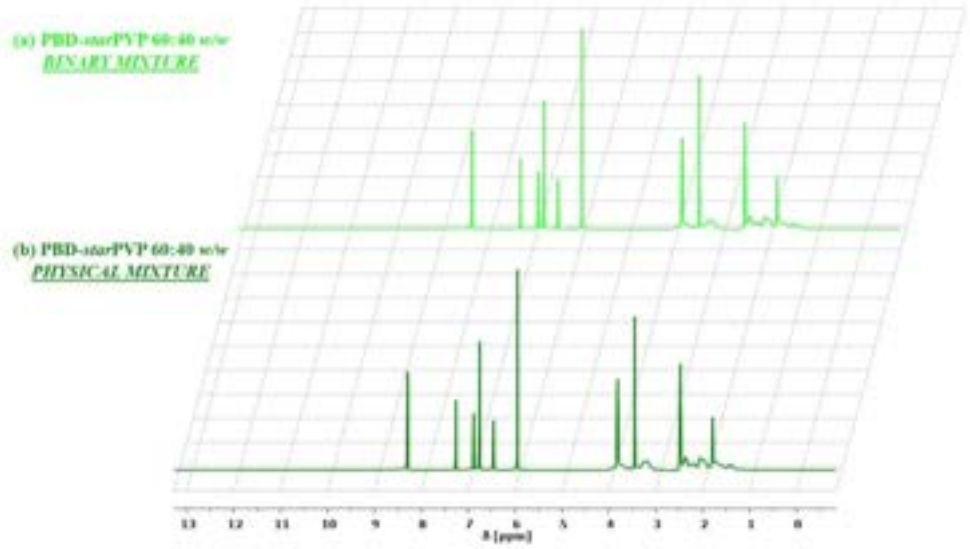

Figure S5. Comparison of ^{1}H NMR spectra of the PBD-*star*PVP 60:40 *w/w* system: **(a)** binary and **(b)** physical mixtures.

DSC data

Table S1. The calorimetric glass transition temperature values (heating rate, ϕ =10 K/min) for the examined PBD-polymer BMs in various weight ratios as well as neat polymers.

Binary mixture, *w/w*	**Glass transition temperature, T_g [K]**		
	PBD-Soluplus	PBD-*lin*PVP	PBD-*star*PVP
90:10	261	262	262
80:20	264	267	267
70:30	265	278	273
60:40	273	292	285
neat polymers	348	451	450

Table S2. The crystallization temperature values for neat PBD and PBD-polymer 90:10 and 80:20 *w/w* mixtures depending on the ϕ.

PBD-EXCs 90:10 and 80:20 *w/w* mixtures				
ϕ [K/min]	T_c [K]			
	neat PBD	PBD-Soluplus 90:10 *w/w*	PBD-Soluplus 80:20 *w/w*	PBD-*lin*PVP 90:10 *w/w*
2	313	345	348	336
4	317	347	349	345
6	–	349	350	–
8	326	351	351	–
20	338	–	–	–

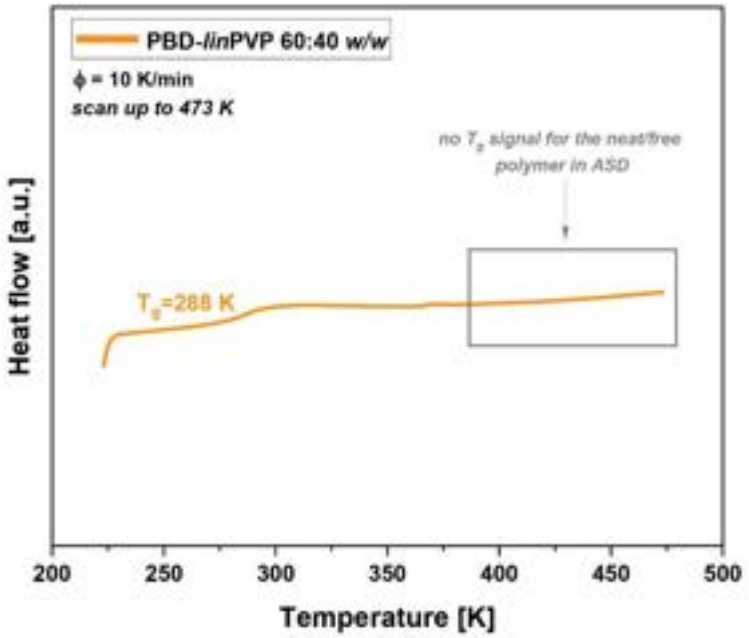

Figure S6. DSC thermogram (ϕ = 10 K/min) for PBD-*lin*PVP 60:40 *w/w* BM heated up to 473 K.

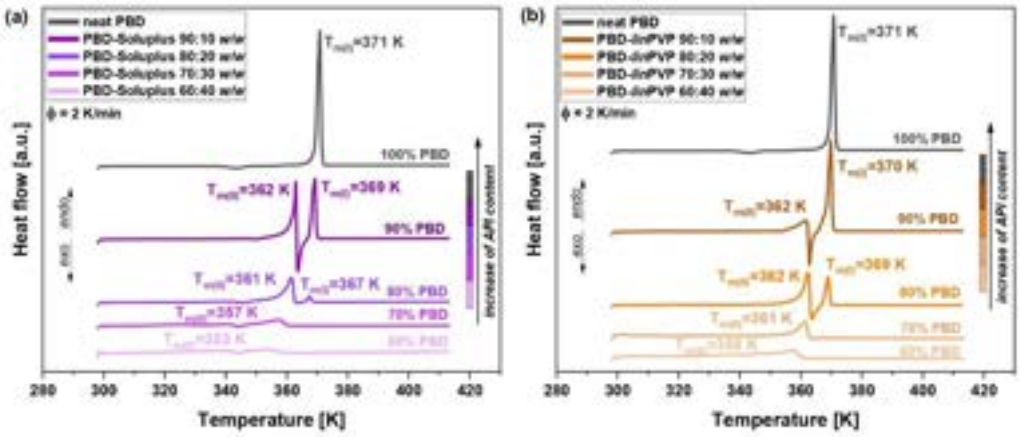

Figure S7. DSC thermograms of binary mixtures: **(a)** PBD-Soluplus and **(b)** PBD-*lin*PVP at a heating rate of 2 K/min. The data for neat PBD are also shown.

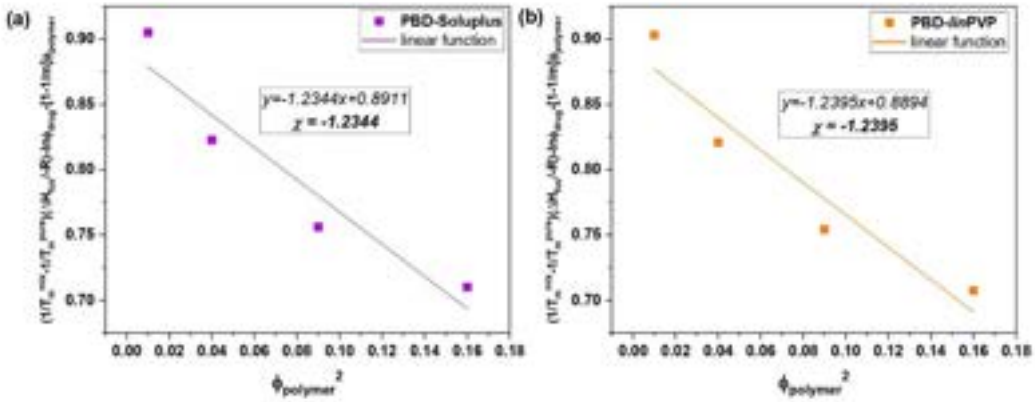

Figure S8. Graphs of $\left(\frac{1}{T_m^{mix}}-\frac{1}{T_m^{pure}}\right)\left(\frac{\Delta H_{fus}}{-R}\right)-ln\phi_{drug}-\left[1-\left(\frac{1}{m}\right)\right]\phi_{polymer}$ vs. $\phi_{polymer}^2$ to determine the χ values for **(a)** PBD-Soluplus and **(b)** PBD-*lin*PVP systems.

To confirm the miscibility of PBD with various types of polymers (Soluplus and PVP), the Flory–Huggins (F-H) theory was applied. This theory assumes that each molecule occupies a single site in the lattice and that the segments are randomly distributed. It is widely used to investigate the miscibility of a polymer with a solvent or another polymer by considering the change in Gibbs free energy before and after mixing.[4] However, if the solvent is replaced with another small molecule, such as a drug molecule, the F-H theory can also be employed to describe the thermodynamics of drug–polymer systems.[5]

The miscibility assessment based on the F-H theory can be carried out using a relatively simple method – namely, the melting point depression approach. It has been proposed that in a well-miscible drug–polymer system, the chemical potential of the drug in the presence of a polymeric carrier should be lower compared to its pure crystalline form, which results in a reduction of both the melting temperature and the enthalpy of fusion. Conversely, in an immiscible system, the chemical potential of the drug tends to remain constant, leading to negligible melting point depression. Based on this rationale, the change in Gibbs free energy can be expressed by the following equation:[6]

$$\Delta G = \mu_{liq} - \mu_{solid} = RTln(a) \quad \text{(S1)}$$

where μ_{liq} and μ_{solid} are the chemical potentials of molten drug and solid crystalline drug, respectively, and a refers to the activity coefficient of the species, which can be defined as:[6]

$$\ln(a) = -\frac{\Delta H_{fus}}{R}\left(\frac{1}{T_m^{mix}} - \frac{1}{T_m^{pure}}\right) \quad \text{(S2)}$$

where T_m^{mix} is melting temperature of drug in the drug-polymer mixture, T_m^{pure} is the melting point of pure crystalline drug, and ΔH_{fus} is the heat of fusion of the drug. In turn, the calculation of the F–H interaction parameter (χ) can be expressed by the following equation:[6]

$$\left(\frac{1}{T_m^{mix}} - \frac{1}{T_m^{pure}}\right) = \frac{-R}{\Delta H_{fus}}\left[ln\phi_{drug} + \left(1 - \frac{1}{m}\right)\phi_{polymer} + \chi\phi_{polymer}^2\right] \quad \text{(S3)}$$

where ϕ_{drug} and $\phi_{polymer}$ are the volume of the drug and polymer, respectively, and m is the ratio of the volume of the polymer to that of the drug. The value of χ can be determined from the slope of the graph by plotting $\left(\frac{1}{T_m^{mix}} - \frac{1}{T_m^{pure}}\right)\left(\frac{\Delta H_{fus}}{-R}\right) - ln\phi_{drug} - \left[1 - \left(\frac{1}{m}\right)\right]\phi_{polymer}$ versus $\phi_{polymer}^2$.

The melting point depression method has often been used as a means of evaluating the miscibility of dispersion systems, in which miscible/homogenous mixtures exhibit significant melting point depression with varying polymer concentrations, whereas in immiscible drug–polymer systems, the depression would be negligible due to the endothermic nature of mixing. Accordingly, the obtained χ value (near the drug's melting point) may reflect miscibility of a given system, where a positive value indicates immiscibility, while a negative χ suggests miscibility.[7]

Accordingly, to estimate the miscibility of the studied PBD–polymer systems, DSC measurements were carried out for the PBD–Soluplus and PBD–*lin*PVP binary mixtures at 90:10, 80:20, 70:30, and 60:40 *w/w*, using a heating rate of 2 K/min. The results of the thermal analysis are presented in **Figure S7**. As observed, the melting point of the drug gradually decreases with increasing polymer content, which is a primary indication of system miscibility. Furthermore, the obtained melting point data were used to plot $\left(\frac{1}{T_m^{mix}} - \frac{1}{T_m^{pure}}\right)\left(\frac{\Delta H_{fus}}{-R}\right) - ln\phi_{drug} - \left[1 - \left(\frac{1}{m}\right)\right]\phi_{polymer}$ versus $\phi_{polymer}^2$ dependencies, with the resulting plots shown in **Figure S8**. As previously mentioned, the interaction parameters were determined from the slope values and were found to be −1.2344 and −1.2395 for the PBD–Soluplus and PBD–*lin*PVP systems, respectively. Thus, according to the F–H theory, the obtained negative χ values suggest that both the commercial copolymer Soluplus and the synthesized PVPs exhibit good miscibility with the studied active pharmaceutical ingredient – PBD.

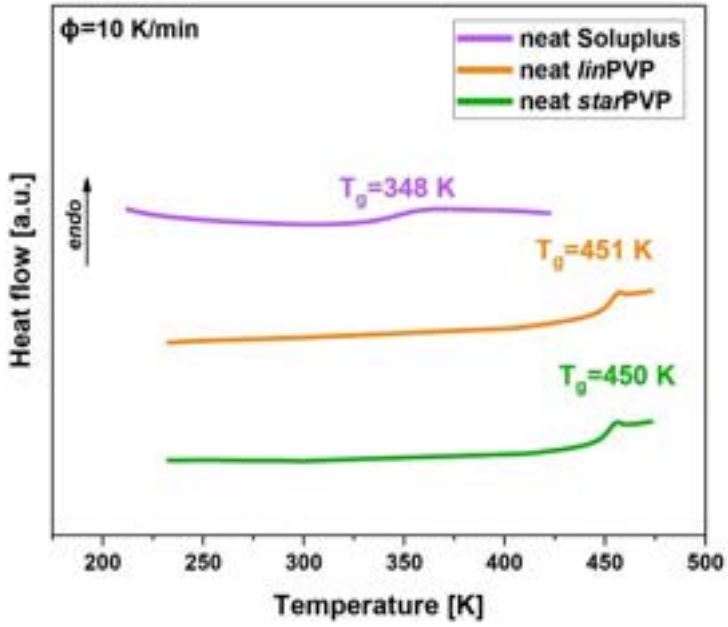

Figure S9. DSC thermograms (ϕ = 10 K/min) collected for neat polymers.

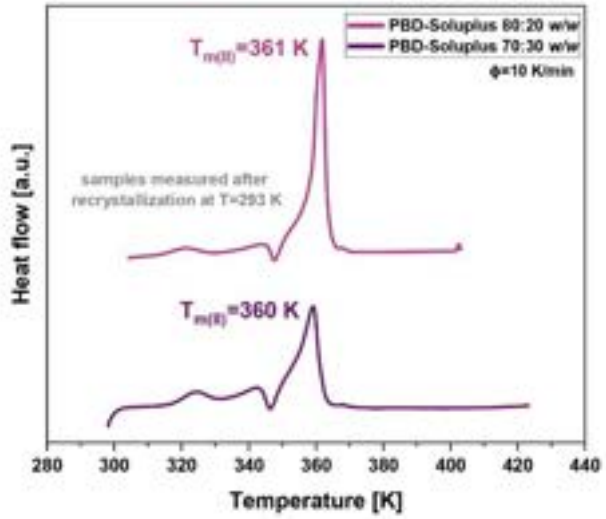

Figure S10. DSC thermograms (ϕ = 10 K/min) of PBD-Soluplus BMs (80:20 and 70:30 *w/w*) after recrystallization at room temperature.

FTIR data

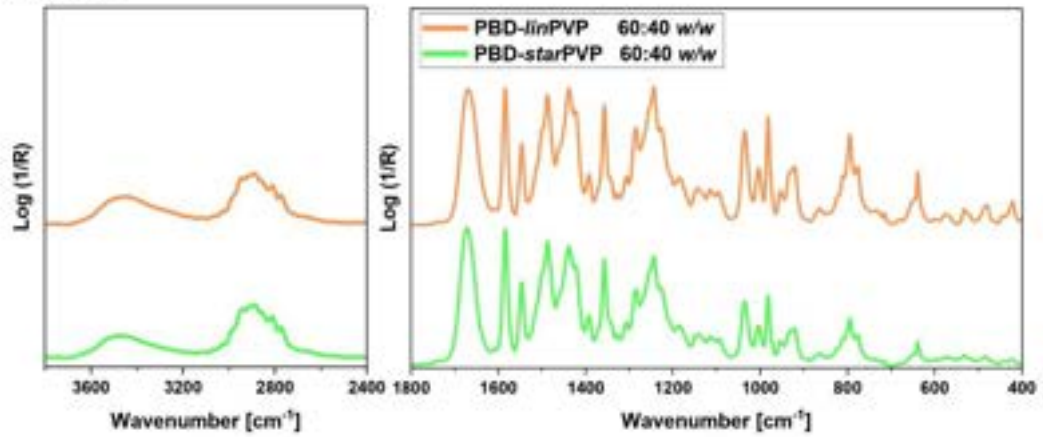

Figure S11. FTIR spectra of PBD-*lin*PVP and PBD-*star*PVP 60:40 *w/w* BMs, presented in the ranges of (left) 3800–2400 cm^{-1} and (right) 1800–400 cm^{-1}.

512

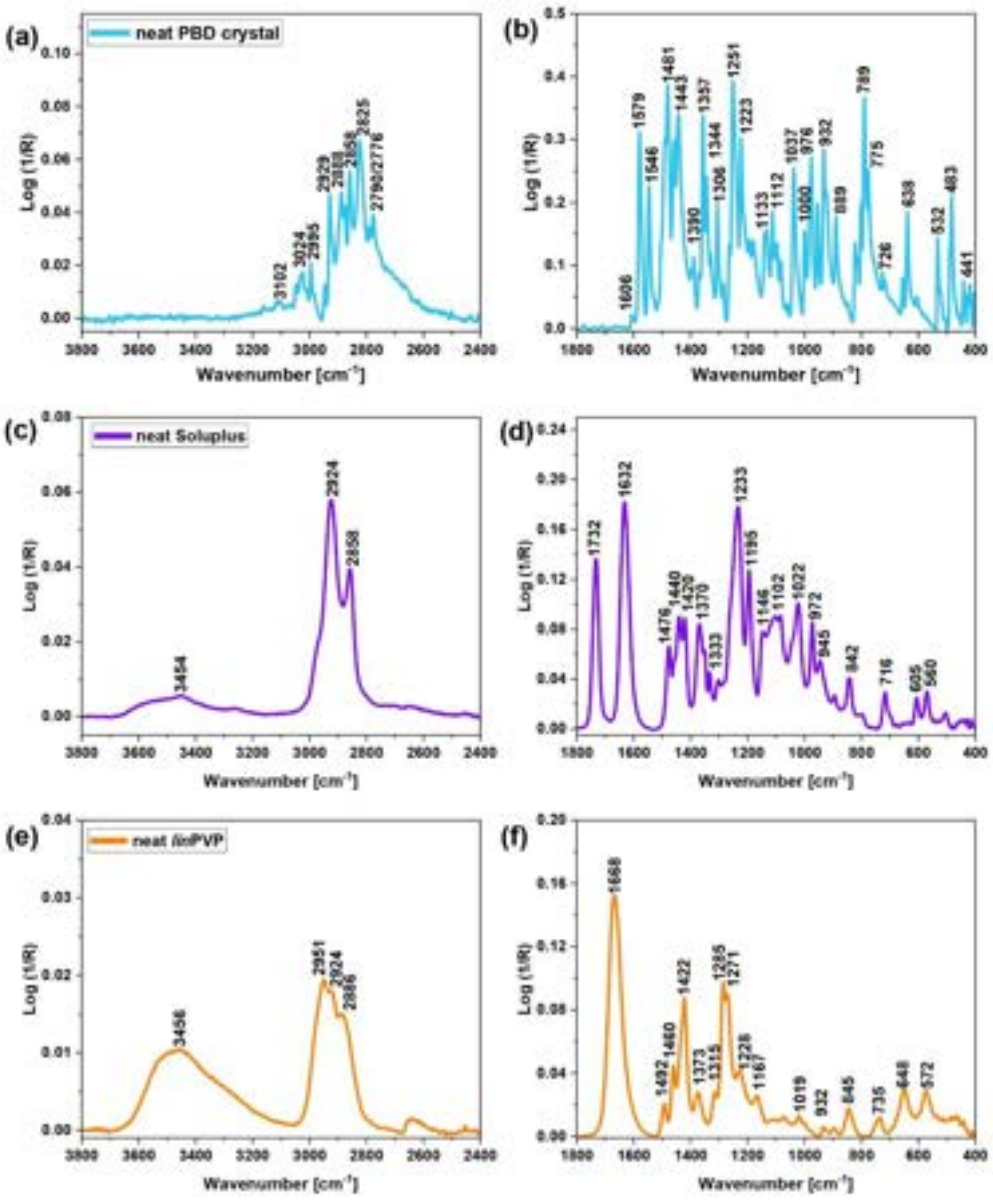

Figure S12. FTIR spectra of crystalline PBD as well as Soluplus and *lin*PVP samples. Data were presented in two spectral regions: **(a,c,e)** 3800–2400 cm^{-1} and **(b,d,f)** 1800–400 cm^{-1}.

The FTIR spectrum of neat crystalline PBD shows prominent absorption signals at several wavenumbers: 3102 and 3024 cm^{-1} (aromatic C-H stretching), 2995 cm^{-1} (asymmetric and symmetric CH_2 stretching), 2929, 2888 and 2858 cm^{-1} (C-H stretching), 2825, 2790 and 2776 cm^{-1} (C-H stretching of 1,3-dioxolane ring, i.e., C-H near oxygens), 1579 cm^{-1} (C=C and C=N ring stretching), 1546 cm^{-1} (conjugated C=C stretching), 1481 cm^{-1} (C-N stretching), 1357 cm^{-1} (additional conjugated C=C stretching), 1306 cm^{-1} (C-O stretching), 1251 cm^{-1} (asymmetric C-O stretching), 1112 cm^{-1} (C-N-C stretching), 1037 cm^{-1} (aromatic C-H stretching), and 976-483 cm^{-1} (C=C and C=N stretching, aromatic out-of-plane C-H deformation) (**Figure S12a,b**).[8,9]

The FTIR spectrum of Soluplus displays the stretching bands at 3454 cm^{-1} (intermolecular H-bonded O-H groups) as well as at 2924 and 2858 cm^{-1} (the asymmetric and symmetric C-H stretching) (**Figure S12c,d**). The strong absorption peaks in this polymer reflect the carbonyl stretching vibrations of the caprolactam ring (C(=O)N tertiary amide group, 1632 cm^{-1}) and the ester group ($OC(=O)CH_3$, 1732 cm^{-1}). The C-O-C stretching can be visible at 1476 cm^{-1}, and the C-H bending is detected at 1440 cm^{-1}. The ester C–O stretching vibrations are observed at 1233 and 1102 cm^{-1}.[9–13] In turn, PVP with linear topology is characterized by the IR peaks at 3456 cm^{-1} (O-H stretching of residual water), 2951 cm^{-1} (asymmetric CH_2 stretching of pyrrolidone ring), 2924 cm^{-1} (symmetric CH_2 stretching of chain), and 2886 cm^{-1} (C-H stretching), 1668 cm^{-1} (C=O stretching), 1492, 1460, 1422 cm^{-1} (C-N stretching and CH_2 scissoring), 1373 cm^{-1} (C-H bending), 1285, 1271, 1228 and 1167 cm^{-1} (C-N stretching and CH_2 wagging), 1019 cm^{-1} (C-C stretching and CH_2 rocking), 932 cm^{-1} (C-C ring breathing), 845 cm^{-1} (C-C ring stretching), 735 cm^{-1} (C-C chain stretching), 648 and 572 cm^{-1} (N-C=O bending, ring deformation) (**Figure S12e,f**).[9,14,15]

BDS data

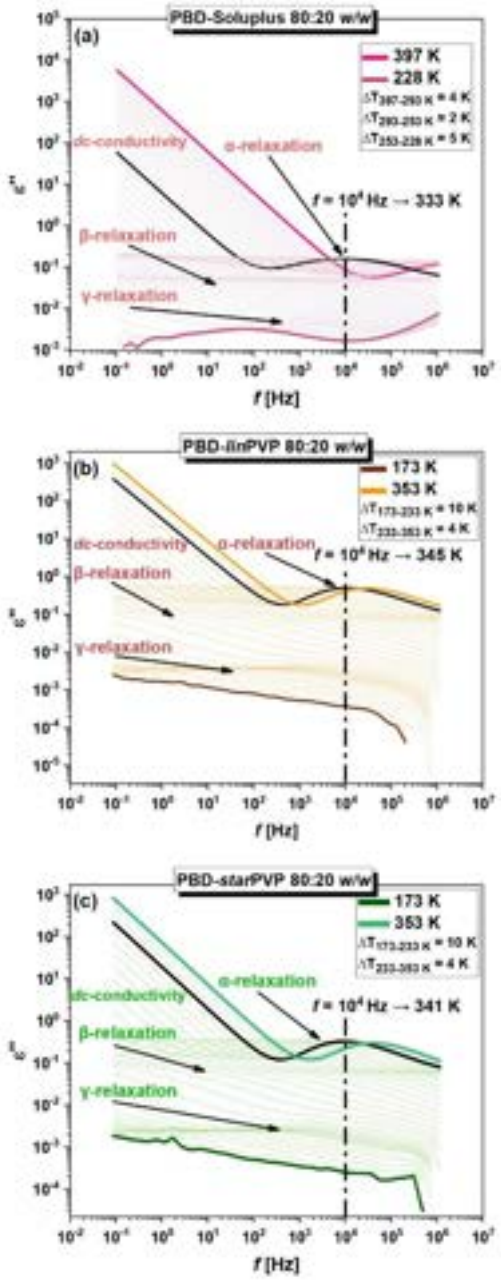

Figure S13. Dielectric loss spectra of **(a)** PBD-Soluplus **(b)**, PBD-*lin*PVP, **(c)**, and PBD-*star*PVP 80:20 *w/w* BMs.

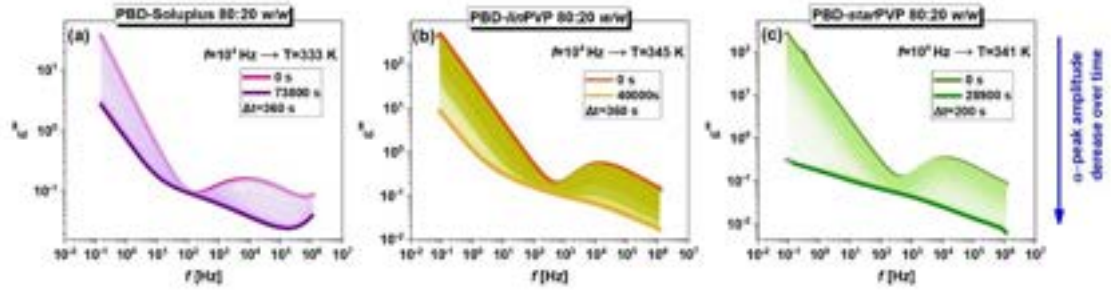

Figure S14. Time evolution of the imaginary (ε'') part of the complex dielectric permittivity plotted versus frequency during the isothermal crystallization of **(a)** PBD-Soluplus 80:20 *w/w*, **(b)** PBD-*lin*PVP 80:20 *w/w*, **(c)** PBD-*star*PVP 80:20 *w/w* at indicated temperatures (f=10^4 Hz).

Table S3. Summary of $T_{c(BDS)}$, $T_{g(DSC)}$ (ϕ = 10 K/min) and $\frac{T_{c(BDS)}}{T_{g(DSC)}}$ values for individual 90:10 and 80:20 *w/w* binary systems.

	API-polymer weight ratio	$T_{c\,(BDS)}$ [K]	$T_{g\,(DSC)}$ [K]	$\frac{T_{c\,(BDS)}}{T_{g\,(DSC)}}$
PBD-Soluplus	90:10	328	261	1.26
	80:20	333	264	1.26
PBD-*lin*PVP	90:10	333	262	1.27
	80:20	345	267	1.29
PBD-*star*PVP	90:10	333	262	1.27
	80:20	341	267	1.28

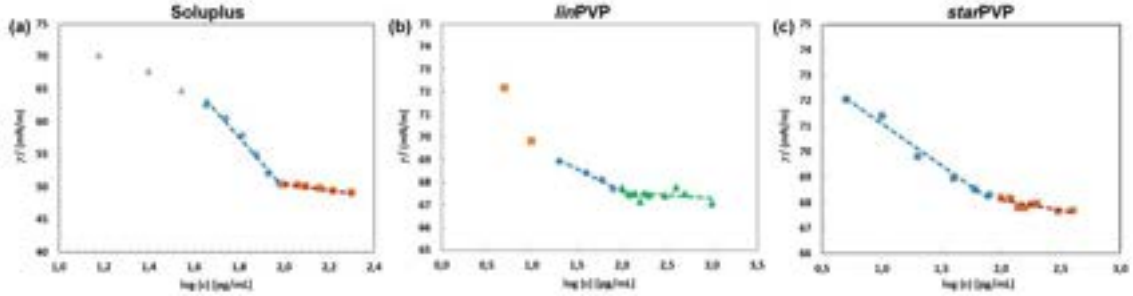

Figure S15. Determination of CMC by measuring the surface tension (γ) at 25 °C of serial dilutions of **(a)** Soluplus, **(b)** *lin*PVP, and **(c)** *star*PVP. The dashed lines are the best linear fits in the two concentration ranges.

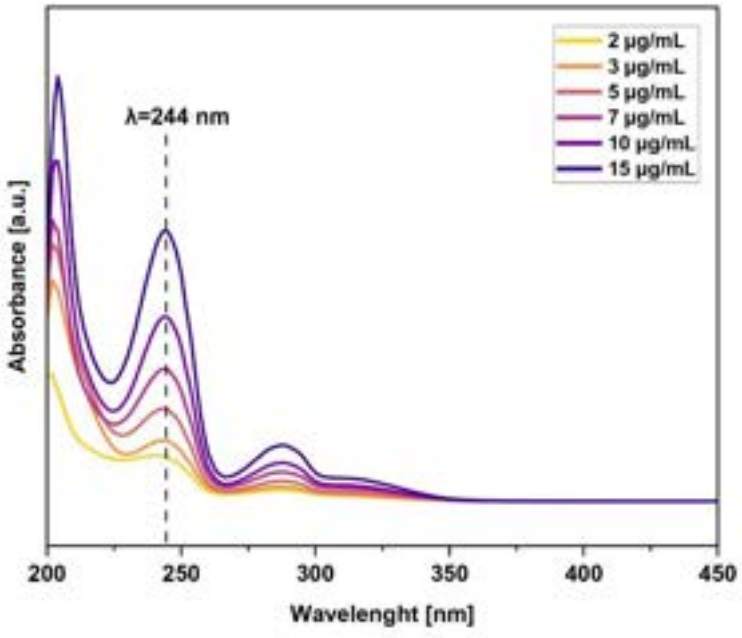

Figure S16. UV-Vis spectra for PBD at different concentrations (in the range of 2–15 µg/mL; solutions in ethanol solvent).

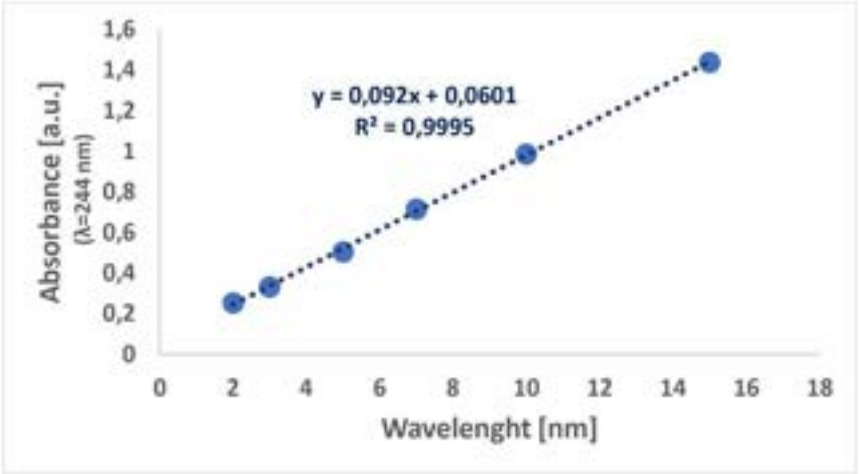

Figure S17. The calibration curve for PBD in ethanol.

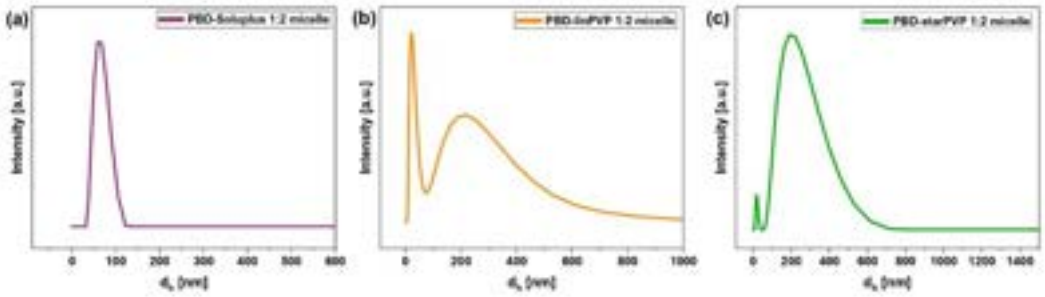

Figure S18. Hydrodynamic diameters (d_h) of obtained micellar systems: **(a)** PBD-Soluplus 1:2, **(b)** PBD-*lin*PVP 1:2, **(c)** PBD-*star*PVP 1:2 (aqueous solutions with a concentration of c = 1 mg/mL).

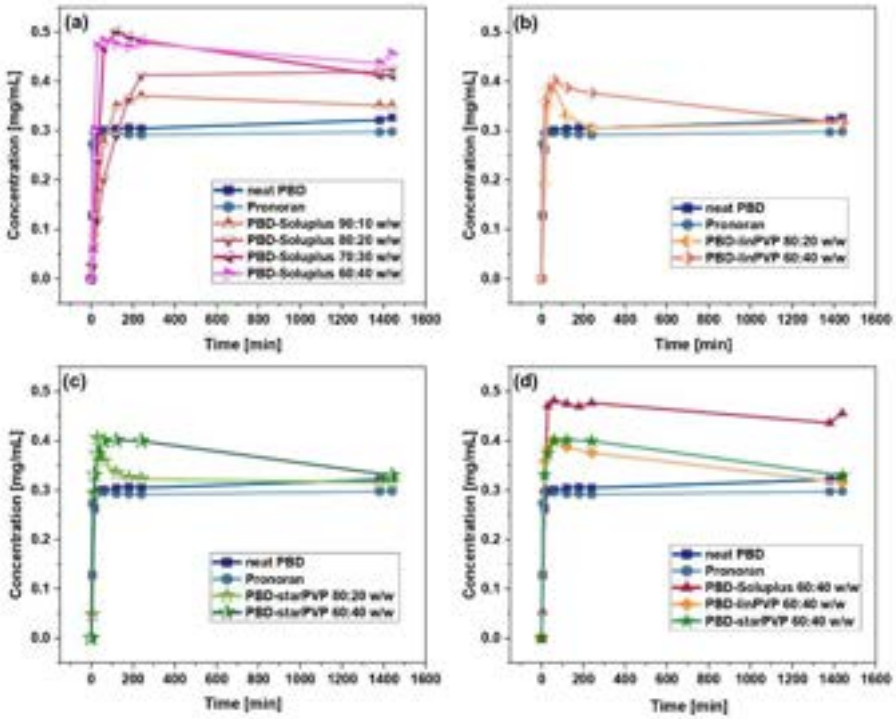

Figure S19. Drug release profile (drug concentration vs. time) from various polymer matrices in **(a)** PBD-Soluplus; **(b)** PBD-*lin*PVP; and **(c)** PBD-*star*PVP BMs. Panel **(d)** presents a comparison of drug release profiles from various polymer matrices for 60:40 *w/w* BMs. Each panel contains two reference samples: neat crystalline PBD and the API Pronoran.

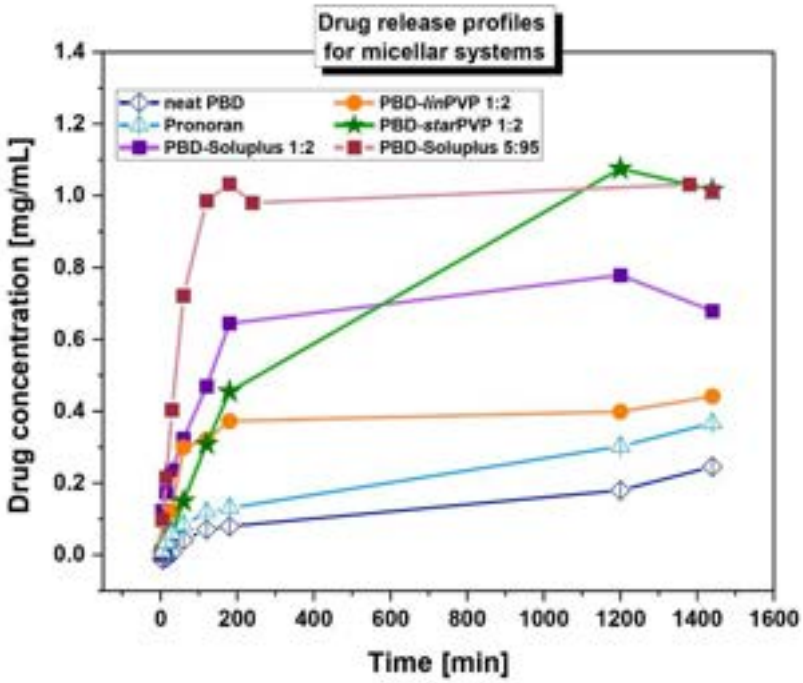

Figure S20. Drug release profiles (drug concentration vs. time) for micellar systems with various polymer matrices, as well as for the reference samples: neat PBD and the Pronoran tablet.

DSC data (drug release studies)

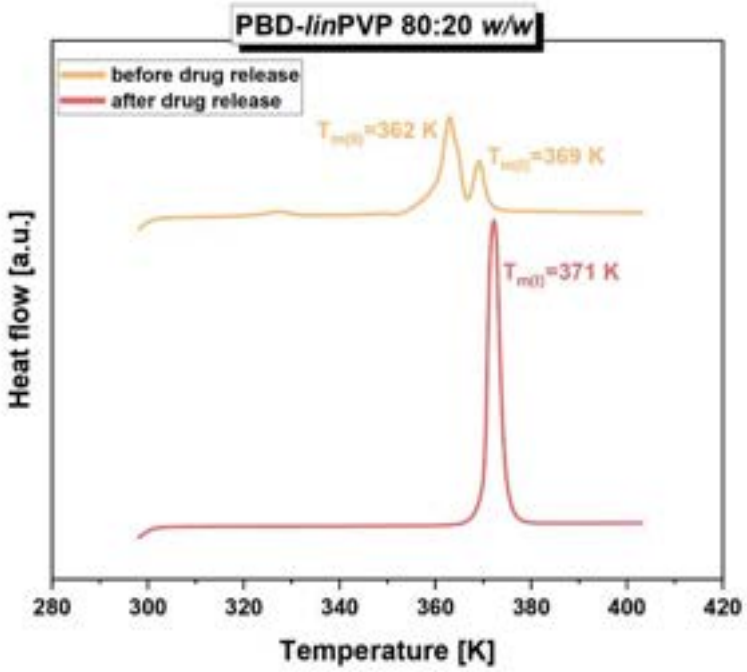

Figure S21. DSC data (ϕ = 10 K/min) for the PBD–*lin*PVP 80:20 *w/w* binary mixture before (orange line) and after (red line) the release process.

References:

(1) Orszulak, L.; Lamrani, T.; Tarnacka, M.; Hachuła, B.; Jurkiewicz, K.; Zioła, P.; Mrozek-Wilczkiewicz, A.; Kamińska, E.; Kamiński, K. The Impact of Various Poly(Vinylpyrrolidone) Polymers on the Crystallization Process of Metronidazole. *Pharmaceutics* **2024**, *16* (1). https://doi.org/10.3390/pharmaceutics16010136.

(2) Orszulak, L.; Lamrani, T.; Bernat, R.; Tarnacka, M.; Żakowiecki, D.; Jurkiewicz, K.; Zioła, P.; Mrozek-Wilczkiewicz, A.; Zięba, A.; Kamiński, K.; Kamińska, E. The Influence of PVP Polymer Topology on the Liquid Crystalline Order of Itraconazole in Binary Systems. *Mol. Pharm.* **2024**, *21* (6), 3027–3039. https://doi.org/10.1021/acs.molpharmaceut.4c00215.

(3) Gottlieb, H. E.; Kotlyar, V.; Nudelman, A. NMR Chemical Shifts of Common Laboratory Solvents as Trace Impurities. *J. Org. Chem.* **1997**, *62* (21), 7512–7515. https://doi.org/10.1021/jo971176v.

(4) Sarode, A. L.; Sandhu, H.; Shah, N.; Malick, W.; Zia, H. Hot Melt Extrusion (HME) for Amorphous Solid Dispersions: Predictive Tools for Processing and Impact of Drug-Polymer Interactions on Supersaturation. *Eur. J. Pharm. Sci.* **2013**, *48* (3), 371–384. https://doi.org/10.1016/j.ejps.2012.12.012.

(5) Zhao, Y.; Inbar, P.; Chokshi, H. P.; Malick, A. W.; Choi, D. S. Prediction of the Thermal Phase Diagram of Amorphous Solid Dispersions by Flory-Huggins Theory. *J. Pharm. Sci.* **2011**, *100* (8), 3196–3207. https://doi.org/10.1002/jps.22541.

(6) Meng, F.; Dave, V.; Chauhan, H. Qualitative and Quantitative Methods to Determine Miscibility in Amorphous Drug-Polymer Systems. *Eur. J. Pharm. Sci. Off. J. Eur. Fed. Pharm. Sci.* **2015**, *77*, 106–111. https://doi.org/10.1016/j.ejps.2015.05.018.

(7) Bansal, K.; Baghel, U. S.; Thakral, S. Construction and Validation of Binary Phase Diagram for Amorphous Solid Dispersion Using Flory-Huggins Theory. *AAPS PharmSciTech* **2016**, *17* (2), 318–327. https://doi.org/10.1208/s12249-015-0343-8.

(8) Bhargavi, C.; Raghuveer, P. Enhancing Nose-To-Brain Delivery of Piribedil: Development of a Nanosuspension Dispersed in Nasal in-Situ Gelling System. *Int. J. Appl. Pharm.* **2024**, *16* (3), 86–101. https://doi.org/10.22159/ijap.2024v16i3.50242.

(9) Socrates, G. Infrared and Raman Characteristic Group Frequencies : Tables and Charts; 2001.

(10) Desai, P.; Chatterjee, B. Comparison of Two Grafted Copolymers, Soluplus and Kollicoat IR, as Solid Dispersion Carriers of Arteether for Oral Delivery Prepared by Different Solvent-Based Methods. *ACS Omega* **2023**, *8* (48), 45337–45347. https://doi.org/10.1021/acsomega.3c04110.

(11) Thakral, N. K.; Ray, A. R.; Bar-Shalom, D.; Eriksson, A. H.; Majumdar, D. K. Soluplus-Solubilized Citrated Camptothecin - A Potential Drug Delivery Strategy in Colon Cancer. *AAPS PharmSciTech* **2012**, *13* (1), 59–66. https://doi.org/10.1208/s12249-011-9720-0.

(12) Lin, S. Y.; Lin, H. L.; Chi, Y. T.; Hung, R. Y.; Huang, Y. T.; Hsieh, W. H.; Kao, C. Y. Influence of Soluplus on Solid-State Properties and Physical Stability of Indomethacin-Saccharin Co-Crystal Formation Prepared by Air-Drying Process. *J. Pharm. Innov.* **2016**, *11* (2), 109–119. https://doi.org/10.1007/s12247-016-9243-z.

(13) Shamma, R. N.; Basha, M. Soluplus®: A Novel Polymeric Solubilizer for Optimization of Carvedilol Solid Dispersions: Formulation Design and Effect of Method of Preparation. *Powder Technol.* **2013**, *237*, 406–414. https://doi.org/https://doi.org/10.1016/j.powtec.2012.12.038.

(14) Rahma, A.; Munir, M. M.; Khairurrijal; Prasetyo, A.; Suendo, V.; Rachmawati, H. Intermolecular Interactions and the Release Pattern of Electrospun Curcumin-Polyvinyl(Pyrrolidone) Fiber. *Biol. Pharm. Bull.* **2016**, *39* (2), 163–173. https://doi.org/10.1248/bpb.b15-00391.

(15) Borodko, Y.; Habas, S. E.; Koebel, M.; Yang, P.; Frei, H.; Somorjai, G. A. Probing the Interaction of Poly (Vinylpyrrolidone) with Platinum Nanocrystals by \mbox{UV}-\mbox{R}aman and \mbox{FTIR}. *J. Phys. Chem. B* **2006**, *110*, 23052–23059.

5. Oświadczenia współautorów prac

Chorzów, 16.04.2026
Miejsce i data

Kamil Kamiński
Imię i nazwisko współautora publikacji

Uniwersytet Śląski w Katowicach
Wydział Nauk Ścisłych i Technicznych
Instytut Fizyki
Afiliacja

OŚWIADCZENIE

Oświadczam, że w pracach:

P1. L. Orszulak, T. Lamrani, M. Tarnacka, B. Hachuła, K. Jurkiewicz, P. Zioła, A. Mrozek-Wilczkiewicz, E. Kamińska, K. Kamiński, **The impact of various poly(vinylpyrrolidone) polymers on the crystallization process of metronidazole**, *Pharmaceutics*, 2024, 16(1), 136.

P2. L. Orszulak, P. Włodarczyk, B. Hachuła, T. Lamrani, K. Jurkiewicz, M. Tarnacka, M. Hreczka, K. Kamiński, E. Kamińska, **Inhibition of naproxen crystallization by polymers: The role of topology and chain length of polyvinylpyrrolidone macromolecules**, *European Journal of Pharmaceutics and Biopharmaceutics*, 2025, 207, 114581.

P3. L. Orszulak, T. Lamrani, R. Bernat, M. Tarnacka, D. Żakowiecki, K. Jurkiewicz, P. Zioła, A. Mrozek-Wilczkiewicz, A. Zięba, K. Kamiński, E. Kamińska, **The influence of PVP polymer topology on the liquid crystalline order of itraconazole in binary systems**, *Molecular Pharmaceutics*, 2024, 21(6), 3027−3039.

P4. L. Orszulak, A. Minecka, R. Bernat, T. Lamrani, K. Jurkiewicz, B. Hachuła, M. Tarnacka, M. Geppert-Rybczyńska, M. Zubko, M. Staniszewska, M. Smoleński, J. Dobosz, G. Garbacz, K. Kamiński, E. Kamińska, **Hydrophilic and amphiphilic macromolecules as modulators of the physical stability and bioavailability of piribedil: a study on binary mixtures and micellar systems**, *Molecular Pharmaceutics*, 2025, 22(8), 4708−4730.

mój udział polegał na nadzorowaniu prowadzonych badań i analiz, dyskusji uzyskanych wyników i korekcie manuskryptów.

Kamil Kaminski

Podpis współautora publikacji

Chorzów, 16.04.2026
Miejsce i data

Karolina Jurkiewicz
Imię i nazwisko współautora publikacji

Uniwersytet Śląski w Katowicach
Wydział Nauk Ścisłych i Technicznych
Instytut Fizyki
Afiliacja

OŚWIADCZENIE

Oświadczam, że w pracach:

P1. L. Orszulak, T. Lamrani, M. Tarnacka, B. Hachuła, K. Jurkiewicz, P. Zioła, A. Mrozek-Wilczkiewicz, E. Kamińska, K. Kamiński, **The impact of various poly(vinylpyrrolidone) polymers on the crystallization process of metronidazole**, *Pharmaceutics*, 2024, 16(1), 136.

P2. L. Orszulak, P. Włodarczyk, B. Hachuła, T. Lamrani, K. Jurkiewicz, M. Tarnacka, M. Hreczka, K. Kamiński, E. Kamińska, **Inhibition of naproxen crystallization by polymers: The role of topology and chain length of polyvinylpyrrolidone macromolecules**, *European Journal of Pharmaceutics and Biopharmaceutics*, 2025, 207, 114581.

P3. L. Orszulak, T. Lamrani, R. Bernat, M. Tarnacka, D. Żakowiecki, K. Jurkiewicz, P. Zioła, A. Mrozek-Wilczkiewicz, A. Zięba, K. Kamiński, E. Kamińska, **The influence of PVP polymer topology on the liquid crystalline order of itraconazole in binary systems**, *Molecular Pharmaceutics*, 2024, 21(6), 3027−3039.

P4. L. Orszulak, A. Minecka, R. Bernat, T. Lamrani, K. Jurkiewicz, B. Hachuła, M. Tarnacka, M. Geppert-Rybczyńska, M. Zubko, M. Staniszewska, M. Smoleński, J. Dobosz, G. Garbacz, K. Kamiński, E. Kamińska, **Hydrophilic and amphiphilic macromolecules as modulators of the physical stability and bioavailability of piribedil: a study on binary mixtures and micellar systems**, *Molecular Pharmaceutics*, 2025, 22(8), 4708−4730.

mój udział polegał na nadzorowaniu pomiarów dyfrakcyjnych, analizie zebranych wyników i ich dyskusji w publikacjach.

.....
podpis współautora publikacji

Chorzów, 16.04.2026
Location and date

Taoufik Lamrani
First and last name of co-author of the publication

University of Silesia in Katowice
Faculty of Science and Technology,
Institute of Physics
Affiliation

STATEMENT

I declare that for the following works:

P1. L. Orszulak, T. Lamrani, M. Tarnacka, B. Hachuła, K. Jurkiewicz, P. Zioła, A. Mrozek-Wilczkiewicz, E. Kamińska, K. Kamiński, **The impact of various poly(vinylpyrrolidone) polymers on the crystallization process of metronidazole**, *Pharmaceutics*, 2024, 16(1), 136.

P2. L. Orszulak, P. Włodarczyk, B. Hachuła, T. Lamrani, K. Jurkiewicz, M. Tarnacka, M. Hreczka, K. Kamiński, E. Kamińska, **Inhibition of naproxen crystallization by polymers: The role of topology and chain length of polyvinylpyrrolidone macromolecules**, *European Journal of Pharmaceutics and Biopharmaceutics*, 2025, 207, 114581.

P3. L. Orszulak, T. Lamrani, R. Bernat, M. Tarnacka, D. Żakowiecki, K. Jurkiewicz, P. Zioła, A. Mrozek-Wilczkiewicz, A. Zięba, K. Kamiński, E. Kamińska, **The influence of PVP polymer topology on the liquid crystalline order of itraconazole in binary systems**, *Molecular Pharmaceutics*, 2024, 21(6), 3027−3039.

P4. L. Orszulak, A. Minecka, R. Bernat, T. Lamrani, K. Jurkiewicz, B. Hachuła, M. Tarnacka, M. Geppert-Rybczyńska, M. Zubko, M. Staniszewska, M. Smoleński, J. Dobosz, G. Garbacz, K. Kamiński, E. Kamińska, **Hydrophilic and amphiphilic macromolecules as modulators of the physical stability and bioavailability of piribedil: a study on binary mixtures and micellar systems**, *Molecular Pharmaceutics*, 2025, 22(8), 4708−4730.

my participation consisted of conducting diffraction experiments, visualizing the obtained data, and carrying out the initial analysis.

.....
Signature of the co-author of the publication

Chorzów, 16.04.2026
Miejsce i data

Magdalena Tarnacka
Imię i nazwisko współautora publikacji

Uniwersytet Śląski w Katowicach
Wydział Nauk Ścisłych i Technicznych
Instytut Fizyki
Afiliacja

OŚWIADCZENIE

Oświadczam, że w pracach:

P1. L. Orszulak, T. Lamrani, M. Tarnacka, B. Hachuła, K. Jurkiewicz, P. Zioła, A. Mrozek-Wilczkiewicz, E. Kamińska, K. Kamiński, **The impact of various poly(vinylpyrrolidone) polymers on the crystallization process of metronidazole**, *Pharmaceutics*, 2024, 16(1), 136.

P2. L. Orszulak, P. Włodarczyk, B. Hachuła, T. Lamrani, K. Jurkiewicz, M. Tarnacka, M. Hreczka, K. Kamiński, E. Kamińska, **Inhibition of naproxen crystallization by polymers: The role of topology and chain length of polyvinylpyrrolidone macromolecules**, *European Journal of Pharmaceutics and Biopharmaceutics*, 2025, 207, 114581.

P3. L. Orszulak, T. Lamrani, R. Bernat, M. Tarnacka, D. Żakowiecki, K. Jurkiewicz, P. Zioła, A. Mrozek-Wilczkiewicz, A. Zięba, K. Kamiński, E. Kamińska, **The influence of PVP polymer topology on the liquid crystalline order of itraconazole in binary systems**, *Molecular Pharmaceutics*, 2024, 21(6), 3027−3039.

P4. L. Orszulak, A. Minecka, R. Bernat, T. Lamrani, K. Jurkiewicz, B. Hachuła, M. Tarnacka, M. Geppert-Rybczyńska, M. Zubko, M. Staniszewska, M. Smoleński, J. Dobosz, G. Garbacz, K. Kamiński, E. Kamińska, **Hydrophilic and amphiphilic macromolecules as modulators of the physical stability and bioavailability of piribedil: a study on binary mixtures and micellar systems**, *Molecular Pharmaceutics*, 2025, 22(8), 4708−4730.

mój udział polegał na przeprowadzeniu pomiarów kalorymetrycznych i dyskusji otrzymanych wyników.

Podpis współautora publikacji

Sosnowiec, 16.04.2026
Miejsce i data

Ewa Kamińska
Imię i nazwisko współautora publikacji

Śląski Uniwersytet Medyczny w Katowicach
Wydział Nauk Farmaceutycznych
Katedra Farmakognozji i Fitochemii
Afiliacja

OŚWIADCZENIE

Oświadczam, że w pracach:

P1. L. Orszulak, T. Lamrani, M. Tarnacka, B. Hachuła, K. Jurkiewicz, P. Zioła, A. Mrozek-Wilczkiewicz, E. Kamińska, K. Kamiński, **The impact of various poly(vinylpyrrolidone) polymers on the crystallization process of metronidazole**, *Pharmaceutics*, 2024, 16(1), 136.

P2. L. Orszulak, P. Włodarczyk, B. Hachuła, T. Lamrani, K. Jurkiewicz, M. Tarnacka, M. Hreczka, K. Kamiński, E. Kamińska, **Inhibition of naproxen crystallization by polymers: The role of topology and chain length of polyvinylpyrrolidone macromolecules**, *European Journal of Pharmaceutics and Biopharmaceutics*, 2025, 207, 114581.

P3. L. Orszulak, T. Lamrani, R. Bernat, M. Tarnacka, D. Żakowiecki, K. Jurkiewicz, P. Zioła, A. Mrozek-Wilczkiewicz, A. Zięba, K. Kamiński, E. Kamińska, **The influence of PVP polymer topology on the liquid crystalline order of itraconazole in binary systems**, *Molecular Pharmaceutics*, 2024, 21(6), 3027−3039.

P4. L. Orszulak, A. Minecka, R. Bernat, T. Lamrani, K. Jurkiewicz, B. Hachuła, M. Tarnacka, M. Geppert-Rybczyńska, M. Zubko, M. Staniszewska, M. Smoleński, J. Dobosz, G. Garbacz, K. Kamiński, E. Kamińska, **Hydrophilic and amphiphilic macromolecules as modulators of the physical stability and bioavailability of piribedil: a study on binary mixtures and micellar systems**, *Molecular Pharmaceutics*, 2025, 22(8), 4708−4730.

mój udział polegał na dyskusji wyników, korekcie manuskryptów oraz odpowiedzi na uwagi Recenzentów, a także finansowaniu w części badań w ramach kierowania projektem NCN OPUS.

.....Ewa Ozimek-Kamińska.....

Podpis współautora publikacji

Chorzów, 16.04.2026
Miejsce i data

Barbara Hachuła
Imię i nazwisko współautora publikacji

Uniwersytet Śląski w Katowicach
Wydział Nauk Ścisłych i Technicznych
Instytut Chemii
Afiliacja

OŚWIADCZENIE

Oświadczam, że w pracach:

P1. L. Orszulak, T. Lamrani, M. Tarnacka, B. Hachuła, K. Jurkiewicz, P. Zioła, A. Mrozek-Wilczkiewicz, E. Kamińska, K. Kamiński, **The impact of various poly(vinylpyrrolidone) polymers on the crystallization process of metronidazole**, *Pharmaceutics*, 2024, 16(1), 136.

P2. L. Orszulak, P. Włodarczyk, B. Hachuła, T. Lamrani, K. Jurkiewicz, M. Tarnacka, M. Hreczka, K. Kamiński, E. Kamińska, **Inhibition of naproxen crystallization by polymers: The role of topology and chain length of polyvinylpyrrolidone macromolecules**, *European Journal of Pharmaceutics and Biopharmaceutics*, 2025, 207, 114581.

P4. L. Orszulak, A. Minecka, R. Bernat, T. Lamrani, K. Jurkiewicz, B. Hachuła, M. Tarnacka, M. Geppert-Rybczyńska, M. Zubko, M. Staniszewska, M. Smoleński, J. Dobosz, G. Garbacz, K. Kamiński, E. Kamińska, **Hydrophilic and amphiphilic macromolecules as modulators of the physical stability and bioavailability of piribedil: a study on binary mixtures and micellar systems**, *Molecular Pharmaceutics*, 2025, 22(8), 4708−4730.

mój udział polegał na wykonaniu pomiarów w podczerwieni, analizie otrzymanych danych, interpretacji wyników i ich dyskusji w artykułach.

Hachuła Barbara
Podpis współautora publikacji

Chorzów, 16.04.2026
Miejsce i data

Roksana Wygoda (wcześniej: Bernat)
Imię i nazwisko współautora publikacji

Uniwersytet Śląski w Katowicach
Wydział Nauk Ścisłych i Technicznych
Instytut Inżynierii Materiałowej
Afiliacja

OŚWIADCZENIE

Oświadczam, że w pracy:

P3. L. Orszulak, T. Lamrani, R. Bernat, M. Tarnacka, D. Żakowiecki, K. Jurkiewicz, P. Zioła, A. Mrozek-Wilczkiewicz, A. Zięba, K. Kamiński, E. Kamińska, **The influence of PVP polymer topology on the liquid crystalline order of itraconazole in binary systems**, *Molecular Pharmaceutics*, 2024, 21(6), 3027−3039.

mój udział polegał na przeprowadzeniu części syntez testowych mających na celu dobór optymalnych warunków otrzymywania PVP o zróżnicowanej topologii, a także na udziale w analizie i dyskusji uzyskanych wyników.

P4. L. Orszulak, A. Minecka, R. Bernat, T. Lamrani, K. Jurkiewicz, B. Hachuła, M. Tarnacka, M. Geppert-Rybczyńska, M. Zubko, M. Staniszewska, M. Smoleński, J. Dobosz, G. Garbacz, K. Kamiński, E. Kamińska, **Hydrophilic and amphiphilic macromolecules as modulators of the physical stability and bioavailability of piribedil: a study on binary mixtures and micellar systems**, *Molecular Pharmaceutics*, 2025, 22(8), 4708−4730.

mój udział polegał na przeprowadzeniu badań uwalniania leku z układów micelarnych, wykonaniu analiz spektrofotometrycznych oraz opracowaniu i wizualizacji uzyskanych danych, w szczególności profili uwalniania substancji czynnej.

Roksana Wygoda
Podpis współautora publikacji

Chorzów, 16.04.2026
Miejsce i data

Monika Geppert-Rybczyńska
Imię i nazwisko współautora publikacji

Uniwersytet Śląski w Katowicach
Wydział Nauk Ścisłych i Technicznych
Instytut Chemii
Afiliacja

OŚWIADCZENIE

Oświadczam, że w pracy:

P4. L. Orszulak, A. Minecka, R. Bernat, T. Lamrani, K. Jurkiewicz, B. Hachuła, M. Tarnacka, M. Geppert-Rybczyńska, M. Zubko, M. Staniszewska, M. Smoleński, J. Dobosz, G. Garbacz, K. Kamiński, E. Kamińska, **Hydrophilic and amphiphilic macromolecules as modulators of the physical stability and bioavailability of piribedil: a study on binary mixtures and micellar systems**, *Molecular Pharmaceutics*, 2025, 22(8), 4708−4730.

mój udział polegał na wykonaniu pomiarów napięcia powierzchniowego dla wodnych roztworów polimerów oraz wyznaczeniu krytycznego stężenia powstawania miceli (CMC).

Monika Geppert-Rybczyńska
Podpis współautora publikacji

Chorzów, 16.04.2026
Miejsce i data

Anna Mrozek-Wilczkiewicz
Imię i nazwisko współautora publikacji

Uniwersytet Śląski w Katowicach
Wydział Nauk Ścisłych i Technicznych
Instytut Fizyki
Afiliacja

OŚWIADCZENIE

Oświadczam, że w pracach:

P1. L. Orszulak, T. Lamrani, M. Tarnacka, B. Hachuła, K. Jurkiewicz, P. Zioła, A. Mrozek-Wilczkiewicz, E. Kamińska, K. Kamiński, **The impact of various poly(vinylpyrrolidone) polymers on the crystallization process of metronidazole**, *Pharmaceutics*, 2024, 16(1), 136.

P3. L. Orszulak, T. Lamrani, R. Bernat, M. Tarnacka, D. Żakowiecki, K. Jurkiewicz, P. Zioła, A. Mrozek-Wilczkiewicz, A. Zięba, K. Kamiński, E. Kamińska, **The influence of PVP polymer topology on the liquid crystalline order of itraconazole in binary systems**, *Molecular Pharmaceutics*, 2024, 21, 3027−3039.

mój udział polegał na nadzorowaniu badań biologicznych i interpretacji wyników dotyczących eksperymentów cytotoksyczności.

.....
Podpis współautora publikacji

Chorzów, 16.04.2026
Miejsce i data

Patryk Zioła
Imię i nazwisko współautora publikacji

Uniwersytet Śląski w Katowicach
Wydział Nauk Ścisłych i Technicznych
Instytut Fizyki
Afiliacja

OŚWIADCZENIE

Oświadczam, że w pracach:

P1. L. Orszulak, T. Lamrani, M. Tarnacka, B. Hachuła, K. Jurkiewicz, P. Zioła, A. Mrozek-Wilczkiewicz, E. Kamińska, K. Kamiński, **The impact of various poly(vinylpyrrolidone) polymers on the crystallization process of metronidazole**, *Pharmaceutics*, 2024, 16(1), 136.

P3. L. Orszulak, T. Lamrani, R. Bernat, M. Tarnacka, D. Żakowiecki, K. Jurkiewicz, P. Zioła, A. Mrozek-Wilczkiewicz, A. Zięba, K. Kamiński, E. Kamińska, **The influence of PVP polymer topology on the liquid crystalline order of itraconazole in binary systems**, *Molecular Pharmaceutics*, 2024, 21, 3027−3039.

mój udział polegał na wykonaniu testów cytotoksyczności dla próbek homopolimerów PVP o różnych topologiach.

Zioła Patryk
.....
Podpis współautora publikacji

Chorzów, 16.04.2026
Miejsce i data

Patryk Włodarczyk
Imię i nazwisko współautora publikacji

Sieć Badawcza Łukasiewicz
Instytut Metali Nieżelaznych
Afiliacja

OŚWIADCZENIE

Oświadczam, że w pracy:

P2. L. Orszulak, P. Włodarczyk, B. Hachuła, T. Lamrani, K. Jurkiewicz, M. Tarnacka, M. Hreczka, K. Kamiński, E. Kamińska, **Inhibition of naproxen crystallization by polymers: The role of topology and chain length of polyvinylpyrrolidone macromolecules**, *European Journal of Pharmaceutics and Biopharmaceutics*, 2025, 207, 114581.

mój udział polegał na przeprowadzeniu badań symulacji dynamiki molekularnej, analizie, wizualizacji oraz dyskusji otrzymanych wyników, a także na wykonaniu części nieizotermicznych pomiarów kalorymetrycznych.

Patryk Włodarczyk
Podpis współautora publikacji

Chorzów, 16.04.2026
Miejsce i data

Marek Hreczka
Imię i nazwisko współautora publikacji

Sieć Badawcza Łukasiewicz
Instytut Metali Nieżelaznych
Afiliacja

OŚWIADCZENIE

Oświadczam, że w pracy:

P2. L. Orszulak, P. Włodarczyk, B. Hachuła, T. Lamrani, K. Jurkiewicz, M. Tarnacka, M. Hreczka, K. Kamiński, E. Kamińska, **Inhibition of naproxen crystallization by polymers: The role of topology and chain length of polyvinylpyrrolidone macromolecules**, *European Journal of Pharmaceutics and Biopharmaceutics*, 2025, 207, 114581.

mój udział polegał na przeprowadzeniu części symulacji dynamiki molekularnej i udziale w dyskusji otrzymanych wyników.

Marek Hreczka
Podpis współautora publikacji

Chorzów, 16.04.2026
Miejsce i data

Maciej Zubko
Imię i nazwisko współautora publikacji

Uniwersytet Śląski w Katowicach
Wydział Nauk Ścisłych i Technicznych
Instytut Inżynierii Materiałowej
Afiliacja

OŚWIADCZENIE

Oświadczam, że w pracy:

P4. L. Orszulak, A. Minecka, R. Bernat, T. Lamrani, K. Jurkiewicz, B. Hachuła, M. Tarnacka, M. Geppert-Rybczyńska, M. Zubko, M. Staniszewska, M. Smoleński, J. Dobosz, G. Garbacz, K. Kamiński, E. Kamińska, **Hydrophilic and amphiphilic macromolecules as modulators of the physical stability and bioavailability of piribedil: a study on binary mixtures and micellar systems**, *Molecular Pharmaceutics*, 2025, 22(8), 4708−4730.

mój udział polegał na przeprowadzeniu pomiarów z wykorzystaniem transmisyjnej mikroskopii elektronowej (TEM) i dyskusji otrzymanych obrazów/zdjęć.

.....
Podpis współautora publikacji

Sosnowiec, 16.04.2026
Miejsce i data

Andrzej Zięba
Imię i nazwisko współautora publikacji

Śląski Uniwersytet Medyczny w Katowicach
Wydział Nauk Farmaceutycznych w Sosnowcu
Katedra i Zakład Chemii Organicznej
Afiliacja

OŚWIADCZENIE

Oświadczam, że w pracy:

P3. L. Orszulak, T. Lamrani, R. Bernat, M. Tarnacka, D. Żakowiecki, K. Jurkiewicz, P. Zioła, A. Mrozek-Wilczkiewicz, A. Zięba, K. Kamiński, E. Kamińska, **The influence of PVP polymer topology on the liquid crystalline order of itraconazole in binary systems**, *Molecular Pharmaceutics*, 2024, 21, 3027−3039.

mój udział polegał na przeprowadzeniu badań spektroskopowych polimerów PVP z wykorzystaniem techniki magnetycznego rezonansu jądrowego (NMR).

Andrzej Zięba
Podpis współautora publikacji

Budenheim, 16.04.2026
Miejsce i data

Daniel Żakowiecki
Imię i nazwisko współautora publikacji

Chemische Fabrik Budenheim KG
Afiliacja

OŚWIADCZENIE

Oświadczam, że w pracy:

P3. L. Orszulak, T. Lamrani, R. Bernat, M. Tarnacka, D. Żakowiecki, K. Jurkiewicz, P. Zioła, A. Mrozek-Wilczkiewicz, A. Zięba, K. Kamiński, E. Kamińska, **The influence of PVP polymer topology on the liquid crystalline order of itraconazole in binary systems**, *Molecular Pharmaceutics*, 2024, 21, 3027−3039.

mój udział polegał na przeprowadzeniu badań rozpuszczalności leku (itrakonazolu) w układach binarnych z wybranymi polimerami, analizie zebranych danych, ich wizualizacji i dyskusji w manuskrypcie.

.....
Podpis współautora publikacji

Sosnowiec, 16.04.2026
Miejsce i data

Aldona Minecka
Imię i nazwisko współautora publikacji

Śląski Uniwersytet Medyczny w Katowicach
Wydział Nauk Farmaceutycznych
Katedra Farmakognozji i Fitochemii
Afiliacja

OŚWIADCZENIE

Oświadczam, że w pracy:

P4. L. Orszulak, A. Minecka, R. Bernat, T. Lamrani, K. Jurkiewicz, B. Hachuła, M. Tarnacka, M. Geppert-Rybczyńska, M. Zubko, M. Staniszewska, M. Smoleński, J. Dobosz, G. Garbacz, K. Kamiński, E. Kamińska, **Hydrophilic and amphiphilic macromolecules as modulators of the physical stability and bioavailability of piribedil: a study on binary mixtures and micellar systems**, *Molecular Pharmaceutics*, 2025, 22(8), 4708−4730.

mój udział polegał na przeprowadzeniu badań dielektrycznych dla mieszanin binarnych Piribedil-Soluplus, wizualizacji danych, ich wstępnej analizie oraz finansowaniu badań w ramach kierowania projektem LIDER.

Aldona Minecka
Podpis współautora publikacji

Wrocław, 16.04.2026
Miejsce i data

Grzegorz Garbacz
Imię i nazwisko współautora publikacji

Physiolution Polska sp. z o.o.
Afiliacja

OŚWIADCZENIE

Oświadczam, że w pracy:

P4. L. Orszulak, A. Minecka, R. Bernat, T. Lamrani, K. Jurkiewicz, B. Hachuła, M. Tarnacka, M. Geppert-Rybczyńska, M. Zubko, M. Staniszewska, M. Smoleński, J. Dobosz, G. Garbacz, K. Kamiński, E. Kamińska, **Hydrophilic and amphiphilic macromolecules as modulators of the physical stability and bioavailability of piribedil: a study on binary mixtures and micellar systems**, *Molecular Pharmaceutics*, 2025, 22(8), 4708−4730.

mój udział polegał na dyskusji otrzymanych profili uwalniania leku (piribedilu).

.....
Podpis współautora publikacji

Wrocław, 16.04.2026
Miejsce i data

Michał Smoleński
Imię i nazwisko współautora publikacji

Physiolution Polska sp. z o.o.
Afiliacja

OŚWIADCZENIE

Oświadczam, że w pracy:

P4. L. Orszulak, A. Minecka, R. Bernat, T. Lamrani, K. Jurkiewicz, B. Hachuła, M. Tarnacka, M. Geppert-Rybczyńska, M. Zubko, M. Staniszewska, M. Smoleński, J. Dobosz, G. Garbacz, K. Kamiński, E. Kamińska, **Hydrophilic and amphiphilic macromolecules as modulators of the physical stability and bioavailability of piribedil: a study on binary mixtures and micellar systems**, *Molecular Pharmaceutics*, 2025, 22(8), 4708−4730.

mój udział polegał na przeprowadzeniu części eksperymentów uwalniania API z amorficznych dyspersji stałych, wizualizacji danych i ich wstępnej analizie.

Michał Smoleński
Podpis współautora publikacji

Wrocław, 16.04.2026
Miejsce i data

Justyna Dobosz
Imię i nazwisko współautora publikacji

Physiolution Polska sp. z o.o.
Afiliacja

OŚWIADCZENIE

Oświadczam, że w pracy:

P4. L. Orszulak, A. Minecka, R. Bernat, T. Lamrani, K. Jurkiewicz, B. Hachuła, M. Tarnacka, M. Geppert-Rybczyńska, M. Zubko, M. Staniszewska, M. Smoleński, J. Dobosz, G. Garbacz, K. Kamiński, E. Kamińska, **Hydrophilic and amphiphilic macromolecules as modulators of the physical stability and bioavailability of piribedil: a study on binary mixtures and micellar systems**, *Molecular Pharmaceutics*, 2025, 22(8), 4708−4730.

mój udział polegał na przeprowadzeniu części eksperymentów uwalniania API z amorficznych dyspersji stałych zawierających różne rodzaje matryc polimerowych.

.....
Podpis współautora publikacji

Wrocław, 16.04.2026
Miejsce i data

Marcela Staniszewska
Imię i nazwisko współautora publikacji

Physiolution Polska sp. z o.o.
Afiliacja

OŚWIADCZENIE

Oświadczam, że w pracy:

P4. L. Orszulak, A. Minecka, R. Bernat, T. Lamrani, K. Jurkiewicz, B. Hachuła, M. Tarnacka, M. Geppert-Rybczyńska, M. Zubko, M. Staniszewska, M. Smoleński, J. Dobosz, G. Garbacz, K. Kamiński, E. Kamińska, **Hydrophilic and amphiphilic macromolecules as modulators of the physical stability and bioavailability of piribedil: a study on binary mixtures and micellar systems**, *Molecular Pharmaceutics*, 2025, 22(8), 4708−4730.

mój udział polegał na przeprowadzeniu części eksperymentów uwalniania API z amorficznych dyspersji stałych, wizualizacji danych i ich wstępnej analizie.

Marcela Staniszewska
Podpis współautora publikacji

6. Podsumowanie i wnioski

Przedstawiona rozprawa doktorska wpisuje się w aktualny i intensywnie rozwijający się nurt badań nad wykorzystaniem polimerów jako nowoczesnych substancji pomocniczych w technologii farmaceutycznej. Jej zasadniczym celem było opracowanie nowych strategii syntezy dobrze zdefiniowanych polimerów PVP o zróżnicowanej topologii i ściśle kontrolowanych parametrach makrostrukturalnych, a następnie ocena ich przydatności w stabilizacji oraz modyfikowaniu właściwości wybranych substancji leczniczych. Podjęta tematyka odpowiada na istotną lukę badawczą, dotyczącą wpływu architektury makrocząsteczek na zachowanie API w układach farmaceutycznych, zwłaszcza w kontekście stabilności fizycznej, hamowania rekrystalizacji, zwiększania rozpuszczalności oraz kształtowania parametrów biofarmaceutycznych.

Cykl czterech publikacji składających się na rozprawę dostarczył oryginalnych i wzajemnie uzupełniających się danych eksperymentalnych, potwierdzających, że topologia, długość łańcucha oraz charakter chemiczny polimeru odgrywają kluczową rolę w projektowaniu efektywnych formulacji API. W badaniach wykazano, że architektura makrocząsteczek wpływa zarówno na mieszalność układów API–polimer, jak i na charakter oddziaływań międzycząsteczkowych, co bezpośrednio przekłada się na kinetykę rekrystalizacji substancji aktywnych w stanie amorficznym. Udowodniono również, że odpowiednio dobrana topologia PVP może skutecznie modulować porządek molekularny i temperatury przejść fazowych ciekłokrystalicznych API, umożliwiając uzyskanie materiałów w pełni amorficznych oraz poprawę rozpuszczalności leku.

Szczególne znaczenie mają wyniki dotyczące wpływu charakteru chemicznego makrocząsteczek na stabilność fizyczną i właściwości farmakokinetyczne badanych układów. W tym obszarze wykazano, że świadomy dobór polimeru hydrofilowego lub amfifilowego może prowadzić do jednoczesnej poprawy stabilności formulacji i parametrów uwalniania substancji aktywnej. Istotnym osiągnięciem poznawczym było także odkrycie nowej, wcześniej nieopisanej formy polimorficznej pirybedylu.

Rozprawa wnosi zatem istotny wkład do rozwoju chemii i fizykochemii polimerów stosowanych w farmacji. Jej nowatorstwo polega nie tylko na opracowaniu skutecznych metod syntezy polimerów PVP o zaawansowanej architekturze, ale również na wykazaniu, że cechy makrostrukturalne polimerów mogą być świadomie wykorzystywane jako narzędzie do sterowania właściwościami fizycznymi substancji aktywnych. Uzyskane rezultaty mają zarówno charakter badań podstawowych, poszerzających wiedzę o zależnościach struktura–funkcja w układach API–polimer, jak i aplikacyjnych, otwierających nowe możliwości racjonalnego projektowania nowoczesnych układów dostarczania leków.

Podsumowując, najważniejsze osiągnięcia naukowe to:

1. Opracowanie skutecznych strategii syntezy dobrze zdefiniowanych polimerów PVP o zróżnicowanej topologii oraz kontrolowanych parametrach makrostrukturalnych;

2. Wykazanie, że topologia oraz długość łańcucha polimerowego w istotny sposób wpływają na zdolność polimeru do hamowania rekrystalizacji API z fazy amorficznej;

3. Potwierdzenie, że skuteczność polimeru jako inhibitora krystalizacji zależy nie tylko od jego stężenia w formulacji, ale również od cech strukturalnych makrocząsteczki, w szczególności od jej architektury;

4. Udowodnienie, że architektura polimeru wpływa na mieszalność układów API–polimer oraz na charakter oddziaływań międzycząsteczkowych, a tym samym na stabilność fizyczną mieszanin binarnych;

5. Wykazanie, że nieliniowe homopolimery PVP mogą skuteczniej niż ich liniowe odpowiedniki zaburzać porządek ciekłokrystaliczny API, prowadząc do zaniku mezofaz i uzyskania materiału w pełni amorficznego;

6. Potwierdzenie, że odpowiedni dobór architektury matrycy polimerowej umożliwia modulowanie porządku molekularnego oraz temperatur przejść fazowych substancji leczniczych, co stwarza możliwość świadomego kształtowania ich właściwości użytkowych.

7. Stwierdzenie, że charakter chemiczny makrocząsteczek (hydrofilowość i amfifilowość) odgrywa istotną rolę w poprawie stabilności fizycznej formulacji oraz parametrów decydujących o efektywności farmaceutycznej API.

8. Dokonanie identyfikacji nowej, wcześniej nieopisanej formy polimorficznej piryibedyilu;

9. Udowodnienie, że parametry makrocząsteczkowe polimerów mogą stanowić ważne narzędzie racjonalnego projektowania nowoczesnych formulacji opartych na układach amorficznych.

Wyniki rozprawy otwierają nowe perspektywy badawcze i aplikacyjne w zakresie projektowania biokompatybilnych nośników polimerowych o zaawansowanej architekturze, przeznaczonych do poprawy rozpuszczalności, stabilności i biodostępności substancji aktywnych.

7. Bibliografia

1. Bayliss, N. & Schmidt, B. V. K. J. Hydrophilic polymers: Current trends and visions for the future. *Prog. Polym. Sci.* **147**, 101753 (2023).
2. Ornaghi, H. L., Monticeli, F. M. & Agnol, L. D. A Review on Polymers for Biomedical Applications on Hard and Soft Tissues and Prosthetic Limbs. *Polymers* vol. 15 4034 at https://doi.org/10.3390/polym15194034 (2023).
3. Zhang, S., Fang, H. & Tian, H. Recent Advances in Degradable Biomedical Polymers for Prevention, Diagnosis and Treatment of Diseases. *Biomacromolecules* **25**, 7015–7057 (2024).
4. Alfinaikh, R. S., Alamry, K. A. & Hussein, M. A. Sustainable and biocompatible hybrid materials-based sulfated polysaccharides for biomedical applications: a review. *RSC Adv.* **15**, 4708–4767 (2025).
5. Kumari, M., Ghosh, N. S., Singh, L. K. & Dubey, A. Natural and synthetic polymers : A comprehensive review of their applications in drug delivery and pharmaceutical research. **12**, 131–144 (2025).
6. Teodorescu, M., Bercea, M. & Morariu, S. Biomaterials of PVA and PVP in medical and pharmaceutical applications: Perspectives and challenges. *Biotechnol. Adv.* **37**, 109–131 (2019).
7. Bejaoui, M., Galai, H., Touati, F. & Kouass, S. Multifunctional Roles of PVP as a Versatile Biomaterial in Solid State. in *Dosage Forms* (ed. Ahmad, U.) (IntechOpen, 2021). doi:10.5772/intechopen.99431.
8. Kurakula, M. & Rao, G. S. N. K. Pharmaceutical assessment of polyvinylpyrrolidone (PVP): As excipient from conventional to controlled delivery systems with a spotlight on COVID-19 inhibition. *J. Drug Deliv. Sci. Technol.* **60**, 102046 (2020).
9. Franco, P. & De Marco, I. The use of poly(N-vinyl pyrrolidone) in the delivery of drugs: A review. *Polymers (Basel).* **12**, 18–21 (2020).
10. Kim, J. M. & Baig, C. Communication: Role of short chain branching in polymer structure and dynamics. *J. Chem. Phys.* **144**, 81101 (2016).
11. Gabriel, C. & Münstedt, H. Influence of long-chain branches in polyethylenes on linear viscoelastic flow properties in shear. *Rheol. Acta* **41**, 232–244 (2002).
12. Choe, D., Jeong, S. H. & Baig, C. Structural, topological, and rheological characteristics of entangled short-chain branched polymer melts under shear flow in comparison with the linear analog. *J. Rheol. (N. Y. N. Y).* **68**, 591–601 (2024).
13. Ramachandran, R. *et al.* Persistence length of short-chain branched polyethylene. *Macromolecules* **41**, 9802–9806 (2008).
14. Haaf, F., Sanner, A. & Straub, F. Polymers of n-vinylpyrrolidone: Synthesis, characterization and uses. *Polymer Journal* vol. 17 143–152 at https://doi.org/10.1295/polymj.17.143 (1985).
15. Nuber, A., Lang, S., Sanner, A. & Schroeder, G. Preparation of polyvinylpyrrolidone. **1985**, 3–5 (1988).
16. Truong, N. P., Jones, G. R., Bradford, K. G. E., Konkolewicz, D. & Anastasaki, A. A

comparison of RAFT and ATRP methods for controlled radical polymerization. *Nat. Rev. Chem.* **5**, 859–869 (2021).

17. Lu, X. *et al.* Controllable synthesis of poly(N-vinylpyrrolidone) and its block copolymers by atom transfer radical polymerization. *Polymer (Guildf).* **48**, 2835–2842 (2007).

18. Yamago, S. *et al.* Highly Versatile Organostibine Mediators for Living Radical Polymerization. *J. Am. Chem. Soc.* **126**, 13908–13909 (2004).

19. Ottou, W. N., Sardon, H., Mecerreyes, D., Vignolle, J. & Taton, D. Update and challenges in organo-mediated polymerization reactions. *Prog. Polym. Sci.* **56**, 64–115 (2016).

20. Guinaudeau, A., Mazières, S., Wilson, D. J. & Destarac, M. Aqueous RAFT/MADIXpolymerisation of N-vinyl pyrrolidone at ambient temperature. *Polym. Chem.* **3**, 81–84 (2012).

21. Perrier, S. & Takolpuckdee, P. Macromolecular design via reversible addition–fragmentation chain transfer (RAFT)/xanthates (MADIX) polymerization. *J. Polym. Sci. Part A Polym. Chem.* **43**, 5347–5393 (2005).

22. Moad, G., Rizzardo, A. E. & A, S. H. T. Living Radical Polymerization by the RAFT Process. 379–410 (2005).

23. Sun, D., Gao, W., Hu, H. & Zhou, S. Why 90% of clinical drug development fails and how to improve it? *Acta Pharm. Sin. B* **12**, 3049–3062 (2022).

24. Abbasi, S. *et al.* Maximizing the Oral Bioavailability of Poorly Water-Soluble Drugs Using Novel Oil-Like Materials in Lipid-Based Formulations. *Mol. Pharm.* **18**, 3281–3289 (2021).

25. Hasa, D. *et al.* Drug salt formation via mechanochemistry: The case study of vincamine. *Mol. Pharm.* **10**, 211–224 (2013).

26. Bhalani, D. V., Nutan, B., Kumar, A. & Singh Chandel, A. K. Bioavailability Enhancement Techniques for Poorly Aqueous Soluble Drugs and Therapeutics. *Biomedicines* **10**, (2022).

27. Laitinen, R., Lo̊bmann, K., Strachan, C. J., Grohganz, H. & Rades, T. Emerging trends in the stabilization of amorphous drugs. *Int. J. Pharm.* **453**, 65–79 (2013).

28. Rams-Baron, M. *et al*. *Amorphous drugs: Benefits and challenges*. *Amorphous Drugs: Benefits and Challenges* (2018). doi:10.1007/978-3-319-72002-9.

29. Kawakami, K. & Pikal, M. J. Calorimetric investigation of the structural relaxation of amorphous materials: Evaluating validity of the methodologies. *J. Pharm. Sci.* **94**, 948–965 (2005).

30. Brough, C. & Williams, R. O. Amorphous solid dispersions and nano-crystal technologies for poorly water-soluble drug delivery. *Int. J. Pharm.* **453**, 157–166 (2013).

31. Huang, Y. & Dai, W.-G. Fundamental aspects of solid dispersion technology for poorly soluble drugs. *Acta Pharm. Sin. B* **4**, 18–25 (2014).

32. Baghel, S., Cathcart, H. & O'Reilly, N. J. Polymeric Amorphous Solid Dispersions: A Review of Amorphization, Crystallization, Stabilization, Solid-State Characterization, and Aqueous Solubilization of Biopharmaceutical Classification System Class II Drugs. *J. Pharm. Sci.* **105**, 2527–2544 (2016).

33. Zhang, J., Guo, M., Luo, M. & Cai, T. Advances in the development of amorphous solid

dispersions: The role of polymeric carriers. *Asian J. Pharm. Sci.* **18**, 100834 (2023).

34. Kurakula, M. & Rao, G. S. N. K. Pharmaceutical assessment of polyvinylpyrrolidone (PVP): As excipient from conventional to controlled delivery systems with a spotlight on COVID-19 inhibition. *J. Drug Deliv. Sci. Technol.* **60**, 102046 (2020).

35. Minecka, A. *et al.* Impact of the Chain Length and Topology of the Acetylated Oligosaccharide on the Crystallization Tendency of Naproxen from Amorphous Binary Mixtures. *Mol. Pharm.* **18**, 347–358 (2021).

36. Song, J. S. & Sohn, Y. T. Crystal forms of naproxen. *Arch. Pharm. Res.* **34**, 87–90 (2011).

37. Tumanova, N. *et al.* Exploring polymorphism and stoichiometric diversity in naproxen/proline cocrystals. *CrystEngComm* **20**, 7308–7321 (2018).

38. Bunjes, H. & Rades, T. Thermotropic liquid crystalline drugs. *J. Pharm. Pharmacol.* **57**, 807–816 (2010).

39. Nandi, R. *et al.* Investigation of liquid crystalline property of a new calamitic liquid crystalline system methyl 4-(4′-(4′′-(decyloxy)benzyloxy) benzylideneamino)benzoate. *Liq. Cryst.* **44**, 1185–1193 (2017).

40. Bushby, R. J. & Kawata, K. Liquid crystals that affected the world: discotic liquid crystals. *Liq. Cryst.* **38**, 1415–1426 (2011).

41. Dierking, I. Handbook of liquid crystals. *Liq. Cryst. Today* **26**, 21–24 (2017).

42. Patterson, J., Bary, A. & Rades, T. Physical stability and solubility of the thermotropic mesophase of fenoprofen calcium as pure drug and in a tablet formulation. *Int. J. Pharm.* **247**, 147–157 (2002).

43. Peeters, J., Neeskens, P., Tollenaere, J. P., Van Remoortere, P. & Brewster, M. E. Characterization of the interaction of 2-hydroxypropyl-β-cyclodextrin With itraconazole at pH 2, 4, and 7. *J. Pharm. Sci.* **91**, 1414–1422 (2002).

44. Chen, Z. *et al.* Organic glasses with tunable liquid-crystalline order through kinetic arrest of end-over-end rotation: The case of saperconazole. *Soft Matter* **16**, 2025–2030 (2020).

45. Heczko, D. *et al.* Varying thermodynamic conditions as a new way to tune the molecular order in glassy itraconazole. *J. Mol. Liq.* **286**, 1–9 (2019).

46. Gujral, A. *et al.* Vapor-Deposited Glasses with Long-Range Columnar Liquid Crystalline Order. *Chem. Mater.* **29**, 9110–9119 (2017).

47. Bishop, C., Gujral, A., Toney, M. F., Yu, L. & Ediger, M. D. Vapor-Deposited Glass Structure Determined by Deposition Rate-Substrate Temperature Superposition Principle. *J. Phys. Chem. Lett.* **10**, 3536–3542 (2019).

48. Mierzwa, M., Rams-Baron, M., Capaccioli, S., Pawlus, S. & Paluch, M. How to align a nematic glassy phase – Different conditions – Different results. *J. Mol. Liq.* **280**, 314–318 (2019).

49. Deleu, D., Northway, M. G. & Hanssens, Y. Clinical pharmacokinetic and pharmacodynamic properties of drugs used in the treatment of Parkinson's disease. *Clin. Pharmacokinet.* **41**, 261–309 (2002).

50. Millan, M. J. From the cell to the clinic: A comparative review of the partial D2/D3 receptor agonist and α2-adrenoceptor antagonist, piribedil, in the treatment of Parkinson's disease.

Pharmacol. Ther. **128**, 229–273 (2010).

51. Perez-Lloret, S. & Rascol, O. Piribedil for the Treatment of Motor and Non-motor Symptoms of Parkinson Disease. *CNS Drugs* **30**, 703–717 (2016).

52. Uppuluri, C. T., Ravi, P. R. & Dalvi, A. V. Design, optimization and pharmacokinetic evaluation of Piribedil loaded solid lipid nanoparticles dispersed in nasal in situ gelling system for effective management of Parkinson's disease. *Int. J. Pharm.* **606**, 120881 (2021).

53. M. Demirel R. H. Müller, F. Kiliç, B. Bozan, Y. Y. Formulation and in vitro-in vivo evaluation of piribedil solid lipid micro- and nanoparticles. *J. Microencapsul.* **18**, 359–371 (2001).

54. Pacułt, J., Rams-Baron, M., Chrząszcz, B., Jachowicz, R. & Paluch, M. Effect of Polymer Chain Length on the Physical Stability of Amorphous Drug-Polymer Blends at Ambient Pressure. *Mol. Pharm.* **15**, 2807–2815 (2018).

55. Sui, X. *et al.* The Effect of PVP Molecular Weight on Dissolution Behavior and Physicochemical Characterization of Glycyrrhetinic Acid Solid Dispersions. *Adv. Polym. Technol.* **2020**, (2020).

56. Mohapatra, S., Samanta, S., Kothari, K., Mistry, P. & Suryanarayanan, R. Effect of Polymer Molecular Weight on the Crystallization Behavior of Indomethacin Amorphous Solid Dispersions. *Cryst. Growth Des.* **17**, 3142–3150 (2017).

57. Maksym, P. *et al.* Pressure-assisted strategy for the synthesis of vinyl pyrrolidone-based macro-star photoiniferters. A route to star block copolymers. *J. Polym. Sci.* **58**, 1393–1399 (2020).

58. Moad, G. RAFT polymerization to form stimuli-responsive polymers. *Polym. Chem.* **8**, 177–219 (2017).

59. Roka, N., Kokkorogianni, O., Kontoes-Georgoudakis, P., Choinopoulos, I. & Pitsikalis, M. Recent Advances in the Synthesis of Complex Macromolecular Architectures Based on Poly(N-vinyl pyrrolidone) and the RAFT Polymerization Technique. *Polymers (Basel).* **14**, (2022).

60. Skotnicki, M., Czerniecka-Kubicka, A., Neilsen, G., Woodfield, B. F. & Pyda, M. Application of advanced thermal analysis for characterization of crystalline and amorphous phases of carvedilol. *J. Pharm. Biomed. Anal.* **217**, 114822 (2022).

61. Lapuk, S. E., Mukhametzyanov, T. A., Schick, C. & Gerasimov, A. V. Crystallization kinetics and glass-forming ability of rapidly crystallizing drugs studied by Fast Scanning Calorimetry. *Int. J. Pharm.* **599**, 120427 (2021).

62. Hurley, D., Davis, M., Walker, G. M., Lyons, J. G. & Higginbotham, C. L. The effect of cooling on the degree of crystallinity, solid-state properties, and dissolution rate of multi-component hot-melt extruded solid dispersions. *Pharmaceutics* **12**, (2020).

63. Paudel, A., Nies, E. & den Mooter, G. Van. Relating hydrogen-bonding interactions with the phase behavior of naproxen/PVP K 25 solid dispersions: evaluation of solution-cast and quench-cooled films. *Mol. Pharm.* **9 11**, 3301–3317 (2012).

64. Teerakapibal, R., Huang, C., Gujral, A., Ediger, M. D. & Yu, L. Organic Glasses with Tunable Liquid-Crystalline Order. *Phys. Rev. Lett.* **120**, 55502 (2018).

8. Lista pozostałych publikacji niewchodzących w cykl rozprawy doktorskiej

- T. Lamrani, L. Orszulak, M. Tarnacka, B. Hachuła, K. Nowakowska, K. Kamiński, K. Jurkiewicz, **Effect of solvent evaporation on the liquid-crystalline order of itraconazole**, *Scientific Reports*, 2025, 15 (1), 40129.

- D. Heczko, B. Hachuła, P. Maksym, K. Kamiński, A. Zięba, L. Orszulak, M. Paluch, E. Kamińska, **The Effect of Various Poly (N-vinylpyrrolidone) (PVP) Polymers on the Crystallization of Flutamide**, *Pharmaceuticals*, 2022, 15 (8), 971.

- R. Bernat, P. Maksym, M. Tarnacka, K. Koperwas, J. Knapik-Kowalczuk, K. Malarz, A. Mrozek-Wilczkiewicz, A. Dzienia, T. Biela, R. Turczyn, L. Orszulak, B. Hachuła, M. Paluch, K. Kamiński, **The effect of high-pressure on organocatalyzed ROP of γ-butyrolactone**, *Polymer*, 2021, 233, 124166.

9. Lista konferencji i seminariów naukowych o zasięgu krajowym i zagranicznym

- V Seminarium Ogólnoakademickie "Metody fizykochemiczne w badaniach naukowych" w Sosnowcu (27 marca 2024) - komunikat posterowy pt. *"The impact of PVP topology on the crystallization of metronidazole – thermal, structural and spectroscopic studies"*.

- 66. Zjazd Polskiego Towarzystwa Chemicznego (PTChem) w Poznaniu (15-20 września 2024) - komunikat sekcyjny pt. „*Poli(winylopirolidon) o zróżnicowanych topologiach jako skuteczne matryce polimerowe w dostrajaniu pożądanych właściwości ciekłokrystalicznych leków"*.

- VI Seminarium Ogólnoakademickie "Metody fizykochemiczne w badaniach naukowych" w Sosnowcu (16 kwietnia 2025) - komunikat posterowy pt. *"Poly(vinylpyrrolidone) with various topologies as effective polymer matrices for tuning the desired properties of liquid crystalline drugs"*.

- 10th International Discussion Meeting on Relaxations in Complex Systems (10thIDMRCS) w Barcelonie (20-25 lipca 2025) - komunikat posterowy pt. *"Hydrophilic and amphiphilic macromolecules as modulators of the physical stability and bioavailability of piribedil"*

- XXV Conference on Applied Crystallography (CAC) w Wiśle (7-10 września 2025) - komunikat posterowy pt.*"Polyvinylpyrrolidone with varied architectures as efficient polymer matrices for tailoring the desired properties of liquid-crystalline pharmaceuticals"*.

10. Inne osiągnięcia

Kierowanie projektami badawczymi

- ***Perły Nauki*** (nr PN/01/0078/2022)

  instytucja finansująca: Ministerstwo Edukacji i Szkolnictwa Wyższego

  tytuł projektu: *Biozgodne polimery o kontrolowanej taktyczności i ich wpływ na stabilność API w układach binarnych*

  okres trwania: maj 2023 – maj 2027

- ***Grant Studencki*** (nr COS.1170.16.2021)

  instytucja finansująca: Uniwersytet Śląski w Katowicach

  tytuł projektu: *Nowoczesne metody syntezy biodegradowalnych biokompatybilnych materiałów polimerowych o różnej topologii przeznaczonych do celów biomedycznych*

  okres trwania: maj 2021 – listopad 2021

Uczestnictwo w projektach badawczych

- 07/2024-03/2025 – wykonawca Chemik w projekcie badawczym ***LIDER*** pn. *„Opracowanie innowacyjnych metod poprawy parametrów farmakokinetycznych i farmakodynamicznych wybranych substancji farmaceutycznie aktywnych (APIs)”* o numerze LIDER/28/0152/L-12/20/NCBR/2021, finansowanym przez Narodowe Centrum Badań i Rozwoju, (okres trwania: marzec 2022 – marzec 2025; dofinansowanie: 1 465 625,00 zł).
- 07/2021-04/2022 – wykonawca Chemik w projekcie badawczym ***Inkubator Innowacyjności 4.0*** pn. *„Nowoczesne metody otrzymywania ultra-czystych biodegradowalnych i biokompatybilnych materiałów polimerowych o zróżnicowanej topologii zawierających segmenty poli(γ-butyrolaktonu). Ocena ich użytkowalności do celów biomedycznych”* o numerze MNISW/2020/335/DIR, finansowanym przez Ministerstwo Edukacji i Nauki, (okres trwania: lipiec 2021 – czerwiec 2022; dofinansowanie: 76 655,52 zł).
- 05/2021 – wykonawca Chemik w projekcie badawczym ***SONATA 14*** pn. *„Innowacyjne metody polimeryzacji „mniej aktywowanych monomerów” (LAMs)”* o numerze DEC-2018/31/D/ST5/03464, finansowanym przez Narodowe Centrum Nauki, (okres trwania: lipiec 2019 – lipiec 2022; dofinansowanie: 984 900,00 zł).

Uczestnictwo w projektach dydaktycznych

- METROPOLITALNY FUNDUSZ WSPIERANIA NAUKI
  pozyskanie finansowania z Górnośląsko-Zagłębiowskiej Metropolii (GZM) w ramach konkursu *"Metropolitalny Fundusz Wspierania Nauki: Studiuj w Metropolii"*
  lipiec-sierpień 2025
  tytuł projektu: *Lato w Laboratorium: Zobacz, jak działa nauka!*
  kwota dofinansowania: 44 910,00 zł

- Science SPARK – Szkoła, Pasja, Aktywność, Rozwój, Kreatywność
  przygotowanie i współprowadzenie wykładów popularnonaukowych dla uczniów w ramach programu *„Odkrywcy"* finansowanego przez Ministerstwo Edukacji i Szkolnictwa Wyższego

Patenty i zgłoszenia patentowe

- Grażyna Szafraniec-Gorol, Stanisław Krompiec, Marek Matussek, Luiza Orszulak, *"Pi-rozszerzona pochodna perylenu oraz sposób jej otrzymywania"*, nr 238588 ***(patent przyznany)***
- Kamil Kamiński, Magdalena Tarnacka, Luiza Orszulak, Roksana Wygoda, Karolina Jurkiewicz, Marian Paluch, Ewa Kamińska, Aldona Minecka, *"Sposób otrzymywania formy polimorficznej (II) pirybedylu"*, nr P.451342 ***(zgłoszenie patentowe, w trakcie oceny)***
- Kamil Kamiński, Magdalena Tarnacka, Luiza Orszulak, Roksana Wygoda, Karolina Jurkiewicz, Marian Paluch, Ewa Kamińska, Aldona Minecka, *„Sposób otrzymywania formy polimorficznej (II) pirybedylu w formulacji z poliwinylopirolidonem"*, nr P.451344 ***(zgłoszenie patentowe, w trakcie oceny)***
- Roksana Wygoda, Luiza Orszulak, Paulina Maksym, Sylwia Golba, Kamil Kamiński, Magdalena Tarnacka, Marian Paluch, Ewa Kamińska, Aldona Minecka, *"Sposób otrzymywania poli(γ-butyrolaktonu) o topologii gwiaździstej"*, P.451633 ***(zgłoszenie patentowe, w trakcie oceny)***

Stypendia

- Stypendium dla najlepszych doktorantów z dotacji projakościowej w roku akademickim 2023/2024.
- Stypendium dla najlepszych doktorantów z dotacji projakościowej w roku akademickim 2024/2025.
- Stypendium dla najlepszych doktorantów z dotacji projakościowej w roku akademickim 2025/2026.